Conservative coupling method between an inviscid compressible fluid flow and a three-dimensional deformable structure with possible fragmentation

Maria Adela Puscas

UNIVERSITÉ PARIS-EST

THÈSE

présentée pour l'obtention du titre de

Docteur de l'Université Paris-Est

Spécialité : Mathématiques Appliquées

par **Maria Adela PUSCAS**

Sujet : **Méthode de couplage conservative entre un fluide compressible non-visqueux et une structure tridimensionnelle déformable pouvant se fragmenter**

Soutenue le 09 10 2014
devant le jury composé de :

Rapporteurs :	Rémi Abgrall
	Jean-Frédéric Gerbeau
Examinateurs :	Christian Mariotti
	Bertrand Maury
	Michel Visonneau
Directeurs de thèse :	Alexandre Ern
	Christian Tenaud
Invité :	Laurent Monasse

Remerciements

Trois années passées à établir des rapports, des comptes rendus, et bien sûr à rédiger mon manuscrit de thèse, me voilà aujourd'hui face à un exercice des plus difficiles, celui de rédiger ma page de remerciement. Non pas que je trouve cet exercice moins intéressant ou fastidieux, mais je crains que les mots employés ne reflètent pas toute la gratitude que j'aimerais témoigner envers tous ceux qui ont contribué, de près ou de loin à l'élaboration de ce projet scientifique.

Beaucoup d'interrogations, de remise en question voire de désespoir ont marqué les débuts de ma thèse. Les nombreuses difficultés rencontrées, liées en grande partie au caractère novateur du sujet proposé, ne m'ont pas découragées, et ont bien au contraire suscité ma curiosité et ma détermination. Grâce à l'appui engagé de mes encadrants et aux nombreuses riches discussions menées depuis le début, je ne pouvais que reprendre confiance et construire méthodiquement un plan de bataille aboutissant à la réalisation des objectifs escomptés. C'est donc en grande partie la présence active de mes encadrants qui a conditionné l'aboutissement de ce travail.

Je tiens à remercier en premier lieu mon directeur de thèse, Alexandre Ern pour ses conseils tant sur le fond que sur la forme. Sa rigueur, sa réactivité et son enthousiasme ont été déterminants à l'aboutissement des travaux dans les délais impartis.

Dès le départ, les échanges que j'ai eus avec mon codirecteur de thèse, Christian Tenaud, ont été très agréables. Je le remercie pour ses conseils avisés et ses remarques pertinentes concernant le schéma numérique ainsi que les résultats obtenus qui ont grandement contribué à l'avancement de mes travaux.

C'est grâce à Christian Mariotti que ce travail de thèse a été initié et dont le CEA a accepté le financement. Dès le départ, il a eu les idées claires sur les objectifs escomptés et les moyens à mettre en œuvre pour les atteindre. Je le remercie d'avoir bien su cadrer le déroulement de la thèse par ses nombreuses et pertinentes interventions lors des réunions de travail.

Laurent Monasse est incontestablement celui avec qui j'ai eu le plus d'échanges, à la fois sur la partie modélisation, mais aussi et surtout sur le débogage du code de simulation numérique. J'ai énormément appris à son contact, ses conseils m'ont fait beaucoup progresser. C'est pourquoi je tiens à le remercier chaleureusement pour sa constante disponibilité, pour tout ce qu'il m'a expliqué et fait partager.

Je remercie également Virginie Daru pour son soutien et l'intérêt qu'elle a montré pour mon sujet de thèse.

J'exprime mes sincères remerciements à tous les membres du jury qui m'ont fait l'honneur de venir assister à ma soutenance de thèse. C'est ainsi que je remercie Bertrand Maury et Michel Visonneau et tout particulièrement les rapporteurs, Rémi Abgrall et Jean-Frédéric Gerbeau, pour avoir examiné le manuscrit et pour les remarques pertinentes qu'ils ont émis, témoignant de leur grand intérêt pour le sujet traité.

Un grand merci à toutes les personnes du CERMICS, du CEA et du LIMSI grâce à qui cette thèse a pu se dérouler dans d'excellentes conditions, en particuliers Jean-François Delmas, Pierre Franck Piserchia, Nicolas Lardjane, Ludovic Aubry, Isabelle Simunic, Nathalie Quelleu, Carherine Baccaert, Maria Biard, Isabelle Rouillon et Christine Bazin.

Durant ces trois années, j'ai pu rencontrer plusieurs doctorants et post-doctorants que je souhaite remercier pour leur amitié, leur bonne humeur et leurs encouragements. Je ne ferai pas une liste de ces personnes au risque d'en oublier.

Je voudrais adresser de très sincères remerciements à tous mes amis. Leur amitié m'a beaucoup apporté.

Grand clin d'œil enfin à toute ma famille pour leur confiance et leur soutien.

Les trois années passées ont été très intenses, riche en émotions, et constituent une expérience unique. J'en garde un excellent souvenir.

Méthode de couplage conservative entre un fluide compressible non-visqueux et une structure tridimensionnelle déformable pouvant se fragmenter

Résumé : Nous développons une méthode de couplage entre un fluide compressible non-visqueux et une structure tridimensionnelle mobile. Nous considérons d'abord une structure rigide, puis déformable, et enfin avec fragmentation. Le couplage repose sur une méthode conservative de type frontières immergées en combinaison avec une méthode de Volumes Finis pour le fluide et une méthode d'Éléments Discrets pour la structure. La méthode de couplage assure la conservation de la masse, de la quantité de mouvement et de l'énergie totale du système. Elle présente également des propriétés de consistance, comme l'absence d'effets de rugosité artificielle sur une paroi rigide. La méthode de couplage est explicite en temps dans le cas d'une structure rigide, et semi-implicite dans le cas d'une structure déformable. La méthode semi-implicite en temps évite que des déformations tangentielles de la structure ne se transmettent au fluide, et la résolution itérative jouit d'une convergence géométrique sous une condition CFL non restrictive sur le pas de temps. Nous présentons des résultats numériques montrant la robustesse de la méthode dans le cas d'une sphère rigide mise en mouvement par une onde de choc, une poutre encastrée fléchie par une onde de choc et un cylindre se fragmentant sous l'action d'une explosion interne.
Mots-clés : Interaction fluide-structure, frontières immergées, couplage tridimensionnel, Volumes Finis, Éléments Discrets, méthode conservative, fragmentation.

Conservative coupling method between an inviscid compressible fluid flow and a three-dimensional deformable structure with possible fragmentation

Abstract : We develop a coupling method between an inviscid compressible fluid and a three-dimensional mobile structure. We consider first a rigid structure, then a deformable, and finally a fragmenting one. The coupling hinges on a Conservative Immersed Boundary method combined with a Finite Volume method for the fluid and a Discrete Element method for the structure. The method yields conservation of mass, momentum, and energy of the system. The method also exhibits consistency properties, such as the absence of numerical roughness on a rigid wall. The method is explicit in time in the case of a rigid structure, and semi-implicit when the structure is deformable. The time semi-implicit method avoids that tangential deformations of the structure impact the fluid, and the method converges geometrically with a non-restrictive CFL condition on the time step. We present numerical results showing the robustness of the method in the case of a rigid sphere lifted by a shock wave, a clamped beam flexed by a shock wave, and a cylinder undergoing fragmentation owing to an intern explosion.
Keywords : Fluid-structure interaction, Immersed Boundary, Three-dimensional coupling, Finite Volumes, Discrete Element, conservative method, fragmentation.

Table des matières

1

Introduction

1.1 Contexte

L'interaction fluide-structure concerne l'étude du comportement dynamique d'une ou plusieurs structures solides mobiles, rigides ou déformables, interagissant avec un écoulement fluide, liquide ou gazeux, intérieur et/ou extérieur à ces structures.

L'interaction fluide-structure se produit lorsque les forces de pression et les forces visqueuses dues à l'écoulement fluide et qui sont exercées sur la surface de la structure en contact avec le fluide, provoquent le déplacement rigide ou avec déformation de la structure. Ce déplacement, à son tour, modifie le domaine fluide et les conditions aux limites, et en conséquence la direction et l'intensité des forces de pression et des forces visqueuses. Ce cycle d'interactions entre le fluide et la structure est résumé dans la Fig. 1.1.

Dans certains cas spécifiques, les effets du fluide peuvent être estimés ou ignorés. Par exemple, les forces aérodynamiques s'exerçant sur une voiture conduite lentement. Dans ce cas, l'influence de l'air sur le véhicule peut être négligée. Cependant, à une certaine vitesse, la résistance aérodynamique commence à jouer un rôle important. Dans ces conditions, l'étude de l'écoulement

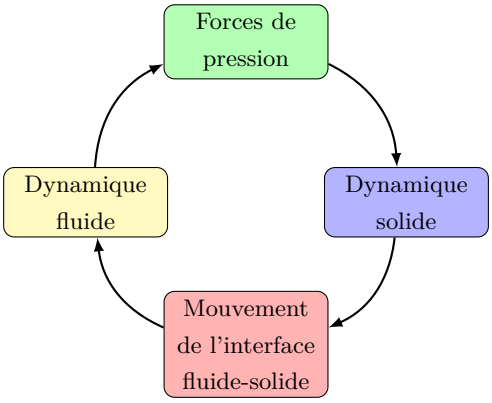

Figure 1.1: Cycle d'interaction fluide-structure

du fluide et de la dynamique de la structure ne peut plus se faire en traitant le fluide et le solide séparément.

Les phénomènes d'interaction fluide-structure jouent un rôle important dans de nombreux domaines scientifiques et d'ingénierie, tels que l'aéronautique, le génie civil, l'énergie, la biologie, le domaine militaire et celui de la prévention du risque, etc.. Quelques exemples sont présentés dans la Fig. 1.2. La compréhension et la prédiction précise des phénomènes d'interaction fluide-structure est importante pour perfectionner la conception des systèmes en jeu, afin d'éviter les problèmes potentiels d'instabilité, améliorer les performances en adaptant la structure, etc..

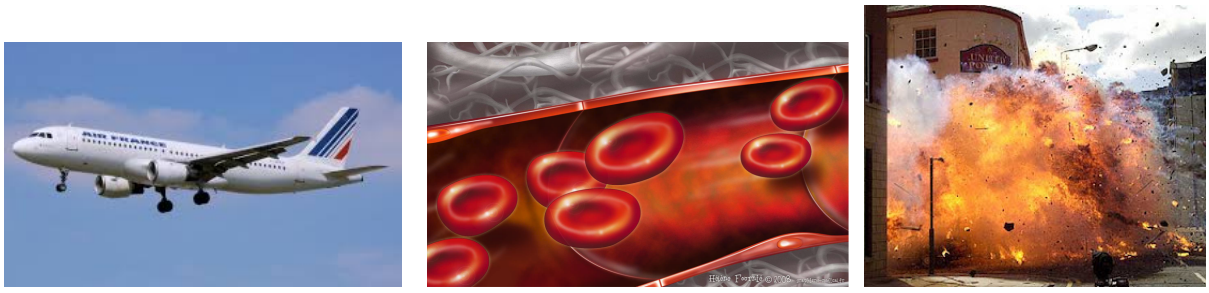

(a) (b) (c)

Figure 1.2: Exemples d'interaction fluide-structure : (a) écoulement autour d'un avion, (b) écoulement sanguin, (c) effets d'une explosion

Parmi cette grande variété de phénomènes d'interaction fluide-structure nous distinguons les situations où le fluide est en phase liquide (écoulement autour d'un sous-marin, écoulement dans les vaisseaux sanguins ou dans le cœur...) et celles où le fluide est en phase gazeuse (action du vent sur une voile de bateau, écoulement autour des avions, effet d'une explosion sur un bâtiment...). En fonction des équations régissant l'écoulement fluide, nous distinguons trois classes principales d'interactions fluide-structure : compressible, faiblement compressible ou incompressible.

Pour la plupart des problèmes d'interaction fluide-structure, les solutions analytiques des équations du modèle sont inconnues. De plus, les expériences de laboratoire sont généralement coûteuses et difficiles à réaliser. Ainsi, la simulation numérique constitue une approche alternative. L'étude approfondie des ces problèmes d'interaction fluide-structure reste un défi en raison de leur forte non-linéarité et de leur nature multidisciplinaire.

Nous nous intéressons plus particulièrement aux applications liées au domaine militaire et à la prévention du risque. Par exemple, les effets d'une explosion sur un bâtiment ou un sous-marin font intervenir des phénomènes non-linéaires complexes (ondes de choc, fissuration, rupture, fragmentation...) [99, 108]. Notre objectif est de simuler l'effet de l'arrivée d'une onde de choc aérienne sur une structure pouvant se fragmenter. L'échelle de temps caractéristique de ces phénomènes est extrêmement courte. Au moment de l'impact, l'effet dominant est causé par la surpression imposée par le fluide. Les effets visqueux jouent un rôle moins important dans la dynamique de ce type d'interaction. C'est pourquoi nous considérons dans cette thèse un écoulement compressible non visqueux.

1.2 État de l'art

Dans cette section, nous considérons un problème prototypique d'interaction fluide-structure ; la Fig. 1.3 montre un domaine fluide contenant un objet solide (ou structure). Nous appelons le domaine commun Ω, le domaine fluide Ω_{F} et le domaine de la structure Ω_{S}. Le couplage

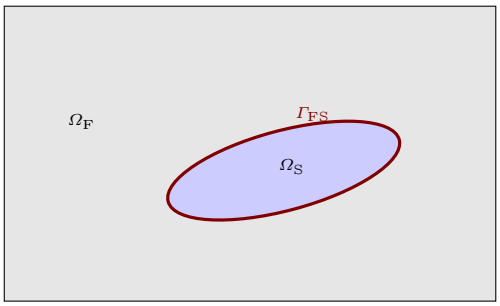

Figure 1.3: Interaction fluide-structure ; frontière Γ_{FS} mobile

est réalisé par des conditions aux limites à l'interface fluide-solide Γ_{FS} reliant les vitesses et les contraintes dans le solide et le fluide. Les conditions suivantes sont imposées sur Γ_{FS} :

$$\mathbf{u}_{\mathrm{F}} = \mathbf{u}_{\mathrm{S}}, \tag{1.1}$$

$$\sigma_{\mathrm{F}} \cdot \mathbf{n}_{\mathrm{F}} = \sigma_{\mathrm{S}} \cdot \mathbf{n}_{\mathrm{S}}, \tag{1.2}$$

où $\mathbf{u}_{\mathrm{F}}$ et $\mathbf{u}_{\mathrm{S}}$, σ_{F} et σ_{S}, $\mathbf{n}_{\mathrm{F}}$ et $\mathbf{n}_{\mathrm{S}}$ sont respectivement la vitesse, la contrainte et la normale extérieure sortante du fluide (variables indicées par F) et du solide (variables indicées par S).

Supposons maintenant que le domaine fluide est rempli d'air et que la structure est mobile. Le mouvement du solide va mettre le fluide en mouvement mais l'air n'agira pas de manière significative sur l'obstacle. Le mouvement de la structure contrôle le mouvement du fluide, mais le mouvement du fluide n'altère pratiquement pas celui de la structure. Maintenant, nous considérons que le fluide présente une onde de choc aérienne à vitesse élevée. L'écoulement du fluide agira sur la surface de la structure en contact avec le fluide, que par la suite nous appelons surface mouillée, et provoquera le déplacement avec ou sans déformation de la structure. Ce déplacement modifie le domaine fluide. Ici, les deux sous-systèmes influent l'un sur l'autre de façon non négligeable. Le domaine commun Ω reste inchangé, mais les sous-domaines Ω_{F} et Ω_{S} évoluent avec le temps. C'est l'une des principales difficultés liées à la modélisation des problèmes d'interaction fluide-structure et à la conception de méthodes numériques pour leur résolution.

1.2.1 Principales classes de méthodes

Les algorithmes d'interaction fluide-structure peuvent généralement être classés en deux catégories : celles relevant d'approches monolithiques et celles relevant d'approches partitionnées. Dans le cas d'approches partitionnées, une distinction importante est l'utilisation de maillage conformes ou non. Dans cette section, nous présentons brièvement ces différents approches.

1.2.1.1 Approche monolithique

L'approche monolithique [12, 34, 53, 54, 74, 94] traite l'écoulement du fluide et la dynamique de la structure dans le même cadre mathématique avec un système d'équations unique pour l'ensemble du problème. Les conditions à l'interface fluide-structure sont implicites dans le système. Les approches monolithiques sont aussi appelées fortement couplées ou directes car les équations fluides et solides sont résolues simultanément à chaque pas de temps, et sont traitées par un même code de calcul. Cette approche peut potentiellement atteindre une meilleure précision que l'approche partitionnée présentée ci-dessous, mais, en revanche, elle peut être très difficile à mettre en œuvre puisque les formalismes employés pour modéliser le fluide et le solide sont généralement différents : la formulation lagrangienne est préférentiellement employée pour décrire les solides tandis que les fluides sont plutôt traités dans une approche eulérienne. De plus, la grande gamme d'échelles de temps et d'espace, les différences drastiques dans le comportement constitutif du fluide et les réponses du solide peuvent conduire à des matrices du système très raides et mal conditionnées, ce qui rend l'approche monolithique difficile et coûteuse à appliquer, en particulier pour les problèmes non-linéaires avec de grands déplacements et de grandes déformations.

1.2.1.2 Approche partitionnée

Dans l'approche partitionnée [5, 24, 27, 31, 32, 65, 84, 85, 107], le système couplé est résolu à chaque pas de temps sous-système par sous-système, successivement ou itérativement, et des variables sont échangées à l'interface fluide-structure. Par conséquent, cette approche est plus flexible dans le sens où différents modèles mathématiques, méthodes numériques et techniques de discrétisation adaptés à chaque milieu (fluide et solide) peuvent être utilisés séparément. Les conditions à l'interface sont prises en compte explicitement afin de respecter la cinématique et les conditions aux limites dynamiques. Pour chaque milieu, un code de calcul spécifique est utilisé, et la difficulté consiste à faire transiter l'information d'un code à l'autre afin de faire communiquer les deux milieux. Une autre difficulté importante réside dans le traitement de l'interface dont la position et la vitesse ne sont pas connues et évoluent généralement au cours du temps. Ainsi, l'approche partitionnée nécessite le suivi de l'interface et des quantités qui y sont attachées, ce qui peut être à la fois délicat et parfois source importante d'erreurs voire de divergence de la méthode.

Les approches partitionnées peuvent être généralement divisées en méthodes **faiblement couplées** et **fortement couplées**. Dans les méthodes faiblement couplées [31, 84], un seul calcul fluide et solide est effectué à chaque pas de temps. Dans les méthodes fortement couplées [10, 11], des sous-itérations sont utilisées pour chacun des solveurs fluide et solide à chaque pas de temps, et par conséquent, ces méthodes sont plus précises et plus stables, mais aussi plus coûteuses en temps de calcul que les méthodes faiblement couplées.

Une attention particulière doit être apportée aux structures légères/souples se déplaçant dans un fluide incompressible dense, afin d'éviter les problèmes d'instabilité numérique causés par l'effet de masse ajoutée [6, 10, 14, 38, 56]. L'effet de masse ajoutée est dû à l'utilisation des déplacements de l'interface de la structure prédite à partir de l'étape précédente de sous-itération, ou de l'étape précédente d'itération, au lieu du déplacement de l'interface de l'étape en cours (sous-itération ou itération courante), ce qui conduit à une prédiction erronée des forces de couplage qui agissent comme une masse supplémentaire, "ajoutée" à l'interface. Les méthodes fortement couplées sont plus performantes car les sous-itérations sont utilisées pour corriger les forces échangées à l'interface, mais les effets de masse ajoutée peuvent encore conduire à des problèmes de convergence [10]. La compressibilité ou l'incompressibilité du fluide en interaction joue également un rôle important dans la stabilité des schémas de couplage fluide-structure.

Dans la mesure où l'approche partitionnée nécessite la connaissance de la position et de la vitesse de l'interface, il est important de se pencher sur les méthodes de définition de cette interface. Dans ce cadre, nous pouvons séparer les méthodes en **méthodes sur maillage fluide conforme** (c'est-à-dire respectant la position courante de l'interface) et **méthodes sur maillage fluide non-conforme**. La procédure utilisée pour imposer les conditions (1.1) et (1.2) à l'interface fluide-solide dépend de la conformité ou non du maillage.

Les méthodes sur maillage fluide conforme [5, 24, 32, 65, 107] tiennent compte des conditions d'interface à l'emplacement de l'interface. Ces méthodes impliquent généralement trois champs qui décrivent respectivement l'écoulement du fluide, la dynamique de la structure et le mouvement de l'interface, ce dernier induisant un mouvement du maillage fluide. En raison du déplacement de la structure solide, un remaillage ou une mise à jour du maillage fluide est nécessaire. Nous pouvons citer ici les méthodes ALE (Arbitrary Lagrangian–Eulerian) [24, 65] et les méthodes mortar [47].

A contrario, les méthodes sur maillage fluide non-conforme traitent l'emplacement de l'interface et les conditions associées comme des contraintes imposées sur les équations de sorte qu'un maillage fluide non-conforme peut être utilisé. Par conséquent, les équations fluides et solides peuvent être résolues de façon indépendante les unes des autres, avec leurs grilles respectives, et un remaillage n'est plus nécessaire. La plupart des méthodes sur maillage fluide non-conforme sont basées sur les méthodes de type frontières immergées qui introduisent des conditions supplémentaires dans la formulation fluide afin d'imposer les conditions aux limites à l'interface fluide-solide. Nous allons maintenant détailler ces méthodes.

1.2.2 Méthodes des domaines fictifs

La méthode des frontières immergées a été développée à l'origine par Peskin [85] pour l'étude du flux sanguin dans le cœur, et a été depuis largement étudiée et appliquée à une grande variété de problèmes d'interaction fluide-structure [30, 46, 58, 60, 61, 106]. Cette méthode résout les équations du fluide avec un terme supplémentaire représentant les effets du solide agissant sur le fluide. Ce terme additionnel est calculé explicitement à partir de la configuration de la structure et est ensuite utilisé dans le calcul de la vitesse du fluide. Les équations du fluide sont résolues sur toute la grille de discrétisation du domaine fluide avec un maillage eulérien fixe et la frontière fluide-solide est suivie séparément [75, 86].

La méthode des frontières immergées développée par Peskin traite uniquement les structures qui n'occupent pas de volume, par exemple une courbe en 2d ou une surface en 3d. Nous avons donc avec les notation de la Fig. 1.3, $\Omega_S = \Gamma_{FS}$. Afin de représenter l'interaction entre un fluide et un solide occupant un volume, les méthodes des domaines immergés ou de domaines fictifs ont été développées. Dans le cadre de ces méthodes, le solide est superposé à la grille de discrétisation du domaine fluide. En conséquence, certaines cellules sont masquées par le solide ("cellules solides"), d'autres sont complètement incluses dans le fluide ("cellules fluides"), les cellules restantes étant coupées par la surface du solide ("cellules coupées"), voir Fig. 1.4. Un état artificiel du fluide est introduit dans les cellules solides afin d'étendre le domaine fluide à toute la grille de discrétisation. La question est alors de savoir quelles conditions imposer afin que les équations régissant le mouvement du fluide prennent en compte correctement la présence du solide.

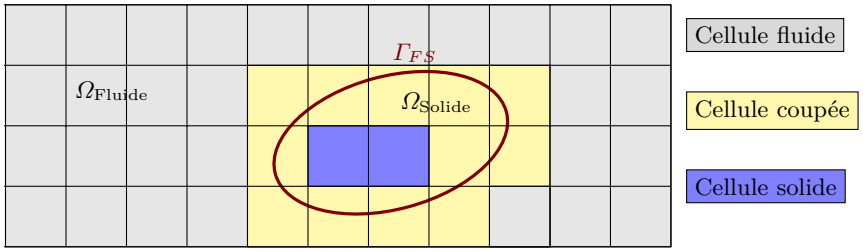

Figure 1.4: Types de ce cellules dans les méthodes des domaines fictifs

Différentes méthodes de domaines fictifs ont été proposées : les méthodes par multiplicateurs de Lagrange [40, 41, 98], les méthodes de forçage direct (Direct Forcing) [30, 48, 76], les méthodes multi-domaines [71, 103, 104], les méthodes Ghost fluid [33, 35, 36, 106], les méthodes conservatives [17, 31, 52, 82, 84, 97], etc. Nous en donnons maintenant un bref aperçu. Pour une revue plus détaillée sur les méthodes des frontières immergées et sur les méthodes numériques de simulation des problèmes d'interaction fluide-structure, voir par exemple [7, 25, 51, 75].

1.2.2.1 Méthodes par multiplicateurs de Lagrange

L'approche par multiplicateurs de Lagrange a été développée par Glowinski et al. [40, 42], et consiste à imposer les conditions aux limites (1.1) et (1.2) dans la formulation variationnelle du fluide par des multiplicateurs de Lagrange. Glowinski et al. ont développé deux approches : une première approche par multiplicateurs de Lagrange de type frontière (Boundary Lagrange multiplier) [42] et une deuxième approche par multiplicateurs de Lagrange distribués (Distributed Lagrange multiplier) [40]. Dans l'approche par multiplicateurs de Lagrange de type frontière, ces derniers sont définis uniquement pour la surface mouillée de la structure immergée dans le fluide (i.e. l'interface fluide-structure). Cela signifie qu'il y a uniquement besoin de mailler cette surface mouillée. Dans l'approche basée sur les multiplicateurs de Lagrange distribués, nous considérons que les multiplicateurs sont répartis sur l'ensemble du domaine immergé. Cela signifie que le domaine dans lequel ils sont définis n'est plus uniquement représenté par l'interface fluide-structure, mais par le volume occupé par la structure immergée. Par conséquent, l'intérieur de la structure doit être maillé.

1.2.2.2 Méthodes multi-domaines

Les méthodes multi-domaines sont basées sur les idées des méthodes de décomposition de domaine. Plusieurs approches ont été proposées pour l'interaction entre un fluide compressible ou incompressible avec des structures rigides fixes ou mobiles.

La méthode Fat Boundary a été développée par Maury [71] afin de résoudre un problème de Poisson dans un domaine avec des trous. L'idée est de remplacer le problème initial par un problème équivalent défini dans un domaine plus simple. Ce domaine plus simple est tel qu'un

maillage Cartésien est autorisé, permettant ainsi l'utilisation de solveurs rapides et de préconditionneurs efficaces. Le problème initial est vu maintenant comme deux sous-problèmes : un "problème global" et un "problème local". Le problème global est défini sur un domaine qui contient le domaine perforé. Le problème local est défini dans un voisinage des trous et un maillage plus fin peut être considéré dans le but de mieux approcher la solution.

Tidriri et Le Tallec [103, 104] ont développé une approche de type décomposition de domaine avec recouvrement pour les équations de Navier–Stokes compressibles. Un maillage Cartésien est utilisé pour le problème global et un deuxième maillage est construit autour de la frontière de chaque trou. La résolution est essentiellement divisée en deux phases, une résolution des équations de Navier–Stokes compressibles sous forme conservative avec une discrétisation de type Volumes Finis dans le domaine global, et une écriture sous forme non-conservative pour les problèmes locaux permettant d'approcher la condition de Dirichlet (1.1) à l'interface. Cette méthode permet la résolution du problème global sur le maillage Cartésien en utilisant des solveurs rapides tels que les transformées de Fourier rapides, tandis que la solution pour le problème local peut être approchée avec précision dans un voisinage du trou.

1.2.2.3 Méthodes de forçage direct et Ghost fluid

Les méthodes de forçage direct modifient les valeurs dans les cellules fluides dans un voisinage de la paroi solide, mais n'assurent pas la conservation exacte de quantités physiques à l'interface fluide-solide [20, 76].

Les méthodes Ghost fluid consistent à modifier la valeur dans les cellules solides (cellules fantômes) afin de calculer les flux fluides avec précision à l'interface. Les méthodes Ghost fluid éliminent souvent la contrainte de conservation de l'énergie afin de tempérer les oscillations numériques parasites à l'interface dans les problèmes d'interaction multifluides [2].

1.2.2.4 Méthodes conservatives

Les méthodes conservatives ont été proposées au départ par Noh [82] pour la résolution du couplage entre une méthode lagrangienne pour le solide et une méthode Volumes Finis eulérienne pour l'écoulement compressible. Ces méthodes consistent en une approche de type Volumes Finis de l'interaction, avec une discrétisation spatiale satisfaisant la conservation de la masse, de la quantité de mouvement et de l'énergie. Dans la formulation Volumes Finis, les flux entre les cellules fluides sont calculés dans un premier temps sans tenir compte de la présence du solide, et dans un deuxième temps, des corrections sont apportées afin de satisfaire la conservation des variables conservatives. Les cellules coupées représentent la principale difficulté de ces méthodes car elles peuvent avoir un volume très petit, ce qui induit une forte diminution du pas de temps afin d'assurer la condition CFL, et donc la stabilité du schéma. Plusieurs méthodes ont été développées afin d'assurer d'une part la conservation des variables conservatives et d'autre part

la stabilité du schéma sans réduction du pas de temps. Par exemple, dans [17] le défaut de conservation est évalué dans chaque cellule coupée et est ensuite redistribué sur la cellule coupée et sur les cellules voisines. Dans [31], les cellules coupées sont mélangées avec une cellule voisine entièrement fluide et dans [52], les cellules coupées sont mélangées dans la direction de la normale extérieure au solide.

1.2.3 Interaction fluide-structure avec fragmentation de la structure

Le phénomène de fragmentation est très complexe et implique la création et la propagation de micro/macro fractures, des phénomènes de plasticité, d'échauffement, etc.. La modélisation et la simulation du processus de fragmentation sont très difficiles. De nombreuses études ont été conduites et représentent encore un domaine de recherche très actif. Les modèles existants ne décrivent pas à ce niveau de détail les processus qui conduisent à la création et à la propagation d'une fracture. Généralement, la fragmentation est réduite à une loi ou un critère relativement simple. Peu de recherches ont été faites sur l'interaction fluide-structure prennent en compte la fragmentation de la structure.

Une approche de type frontières immergées pour l'interaction fluide-structure a été développée dans le cas de la fracture et la fragmentation de coques minces [15, 21]. La méthode couple la fracture d'une coque mince discrétisée de façon Lagrangienne par une méthode Éléments Finis, et l'écoulement fluide discrétisé de façon Eulérienne par une méthode Volumes Finis sur un maillage Cartésien. Cette méthode utilise l'approche Level Set pour suivre la surface du solide immergé, et la méthode Ghost fluid afin d'imposer les conditions aux limites à l'interface fluide-structure. Le critère de fracturation de la coque mince est basé sur une interface coercive et utilise des éléments pré-fracturés pour modéliser la fracture. La connaissance de l'endroit où se produira la rupture est donc nécessaire. En outre, la pénétration du fluide à travers l'ouverture de la fracture nécessite la connaissance de sa forme.

Dans [92], une méthode de type Particules Immergées [102] a été développée pour un fluide compressible en interaction avec des coques minces pouvant se fracturer, sans connaissance *a priori* de la localisation de la fracture. La fracture est modélisée avec un critère de fracturation discret ou un critère de fracturation volumique. Cette méthode traite à la fois le fluide et la structure par des méthodes sans maillage (Meshfree Particles). Le solide est immergé dans le fluide. Le fluide est modélisé par une approche Lagrangienne, et dans le cas de grandes déformations, la ré-initialisation des particules de fluide est nécessaire. Cette ré-initialisation met en défaut la conservation de l'énergie [92].

Une autre approche de type frontières immergées pour l'interaction entre un écoulement compressible et la fracturation d'une coque mince a été développée dans [66], sans connaissance *a priori* de l'endroit où se produit la fracture. Le fluide est discrétisé en utilisant la méthode des Volumes Finis. La structure qui se fracture combine la méthode Extended Finite Element (X-FEM) [23, 101] avec une loi coercive pour la fracturation.

1.2.4 Choix de la méthode de couplage

Dans le cadre des applications auxquelles nous nous intéressons, le fluide est compressible non-visqueux et le solide subit de grands déplacements et de grandes déformations pouvant aller jusqu'à la fragmentation. Ainsi, les méthodes les plus adaptées sont les méthodes de domaine fictif évitant le remaillage du domaine fluide.

Une question importante dans l'interaction fluide compressible-structure est la conservation de la masse, de la quantité de mouvement et de l'énergie. En effet, la capture précise des chocs est basée sur les propriétés de conservation, et la préservation des propriétés physiques est un ingrédient important. C'est pour ces considérations que nous nous sommes tournés vers les méthodes conservatives afin de réaliser le couplage.

Une méthode de couplage conservative en deux dimensions d'espace entre un fluide compressible non-visqueux et un solide déformable subissant de grands déplacements a été développée dans [79, 80]. L'écoulement est régi par les équations d'Euler sous forme conservative. La résolution numérique de ces équations est basée sur une méthode explicite de type Volumes Finis sur une grille Cartésienne. Le solide est discrétisé par des Éléments Discrets. Cette méthode décrit la dynamique du milieu continu par l'interaction entre des particules supposées rigides via des forces et des moments [69, 81].

Une des contributions principales de cette thèse est l'extension de la méthode conservative développée dans [79, 80] pour des solides bidimensionnels sans fragmentation au cas de solides tridimensionnels déformables pouvant se fragmenter. L'extension tridimensionnelle est loin d'être simple puisqu'elle pose de nombreux défis tant au niveau numérique qu'algorithmique, une difficulté majeure étant le traitement des divers aspects géométriques en trois dimensions (recherche et calcul des intersections entre des objets tridimensionnels, reconstruction de maillages, etc.). Enfin, dans le cas de la fragmentation du solide, de nouveaux aspects doivent être pris en compte, notamment un changement de topologie, la définition d'un nouveau type de cellules (de type "vide") et la modélisation de la pénétration du fluide dans la fissure.

1.3 Discrétisation fluide

Le fluide est modélisé par les équations d'Euler (écoulement compressible non-visqueux) qui s'écrivent en coordonnées Cartésiennes :

$$\frac{\partial U}{\partial t} + \frac{\partial F(U)}{\partial x} + \frac{\partial G(U)}{\partial y} + \frac{\partial H(U)}{\partial z} = 0, \tag{1.3}$$

$$U = \begin{pmatrix} \rho \\ \rho u \\ \rho v \\ \rho w \\ \rho E \end{pmatrix}, F(U) = \begin{pmatrix} \rho u \\ \rho u^2 + p \\ \rho uv \\ \rho uw \\ (\rho E + p)u \end{pmatrix}, G(U) = \begin{pmatrix} \rho v \\ \rho uv \\ \rho v^2 + p \\ \rho vw \\ (\rho E + p)v \end{pmatrix}, H(U) = \begin{pmatrix} \rho w \\ \rho uw \\ \rho vw \\ \rho w^2 + p \\ (\rho E + p)w \end{pmatrix},$$

où ρ est la densité, p la pression, (u, v, w) les composantes du vecteur vitesse $\overrightarrow{u}$ et E la densité d'énergie totale. La pression dans le fluide est modélisée par l'équation d'état d'un gaz parfait $p = (\gamma - 1)\rho e$, e étant l'énergie interne spécifique avec $E = e + \frac{1}{2}(u^2 + v^2 + w^2)$ et $\gamma = 1.4$ le rapport des chaleurs spécifiques, supposé constant. Dans ce qui suit, nous appellerons $F(U)$, $G(U)$ et $H(U)$ les "fonctions flux" et une valeur particulière de U un "état".

L'équation (1.3) est discrétisée selon une approche de type Volumes Finis. Pour cela, nous fixons au préalable les notations pour le maillage. Nous notons $C_{i,j,k}$ une cellule de la grille fluide de dimensions :

$$\Delta x_{i,j,k} = x_{i+1/2,j,k} - x_{i-1/2,j,k},$$
$$\Delta y_{i,j,k} = y_{i,j+1/2,k} - y_{i,j-1/2,k},$$
$$\Delta z_{i,j,k} = z_{i,j,k+1/2} - z_{i,j,k-1/2},$$

et $V_{i,j,k} = (\Delta x\, \Delta y\, \Delta z)_{i,j,k}$ est le volume de la cellule. Nous définissons le pas de temps $\Delta t = t^{n+1} - t^n$ entre les instants t^n et t^{n+1} supposé constant pour simplifier. En intégrant l'équation (1.3) sur l'intervalle de temps $[t^n, t^{n+1}]$ et sur chacune des cellules $C_{i,j,k}$ et en utilisant la formule de la divergence, nous obtenons

$$\int_{C_{i,j,k}} \Big\{U(t^{n+1}, x, y, z) - U(t^n, x, y, z)\Big\}\, dx\, dy\, dz + \sum_{a \in \tau_{i,j,k}} \int_{t^n}^{t^{n+1}} \int_a \{n_{x,a}\, F(U(t, x, y, z)) + n_{y,a}\, G(U(t, x, y, z)) + n_{z,a}\, H(U(t, x, y, z))\}\, d\gamma dt = 0.$$

où $\tau_{i,j,k}$ désigne l'ensemble des faces a de la cellule $C_{i,j,k}$, et $\overrightarrow{n_a}$ est la normale extérieure à $\partial C_{i,j,k}$ au niveau de la face a ayant pour composantes Cartésiennes $(n_{x,a}, n_{y,a}, n_{z,a})$.

La méthode des Volumes Finis consiste à introduire comme inconnue la valeur moyenne $U^n_{i,j,k}$ de U dans $C_{i,j,k}$ au temps t^n :

$$U^n_{i,j,k} \approx \frac{1}{V_{i,j,k}} \int_{C_{i,j,k}} U(t^n, x, y, z)\, dx\, dy\, dz,$$

puis à exprimer les flux d'interface F^n_a, G^n_a et H^n_a, qui approchent respectivement les intégrales des flux physiques F, G et H au cours du pas de temps. Par exemple, pour F, il s'agit de définir un flux d'interface tel que

$$F^n_a \approx \frac{1}{\Delta t \mid a \mid} \int_{t^n}^{t^{n+1}} \int_a F(U(t, x, y, z)))\, d\gamma\, dt,$$

où $\mid a \mid$ est la mesure de la face, en fonction de l'ensemble des variables $\left\{U^n_{l,k,r}, 1 \leq l \leq I, 1 \leq k \leq J, 1 \leq r \leq K\right\}$, de façon à faire avancer sur le pas de temps Δt les variables conservatives :

$$U^{n+1}_{i,j,k} = U^n_{i,j,k} - \frac{\Delta t}{V_{i,j,k}} \sum_{a \in \tau_{i,j,k}} \mid a \mid \ \left(n_{x,a}\, F^n_a + n_{y,a}\, G^n_a + n_{z,a}\, H^n_a\right). \tag{1.4}$$

Il s'agit d'une méthode explicite dans laquelle les flux numériques sont évalués uniquement à partir des états au temps t^n. Dans ce qui suit, nous nous plaçons dans le cas particulier d'un maillage Cartésien appelé par la suite "grille fluide". De ce fait, l'interface a est désignée par le biais d'indices $\{i \pm 1/2, j, k\}$, $\{i, j \pm 1/2, k\}$ ou $\{i, j, k \pm 1/2\}$ et nous avons $n_{x,a} = (\pm 1, 0, 0), n_{y,a} = (0, \pm 1, 0)$ ou $n_{z,a} = (0, 0, \pm 1)$. L'équation (1.4) devient

$$U^{n+1}_{i,j,k} = U^n_{i,j,k} + \Delta t \left(\frac{F^n_{i-1/2,j,k} - F^n_{i+1/2,j,k}}{\Delta x_{i,j,k}} + \frac{G^n_{i,j-1/2,k} - G^n_{i,j+1/2,k}}{\Delta y_{i,j,k}} + \frac{H^n_{i,j,k-1/2} - H^n_{i,j,k+1/2}}{\Delta z_{i,j,k}} \right).$$

Nous avons choisi de calculer les flux numériques $F_{i\pm1/2,j,k}$, $G_{i,j\pm1/2,k}$, $H_{i,j,k\pm1/2}$ en utilisant le flux One Step Monotonicity Preserving (OSMP) [18] que nous allons maintenant décrire.

1.3.1 Flux OSMP unidimensionnel

Nous nous plaçons d'abord dans le cas unidimensionnel. Les équations d'Euler s'écrivent :

$$\frac{\partial U}{\partial t} + \frac{\partial F(U)}{\partial x} = 0, \tag{1.5}$$

avec le vecteur des variables conservatives $U = (\rho, \rho u, \rho E)^t$ et la fonction flux $F(U) = (\rho u, \rho u^2 + p, (\rho E + p)u)^t$. Notons $A(U)$ la matrice jacobienne de F par rapport aux variables conservatives. L'expression de la matrice $A(U)$ est

$$A(U) = \begin{pmatrix} 0 & 1 & 0 \\ -\frac{\gamma-1}{2}u^2 & (3-\gamma)u & \gamma - 1 \\ \left(\frac{\gamma-1}{2}u^2 - H\right) u & H - (\gamma-1)u^2 & \gamma u \end{pmatrix},$$

H étant l'enthalpie totale définie par $H = E + \dfrac{p}{\rho}$. La matrice jacobienne est diagonalisable à valeurs propres réelles distinctes notées λ_k. Nous appelons R la matrice des vecteurs propres à droite et R_k le vecteur propre (vecteur colonne) associé à la valeur propre λ_k. De même, nous appelons L la matrice des vecteurs propres à gauche et L_k le vecteur propre (vecteur ligne) associé à la valeur propre λ_k.

Nous nous plaçons sur un maillage du plan (x, t) défini par les points $x_{i+1/2}$ et le pas de temps Δt. Le pas d'espace est noté $\Delta x_i = x_{i+1/2} - x_{i-1/2}$. Notons U^n_i une approximation de la valeur moyenne de U dans la cellule $\left[x_{i-1/2}, x_{i+1/2}\right]$ au temps t^n. Le flux numérique OSMP [18], désigné par $F^{n,p}_{i\pm1/2}$, est un flux numérique décentré de type Roe d'ordre p par une montée en ordre de

type Lax–Wendroff. Le schéma Volumes Finis pour les équations d'Euler unidimensionnelles s'écrit

$$U_i^{n+1} = U_i^n + \Delta t \, \frac{F_{i-1/2}^{n,p} - F_{i+1/2}^{n,p}}{\Delta x_i},$$

$$F_{i+1/2}^{n,p} = F_{i+1/2}^{n,\mathrm{Roe}} + \frac{1}{2} \sum_{k=1}^{3} \phi_{k,i+1/2}^{p} \, R_{k,i+1/2}. \tag{1.6}$$

Le flux numérique du schéma de Roe est donné par

$$F_{i+1/2}^{n,\mathrm{Roe}} = \frac{1}{2} \left(F(U_i^n) + F(U_{i+1}^n) \right) - \frac{1}{2} |\tilde{A}_{i+1/2}^n| \left(U_{i+1}^n - U_i^n \right).$$

La matrice jacobienne $\tilde{A}_{i+1/2}^n$ est égale à la matrice A calculée pour un état moyen $\tilde{U}_{i+1/2}^n$ appelé moyenne de Roe, afin d'assurer la consistance du flux numérique. Cet état est défini par

$$\begin{aligned}
\tilde{\rho}_{i+1/2}^n &= \sqrt{\rho_i^n \rho_{i+1}^n}, \\
\tilde{u}_{i+1/2}^n &= \frac{u_{i+1}^n \sqrt{\rho_{i+1}^n} + u_i^n \sqrt{\rho_i^n}}{\sqrt{\rho_{i+1}^n} + \sqrt{\rho_i^n}}, \\
\tilde{H}_{i+1/2}^n &= \frac{H_{i+1}^n \sqrt{\rho_{i+1}^n} + H_i^n \sqrt{\rho_i^n}}{\sqrt{\rho_{i+1}^n} + \sqrt{\rho_i^n}}.
\end{aligned}$$

Le schéma de Roe est du premier ordre et est stable sous la condition CFL

$$\forall \, i, \quad \frac{\Delta t}{\Delta x_i} < \frac{1}{(|u| + c)},$$

où c est la vitesse du son définie par $c^2 = \dfrac{\gamma p}{\rho}$. Il autorise la génération de solutions multiples qui ne satisfont pas au second principe de la Thermodynamique (solutions non-entropiques). Une correction entropique doit être ajoutée [19].

Les fonctions ϕ^p dans (1.6) sont des termes correctifs afin d'obtenir formellement l'ordre p. Elles sont construites par modification de l'équation équivalente afin de contrôler l'erreur de troncature. Ces fonctions peuvent être écrites comme la somme d'une fonction paire et d'une fonction impaire :

$$\phi_{k,i+1/2}^{p} = \sum_{m=1}^{j} \phi_{k,i+1/2}^{2m} + \mathrm{sign}(\lambda_{k,i+1/2}) \sum_{m=1}^{j_1} \phi_{k,i+1/2}^{2m+1},$$

où $j = \lfloor \frac{p}{2} \rfloor$, $j_1 = \lfloor \frac{p-1}{2} \rfloor$ et $\lfloor \cdot \rfloor$ désigne la partie entière. Les fonctions paires et impaires sont données par les formules de récurrence suivantes :

$$\phi^{2m}_{k,i+1/2} = \sum_{l=0}^{2m-2} (-1)^l C^l_{2m-2} \left(c_{2m}\delta\alpha\right)_{k,i+1/2+m-1-l},$$
$$\phi^{2m+1}_{k,i+1/2} = \sum_{l=0}^{2m-1} (-1)^l C^l_{2m-1} \left(c_{2m+1}\delta\alpha\right)_{k,i+1/2+(m-1-l)sign(\lambda_{k,i+1/2})},$$

où $C^m_q = \frac{q!}{(q-m)!m!}$ est le coefficient binomial de Pascal et $(\delta\alpha)_{k,i+1/2}$ est le k-ème invariant de Riemann de la matrice jacobienne donné par

$$(\delta\alpha)_{k,i+1/2} = R_k(U^n_{i+1} - U^n_i).$$

Les coefficients c_r dépendent de la CFL locale $\zeta_{k,i+1/2} = \dfrac{\Delta x_i}{\Delta t}\lambda_{k,i+1/2}$, et sont donnés par

$$(c_2)_{k,i+1/2} = |\lambda_{k,i+1/2}|(1 - |\zeta_{k,i+1/2}|),$$
$$(c_{r+1})_{k,i+1/2} = \frac{|\zeta_{k,i+1/2}| + (-1)^r \lfloor \frac{r+1}{2} \rfloor}{r+1}(c_r)_{k,i+1/2},\ r \geq 2.$$

1.3.2 Flux OSMP multidimensionnel

L'extension au cas multidimensionnel consiste à effectuer un splitting directionnel de type Strang [100], en résolvant alternativement des problèmes unidimensionnels dans chaque direction. En notant $L_x(\Delta t)$, $L_y(\Delta t)$, $L_z(\Delta t)$ les opérateurs d'approximation spatiale par Volumes Finis pour l'intégration du pas de temps Δt dans les directions x, y, z respectivement :

$$L_x(\Delta t)W = W - \Delta t \left(\frac{F_{i+1/2,j,k}(W) - F_{i-1/2,j,k}(W)}{\Delta x} \right),$$
$$L_y(\Delta t)W = W - \Delta t \left(\frac{G_{i,j+1/2,k}(W) - G_{i,j-1/2,k}(W)}{\Delta x} \right),$$
$$L_z(\Delta t)W = W - \Delta t \left(\frac{H_{i,j,k+1/2}(W) - H_{i,j,k-1/2}(W)}{\Delta x} \right),$$

et en notant $L_{x,y,z}(\Delta t) = L_x(\Delta t)L_y(\Delta t)L_z(\Delta t)$ et de même pour $L_{x,z,y}$, etc., nous retrouvons formellement un opérateur d'ordre deux en temps tous les six pas de temps si les opérateurs L_x, L_y et L_z ne commutent pas (ce qui est généralement le cas), avec

$$U^{n+6}_{i,j,k} = L_{x,y,z}(\Delta t)\, L_{x,z,y}(\Delta t)\, L_{y,x,z}(\Delta t)\, L_{y,z,x}(\Delta t)\, L_{z,x,y}(\Delta t)\, L_{z,y,x}(\Delta t)\, U^n_{i,j,k}.$$

1.4 Discrétisation solide

Les méthodes numériques utilisées pour la simulation de la fragmentation solide peuvent généralement être classées en deux catégories. La première catégorie est donnée par les méthodes numériques utilisant un maillage du domaine. L'exemple le plus connu correspond aux méthodes des Éléments finis. Ces méthodes nécessitent un remaillage du domaine lorsque la fracture se propage. Les methodes X-FEM [23, 88, 101] et les méthodes cohésives [77] ont été développées pour éviter ce remaillage.

La deuxième catégorie est donnée par les méthodes sans maillage. Ces méthodes sans maillage traitent la fracture, les grands déplacements, la fragmentation dynamique, et les problèmes de contact. Elles modélisent les matériaux à l'aide d'un ensemble de particules discrètes en interaction. Ainsi, le domaine solide est composé de particules reliées par des liens. Lorsque deux particules sont en contact, il est nécessaire de définir la loi d'interaction entre elles en termes de forces et de moments. La complexité réside dans l'expression de ces forces et moments. Les méthodes les plus connues dans cette catégorie sont les méthodes Smooth Particle Hydrodynamics [70, 78, 93], les méthodes des Éléments Discrets [69, 79, 81] et les méthodes Lattice Models [68, 96].

Pour cette thèse nous avons employé la méthode des Éléments Discrets [79, 81] afin de modéliser et simuler des phénomènes où la fragmentation dynamique intervient. Le solide est discrétisé en utilisant un nombre fini de particules rigides. Les particules sont des polyèdres convexes (Fig. 1.5). Chaque particule est régie par les équations classiques de la mécanique. Les particules interagissent par des forces et des moments, ce qui permet de retrouver le comportement macroscopique du solide déformable, voire fragmentable lorsque le lien entre deux particules est rompu.

1.4.1 Description du contact entre particules

Soit I une particule solide. Plusieurs quantités y sont attachées, à savoir la masse m_I, la position du centre de masse $\overrightarrow{X}_I$, la vitesse du centre de masse $\overrightarrow{V}_I$, la matrice de rotation $\mathbf{Q}_I$, le moment cinétique $\mathbf{P}_I$ et les moments principaux d'inertie I_I^i, $i \in \{1,2,3\}$. Nous désignons par $\mathbf{D}_I$ la matrice diagonale associée aux moments d'inertie principaux $\mathbf{D}_I = \text{diag}(d_I^1, d_I^2, d_I^3)$ où $d_I^i = \frac{1}{2}\left(I_I^1 + I_I^2 + I_I^2\right) - I_I^i$, $i \in \{1,2,3\}$.

Nous désignons par τ_I la liste des particules reliées à la particules I. Pour chaque lien entre deux particules I et J, plusieurs quantités sont définies, à savoir la distance entre ces particules D_{IJ}, la surface de contact S_{IJ}, le centre de gravité de la surface de contact $\overrightarrow{G}_{IJ}$, la direction normale à la surface de contact $\overrightarrow{n}_{IJ}$. Nous définissons également deux autres directions formant un repère orthonormé avec le vecteur $\overrightarrow{n}_{IJ}$ pour le lien initial entre les particules $\overrightarrow{s}_{IJ}$ et $\overrightarrow{t}_{IJ}$. Les quantités avec un exposant 0 correspondent à l'instant initial : $\overrightarrow{X}_I^0$, D_{IJ}^0 et $\overrightarrow{n}_{IJ}^0$.

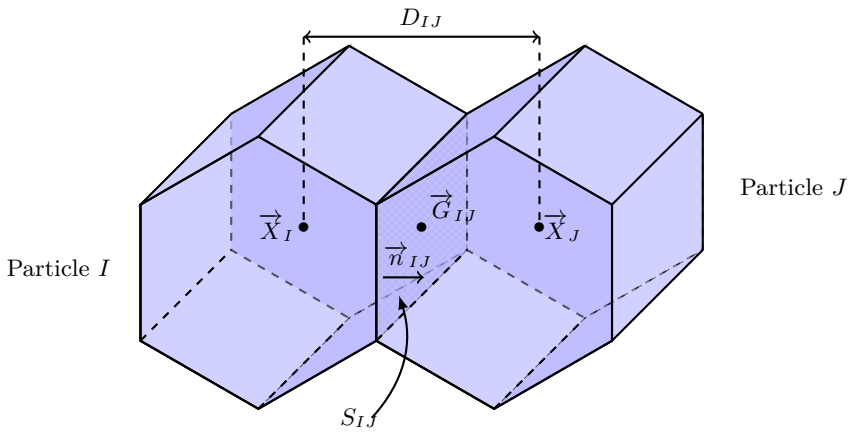

Figure 1.5: Surface de contact entre deux particules I et J.

Le choix de modélisation des forces et moments entre les particules I et J correspond à un comportement linéaire élastique de la structure [79, 81]. Soit ν le coefficient de Poisson et E le module d'Young. La force entre les particules I et J est définie par l'expression suivante :

$$\begin{aligned}\overrightarrow{F}_{IJ} =& \frac{S_{IJ}}{D^0_{IJ}} \frac{E}{1+\nu} \overrightarrow{\Delta u}_{IJ} \\ &+ S_{IJ} \frac{E\nu}{(1+\nu)(1-2\nu)} \varepsilon^v_{IJ} \left(\overrightarrow{n}_{IJ} + \frac{1}{D_{IJ}} \overrightarrow{\Delta u}_{IJ} - \frac{1}{D_{IJ}} (\overrightarrow{\Delta u}_{IJ} \cdot \overrightarrow{n}_{IJ}) \overrightarrow{n}_{IJ} \right),\end{aligned} \tag{1.7}$$

où $\overrightarrow{\Delta u}_{IJ}$ est le vecteur déplacement à la surface de contact entre les particules I et J :

$$\overrightarrow{\Delta u}_{IJ} = \overrightarrow{X}_I - \overrightarrow{X}_J + \mathbf{Q}_J \cdot \overrightarrow{X}^0_J \overrightarrow{G}_{IJ} - \mathbf{Q}_I \cdot \overrightarrow{X}^0_I \overrightarrow{G}_{IJ},$$

et ε^v_{IJ} la déformation volumique du lien entre I et J égale à la somme des déformation volumiques de ces deux particules : $\varepsilon^v_{IJ} = \varepsilon^v_I + \varepsilon^v_J$. La déformation volumique élastique de la particule I est prise égale à :

$$\varepsilon^v_I = \sum_{J \in \tau_I} \frac{1}{2} \frac{S_{IJ}}{V_I + 3\frac{\nu}{1-2\nu} V^l_I} \overrightarrow{\Delta u}_{IJ} \cdot \overrightarrow{n}_{IJ},$$

où V_I est le volume de la particule I et V^l_I son volume libre ; le volume libre de la particule I est définit comme la somme des volumes des pyramides ayant comme base ses faces libres (les faces qui ne sont pas reliées aux particules voisines) et comme apex le centre de masse de la particule I.

Le moment entre I et J se décompose comme suit :

$$\overrightarrow{\mathcal{M}}_{IJ} = \overrightarrow{\mathcal{M}}^t_{IJ} + \overrightarrow{\mathcal{M}}^f_{IJ}, \tag{1.8}$$

avec $\overrightarrow{\mathcal{M}}^t_{IJ}$ le moment de la force $\overrightarrow{F}_{IJ}$ défini par la relation suivante :

$$\overrightarrow{\mathcal{M}}^t_{IJ} = \frac{S_{IJ}}{D^0_{IJ}} \frac{E}{1+\nu} \left(\mathbf{Q}_I \cdot \overrightarrow{X}^0_I \overrightarrow{G}_{IJ} \right) \wedge \overrightarrow{\Delta u}_{IJ} + S_{IJ} \frac{E\nu}{(1+\nu)(1-2\nu)} \varepsilon^v_{IJ} \left(\mathbf{Q}_I \cdot \overrightarrow{X}^0_I \overrightarrow{G}_{IJ} \right) \wedge \overrightarrow{n}_{IJ}, \tag{1.9}$$

et $\overrightarrow{\mathcal{M}}^f_{IJ}$ le moment de flexion-torsion donné par l'équation suivante :

$$\begin{aligned}\overrightarrow{\mathcal{M}}^f_{IJ} = \frac{S_{IJ}}{D^0_{IJ}}(&\alpha_n(\mathbf{Q}_I \cdot \overrightarrow{n}^0_{IJ}) \wedge (\mathbf{Q}_J \cdot \overrightarrow{n}^0_{IJ}) + \alpha_s(\mathbf{Q}_I \cdot \overrightarrow{s}_{IJ}) \wedge (\mathbf{Q}_J \cdot \overrightarrow{s}_{IJ}) \\ &+ \alpha_t(\mathbf{Q}_I \cdot \overrightarrow{t}_{IJ}) \wedge (\mathbf{Q}_J \cdot \overrightarrow{t}_{IJ})),\end{aligned} \tag{1.10}$$

où les coefficients α_n, α_s et α_t sont exprimés par les propriétés élastiques du lien et par le tenseur d'inertie de la surface de contact entre les particules I et J :

$$\begin{aligned}\alpha_n &= \frac{(1+2\nu)E}{4(1+\nu)S_{IJ}}(I^s_{IJ} + I^t_{IJ}),\\ \alpha_s &= \frac{E}{4(1+\nu)S_{IJ}}((3+2\nu)I^s_{IJ} - (1+2\nu)I^t_{IJ}),\\ \alpha_t &= \frac{E}{4(1+\nu)S_{IJ}}((3+2\nu)I^t_{IJ} - (1+2\nu)I^s_{IJ}).\end{aligned}$$

Les I^s_{IJ} et I^t_{IJ} sont les moments principaux d'inertie de la surface de contact entre les particules I et J :

$$I^s_{IJ} = \int\int_{S_{IJ}} \left(Y\overrightarrow{G}_{IJ} \cdot \overrightarrow{s}_{IJ}\right)^2 dY \quad \text{et} \quad I^t_{IJ} = \int\int_{S_{IJ}} \left(Y\overrightarrow{G}_{IJ} \cdot \overrightarrow{t}_{IJ}\right)^2 dY.$$

1.4.2 Schéma d'intégration en temps

L'intégration en temps du solide est explicite et utilise le schéma de Verlet pour la translation et le schéma RATTLE pour la rotation. Cela s'écrit pour la particule I :

$$\overrightarrow{V}^{n+\frac{1}{2}}_I = \overrightarrow{V}^n_I + \frac{\Delta t}{2m_I}\overrightarrow{F}^n_{I,\text{int}}, \tag{1.11}$$

$$\overrightarrow{X}^{n+1}_I = \overrightarrow{X}^n_I + \Delta t\overrightarrow{V}^{n+\frac{1}{2}}_I, \tag{1.12}$$

$$\mathbf{P}^{n+\frac{1}{2}}_I = \mathbf{P}^n_I + \frac{\Delta t}{4}\mathbf{j}(\overrightarrow{\mathcal{M}}^n_{I,\text{int}})\mathbf{Q}^n_I + \frac{\Delta t}{2}\boldsymbol{\Upsilon}^n_I\mathbf{Q}^n_I, \tag{1.13}$$

$$\mathbf{Q}^{n+1}_I = \mathbf{Q}^n_I + \Delta t\mathbf{P}^{n+\frac{1}{2}}_I\mathbf{D}^{-1}_I, \tag{1.14}$$

$$\overrightarrow{V}^{n+1}_I = \overrightarrow{V}^{n+\frac{1}{2}}_I + \frac{\Delta t}{2m_I}\overrightarrow{F}^{n+1}_{I,\text{int}}, \tag{1.15}$$

$$\mathbf{P}^{n+1}_I = \mathbf{P}^{n+\frac{1}{2}}_I + \frac{\Delta t}{4}\mathbf{j}(\overrightarrow{\mathcal{M}}^{n+1}_{I,\text{int}})\mathbf{Q}^{n+1}_I + \frac{\Delta t}{2}\tilde{\boldsymbol{\Upsilon}}^{n+1}_I\mathbf{Q}^{n+1}_I, \tag{1.16}$$

où dans (1.13) $\boldsymbol{\Upsilon}^n_I$ est une matrice symétrique telle que

$$(\mathbf{Q}^{n+1}_I)^t\mathbf{Q}^{n+1}_I = \mathbf{I}, \tag{1.17}$$

avec $\mathbf{I}$ la matrice identité dans $\mathbb{R}^3$, et où dans (1.16) $\tilde{\boldsymbol{\Upsilon}}^{n+1}_I$ est une matrice symétrique telle que

$$(\mathbf{Q}^{n+1}_I)^t\mathbf{P}^{n+1}_I\mathbf{D}^{-1}_I + \mathbf{D}^{-1}_I(\mathbf{P}^{n+1}_I)^t\mathbf{Q}^{n+1}_I = \mathbf{0}. \tag{1.18}$$

Les matrices $\boldsymbol{\Upsilon}_I^n$ et $\tilde{\boldsymbol{\Upsilon}}_I^{n+1}$ sont les multiplicateurs de Lagrange associés aux contraintes (1.17) et (1.18) [80]. L'application $\mathbf{j} : \mathbb{R}^3 \to \mathbb{R}^{3\times 3}$ est telle que $\mathbf{j}(\overrightarrow{x})\overrightarrow{y} = \overrightarrow{x} \wedge \overrightarrow{y}$, $\forall\ \overrightarrow{x},\ \overrightarrow{y} \in \mathbb{R}^3$. La force $\overrightarrow{F}_{I,\text{int}}^n$ et le moment $\overrightarrow{\mathcal{M}}_{I,\text{int}}^n$ sont les résultats des interactions de la particule I avec les particules voisines et sont évalues en utilisant (1.7) et (1.8) pout tout J appartenant à τ_I :

$$\overrightarrow{F}_{I,\text{int}}^n = \sum_{J\in\tau_I} \overrightarrow{F}_{IJ}^n \quad \text{et} \quad \overrightarrow{\mathcal{M}}_{I,\text{int}}^n = \sum_{J\in\tau_I} \overrightarrow{\mathcal{M}}_{IJ}^n.$$

L'algorithme d'intégration en temps étant explicite, le pas de temps est soumis à une conditions CFL. Cette condition assure que le déplacement de chaque particules est inférieur à la taille caractéristique de la particule et que la rotation pendent le pas de temps est inférieure à $\frac{\pi}{8}$.

La méthode des Éléments Discrets traite la fragmentation en rompant le lien entre particules, selon un critère de rupture défini au niveau des faces en contact entre les particules. Des problèmes de fragmentation dynamique utilisant la méthode des Éléments Discrets [79, 81] ont été étudiés dans [73], avec les critères de Camacho–Ortiz [13] et celui de Denoual et al. [22]. Le critère de Camacho–Ortiz exprime l'endommagement comme une fonction de l'ouverture de la fissure. Quand les efforts locaux atteignent un certain seuil, cette fonction décroit linéairement jusqu'au moment de la rupture. Le critère de Denoual et al. repose sur une formulation probabiliste où l'endommagement est introduit par unité de volume distribué selon une loi de Weibull. Nous reviendrons sur le choix du critère de rupture dans le chapitre 4.

1.5 Plan de la thèse

Le plan de cette thèse est le suivant. Dans le deuxième chapitre, nous décrivons la méthode de couplage entre un fluide compressible non-visqueux et une structure rigide tridimensionnelle subissant de grands déplacements. Le solide étant rigide, il est décrit par une seule particule. L'algorithme de couplage en temps est explicite et assure la conservation de la masse, de la quantité de mouvement et de l'énergie totale du système couplé. La méthode présente en outre plusieurs propriétés de consistance dans des cas simples, telles que la préservation du mouvement uniforme d'un solide sans rotation dans un fluide ayant la même vitesse, ainsi que la préservation du glissement d'un écoulement le long d'une paroi rigide fixe (absence d'effets de rugosité artificielle à la paroi). Nous présentons les algorithmes géométriques nécessaires à l'implémentation du schéma de couplage tridimensionnel. Nous présentons également des résultats numériques montrant en particulier la conservation de la masse du fluide et de l'énergie totale du système couplé, et la capacité de la méthode à gérer l'interaction entre un fluide présentant de fortes discontinuités avec un solide rigide subissant de grands déplacements. Des comparaissons avec le cas bidimensionnel sont également présentées. Ce travail a fait l'objet d'un article soumis pour publication au SIAM Journal on Scientific Computing [89].

Dans le troisième chapitre, nous étendons la méthode de couplage au cas d'une structure déformable tridimensionnelle subissant de grands déplacements (mais sans fragmentation). Une méthode semi-implicite en temps est employée pour l'évaluation des forces et moments exercés par le fluide sur la surface mouillée du solide pendant le pas de temps. À nouveau, la méthode de couplage assure la conservation de la masse, de la quantité de mouvement et de l'énergie totale du système couplé. Le coût de calcul pour la discrétisation des parties fluides et solides réside principalement dans l'évaluation des flux dans la méthode des Volumes Finis, et des forces et moments dans la méthode des Éléments Discrets. L'algorithme de couplage en temps semi-implicite évalue ces termes une seule fois par pas de temps, assurant ainsi l'efficacité de la méthode. Nous montrons que l'algorithme de couplage semi-implicite en temps a une convergence géométrique sous une condition CFL sur le pas de temps, cette condition étant en pratique moins restrictive que la condition CFL fluide, sous l'hypothèse d'une densité plus importante du solide par rapport à celle du fluide. Un intérêt du schéma semi-implicite en temps est de préserver la conservation d'un fluide au repos autour d'une paroi ayant uniquement des vitesses tangentielles de déformation. En revanche, cette propriété n'est pas préservée par le schéma explicite en temps, ce qui conduit à des fluctuations de pression au niveau de la paroi déformée tangentiellement, comme nous l'illustrons numériquement. Enfin, nous présentons des résultats numériques montrant la robustesse de la méthode dans le cas d'un solide déformable avec de grands déplacements, couplé à un écoulement fluide compressible non-visqueux. Ce travail a fait l'objet d'un article soumis pour publication au Journal of Computational Physics [91].

Dans le quatrième chapitre, nous décrivons l'extension de l'algorithme de couplage afin de prendre en compte la fragmentation du solide. Le critère de rupture employé est l'allongement à la rupture. Pendant le processus de fragmentation, du vide entre les particules du solide peut apparaître. Cela est dû au fait que la vitesse de propagation de la fissure peut être supérieure à celle du son dans le fluide. Du vide entre les particules du solide apparaît également lorsqu'une fissure interne se produit dans le solide. Cela conduit à des cellules fluides avec pression et densité très faibles voire nulles. Dans les zones adjacentes aux zones vides, le problème de Riemann est résolu avec le flux numérique de Lax–Friedrichs près de la zone vide, ce dernier présentent l'avantage d'éviter des divisions par zéro ou des quantités très petites. À nouveau, la méthode de couplage assure la conservation de la masse, de la quantité de mouvement et de l'énergie totale du système couplé. Nous présentons des résultats numériques montrant la robustesse de la méthode dans le cas des solides se fragmentant sous l'action d'une explosion. Ce travail a fait l'objet d'un article soumis pour publication au International Journal for Numerical Methods in Engineering [90].

Dans le chapitre final, nous tirons les conclusions de ce travail et dégageons diverses perspectives pour la poursuite des travaux.

2

A three-dimensional conservative coupling method between an inviscid compressible flow and a moving rigid structure

This chapter is submitted to SIAM Journal on Scientific Computing [89].

2.1 Introduction

A large number of engineering problems involve fluid-structure interactions. The study of such phenomena is motivated by the fact that the consequences are sometimes catastrophic for the

mechanical structure. In the military or safety domains, the effects of an explosion on a building or on a submarine involve complex non-linear phenomena (shock waves, cracking, rupture, ...) [99, 108]. The characteristic time scale of these phenomena is extremely short and the driving effect of the interaction is the overpressure. Viscous effects therefore play a lesser role in the dynamics of this type of coupled system. With an eye toward these applications, we consider in this chapter an inviscid compressible flow model on the fluid side with shock waves and a rigid object on the solid side.

Fully Eulerian [34, 74] and fully Lagrangian methods [54] have been proposed for the simulation of fluid-structure interaction. However, monolithic Eulerian or Lagrangian approaches are in general limited to the case where the fluid and the solid behave according to similar equations with different parameters. In most numerical schemes, the fluid is classically described in Eulerian formulation and the solid in Lagrangian formulation. In this framework, the main challenges in fluid-structure interaction are the computation of the fluid forces that act on the solid and the modification of the fluid domain due to the displacement of the solid. Two main classes of methods have been developed: Arbitrary Lagrangian-Eulerian (ALE) methods [24, 65] and fictitious domain methods [27, 31, 84, 85]. The ALE method deforms the fluid domain in order to follow the movement of the structure. Such a method hinges on a mesh fitting the solid boundaries, and this often involves costly remeshing of the fluid domain when the solid goes through large displacements or rupture. For these reasons, we choose to use a fictitious domain method.

In fictitious domain methods, the solid is superimposed to the fixed fluid grid and additional terms are introduced in the fluid formulation to impose the fluid boundary conditions at the solid boundary. Various types of fictitious domain methods have been proposed. Non-conservative Immersed Boundary methods have been first developed for incompressible flows [20, 30, 85]. An important issue in compressible fluid-structure interaction is the conservation of mass, momentum, and energy. The accurate capture of shocks is based on conservation properties, and the preservation of physical properties is an important ingredient towards an effective numerical method. In addition, verifying conservation at the discrete level is a natural means to assess the numerical stability of the scheme. Conservative Immersed Boundary methods [17, 31, 84, 97] and Ghost Fluid methods [33, 35, 106] have been proposed for elliptic problems and compressible fluids. Conservative Immersed Boundary methods are built in such a way that the spatial discretization satisfies mass, momentum, and energy conservation. Ghost Fluid methods consist in modifying the value of ghost cells (covered by the solid) in order to compute the fluid fluxes accurately at the interface. Ghost Fluid methods often eliminate the constraint of energy conservation in order to eliminate spurious numerical oscillations at the material interface in compressible multifluid interaction problems [2].

In this chapter, we use the Conservative Immersed Boundary method developed in [84] in combination with a Finite Volume method for the fluid and a Discrete Element method for the solid. The Finite Volume method is computed on a Cartesian grid, using high-order upwind

fluxes computed with a Lax-Wendroff approach [18]. The Discrete Element method [69, 81] is a particle method for elastodynamics, in which particles interact through forces and torques yielding the macroscopic behaviour of the assembly. Herein, the solid being rigid, is consists of a single particle. Both methods being time-explicit and computationally expensive, we develop a coupling algorithm based on an explicit time-marching procedure. The two-dimensional version of these ideas was presented in [80]. Herein, we extend the results to the three-dimensional case. This is by no means straightforward since the three-dimensional extension poses numerous challenges at the computational and algorithmic levels. The present method yields exact conservation of mass, momentum and energy of the system, and also exhibits important consistency properties, such as conservation of uniform movement of both fluid and solid as well as the absence of numerical roughness on a straight boundary. The fluid solver used in this work is formally high-oder in smooth regions so as to limit numerical diffusion, but in the presence of shocks, the fluid limiters reduce the order to first order. Still the use of a high-order fluid solver is advantageous to limit numerical diffusion [18]. The solid boundary conditions in the fluid are also first order so that the coupling method is globally first order.

This chapter starts in Section 2 with a brief description of the discretization methods for the inviscid compressible fluid and the moving rigid solid. In Section 3, we present the conservative coupling method based on an explicit time-marching procedure. In Section 4, we derive several properties of the coupling method. In Section 5, we describe the main geometric algorithms required for the implementation of the three-dimensional coupling scheme. In Section 6, we present numerical results showing in particular the energy and mass conservation achieved by the coupling scheme and the ability of the method to compute the interaction of strong discontinuities with rigid solids undergoing large displacement. Comparisons with two-dimensional numerical results are presented. Finally, conclusions are made in Section 7.

2.2 Fluid and solid description

2.2.1 Inviscid compressible flow

The fluid is modelled by the Euler equations expressing conservation of mass, momentum, and energy for an inviscid compressible flow, which are written in Cartesian coordinates as follows:

$$\frac{\partial}{\partial t}U + \frac{\partial}{\partial x}F(U) + \frac{\partial}{\partial y}G(U) + \frac{\partial}{\partial z}H(U) = 0, \tag{2.1}$$

$$U = \begin{pmatrix} \rho \\ \rho u \\ \rho v \\ \rho w \\ \rho E \end{pmatrix}, F(U) = \begin{pmatrix} \rho u \\ \rho u^2 + p \\ \rho uv \\ \rho uw \\ (\rho E + p)u \end{pmatrix}, G(U) = \begin{pmatrix} \rho v \\ \rho uv \\ \rho v^2 + p \\ \rho vw \\ (\rho E + p)v \end{pmatrix}, H(U) = \begin{pmatrix} \rho w \\ \rho uw \\ \rho vw \\ \rho w^2 + p \\ (\rho E + p)w \end{pmatrix},$$

where ρ is the mass density, p the pressure, (u, v, w) the Cartesian components of the velocity vector $\overrightarrow{u}$ and E the total energy. The pressure in the fluid is modelled by the state equation of a perfect gas: $p = (\gamma - 1)\rho e$, e being the specific internal energy with $E = e + \frac{1}{2}(u^2 + v^2 + w^2)$ and $\gamma = 1.4$ the ratio of specific heats, assumed to be constant.

The discretization of these equations is based on an explicit Finite Volume method on a Cartesian grid with directional operator splitting. For the flux calculation we use the OSMP numerical scheme which is a one-step monotonicity-preserving high-order scheme [18]. It is derived using a coupled space-time Lax-Wendroff approach, where the formal order of accuracy in the scalar case can be set to an arbitrary order. In the present work, we use order 11. The coupling method is actually independent from the numerical scheme used for the flux calculation. The time step, which is subjected to a CFL stability condition, is taken constant for simplicity and is denoted Δt. We introduce the discrete times $t^n = n\Delta t$, for all $n \geq 0$.

2.2.2 Rigid moving solid

We consider a polyhedral rigid body. The solid is assumed to be star-shaped with respect to its center of mass and its faces are assumed to be star-shaped with respect to their center of mass. Working with triangular faces simplifies the geometric algorithms. Thus, up to a preliminary subdivision of the polygonal faces, we consider that the solid faces are triangles. We define the thickness of the solid as the radius of the inscribed sphere. Thereafter, we assume that the solid has a thickness greater than or equal to two fluid grid cells.

Various quantities are attached to the solid body, namely the position of his center of mass $\overrightarrow{X}$, the rotation matrix $\mathbf{Q}$, the velocity of the center of mass $\overrightarrow{V}$, the angular momentum matrix $\mathbf{P}$, the mass m, and the principal moments of inertia I^1, I^2 and I^3. Let $\mathbf{D} = diag(d^1, d^2, d^3)$ with $d^i = \frac{1}{2}\left(I^1 + I^2 + I^2\right) - I^i$, $i \in \{1, 2, 3\}$. We recall the explicit solid time-integration scheme used in [80], consisting of the Verlet scheme for translation and the RATTLE scheme for rotation:

$$\overrightarrow{V}^{n+\frac{1}{2}} = \overrightarrow{V}^n + \frac{\Delta t}{2m}\overrightarrow{F}^n_{\text{fluid}}, \tag{2.2}$$

$$\overrightarrow{X}^{n+1} = \overrightarrow{X}^n + \Delta t\overrightarrow{V}^{n+\frac{1}{2}}, \tag{2.3}$$

$$\mathbf{P}^{n+\frac{1}{2}} = \mathbf{P}^n + \frac{\Delta t}{4}\mathbf{j}(\overrightarrow{\mathcal{M}}^n_{\text{fluid}})\mathbf{Q}^n + \frac{\Delta t}{2}\mathbf{\Upsilon}^n\mathbf{Q}^n, \tag{2.4}$$

$$\mathbf{Q}^{n+1} = \mathbf{Q}^n + \Delta t\mathbf{P}^{n+\frac{1}{2}}\mathbf{D}^{-1}, \tag{2.5}$$

$$\overrightarrow{V}^{n+1} = \overrightarrow{V}^{n+\frac{1}{2}} + \frac{\Delta t}{2m}\overrightarrow{F}^n_{\text{fluid}}, \tag{2.6}$$

$$\mathbf{P}^{n+1} = \mathbf{P}^{n+\frac{1}{2}} + \frac{\Delta t}{4}\mathbf{j}(\overrightarrow{\mathcal{M}}^n_{\text{fluid}})\mathbf{Q}^{n+1} + \frac{\Delta t}{2}\tilde{\mathbf{\Upsilon}}^{n+1}\mathbf{Q}^{n+1}, \tag{2.7}$$

where in (2.4), $\mathbf{\Upsilon}^n$ is a symmetric matrix such that

$$(\mathbf{Q}^{n+1})^t\mathbf{Q}^{n+1} = \mathbf{I}, \tag{2.8}$$

with $\mathbf{I}$ the identity matrix in $\mathbb{R}^3$, and in (2.7), $\tilde{\mathbf{\Upsilon}}^{n+1}$ a symmetric matrix such that

$$(\mathbf{Q}^{n+1})^t\mathbf{P}^{n+1}\mathbf{D}^{-1} + \mathbf{D}^{-1}(\mathbf{P}^{n+1})^t\mathbf{Q}^{n+1} = \mathbf{0}, \tag{2.9}$$

which is the constraint associated with the derivation in time of $\mathbf{Q}^t\mathbf{Q} = \mathbf{I}$, using the definition of $\mathbf{P} = \dot{\mathbf{Q}}\mathbf{D}$. The matrices $\mathbf{\Upsilon}^n$ and $\tilde{\mathbf{\Upsilon}}^{n+1}$ are the Lagrange multipliers associated with the constraints (2.8) and (2.9), see [80]. In addition, $\overrightarrow{F}^n_{\text{fluid}}$ and $\overrightarrow{\mathcal{M}}^n_{\text{fluid}}$ denote the fluid forces and torques applied to the solid and the map $\mathbf{j} : \mathbb{R}^3 \to \mathbb{R}^{3\times3}$ is such that $\mathbf{j}(\overrightarrow{x})\overrightarrow{y} = \overrightarrow{x} \wedge \overrightarrow{y}$ for all $\overrightarrow{x}$, $\overrightarrow{y} \in \mathbb{R}^3$.

The time-integration scheme for the solid being explicit, the time step is restricted by a CFL stability condition, which is in general less stringent than the fluid CFL stability condition.

2.3 Coupling method

In the Immersed Boundary method, the solid is superimposed to the fluid grid, leading to fluid-solid mixed cells, thereafter called “cut-cells". The solid faces are collected in the set $\mathfrak{F}$, and a generic element of $\mathfrak{F}$ is denoted by $\mathcal{F}$. Owing to the movement of the solid, the solid faces, as set of points in $\mathbb{R}^3$, are time-dependent, and we set $\mathcal{F}^n = \mathcal{F}(t^n)$ for all $n \geq 0$. Each solid face $\mathcal{F}(t)$ is assigned a unit normal vector $\overrightarrow{\nu}_{\mathcal{F}}(t)$ (pointing from the solid to the fluid). Finally, we denote by $\Omega_{\text{solid}}(t)$ the solid domain and by Ω_{fluid} the fluid domain.

2.3.1 Treatment of the cut-cells

Recalling that we use a Cartesian grid for the fluid, we denote with integer subscripts i, j, k quantities related to the center of cells and with half-integer subscripts quantities related to the center of faces of the fluid grid cells. For instance, the interface between cells $C_{i,j,k}$ and $C_{i+1,j,k}$ is denoted by $\partial C_{i+\frac{1}{2},j,k}$. Let $C_{i,j,k}$ be a cut-cell of size $(\Delta x_{i,j,k},\ \Delta y_{i,j,k},\ \ \Delta z_{i,j,k})$. The relevant geometric quantities describing the intersection between the moving solid and the cell $C_{i,j,k}$ are (see Fig. 2.1):

– The **volume fraction** $0 \leqslant \Lambda_{i,j,k}(t) \leqslant 1$ occupied by the solid in the cell $C_{i,j,k}$ at time t:

$$\Lambda_{i,j,k}(t) = \frac{\mathcal{V}_{i,j,k}(t)}{V_{i,j,k}},$$

$V_{i,j,k} = (\Delta x\, \Delta y\, \Delta z)_{i,j,k}$ being the volume of $C_{i,j,k}$ where the solid occupies the volume $\mathcal{V}_{i,j,k}(t)$ at time t:

$$\mathcal{V}_{i,j,k}(t) = \int_{C_{i,j,k}\cap\,\Omega_{\text{solid}}(t)} dx\, dy\, dz.$$

When the volume fraction is evaluated at the discrete time t^n, we use the notation $\Lambda^n_{i,j,k}$.

– The **side area fraction** $0 \leqslant \lambda^{n+\frac{1}{2}}_{i\pm\frac{1}{2},j,k}, \lambda^{n+\frac{1}{2}}_{i,j\pm\frac{1}{2},k}, \lambda^{n+\frac{1}{2}}_{i,j,k\pm\frac{1}{2}} \leqslant 1$ of each fluid grid cell face averaged over the time interval $\left[t^n, t^{n+1}\right]$; for example, on the face $\partial C_{i+\frac{1}{2},j,k}$, we define

$$\lambda^{n+\frac{1}{2}}_{i+\frac{1}{2},j,k} = \frac{\mathcal{A}^{n+\frac{1}{2}}_{i+\frac{1}{2},j,k}}{(\Delta y \Delta z)_{i,j,k}},$$

where

$$\mathcal{A}^{n+\frac{1}{2}}_{i+\frac{1}{2},j,k} = \frac{1}{\Delta t} \int_{t^n}^{t^{n+1}} \left(\int_{\partial C_{i+\frac{1}{2},j,k} \cap \Omega_{\text{solid}}(t)} dy\, dz \right) dt.$$

– The **boundary area**, denoted by $A^{n+\frac{1}{2}}_{i,j,k,\mathcal{F}}$, is the area of the intersection of the solid face $\mathcal{F}(t)$ with $C_{i,j,k}$ averaged over the time interval $\left[t^n, t^{n+1}\right]$:

$$A^{n+\frac{1}{2}}_{i,j,k,\mathcal{F}} = \frac{1}{\Delta t} \int_{t^n}^{t^{n+1}} \left(\int_{C_{i,j,k} \cap \mathcal{F}(t)} ds \right) dt.$$

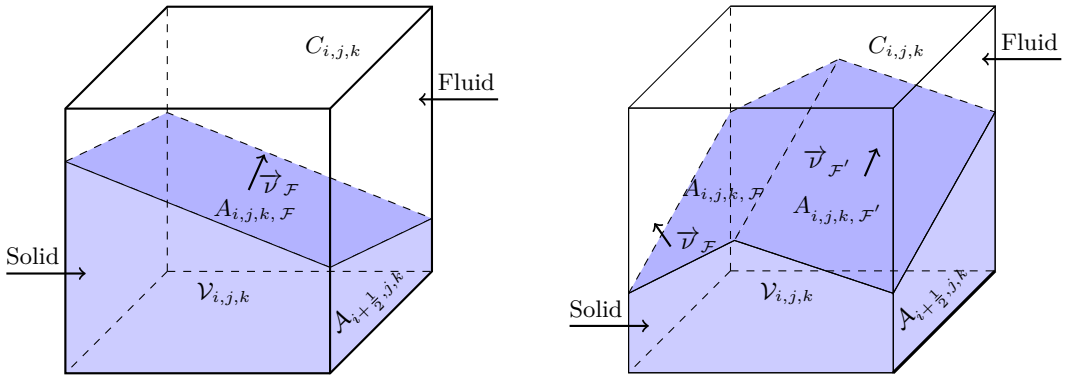

Fig. 2.1: Two illustrations of a cut-cell. Left panel: the cell is intersected by one solid face. Right panel: the cell is intersected by two solid faces.

We take into account the position of the solid in the fluid domain by modifying the fluid fluxes in cut-cells. Consider such a cut-cell partially intersected by the solid, see Fig. 2.1. We denote by $U^n_{i,j,k}$ the average value of U on the fluid volume cell $C_{i,j,k}$. Integrating (2.1) on this cut-cell over the time interval $\left[t^n, t^{n+1}\right]$ and applying the divergence theorem yields

$$\left(1 - \Lambda^{n+1}_{i,j,k}\right) U^{n+1}_{i,j,k} = \left(1 - \Lambda^{n}_{i,j,k}\right) U^{n}_{i,j,k} + \Delta t\, \Phi^{n+\frac{1}{2}}_{i,j,k,\,\text{fluid}} + \Delta t\, \Phi^{n+\frac{1}{2}}_{i,j,k,\,\text{solid}}, \tag{2.10}$$

with the fluid flux

$$\begin{aligned}
\Phi^{n+\frac{1}{2}}_{i,j,k,\,\text{fluid}} = &\frac{(1 - \lambda^{n+\frac{1}{2}}_{i-\frac{1}{2},j,k})}{\Delta x_{i,j,k}} F^{n+\frac{1}{2}}_{i-\frac{1}{2},j,k} - \frac{(1 - \lambda^{n+\frac{1}{2}}_{i+\frac{1}{2},j,k})}{\Delta x_{i,j,k}} F^{n+\frac{1}{2}}_{i+\frac{1}{2},j,k} \\
&+ \frac{(1 - \lambda^{n+\frac{1}{2}}_{i,j-\frac{1}{2},k})}{\Delta y_{i,j,k}} G^{n+\frac{1}{2}}_{i,j-\frac{1}{2},k} - \frac{(1 - \lambda^{n+\frac{1}{2}}_{i,j+\frac{1}{2},k})}{\Delta y_{i,j,k}} G^{n+\frac{1}{2}}_{i,j+\frac{1}{2},k} \\
&+ \frac{(1 - \lambda^{n+\frac{1}{2}}_{i,j,k-\frac{1}{2}})}{\Delta z_{i,j,k}} H^{n+\frac{1}{2}}_{i,j,k-\frac{1}{2}} - \frac{(1 - \lambda^{n+\frac{1}{2}}_{i,j,k+\frac{1}{2}})}{\Delta z_{i,j,k}} H^{n+\frac{1}{2}}_{i,j,k+\frac{1}{2}},
\end{aligned}$$

and the solid flux

$$\Phi^{n+\frac{1}{2}}_{i,j,k,\,\text{solid}} = \frac{1}{V_{i,j,k}} \sum_{\{\mathcal{F}\in\mathfrak{F}\,|\,\mathcal{F}^{n+1}\cap C_{i,j,k}\neq\emptyset\}} \phi^{n+\frac{1}{2}}_{i,j,k,\,\mathcal{F}}.$$

The solid flux $\Phi^{n+\frac{1}{2}}_{i,j,k,\,\text{solid}}$ in (2.10) results from the presence of the solid boundaries in the cell $C_{i,j,k}$, see Section 2.8. This flux takes into account the exchange of energy and momentum between the solid and the fluid resulting from the pressure forces.

The computation of the time-average of the side area fractions $\lambda^{n+\frac{1}{2}}$ (for simplicity, subscripts related to the fluid grid cells or faces are omitted when they play no relevant role) and of the solid flux $\phi^{n+\frac{1}{2}}_{\mathcal{F}}$ attached to $\mathcal{F}$ (involving the computation of the boundary area $A^{n+\frac{1}{2}}_{\mathcal{F}}$), as considered in [31], can be very complex in three dimensions. Instead, as in [80], we evaluate the side area fraction at time t^{n+1} in $\Phi^{n+\frac{1}{2}}_{\text{fluid}}$, which we now denote $\Phi^{n+1}_{\text{fluid}}$, and we evaluate the solid flux, which we now denote Φ^{n}_{solid}, by using the boundary area $A^{n}_{\mathcal{F}}$. This leads to the following approximation of (2.10):

$$\left(1-A^{n+1}_{i,j,k}\right)U^{n+1}_{i,j,k} = \left(1-A^{n+1}_{i,j,k}\right)U^{n}_{i,j,k} + \Delta t\,\Phi^{n+1}_{i,j,k,\,\text{fluid}} + \Delta t\,\Phi^{n}_{i,j,k,\,\text{solid}} + \Delta U^{n,n+1}_{i,j,k}, \tag{2.11}$$

where the fluid flux $\Phi^{n+1}_{i,j,k,\,\text{fluid}}$ is now given by

$$\begin{aligned}\Phi^{n+1}_{i,j,k,\,\text{fluid}} =& \frac{(1-\lambda^{n+1}_{i-\frac{1}{2},j,k})}{\Delta x_{i,j,k}}F^{n}_{i-\frac{1}{2},j,k} - \frac{(1-\lambda^{n+1}_{i+\frac{1}{2},j,k})}{\Delta x_{i,j,k}}F^{n}_{i+\frac{1}{2},j,k}\\ &+ \frac{(1-\lambda^{n+1}_{i,j-\frac{1}{2},k})}{\Delta y_{i,j,k}}G^{n}_{i,j-\frac{1}{2},k} - \frac{(1-\lambda^{n+1}_{i,j+\frac{1}{2},k})}{\Delta y_{i,j,k}}G^{n}_{i,j+\frac{1}{2},k}\\ &+ \frac{(1-\lambda^{n+1}_{i,j,k-\frac{1}{2}})}{\Delta z_{i,j,k}}H^{n}_{i,j,k-\frac{1}{2}} - \frac{(1-\lambda^{n+1}_{i,j,k+\frac{1}{2}})}{\Delta z_{i,j,k}}H^{n}_{i,j,k+\frac{1}{2}},\end{aligned}$$

the solid flux $\Phi^{n}_{i,j,k,\,\text{solid}}$ is now given by

$$\Phi^{n}_{i,j,k,\,\text{solid}} = \frac{1}{V_{i,j,k}} \sum_{\{\mathcal{F}\in\mathfrak{F}\,|\,\mathcal{F}^{n+1}\cap C_{i,j,k}\neq\emptyset\}} \phi^{n}_{i,j,k,\,\mathcal{F}}, \tag{2.12}$$

and the so called swept amount

$$\Delta U^{n,n+1}_{i,j,k} = \sum_{\{\mathcal{F}\in\mathfrak{F}\,|\,\mathcal{F}^{n+1}\cap C_{i,j,k}\neq\emptyset\}} \Delta U^{n,n+1}_{i,j,k,\,\mathcal{F}},$$

where $\Delta U^{n,n+1}_{\mathcal{F}}$ denotes the amount of U swept by the movement of the solid face $\mathcal{F}$ during the time step from t^n to t^{n+1}. The detailed procedure to compute these quantities is described in Section 2.3.3.

One possible difficulty with Immersed Boundary methods is that they can involve small cut-cells (in the sense that the solid volume fraction is greater than, say, 0.5). In order to ensure

the CFL stability condition of the fluid scheme on these cells, the time step should be decreased to an unacceptably small value. To deal with this issue, we use a conservative mixing process following the ideas developed in [52]. Let C_p be a small cell and let C_n be a neighbouring cell with $\Lambda_n < \Lambda_p$ (see Fig. 2.2). We define the following exchange terms: $E_{pn} = \dfrac{(1-\Lambda_n)}{(2-\Lambda_p-\Lambda_n)}(U_n - U_p)$ and $E_{np} = \dfrac{(1-\Lambda_p)}{(2-\Lambda_p-\Lambda_n)}(U_p - U_n)$, and we set $U_p \leftarrow U_p + E_{pn}$ and $U_n \leftarrow U_n + E_{np}$.

The mixing procedure is conservative since $(1-\Lambda_p)E_{pn} + (1-\Lambda_n)E_{np} = 0$ and ensures that the equivalent volume of a small cell is compatible with the usual CFL condition using the standard-size cells.

Another issue is the overlap of the stencil used in the FVM with the solid. Indeed, near the solid, the states needed to calculate the fluid fluxes may be located in cells completely occupied by the solid, “ghost-cells" (see Fig. 2.3). To deal with this issue we follow the ideas developed in Ghost Fluid methods [33, 35, 106], by setting in these ghost cells a fictitious state. We define within these cells an artificial state from the states associated with the mirror cells relatively to the fluid-solid interface. Let C_g be a ghost cell and let C_m be the mirror cell relatively to the fluid-solid interface, we set $\rho_g = \rho_m$, $p_g = p_m$, and $\overrightarrow{u}_g = \overrightarrow{u}_m - 2\overrightarrow{v}_{\mathcal{F}}\left(\overrightarrow{u}_m - \overrightarrow{V}_{\mathcal{F}}\right)\overrightarrow{v}_{\mathcal{F}}$, where $\mathcal{F}$ is the closest solid face in contact with the fluid and $\overrightarrow{V}_{\mathcal{F}}$ denotes the velocity of $\mathcal{F}$.

This treatment possibly affects the order of the method (computation of the fluid flux) but not the conservation. One possibility to improve the order is by interpolation but it requires specified care to avoid non-physically interpolated states. Since the primary focus of this study is the conservation issue rather than the improvement of the order in the vicinity of the boundary, we have resorted to first order mirroring.

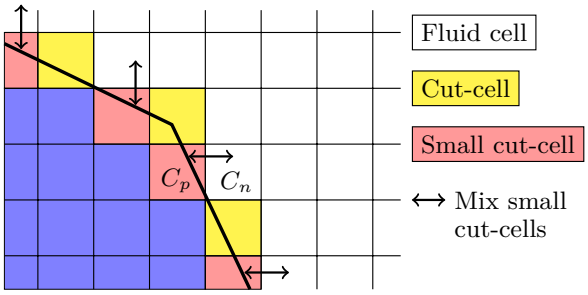

Fig. 2.2: Mix small cut-cells

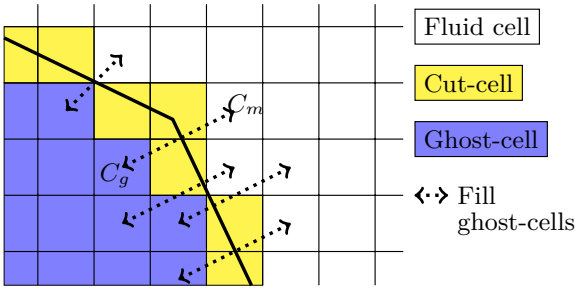

Fig. 2.3: Fill ghost cells

2.3.2 Main steps of the coupling algorithm

The time-integration scheme for fluid-structure interaction is based on a partitioned approach where the coupling is achieved through boundary conditions at the fluid-solid interface. In our case, for an inviscid fluid, we consider perfect slip boundary conditions at the fluid-solid interface:

$$\overrightarrow{u}_{\text{fluid}} \cdot \overrightarrow{\nu}_{\text{fluid}} + \overrightarrow{u}_{\text{solid}} \cdot \overrightarrow{\nu}_{\text{solid}} = 0, \quad \boldsymbol{\sigma}_{\text{fluid}} \cdot \overrightarrow{\nu}_{\text{fluid}} + \boldsymbol{\sigma}_{\text{solid}} \cdot \overrightarrow{\nu}_{\text{solid}} = 0,$$

where $\overrightarrow{u}_{\text{fluid}}$ and $\overrightarrow{u}_{\text{solid}}$, $\boldsymbol{\sigma}_{\text{fluid}}$ and $\boldsymbol{\sigma}_{\text{solid}}$, $\overrightarrow{\nu}_{\text{fluid}}$ and $\overrightarrow{\nu}_{\text{solid}}$ are respectively the velocities, stresses and outward pointing normals for the fluid and solid.

At the beginning of the time step from t^n to t^{n+1}, we know the state of the fluid U^n, the position and rotation of the solid $(\overrightarrow{X}^n, \mathbf{Q}^n)$, as well as the velocity of its center of mass and its angular momentum $(\overrightarrow{V}^n, \mathbf{P}^n)$. The general procedure for the conservative coupling method can be described by the following five steps:

1. The fluid fluxes F^n, G^n, H^n are precomputed at all the cell faces of the fluid grid, without taking into account the presence of the solid. We use the OSMP11 scheme with directional operator splitting. For instance,

   $$U_{i,j,k}^{n+1} = L_x(\Delta t) L_y(\Delta t) L_z(\Delta t)\, U_{i,j,k}^n,$$

   where L_x, L_y, L_z are respectively the operators corresponding to the integration of a time step Δt in the x, y and z directions. For instance,

   $$L_x(\Delta t) W = W - \Delta t \left(\frac{F_{i+\frac{1}{2},j,k}(W) - F_{i-\frac{1}{2},j,k}(W)}{\Delta x} \right).$$

   Thus, second-order time accuracy is recovered every six time steps (corresponding to all L_x, L_y, and L_z permutations) if the directional operators do not commute. We denote by $\overline{p}_x^n$, $\overline{p}_y^n$, and $\overline{p}_z^n$ the pressures used in the application of the operators L_x, L_y, and L_z respectively. These pressures are used to determine the forces exerted by the fluid on the solid during the time step.
2. The fluid force $\overrightarrow{F}_{\mathcal{F},\,\text{fluid}}^n$ acting on the solid face $\mathcal{F}^n$ is equal to the force exerted by these pressures on the surface in contact with the fluid:

   $$\overrightarrow{F}_{\mathcal{F},\,\text{fluid}}^n = \left(-\int_{\mathcal{F}^n} \overline{p}_x^n\, \nu_{x,\mathcal{F}}^n,\; -\int_{\mathcal{F}^n} \overline{p}_y^n\, \nu_{y,\mathcal{F}}^n,\; -\int_{\mathcal{F}^n} \overline{p}_z^n\, \nu_{z,\mathcal{F}}^n \right)^t. \tag{2.13}$$

   The total fluid pressure force acting on the solid is the sum of the contributions on each face:

   $$\overrightarrow{F}_{\text{fluid}}^n = \sum_{\mathcal{F} \in \mathfrak{F}} \overrightarrow{F}_{\mathcal{F},\text{fluid}}^n. \tag{2.14}$$

   The fluid torques $\overrightarrow{\mathcal{M}}_{\text{fluid}}^n$ are the sum of the torques of the pressure forces at the center of mass of the solid:

   $$\overrightarrow{\mathcal{M}}_{\text{fluid}}^n = \sum_{\mathcal{F} \in \mathfrak{F}} \overrightarrow{F}_{\mathcal{F},\text{fluid}}^n \wedge (\overrightarrow{X}_{\mathcal{F}}^n - \overrightarrow{X}^n), \tag{2.15}$$

   where $\overrightarrow{X}_{\mathcal{F}}^n$ is the center of mass of the solid face $\mathcal{F}^n$ and $\overrightarrow{X}^n$ the center of mass of the solid.

3. The solid is advanced in time. The position of the solid (submitted to a constant external fluid force) is integrated using the Verlet scheme for translation and the RATTLE scheme for rotation (see Section 2.2.2).
4. The volume fractions Λ^{n+1} and side area fractions λ^{n+1} can then be computed using the new position of the solid boundary. The fluid fluxes are modified using Λ^{n+1}, Λ^n, λ^{n+1}, the pressures $\overline{p}_x^n$, $\overline{p}_y^n$ and $\overline{p}_z^n$ and the velocity of the boundary in order to enforce the conservation of fluid mass and of the total momentum and energy of the system. At this stage, we can also calculate the swept amount $\Delta U_{\mathcal{F}}^{n,n+1}$.
5. The final value of the state $U_{i,j,k}^{n+1}$ in the cell is calculated using (2.11). Owing to the perfect slip conditions at the solid boundary, the flux $\phi_{\mathcal{F}}^n$ is given by

$$\phi_{\mathcal{F}}^n = \left(0,\, \Pi_{x,\mathcal{F}}^n,\, \Pi_{y,\mathcal{F}}^n,\, \Pi_{z,\mathcal{F}}^n,\, \overrightarrow{V}_{\mathcal{F}}^{n+\frac{1}{2}} \cdot \overrightarrow{\Pi}_{\mathcal{F}}^n\right)^t, \tag{2.16}$$

where

$$\overrightarrow{\Pi}_{\mathcal{F}}^n = \left(\int_{\mathcal{F}^n} \overline{p}_x^n\, \nu_{x,\mathcal{F}}^n,\, \int_{\mathcal{F}^n} \overline{p}_y^n\, \nu_{y,\mathcal{F}}^n,\, \int_{\mathcal{F}^n} \overline{p}_z^n\, \nu_{z,\mathcal{F}}^n\right)^t = -\overrightarrow{F}_{\mathcal{F},\,\text{fluid}}^n,$$

and $\overrightarrow{V}_{\mathcal{F}}^{n+\frac{1}{2}}$ is the velocity of the center of mass of the solid face $\mathcal{F}^n$:

$$\overrightarrow{V}_{\mathcal{F}}^{n+\frac{1}{2}} = V^{n+\frac{1}{2}} + \overrightarrow{\Omega}^{n+\frac{1}{2}} \wedge (\overrightarrow{X}_{\mathcal{F}}^n - \overrightarrow{X}^n), \tag{2.17}$$

where $V^{n+\frac{1}{2}}$ and $\overrightarrow{\Omega}^{n+\frac{1}{2}}$ are, respectively, the average velocity and rotation velocity of the solid in the time interval $\left[t^n,\, t^{n+1}\right]$. We define the angular velocity $\overrightarrow{\Omega}^{n+\frac{1}{2}}$ at time $(n+\frac{1}{2})\Delta t$ using the relation

$$\mathbf{j}(\overrightarrow{\Omega}^{n+\frac{1}{2}}) = \frac{1}{2}\mathbf{P}^{n+\frac{1}{2}}\mathbf{D}^{-1}(\mathbf{Q}^n + \mathbf{Q}^{n+1})^t.$$

We finish by mixing the small cut-cells, and we fill the ghost-cells in order to prepare the next time step (see Section 2.3.1). The general structure of the coupling scheme is presented in Fig. 2.4.

2.3.3 Swept amount

We now detail the computation of the amount swept by the movement of the solid interface during the time step from t^n to t^{n+1} and its distribution over the cut-cells. We first subdivide each solid face $\mathcal{F}^n$ and $\mathcal{F}^{n+1}$ into a set of triangles (called sub-faces) entirely contained in one cell. We then compute the amount swept by the movement of each sub-face and we attribute this amount to the cell containing the sub-face at time t^{n+1}.

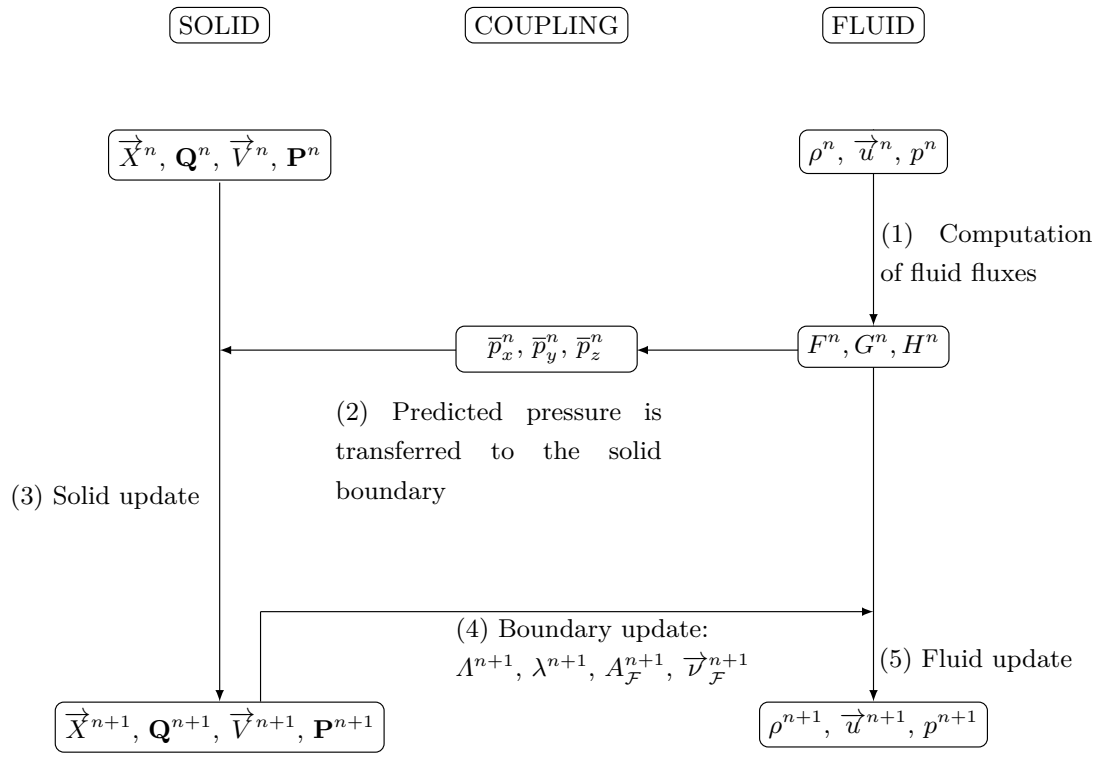

Fig. 2.4: Structure of the coupling scheme

2.3.3.1 Map between $\mathcal{F}^n$ and $\mathcal{F}^{n+1}$ and sub-mesh

To facilitate the computation of the swept amount $\Delta U_{\mathcal{F}}^{n,n+1}$, we subdivide each solid face $\mathcal{F}$ into a set of triangles (called sub-faces) that are contained in one fluid grid cell (not necessary the same) at times t^n and t^{n+1}. We define a piecewise affine map $\Psi_{n,n+1}$ from $\mathcal{F}^n$ to $\mathcal{F}^{n+1}$. If a triangular sub-face has vertices $\overline{a}_1^n$, $\overline{a}_2^n$ and $\overline{a}_3^n$, we can express a point x of the sub-face at time t^n as the weighted combination: $x = \alpha_1(x)\overline{a}_1^n + \alpha_2(x)\overline{a}_2^n + \alpha_3(x)\overline{a}_3^n$; $\alpha_1(x), \alpha_2(x), \alpha_3(x) \geq 0$, $\alpha_1(x) + \alpha_2(x) + \alpha_3(x) = 1$. The local map $\Psi_{n,n+1}$ is then defined as

$$\Psi_{n,n+1}(x) = \alpha_1(x)\overline{a}_1^{n+1} + \alpha_2(x)\overline{a}_2^{n+1} + \alpha_3(x)\overline{a}_3^{n+1}. \tag{2.18}$$

Let us consider the case of Fig. 2.5: in panel 2.5a, we have drawn the intersection of the solid face $\mathcal{F}$ with a fluid grid cell $C_{i,j,k}$ at time t^n and in panel 2.5b, the intersection at time t^{n+1}. Using the map (2.18), we now can draw the intersection on the same plane, see Fig. 2.6, where we have also drawn the whole face $\mathcal{F}$. If we now consider the intersection of $\mathcal{F}$ with all the fluid grid cells, we can obtain the result shown in Fig. 2.7: the intersections at time t^n mapped by $\Psi_{n,n+1}$ are drawn in continuous lines, and the intersections at time t^{n+1} in dashed lines. We denote these polygonal meshes respectively with $S_{\mathcal{F}}^n$ and $S_{\mathcal{F}}^{n+1}$. The idea is now to intersect $\Psi_{n,n+1}(S_{\mathcal{F}}^n)$ with $S_{\mathcal{F}}^{n+1}$. We triangulate the polygonal mesh obtained by the previous intersections at time t^n and t^{n+1} in order to build a sub-mesh of both $S_{\mathcal{F}}^n$ and $S_{\mathcal{F}}^{n+1}$ (see Fig.2.8). Thus, the solid face $\mathcal{F}$ is decomposed into a set of triangles, called sub-faces, denoted by f, so that $\mathcal{F} = \cup f$. As for $\mathcal{F}$, we set $f^n = f(t^n)$ for all $n \geq 0$.

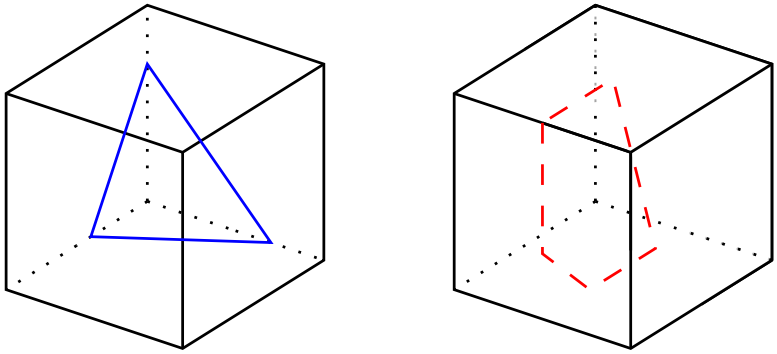

(a) $C_{i,j,k} \cap \mathcal{F}^n$ (b) $C_{i,j,k} \cap \mathcal{F}^{n+1}$

Fig. 2.5: Intersections between a fluid cell and a solid face at time t^n (a) and t^{n+1} (b).

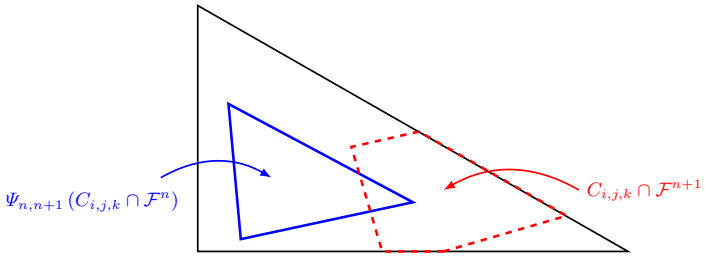

Fig. 2.6: Intersections between a solid face and one fluid grid cell at time t^n (continuous line) and t^{n+1} (dashed line).

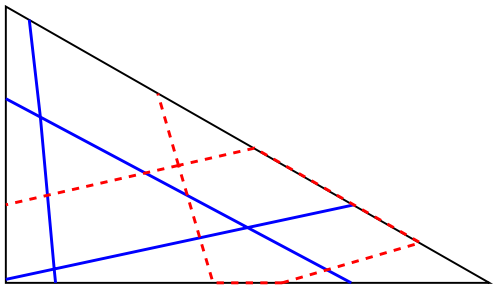

Fig. 2.7: Position of the two intersections: the corresponding meshes at time t^n (continuous line) and t^{n+1} (dashed line).

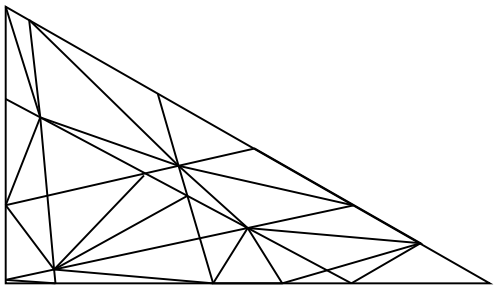

Fig. 2.8: Triangular sub-mesh

2.3.3.2 Integral over the prism and distribution over the cut-cells

The amount swept by the sub-face f during the time step from t^n to t^{n+1} assigned to the cell containing f at time t^{n+1}, denoted $\Delta U^{n,n+1}_{i,j,k,f}$, is the integral of U^n on the prism (possibly twisted, see Section 2.5.2) K_f whose bases are f^n and f^{n+1}:

$$\Delta U^{n,n+1}_{i,j,k,f} = \frac{1}{V_{i,j,k}} \int_{K_f} U\left(t^n, x, y, z\right) \, dx \, dy \, dz.$$

Since U^n is piecewise constant, the integral over the prism K_f is equal to

$$\int_{K_f} U\,(t^n,x,y,z)\;dx\,dy\,dz = \sum_{\{C_{p,q,r}\,|\,K_f\cap C_{p,q,r}\neq\emptyset\,\}} \mathcal{V}_{p,q,r}\,U^n_{p,q,r},$$

where $\mathcal{V}_{p,q,r}$ is the signed volume (in the sense that it can be positive if the prism is positively oriented or negative if it is not) of the intersection between the prism K_f and the fluid grid cell $C_{p,q,r}$ (see Section 2.5.2 for computation details). Thus, $\Delta U^{n,n+1}_{i,j,k,f}$ is given by

$$\Delta U^{n,n+1}_{i,j,k,f} = \frac{1}{V_{i,j,k}} \sum_{\{C_{p,q,r}\,|\,K_f\cap C_{p,q,r}\neq\emptyset\,\}} \mathcal{V}_{p,q,r}\,U^n_{p,q,r},$$

and, finally the swept amount assigned to the cell $C_{i,j,k}$ is the sum of the amount swept by each sub-face f^{n+1} contained in the cell,

$$\Delta U^{n,n+1}_{i,j,k} = \sum_{\{\mathcal{F}\in\mathfrak{F}\,|\,\mathcal{F}^{n+1}\cap C_{i,j,k}\neq\emptyset\}} \sum_{\{f\subset\mathcal{F}^{n+1}|\,f^{n+1}\subset C_{i,j,k}\}} \Delta U^{n,n+1}_{i,j,k,f}\,.$$

As a result, the swept amount verifies

$$\sum_{C_{i,j,k}} \sum_{\{\mathcal{F}\in\mathfrak{F}\,|\,\mathcal{F}^{n+1}\cap C_{i,j,k}\neq\emptyset\}} \Delta U^{n,n+1}_{i,j,k,\mathcal{F}} = \sum_{C_{i,j,k}} (\Lambda^{n+1}_{i,j,k} - \Lambda^n_{i,j,k})U^n_{i,j,k}. \tag{2.19}$$

Finally, we notice that we could have computed directly the integration over the polyhedron $\cup_{t\in[t^n,t^{n+1}]}\mathcal{F}\cap C_{i,j,k}$, without finding a sub-triangular mesh. However, this integration is far more complex computationally than on triangular prisms and the distribution of $\Delta U^{n,n+1}$ over cells would become less accurate.

2.3.4 Evaluation of the fluid pressure forces

In order to ensure the conservation of momentum and energy of the system during the time-step, we need to use the same geometric quantities for the computation of the fluid forces acting on the solid, see (2.13), and for the solid flux, see (2.16). We choose here an explicit method which also satisfies consistency properties. The fluid force acting on the solid face $\mathcal{F}$ is evaluated using $\mathcal{F}^n$, and we split this face among all the sub-faces contained in $\mathcal{F}^n$. This yields

$$\overrightarrow{F}^n_{\mathcal{F},\text{fluid}} = -\overrightarrow{\Pi}^n_{\mathcal{F}} = \sum_{f\subset\mathcal{F}^n} \overrightarrow{F}^n_{f,\text{fluid}},$$

with

$$\overrightarrow{F}^n_{f,\text{fluid}} = \left(-\bar{p}^n_x A^n_f\,\nu^n_{x,f},\,-\bar{p}^n_y A^n_f\,\nu^n_{y,f},\,-\bar{p}^n_z A^n_f\,\nu^n_{z,f}\right)^t := -\overrightarrow{\Pi}^n_f.$$

The reason for the computation of the $\bar{p}^n_x$, $\bar{p}^n_y$, $\bar{p}^n_z$ on f^n is the fact that each sub-face f^n is contained only in one cell at time t^n.

In the computation of the solid flux Φ^n_{solid}, we also use a spiting among the sub-faces,

$$\phi^n_{i,j,k,\mathcal{F}} = \sum_{\{f^n \subset \mathcal{F}^n \,|\, f^{n+1} \subset C_{i,j,k}\}} \phi^n_{i,j,k,f},$$

where

$$\phi^n_{i,j,k,f} = \left(0,\, \Pi^n_{x,f},\, \Pi^n_{y,f},\, \Pi^n_{z,f},\, \overrightarrow{V}^{n+\frac{1}{2}}_f \cdot \overrightarrow{\Pi}^n_f\right)^t,$$

and the velocity $\overrightarrow{V}^{n+\frac{1}{2}}_f$ is evaluated as

$$\overrightarrow{V}^{n+\frac{1}{2}}_f = V^{n+\frac{1}{2}} + \overrightarrow{\Omega}^{n+\frac{1}{2}} \wedge (\overrightarrow{X}^n_f - \overrightarrow{X}^n),$$

where $\overrightarrow{X}^n_f$ is the center of mass of the sub-face f^n and $\overrightarrow{X}^n$ the center of mass of the solid.

2.4 Properties of the coupling scheme

2.4.1 Conservation of mass, momentum, and energy

Conservation of mass, momentum, and energy holds for periodic boundary conditions and more generally in all the cases where such properties hold at the continuous level (i.e. mass and energy with fixed boundaries, conservation when boundaries are far ...).

For simplicity, we assume that the fluid grid is uniform and we denote by V the volume of the fluid grid cells, $V = (\Delta x \Delta y \Delta z)$. We sum (2.11) over all the fluid grid cells $C_{i,j,k}$; owing to the cancellation of fluxes on each fluid grid cell face, we infer that

$$\sum_{C_{i,j,k}} \left(1 - \Lambda^{n+1}_{i,j,k}\right) U^{n+1}_{i,j,k} = \sum_{C_{i,j,k}} \left(1 - \Lambda^{n+1}_{i,j,k}\right) U^n_{i,j,k} + \frac{\Delta t}{V} \sum_{C_{i,j,k}} \sum_{\{\mathcal{F} \in \mathfrak{F} \,|\, \mathcal{F}^{n+1} \cap C_{i,j,k} \neq \emptyset\}} \phi^n_{i,j,k,\mathcal{F}} + \sum_{C_{i,j,k}} \sum_{\{\mathcal{F} \in \mathfrak{F} \,|\, \mathcal{F}^{n+1} \cap C_{i,j,k} \neq \emptyset\}} \Delta U^{n,n+1}_{i,j,k,\mathcal{F}}.$$

Using (2.19) yields

$$\sum_{C_{i,j,k}} \left(1 - \Lambda^{n+1}_{i,j,k}\right) U^{n+1}_{i,j,k} = \sum_{C_{i,j,k}} \left(1 - \Lambda^n_{i,j,k}\right) U^n_{i,j,k} + \frac{\Delta t}{V} \sum_{\mathcal{F} \in \mathfrak{F}} \phi^n_{\mathcal{F}}.$$

We finally obtain

$$\frac{1}{V} \int_{\Omega^{n+1}_{\text{fluid}}} U^{n+1} = \frac{1}{V} \int_{\Omega^n_{\text{fluid}}} U^n + \frac{\Delta t}{V} \sum_{\mathcal{F} \in \mathfrak{F}} \phi^n_{\mathcal{F}}. \tag{2.20}$$

The expression of $\phi_{\mathcal{F}}^n$ in (2.16) shows that the first component is equal to zero. Hence, the first component of (2.20) expresses the fluid mass conservation. Replacing the expression of $\phi_{\mathcal{F}}^n$ from (2.16) in the fluid momentum and energy equations, leads to

$$\int_{\Omega_{\text{fluid}}^{n+1}} \rho^{n+1} \overrightarrow{u}^{n+1} = \int_{\Omega_{\text{fluid}}^{n}} \rho^n \overrightarrow{u}^n + \Delta t \sum_{\mathcal{F}\in\mathfrak{F}} \int_{\mathcal{F}^n} \overrightarrow{\Pi}_{\mathcal{F}}^n,$$
$$\int_{\Omega_{\text{fluid}}^{n+1}} \rho^{n+1} E^{n+1} = \int_{\Omega_{\text{fluid}}^{n}} \rho^n E^n + \Delta t \sum_{\mathcal{F}\in\mathfrak{F}} \int_{\mathcal{F}^n} \overrightarrow{V}_{\mathcal{F}}^{n+\frac{1}{2}} \cdot \overrightarrow{\Pi}_{\mathcal{F}}^n.$$

The fluid pressure force applied on the solid face $\mathcal{F} \in \mathfrak{F}$ during the time step is given by (2.13). The solid momentum variation induced by the pressure forces on $\mathcal{F}$, denoted $\Delta P_{\mathcal{F}}$, and the corresponding energy variation, denoted $\Delta E_{\mathcal{F}}$, are given by

$$\Delta P_{\mathcal{F}} = \Delta t \, \overrightarrow{F}_{\mathcal{F},\text{fluid}}^n = -\Delta t \int_{\mathcal{F}^n} \overrightarrow{\Pi}_{\mathcal{F}}^n, \tag{2.21}$$
$$\Delta E_{\mathcal{F}} = \Delta t \, \overrightarrow{F}_{\mathcal{F},\text{fluid}}^n \cdot \overrightarrow{V}_{\mathcal{F}}^{n+\frac{1}{2}} = -\Delta t \, \overrightarrow{V}_{\mathcal{F}}^{n+\frac{1}{2}} \cdot \int_{\mathcal{F}^n} \overrightarrow{\Pi}_{\mathcal{F}}^n. \tag{2.22}$$

Thus, the balance of momentum and energy in the fluid domain results in

$$\int_{\Omega_{\text{fluid}}^{n+1}} \rho^{n+1} \, \overrightarrow{u}^{n+1} + \sum_{\mathcal{F}\in\mathfrak{F}} \Delta P_{\mathcal{F}} = \int_{\Omega_{\text{fluid}}^{n}} \rho^n \overrightarrow{u}^n,$$
$$\int_{\Omega_{\text{fluid}}^{n+1}} \rho^{n+1} E^{n+1} + \sum_{\mathcal{F}\in\mathfrak{F}} \Delta E_{\mathcal{F}} = \int_{\Omega_{\text{fluid}}^{n}} \rho^n E^n.$$

This proves the balance of the momentum and energy on each time step.

2.4.2 Consistency

2.4.2.1 Perfect slipping along a wall

We consider a rigid, fixed solid consisting of a semi-infinite half-space and a constant fluid state such that $\rho^n = \rho_0$, $\overrightarrow{u}^n = \overrightarrow{u}_0 = (u_0, v_0, w_0)$, $p^n = p_0$. The fluxes are such that

$$F_{i-\frac{1}{2},j,k} = F_{i+\frac{1}{2},j,k} = \Big(\rho_0 \, u_0, \, \rho_0 \, u_0^2 + p, \, \rho_0 \, u_0 \, v_0, \, \rho_0 \, u_0 \, w_0, \, (\rho_0 \, E + p) u_0\Big)^t,$$

$$G_{i,j-\frac{1}{2},k} = G_{i,j+\frac{1}{2},k} = \Big(\rho_0 \, v_0, \, \rho_0 \, u_0 \, v_0, \, \rho_0 \, v_0^2 + p, \, \rho_0 \, v_0 \, w_0, \, (\rho_0 \, E + p) v_0\Big)^t,$$

$$H_{i,j,k-\frac{1}{2}} = H_{i,j,k+\frac{1}{2}} = \Big(\rho_0 \, w_0, \, \rho_0 \, u_0 \, w_0, \, \rho_0 \, v_0 \, w_0, \, \rho_0 \, w_0^2 + p, \, (\rho_0 \, E + p) w_0\Big)^t.$$

The pressure on the boundary of the solid is $\bar{p}_x = \bar{p}_y = \bar{p}_z = p_0$. The solid boundary is a straight planar boundary with a constant normal vector $\overrightarrow{\nu}$ such that $\overrightarrow{\nu} \cdot \overrightarrow{u}_0 = 0$. Since the solid is

fixed, Λ, λ, $A_{\mathcal{F}}$ remain constant in time, the swept amount $\Delta U_{\mathcal{F}}^{n,n+1}$ is equal to zero, and we obtain

$$\begin{aligned}(1-\Lambda_{i,j,k})\,U_{i,j,k}^{n+1} = {} & (1-\Lambda_{i,j,k})\,U_0 \\ & - \frac{\Delta t}{V_{i,j,k}} \sum_{\{\mathcal{F}\in\mathfrak{F}\,|\,\mathcal{F}\cap C_{i,j,k}\neq\emptyset\}} A_{\mathcal{F}}\left(F_{i+\frac{1}{2},j,k}\nu^x + G_{i,j+\frac{1}{2},k}\nu^y + H_{i,j,k+\frac{1}{2}}\nu^z\right) \\ & + \frac{\Delta t}{V_{i,j,k}} \sum_{\{\mathcal{F}\in\mathfrak{F}\,|\,\mathcal{F}\cap C_{i,j,k}\neq\emptyset\}} \phi_{i,j,k,\mathcal{F}}.\end{aligned}$$

The flux on the solid face $\mathcal{F}$ is calculated using (2.16), so the system (2.11) reduces to

$$(1-\Lambda_{i,j,k})\,\rho_{i,j,k}^{n+1} = (1-\Lambda_{i,j,k})\,\rho_0 - \frac{\Delta t}{V_{i,j,k}} \sum_{\{\mathcal{F}\in\mathfrak{F}\,|\,\mathcal{F}\cap C_{i,j,k}\neq\emptyset\}} A_{\mathcal{F}}\rho_0(\overrightarrow{\nu}\cdot\overrightarrow{u}_0),$$

$$\begin{aligned}(1-\Lambda_{i,j,k})\,(\rho\overrightarrow{u})_{i,j,k}^{n+1} = {} & (1-\Lambda_{i,j,k})\,\rho_0\overrightarrow{u}_0 \\ & - \frac{\Delta t}{V_{i,j,k}} \sum_{\{\mathcal{F}\in\mathfrak{F}\,|\,\mathcal{F}\cap C_{i,j,k}\neq\emptyset\}} A_{\mathcal{F}}\left((\overrightarrow{\nu}\cdot\overrightarrow{u}_0)\rho_0\,\overrightarrow{u}_0 + p_0\,\overrightarrow{\nu}\right) \\ & + \frac{\Delta t}{V_{i,j,k}} \sum_{\{\mathcal{F}\in\mathfrak{F}\,|\,\mathcal{F}\cap C_{i,j,k}\neq\emptyset\}} A_{\mathcal{F}}p_0\,\overrightarrow{\nu},\end{aligned}$$

$$(1-\Lambda_{i,j,k})\,(\rho E)_{i,j,k}^{n+1} = (1-\Lambda_{i,j,k})\,\rho_0 E_0 - \frac{\Delta t}{V_{i,j,k}} \sum_{\{\mathcal{F}\in\mathfrak{F}\,|\,\mathcal{F}\cap C_{i,j,k}\neq\emptyset\}} A_{\mathcal{F}}(\overrightarrow{\nu}\cdot\overrightarrow{u}_0)(\rho_0 e_0 + p_0).$$

We finally obtain $U_{i,j,k}^{n+1} = U_0$. This result shows that the coupling algorithm preserves exactly a uniform constant flow parallel to a rigid half-plane, even in the case where the solid faces is are aligned with the fluid grid. In other words, no artificial roughness appears on the solid walls.

2.4.2.2 Consistency with uniform solid translation

We consider an arbitrarily shaped rigid body moving at constant velocity and without rotation, immersed in a uniform fluid flowing at the same velocity.

The volume swept by the solid face $\mathcal{F}$ during the time step is $\Delta t\,A_{\mathcal{F}}\overrightarrow{u}_0\cdot\overrightarrow{\nu}_{\mathcal{F}}$ (the solid moves without rotation, so the normal vector $\overrightarrow{\nu}_{\mathcal{F}}(t)$ to the $\mathcal{F}(t)$ is constant in time), so the swept amount is

$$\sum_{\{\mathcal{F}\in\mathfrak{F}\,|\,\mathcal{F}^{n+1}\cap C_{i,j,k}\neq\emptyset\}} \Delta U_{i,j,k,\mathcal{F}}^{n,n+1} = \frac{\Delta t}{V_{i,j,k}} \sum_{\{\mathcal{F}\in\mathfrak{F}\,|\,\mathcal{F}^{n+1}\cap C_{i,j,k}\neq\emptyset\}} A_{\mathcal{F}}(\overrightarrow{u}_0\cdot\overrightarrow{\nu}_{\mathcal{F}})U_0.$$

The first component of system (2.11) is given by

$$\left(1-\Lambda_{i,j,k}^{n+1}\right)\rho_{i,j,k}^{n+1}=\left(1-\Lambda_{i,j,k}^{n+1}\right)\rho_0-\frac{\Delta t}{V_{i,j,k}}\sum_{\{\mathcal{F}\in\mathfrak{F}\,|\,\mathcal{F}^{n+1}\cap C_{i,j,k}\neq\emptyset\}}A_{\mathcal{F}}\rho_0(\overrightarrow{u}_0\cdot\overrightarrow{\nu}_{\mathcal{F}})$$
$$+\frac{\Delta t}{V_{i,j,k}}\sum_{\{\mathcal{F}\in\mathfrak{F}\,|\,\mathcal{F}^{n+1}\cap C_{i,j,k}\neq\emptyset\}}A_{\mathcal{F}}(\overrightarrow{u}_0\cdot\overrightarrow{\nu}_{\mathcal{F}})\rho_0=\left(1-\Lambda_{i,j,k}^{n+1}\right)\rho_0.$$

The second component of system (2.11) is equal to

$$(1-\Lambda_{i,j,k})\,(\rho u)_{i,j,k}^{n+1}=(1-\Lambda_{i,j,k})\,\rho_0u_0-\frac{\Delta t}{V_{i,j,k}}\sum_{\{\mathcal{F}\in\mathfrak{F}\,|\,\mathcal{F}^{n+1}\cap C_{i,j,k}\neq\emptyset\}}A_{\mathcal{F}}\left((\overrightarrow{\nu}_{\mathcal{F}}\cdot\overrightarrow{u}_0)\rho_0u_0+p_0\,\nu_{\mathcal{F}}^x\right)$$
$$+\frac{\Delta t}{V_{i,j,k}}\sum_{\{\mathcal{F}\in\mathfrak{F}\,|\,\mathcal{F}^{n+1}\cap C_{i,j,k}\neq\emptyset\}}p_0\,\nu_{\mathcal{F}}^x$$
$$+\frac{\Delta t}{V_{i,j,k}}\sum_{\{\mathcal{F}\in\mathfrak{F}\,|\,\mathcal{F}^{n+1}\cap C_{i,j,k}\neq\emptyset\}}A_{\mathcal{F}}(\overrightarrow{\nu}_{\mathcal{F}}\cdot\overrightarrow{u}_0)\rho_0u_0=(1-\Lambda_{i,j,k})\,\rho_0\,u_0.$$

Similarly, we obtain $U_{i,j,k}^{n+1}=U_0$. This shows that the constant flow is left unchanged by the coupling algorithm. Since the solid is a closed set, $\sum_{\mathcal{F}\in\mathfrak{F}}A_{\mathcal{F}}\overrightarrow{\nu}_{\mathcal{F}}=0$. Using (3.23), the fluid forces are

$$\overrightarrow{F}_{\text{fluid}}^{\,n}=-\sum_{\mathcal{F}\in\mathfrak{F}}p_0A_{\mathcal{F}}\overrightarrow{\nu}_{\mathcal{F}}=0.$$

In the same way, the fluid torques cancel. This shows that the uniform movement of the fluid and of the solid is conserved by the coupling algorithm.

2.4.3 Quasi-conservation of energy for the rigid solid

Let $\mathcal{E}_s^n$ be the solid energy at time t^n defined as

$$\mathcal{E}_s^n=\frac{1}{2}m\|\overrightarrow{V}^n\|^2+\frac{1}{2}tr\left(\mathbf{P}^n\mathbf{D}^{-1}(\mathbf{P}^n)^t\right).$$

Proposition 2.1. *The variation of the solid energy over a time step in terms of the fluid forces and torques and of the velocity of the solid is*

$$\mathcal{E}_s^{n+1}=\mathcal{E}_s^n+\Delta t\overrightarrow{F}_{fluid}^{\,n}\cdot\overrightarrow{V}^{n+\frac{1}{2}}+\Delta t\overrightarrow{\mathcal{M}}_{fluid}^{n}\cdot\overrightarrow{\Omega}^{n+\frac{1}{2}}+\frac{\Delta t^2}{8}tr\left(\mathbf{\Upsilon}^n\mathbf{Q}^n\mathbf{D}^{-1}(\mathbf{Q}^n)^t\mathbf{\Upsilon}^n\right)$$
$$-\frac{\Delta t^2}{8}tr\left(\tilde{\mathbf{\Upsilon}}^{n+1}\mathbf{Q}^{n+1}\mathbf{D}^{-1}(\mathbf{Q}^{n+1})^t\tilde{\mathbf{\Upsilon}}^{n+1}\right)+\frac{\Delta t^2}{32}tr\left(\mathbf{j}(\overrightarrow{\mathcal{M}}_{fluid}^{n})\mathbf{Q}^n\mathbf{D}^{-1}(\mathbf{Q}^n)^t\mathbf{j}(\overrightarrow{\mathcal{M}}_{fluid}^{n})\right)$$
$$-\frac{\Delta t^2}{32}tr\left(\mathbf{j}(\overrightarrow{\mathcal{M}}_{fluid}^{n})\mathbf{Q}^{n+1}\mathbf{D}^{-1}(\mathbf{Q}^{n+1})^t\mathbf{j}(\overrightarrow{\mathcal{M}}_{fluid}^{n})\right).$$

Using the expression of $\overrightarrow{\mathcal{M}}_{\text{fluid}}^{n}$ in (2.17) and the expression of $\overrightarrow{V}_{\mathcal{F}}^{n+\frac{1}{2}}$ in (2.15), leads to

$$\mathcal{E}_s^{n+1} = \mathcal{E}_s^n + \Delta t \sum_{\mathcal{F}\in\mathfrak{F}} \overrightarrow{F}^n_{\mathcal{F},\text{fluid}} \cdot \overrightarrow{V}^{n+\frac{1}{2}}_{\mathcal{F}} + \frac{\Delta t^2}{8} tr\left(\boldsymbol{\Upsilon}^n \mathbf{Q}^n \mathbf{D}^{-1} (\mathbf{Q}^n)^t \boldsymbol{\Upsilon}^n\right)$$
$$- \frac{\Delta t^2}{8} tr\left(\tilde{\boldsymbol{\Upsilon}}^{n+1} \mathbf{Q}^{n+1} \mathbf{D}^{-1} (\mathbf{Q}^{n+1})^t \tilde{\boldsymbol{\Upsilon}}^{n+1}\right) + \frac{\Delta t^2}{32} tr\left(\mathbf{j}(\overrightarrow{\mathcal{M}}^n_{\text{fluid}}) \mathbf{Q}^n \mathbf{D}^{-1} (\mathbf{Q}^n)^t \mathbf{j}(\overrightarrow{\mathcal{M}}^n_{\text{fluid}})\right)$$
$$- \frac{\Delta t^2}{32} tr\left(\mathbf{j}(\overrightarrow{\mathcal{M}}^n_{\text{fluid}}) \mathbf{Q}^{n+1} \mathbf{D}^{-1} (\mathbf{Q}^{n+1})^t \mathbf{j}(\overrightarrow{\mathcal{M}}^n_{\text{fluid}})\right).$$

The works of fluid forces and torques cancel with their discrete counterpart in the fluid integration scheme. Concerning the additional four terms, in the two-dimensional case, they vanish due to the commutation of the rotation matrices and their commutation with the matrices $\mathbf{D}$ and $\mathbf{j}(\mathcal{M})$. In the three-dimensional case, the conservation of energy is not exact anymore. However, the discrepancy is limited: the Lagrange multipliers $\boldsymbol{\Upsilon}^n$ and $\tilde{\boldsymbol{\Upsilon}}^{n+1}$ are close enough to one another if the rotation matrices $\mathbf{Q}^n$ and $\mathbf{Q}^{n+1}$ are close. This provides a second-order error on the energy in terms of the time-step, which we have checked in practice. Therefore, we obtain a quasi-conservation of energy in that case.

Proof. Recall that if $\mathbf{A}$ and $\mathbf{S}$ are respectively a skew-symmetric and a symmetric matrix, then

$$tr(\mathbf{AS}) = 0. \tag{2.23}$$

Developing $\mathcal{E}_s^{n+1}$ using equations (2.2)–(2.7), we obtain

$$\mathcal{E}_s^{n+1} = \frac{1}{2} m \|\overrightarrow{V}^n\|^2 + \Delta t \overrightarrow{F}^n_{\text{fluid}} \cdot \overrightarrow{V}^{n+\frac{1}{2}} + \frac{1}{2} tr\left(\mathbf{P}^n \mathbf{D}^{-1} (\mathbf{P}^n)^t\right) + \frac{\Delta t}{2} tr\left(\mathbf{P}^{n+1} \mathbf{D}^{-1} (\mathbf{Q}^{n+1})^t \tilde{\boldsymbol{\Upsilon}}^{n+1}\right)$$
$$+ \frac{\Delta t}{2} tr\left(\mathbf{P}^n \mathbf{D}^{-1} (\mathbf{Q}^n)^t \boldsymbol{\Upsilon}^n\right) + \frac{\Delta t}{2} tr\left(\mathbf{j}(\overrightarrow{\mathcal{M}}^n_{\text{fluid}})(\mathbf{Q}^n + \mathbf{Q}^{n+1}) \mathbf{D}^{-1} (\mathbf{P}^{n+\frac{1}{2}})^t\right)$$
$$+ \frac{\Delta t^2}{8} tr\left(\boldsymbol{\Upsilon}^n \mathbf{Q}^n \mathbf{D}^{-1} (\mathbf{Q}^n)^t \boldsymbol{\Upsilon}^n\right) - \frac{\Delta t^2}{8} tr\left(\tilde{\boldsymbol{\Upsilon}}^{n+1} \mathbf{Q}^{n+1} \mathbf{D}^{-1} (\mathbf{Q}^{n+1})^t \tilde{\boldsymbol{\Upsilon}}^{n+1}\right)$$
$$+ \frac{\Delta t^2}{32} tr\left(\mathbf{j}(\overrightarrow{\mathcal{M}}^n_{\text{fluid}}) \mathbf{Q}^n \mathbf{D}^{-1} (\mathbf{Q}^n)^t \mathbf{j}(\overrightarrow{\mathcal{M}}^n_{\text{fluid}})\right) - \frac{\Delta t^2}{32} tr\left(\mathbf{j}(\overrightarrow{\mathcal{M}}^n_{\text{fluid}}) \mathbf{Q}^{n+1} \mathbf{D}^{-1} (\mathbf{Q}^{n+1})^t \mathbf{j}(\overrightarrow{\mathcal{M}}^n_{\text{fluid}})\right).$$

Using (2.23), (2.9) at times t^n and t^{n+1} and the symmetry of $\boldsymbol{\Upsilon}^n$ and $\tilde{\boldsymbol{\Upsilon}}^{n+1}$, the fourth and fifth term vanish. We now prove the following result to estimate the sixth term on the right-hand side.

Lemma 2.1. *$\mathbf{P}^{n+\frac{1}{2}} \mathbf{D}^{-1} (\mathbf{Q}^n + \mathbf{Q}^{n+1})^t$ is a skew-symmetric matrix, so that we can define the angular velocity vector $\overrightarrow{\Omega}^{n+\frac{1}{2}}$ at time $(n+\frac{1}{2})\Delta t$ by $\mathbf{j}(\overrightarrow{\Omega}^{n+\frac{1}{2}}) = \frac{1}{2} \mathbf{P}^{n+\frac{1}{2}} \mathbf{D}^{-1} (\mathbf{Q}^n + \mathbf{Q}^{n+1})^t$.*

Proof. Let us note that $\mathbf{P}^{n+\frac{1}{2}} \mathbf{D}^{-1} = \frac{1}{\Delta t} (\mathbf{Q}^{n+1} - \mathbf{Q}^n)$. It follows that

$$\mathbf{P}^{n+\frac{1}{2}} \mathbf{D}^{-1} (\mathbf{Q}^n + \mathbf{Q}^{n+1})^t = \frac{1}{\Delta t} (\mathbf{Q}^{n+1} - \mathbf{Q}^n)(\mathbf{Q}^n + \mathbf{Q}^{n+1})^t = \frac{1}{\Delta t} (\mathbf{Q}^{n+1} (\mathbf{Q}^n)^t - \mathbf{Q}^n (\mathbf{Q}^{n+1})^t).$$

which proves the result.

We can now finish the proof. It is straightforward to see that

$$tr\left(\mathbf{j}(\overrightarrow{\mathcal{M}}^n_{\text{fluid}}) \mathbf{j}(\overrightarrow{\Omega}^{n+\frac{1}{2}})\right) = -2 \overrightarrow{\mathcal{M}}^n_{\text{fluid}} \cdot \overrightarrow{\Omega}^{n+\frac{1}{2}}.$$

Finally, we obtain the variation of the discrete solid energy in terms of the fluid forces and torques and of the velocity of the solid as follows:

$$\mathcal{E}_s^{n+1} = \mathcal{E}_s^n + \Delta t \overrightarrow{F}^n_{\text{fluid}} \cdot \overrightarrow{V}^{n+\frac{1}{2}} + \Delta t \overrightarrow{\mathcal{M}}^n_{\text{fluid}} \cdot \overrightarrow{\Omega}^{n+\frac{1}{2}} + \frac{\Delta t^2}{8} tr\left(\boldsymbol{\Upsilon}^n \mathbf{Q}^n \mathbf{D}^{-1} (\mathbf{Q}^n)^t \boldsymbol{\Upsilon}^n\right)$$
$$- \frac{\Delta t^2}{8} tr\left(\tilde{\boldsymbol{\Upsilon}}^{n+1} \mathbf{Q}^{n+1} \mathbf{D}^{-1} (\mathbf{Q}^{n+1})^t \tilde{\boldsymbol{\Upsilon}}^{n+1}\right) + \frac{\Delta t^2}{32} tr\left(\mathbf{j}(\overrightarrow{\mathcal{M}}^n_{\text{fluid}}) \mathbf{Q}^n \mathbf{D}^{-1} (\mathbf{Q}^n)^t \mathbf{j}(\overrightarrow{\mathcal{M}}^n_{\text{fluid}})\right)$$
$$- \frac{\Delta t^2}{32} tr\left(\mathbf{j}(\overrightarrow{\mathcal{M}}^n_{\text{fluid}}) \mathbf{Q}^{n+1} \mathbf{D}^{-1} (\mathbf{Q}^{n+1})^t \mathbf{j}(\overrightarrow{\mathcal{M}}^n_{\text{fluid}})\right).$$

2.5 Geometric algorithms for the coupling scheme

In this section, we present the geometric algorithms required for the implementation of the coupling scheme. We first describe the algorithms used for the detection of the cut-cells as well as the computation of the required informations for each of them. Afterwards, the algorithm used for the evaluation of the swept amount due to the movement of the solid faces during a time step is presented.

2.5.1 Cut-cell volume

At each time step, intersections between the solid boundary and the fluid grid cells need to be computed. The Immersed Boundary method uses various geometric quantities (the volume occupied by the solid in the cut-cell, the occupation of the cut-cell faces, and the boundary areas, see Fig. 2.1) generated by these intersections. The fluid is discretized and solved on a Cartesian grid. If the solid is not convex, we decompose it into a finite number of convex polyhedral particles. The algorithm introduced here operates on individual fluid grid cells, one at a time. The first part identifies the cut-cells, and the second part computes the polyhedron resulting from the intersection between the fluid grid cell C and each particle P composing the solid S.

We distinguish intersection tests which do not construct any intersection objects and intersection algorithms which construct the intersection objects. The first type of algorithm tests if the objects intersect and is fast as it stops after the first encountered intersection. The second type of algorithm constructs all intersection objects. Checking for intersection is easier and much faster than actually computing the intersection result. The algorithm hinges on two major tasks:

1. **Do convex 3d polyhedra P and Q intersect?**
   For the intersection detection tests, a classical efficient algorithm consists in approximating the geometric primitives (the polyhedra P and Q) with their axis-aligned bounding boxes. If the bounding boxes do not intersect, then the objects do not either. Only when a pair of

boxes intersect, the exact answer is tested on the complex geometric primitives contained in the boxes.

2. **Given intersecting convex 3d polyhedra P and Q, compute their intersection**. The polyhedra being convex, we triangulate all the faces of P and Q and compute the intersection between the triangular faces from P and the triangular faces from Q. Thus the problem can be reduced to the computation of the intersection between triangles in three-dimensional space. The intersection can be empty, a point, a segment, a triangle, or a polygon. Finally, the polyhedron resulting from the intersection of P and Q is obtained by the computation of the convex hull of all the end points of the segments, triangles and polygons resulting from the intersection between all the triangular faces of P and Q.

The algorithm for computing the intersection between a fluid grid cell C and a convex solid particle P is described in Algorithm 1. All the three-dimensional geometric tasks are handled by CGAL (Computational Geometry Algorithms Library) which is an open source C++ library that contains primitives, data structures and algorithms for computational geometry, as well as a comprehensive documentation [1].

Algorithm 1 Intersection between a fluid grid cell C and a convex solid particle P (intersection between 3d convex objects)

Associate a bounding Box to $C \Longrightarrow Box\_C$
Associate a bounding Box to $P \Longrightarrow Box\_P$
if $(Box\_C \cap Box\_P \neq \emptyset)$ **then**
  if $(C \subset P)$ **then**
    Intersection result is C
  else
    Search vertices of P contained in C: $Vertex\_P \in C$
    for $Faces\_P = 0$ to $Faces\_P = Nb\_faces\_P$ **do** ▷ Loop over the triangular faces of P
      if $(Box\_C \cap Faces\_P \neq \emptyset)$ **then**
        for $Faces\_C = 0$ to $Faces\_C = Nb\_faces\_C$ **do** ▷ Loop over the triangular faces of C
          Search vertices of C contained in P: $Vertex\_C \in P$
          if $(Faces\_C \cap Faces\_P \neq \emptyset)$ **then**
            Compute the intersection between $Faces\_C$ **and** $Faces\_P$
            ▷ Intersections between triangles in 3d
          end if
        end for
      end if
    end for
  end if
end if

The time required for the determination of the intersections between the solid and the Cartesian fluid grid and for the computation of the volume of the resulting cut-cells, the occupation of the cut-cells faces and the boundary areas, appears to be comparable to the CPU time required

for a fluid flux calculation on one time step in the present test cases. As the cut-cell volume calculation is performed for each cut-cell separately, the CPU time required for the volume calculation routine scales linearly with the number of cut-cells and the number of the triangles describing the surface of the solid.

2.5.2 Swept amount

For the computation of the amount swept by the movement of the solid face during a time step, we use the following algorithm which we decompose into two major steps:

1. The first step consists in decomposing the solid faces into triangular sub-faces entirely contained in a cell at the discrete times n and $n+1$ (not necessarily the same). The detailed procedure is described in Section 2.3.3.
2. The second step consists in calculating the amount swept by the movement of the triangular sub-face between the discrete times n and $n+1$.

The amount swept by the movement of a triangular sub-face over the time step is the integral of U^n over the prism K_f whose bases are the triangular sub-faces at the discrete times n and $n+1$, denoted by T^n and T^{n+1} respectively. The lateral faces of the prism are not necessarily planar. In the case where the prism is entirely contained in one cell we can calculate its signed volume by using the following formula for a prism $P(A_1B_1C_1, A_2B_2C_2)$ whose bases are the triangles $T(A_1B_1C_1)$ and $T(A_2B_2C_2)$:

$$\begin{aligned} Vol(P) =& \frac{1}{36}\left(2\overrightarrow{A_1B_1}\wedge\overrightarrow{A_1C_1}+2\overrightarrow{A_2B_2}\wedge\overrightarrow{A_2C_2}+\overrightarrow{A_1B_1}\wedge\overrightarrow{A_2C_2}+\overrightarrow{A_2B_2}\wedge\overrightarrow{A_1C_1}\right)\cdot \\ & \left(\overrightarrow{A_1A_2}+\overrightarrow{B_1B_2}+\overrightarrow{C_1C_2}\right) \end{aligned}$$

Otherwise, since U^n is piecewise constant, the integral of U^n over the prism is computed by first determining the intersection between the prism and the Cartesian fluid grid. Due to the CFL condition, at most eight fluid grid cells intersect the prism K_f. In order to compute these intersections, we triangulate the lateral faces of the prism with respect to the barycenter of the end-points, and we decompose the prism into tetrahedra (see Fig. 2.9). Supposing that the prism bases are the triangles $T(A_1B_1C_1)$ and $T(A_2B_2C_2)$, we define the points (A, B, C) as barycenters of the four end points of the possibly non-planar faces:

$$A=\frac{1}{4}(B_1+B_2+C_1+C_2),\quad B=\frac{1}{4}(A_1+A_2+C_1+C_2)\quad\text{and}\quad C=\frac{1}{4}(A_1+A_2+B_1+B_2).$$

The tetrahedra composing the prism are: $T(A_1A_2CB)$, $T(B_1B_2AC)$, $T(C_1C_2BA)$, $T(A_1CC_1B)$, $T(B_1AC_1C)$, $T(ACBC_1)$, $T(ABCC_2)$, $T(AB_2C_2C)$, $T(A_1B_1C_1C)$, $T(A_2C_2CB)$, and $T(A_2B_2CC_2)$. Finally, we compute the intersections of these tetrahedra with the fluid grid cells. In particular, we reduce the computation of the intersection between the prism and the Cartesian fluid grid, by proceeding as in Section 2.5.1, to the computation of intersection between triangles in tree-dimension by considering the intersection between the faces of tetrahedra and the triangulated cell faces.

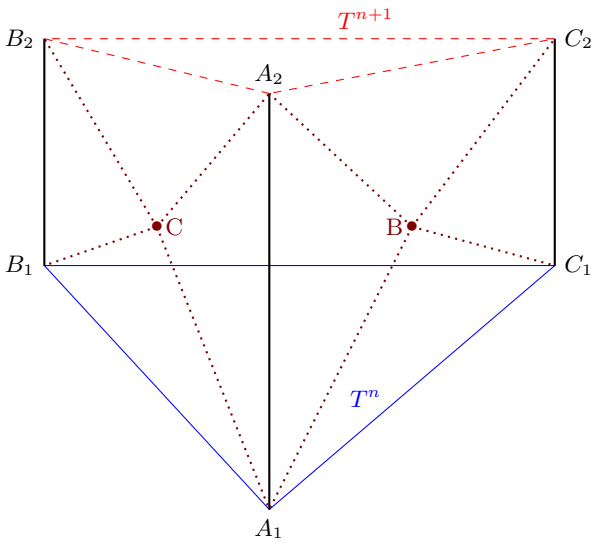

Fig. 2.9: Cutting the "prism" whose bases are T^n (continuous line) and T^{n+1} (dashed line) into tetrahedra.

2.6 Numerical results

In this section we present numerical results. We first verify the conservation properties of the scheme. Then, we consider the interaction of a shock wave with comparison to 2D results and with a sphere.

2.6.1 Conservation of mass and energy

In order to verify the conservation of mass and energy by the coupling scheme, we consider a test case consisting of a simple shock tube in a straight rectangular channel and a rigid mobile solid inside this channel. The computational domain is the rectangular box $[0,\,2] \times [0,\,1] \times [0,\,1]$m and the initial flow field is given by

$$\begin{cases} \rho = 1.4\,kg.m^{-3},\ u = v = w = 0\,m.s^{-1},\ p = 5\,Pa, & \text{if } x < 0.16\,m, \\ \rho = 1.4\,kg.m^{-3},\ u = v = w = 0\,m.s^{-1},\ p = 1\,Pa, & \text{if } x \geq 0.16\,m. \end{cases}$$

The initial position of the solid corresponds to the cuboid $(x, y, z) \in [0.4,\,0.9] \times [0.4,\,0.6] \times [0.4,\,0.6]$m. The computation is performed on a $(140 \times 70 \times 70)$ grid with periodic boundary conditions. The simulation time is $t = 1$s.

The pressure and density distribution along the line $\{y = 0.5\,m, z = 0.75\,m\}$ are shown in Fig. 2.10. We observe that the shocks and rarefaction waves are well captured, without spurious oscillations. The resolution of the shocks is obviously moderate due to the relative coarseness of the fluid grid.

In Fig. 2.11a we present the relative conservation error of fluid mass, computed from the difference between the initial total mass and the total mass computed at the different time steps.

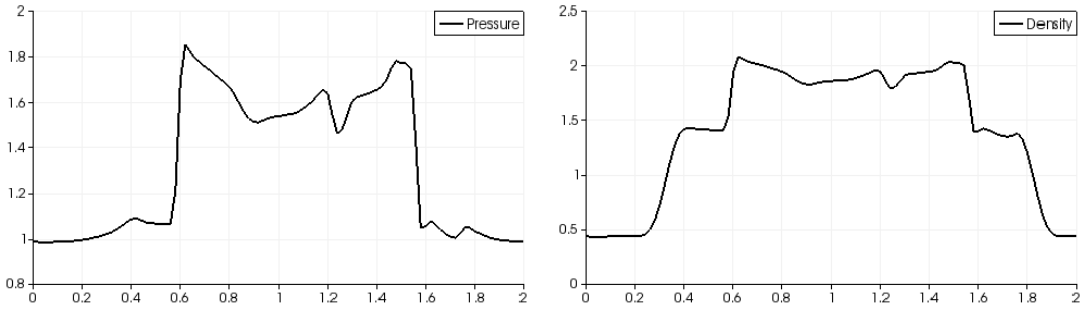

(a) (b)

Fig. 2.10: Pressure distribution (a) and density distribution (b) along the line $\{y = 0.5\,m, z = 0.75\,m\}$ at time $t = 1$s.

This mass difference is normalized by the maximum amount of mass swept by the movement of the solid. In Fig. 2.11b we present the relative energy conservation error, computed as the difference between the initial energy and the energy computed at the different time steps. This energy difference is normalized by the maximum energy exchange between the fluid and the solid, which is the relevant quantity to evaluate the relative effect of coupling on energy conservation. We observe a small variation of both mass and energy, without any clear growth or decrease of either quantity. The variation of mass is as low as 0.01% of the mass swept by the solid and the variation of energy is as low as 0.01% of the energy exchange in the system. The main effect accounting for these variations are the rounding errors involved in the evaluation of geometric quantities in cut-cells, since both mass and energy are impacted at similar levels.

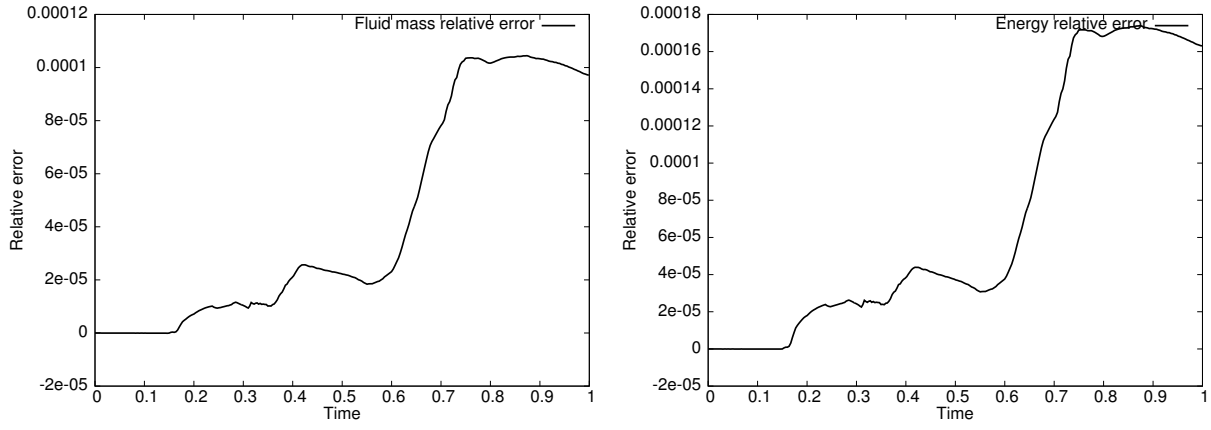

(a) (b)

Fig. 2.11: Relative conservation error on (a) fluid mass and (b) system energy.

2.6.2 Interaction of a shock wave and a cylinder

This moving body test case was first proposed in two space dimensions in [31] using a conservative method and has been studied both with conservative [52, 80] and nonconservative methods [3, 37, 95]. We treat it here in three space dimensions, the third coordinate being degenerate.

A planar shock interacts with a rigid mobile cylinder of density 7.6 kg.m^{-3} in a channel. The side boundaries of the domain are rigid walls while the left and right boundaries are respectively inflow and outflow boundaries. The computational domain is the parallelepiped box $[0,\,1] \times [0,\,0.2] \times [0,\,0.2]$m. The shock is initially set up to a Mach number of 3, so that the initial values are

$$\begin{cases} \rho = 3.857\, kg.m^{-3},\ p = 10.333\, Pa,\ u = 2.6929\, m.s^{-1},\ v = w = 0\, m.s^{-1}, & \text{if } x < 0.08\, m, \\ \rho = 1\, kg.m^{-3},\ p = 1\, Pa,\ u = v = w = 0\, m.s^{-1}, & \text{if } x \geq 0.08\, m. \end{cases}$$

The cylinder lies on the lower wall of the channel with its axis along the z-axis. The initial position of the center of mass of the cylinder is $(0.15, 0.05, 0.1)$m, the radius of the cylinder is $R = 0.05\, m$ and its length is $L = 0.2\, m$. The circular section of the cylinder is approximated by a regular polygon with 50 faces.

The computation is performed on a $200 \times 40 \times 40$ grid. We impose inflow and outflow boundary conditions at $x = 0\, m$ and $x = 1\, m$ respectively and mirror boundary conditions on the remaining outer boundaries of the fluid domain. The simulation time is $t = 0.255$ s.

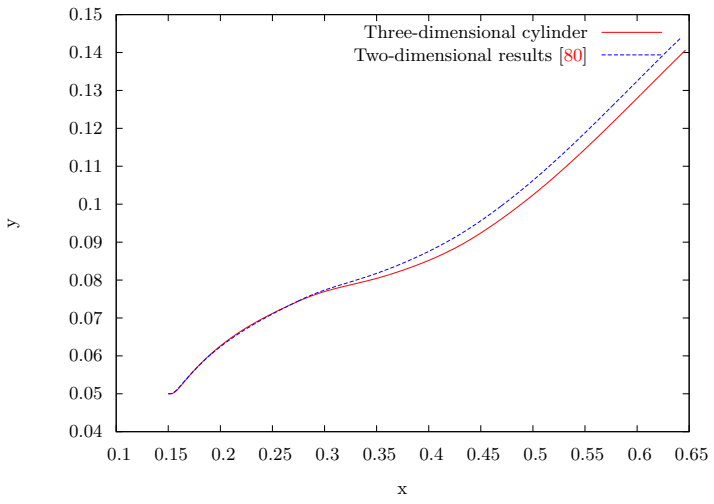

Fig. 2.12: Trajectory of the center of mass of the cylinder in the (x, y)-plane.

The impinging shock wave impacts the cylinder and is partially reflected, while part of the shock wave moves over the cylinder and part of its energy is transferred as kinetic energy to the cylinder. The reflected shock then reflects on the lower wall ($y = 0$), creating an overpressure under the cylinder and lifting it up. Subsequently, a fluid flow develops under the cylinder,

resulting in a contact discontinuity which exhibits Kelvin-Helmholtz instabilities. Complex interactions between the cylinder, the walls and the reflected shocks then occur. In Fig. 2.12 we display the trajectory of the cylinder in the plane (x, y) compared to the two-dimensional trajectory of [80] with the same fluid discretization. The final position of the center of mass of the cylinder is $(0.6465, 0.1406, 0.099994)$m. In comparison, the two-dimensional results in [80] yield $(0.643, 0.144)$m with a similar fluid discretization. This discrepancy is related to the small number of faces (50) of the polygon approximating the circular section in the three-dimensional case compared to the 1240 faces used in the two-dimensional case.

The system is symmetric with respect to the plane $z = 0.1\,m$. We note that the final position of the center of mass of the cylinder remains close to $z = 0.1\,m$. In addition, the velocity of the fluid in the z direction remains small and limited to the Kelvin-Helmholtz instability zones where three-dimensional structures occur. Apart from these features, the invariance in the z direction is well preserved. 30 iso-contours of density and pressure at the final time are plotted in Fig. 2.13a and Fig. 2.13b, respectively. The position of the shocks agrees very well with [80].

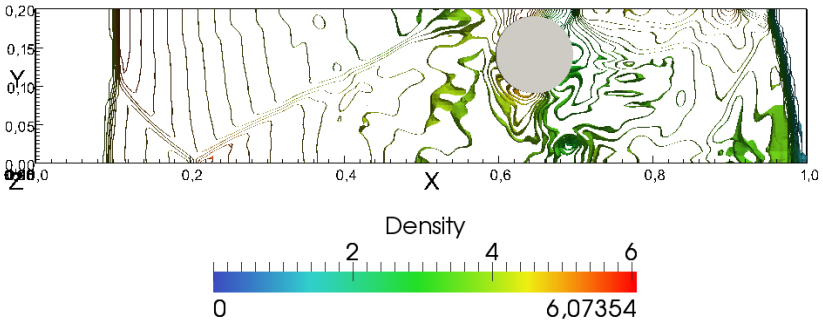

(a)

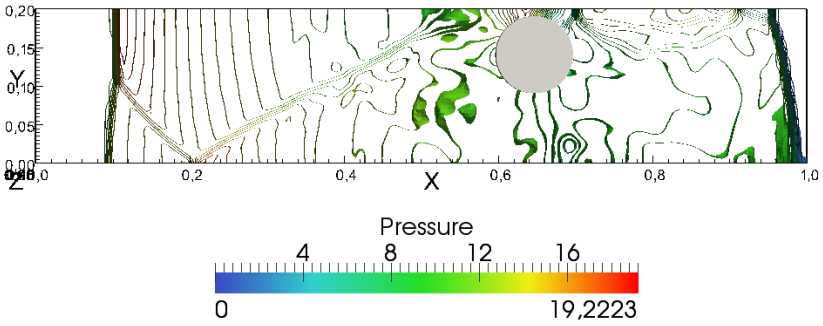

(b)

Fig. 2.13: Shock wave/cylinder interaction: 30 iso-contours of density (a) and pressure (b) at time $t = 0.255$ s.

2.6.3 Interaction of a shock wave and a sphere

In this problem, a planar shock interacts with a rigid mobile sphere in a channel. The side boundaries of the domain are rigid walls while the left and right boundaries are respectively inflow and outflow boundaries. The computational domain is the parallelepiped box $[0,\,1] \times [0,\,0.2] \times [0,\,0.2]$m. The shock is initially set up to a Mach number of 3, so that the initial values are

$$\begin{cases} \rho = 3.857\, kg.m^{-3},\ p = 10.333\, Pa,\ u = 2.6929\, m.s^{-1},\ v = w = 0\, m.s^{-1}, & \text{if } x < 0.08\, m, \\ \rho = 1\, kg.m^{-3},\ p = 1\, Pa,\ u = v = w = 0\, m.s^{-1}, & \text{if } x \geq 0.08\, m. \end{cases}$$

The initial position of the center of mass of the sphere is $(0.15, 0.05, 0.1)$m, and the radius of the sphere is $R = 0.05\, m$. The sphere is approximated by a polyhedron discretized with 236 faces.

The computation is performed on a $400 \times 80 \times 80$ grid. We impose inflow and outflow boundary conditions at $x = 0\, m$ and $x = 1\, m$ respectively and mirror boundary conditions on the remaining outer boundaries of the fluid domain. The simulation time is $t = 0.255$ s.

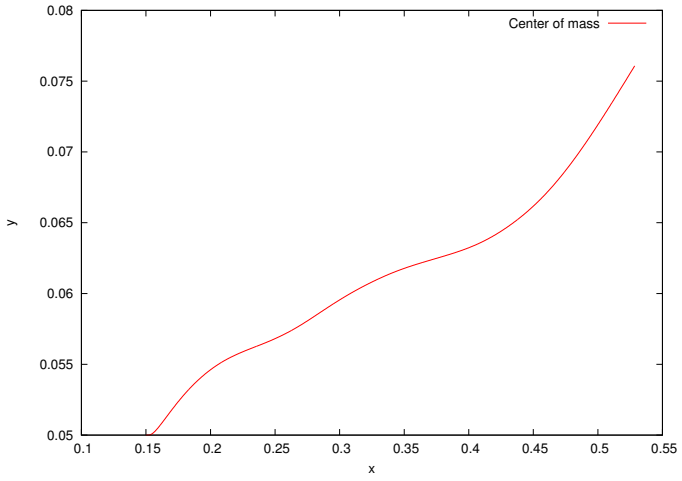

Fig. 2.14: Trajectory of the center of mass of the sphere in the (x, y)-plane.

In the same way that the cylinder interacted with the shock wave in the previous test case (Section 2.6.2), complex interactions between the sphere, the walls and the reflected shocks occur, creating an overpressure under the sphere and lifting it up. In Fig. 2.14 we display the trajectory of the sphere in the plane (x, y). The final position of the center of mass of the sphere is $(0.529\, m, 0.0776\, m, 0.0984\, m)$. The physical system is symmetric with regard to the plane $z = 0.1\, m$. This feature is fairly well preserved by the numerical results, even though the polyhedron itself is not perfectly symmetric. As a result, the sphere mass center is no longer exactly at $z = 0.1\, m$ at $t = 0.255$ s. 30 iso-contours of density and pressure at the final time

are plotted in Fig. 2.15a and Fig. 2.15b, respectively. This computation shows the ability of the coupling algorithm to compute the interaction of strong discontinuities with irregular moving boundaries.

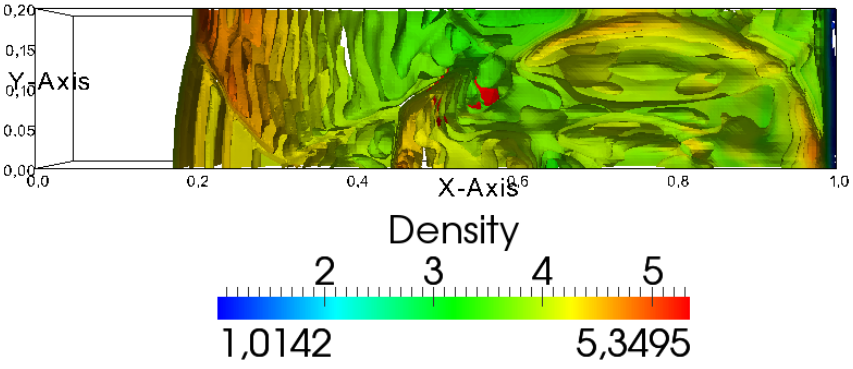

(a)

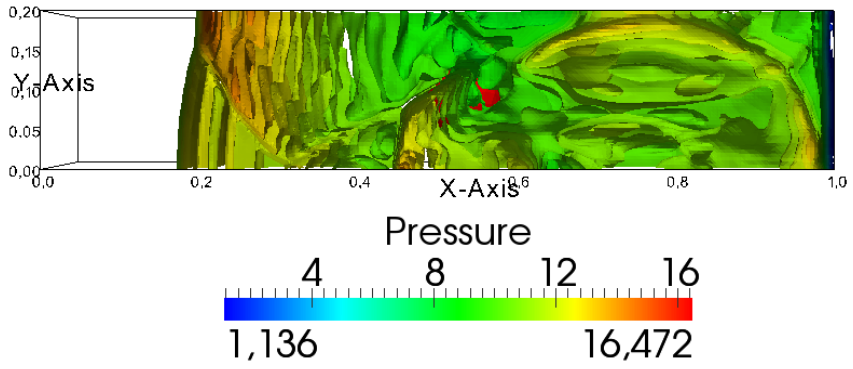

(b)

Fig. 2.15: Shock wave/sphere interaction: 30 iso-contours of density (a) and pressure (b) at time $t = 0.255$ s.

2.6.4 Interaction of a shock wave with rotating doors

This case is a three-dimensional analogue of the two-dimensional case presented in [80]. It demonstrates the ability of the method to deal with separating or closing solid boundaries and fluid cells including several moving boundaries. These features are of foremost importance in view of being able to deal with fracturing solids.

Four doors initially close a canal and are impacted from the left by a Mach 3 shock. The canal is bounded by four fixed rigid walls on the sides while the two ends along the x axis have inflow and outflow boundary conditions. The fluid domain is the parallelepiped box $[0,\,2]\times[0,\,0.5]\times[0,\,0.5]$m and is discretized using a $200 \times 50 \times 50$ grid. The shock is initialized as follows:

$$\begin{cases} \rho = 3.85\,kg.m^{-3},\ p = 10.33\,Pa,\ u = 2.6929\,m.s^{-1},\ v = w = 0\,m.s^{-1}, & \text{if } x < 0.43\,m, \\ \rho = 1\,kg.m^{-3},\ p = 1\,Pa,\ \overrightarrow{u} = \overrightarrow{0}\ m.s^{-1}, & \text{if } x \geq 0.43\,m. \end{cases}$$

The doors are four prisms based on rectangle isoceles triangles, completed on their boundaries by half cylinders. They are presented in Fig. 2.16. Each of them rotates freely around a rotation axis aligned with the axis of the half cylinder on the hypotenuse of the rectangle triangle while its other degrees of freedom are fixed. The diameter of the cylinders is equal to the width of the doors and is 0.05m. The density of the doors is 0.5kg.m^{-3}. The doors entirely block the canal initially.

After the incident shock hits the doors, it reflects to the left and the doors open due to the increase in pressure. The rotation of one of the doors is presented in Fig. 2.17. Due to the symmetry of the problem, the rotation of each door should be the same, and we have verified that the solution is almost symmetric. We observe that the doors are rotated all the way to 90 degrees, at which point they stop, having removed the fluid from the cells next to the boundary wall. In Fig. 2.18 and 2.19, we present the evolution of the fluid density field in planes $z = 0.25\text{m}$ and $y = z$, respectively, at times 0.02s, 0.05s, 0.1s and 0.25s. In order to help visualize the fluid flow, we have removed the particule with rotation axis ($x = 0.5\text{m}$, $z = 0.45\text{m}$) in both figures. The opening of the doors results in compression waves being created by the movement of the doors, while the pressure and density decrease in the center of the canal. Complex interactions of waves occur due to door movements and interaction with walls. Once the doors are rotated at 90 degrees, the fluid evolution is similar to a nozzle flow due to the static presence of the doors. We note the fact that the symmetry of the flow about the planes of symmetry of the canal is very well preserved by the coupling method.

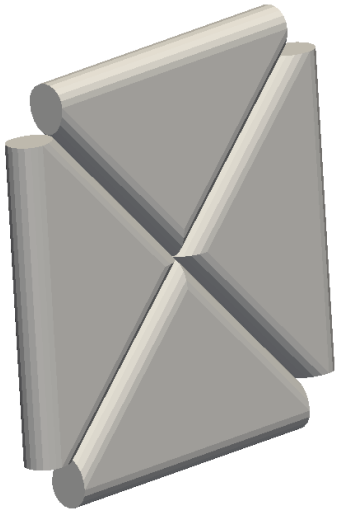

Fig. 2.16: Image of the initial position of the doors.

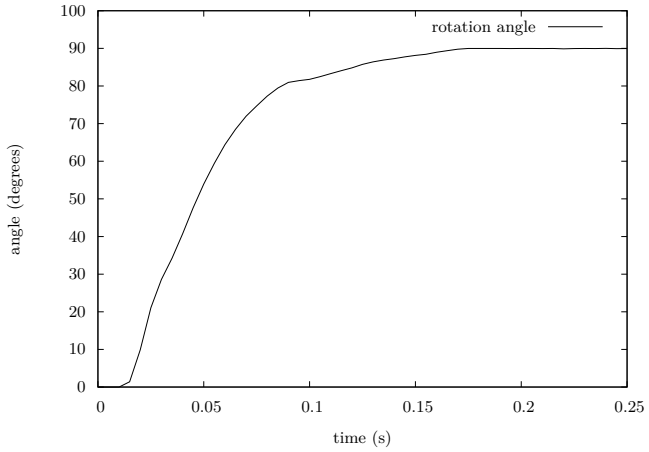

Fig. 2.17: Evolution of the rotation of the doors in time .

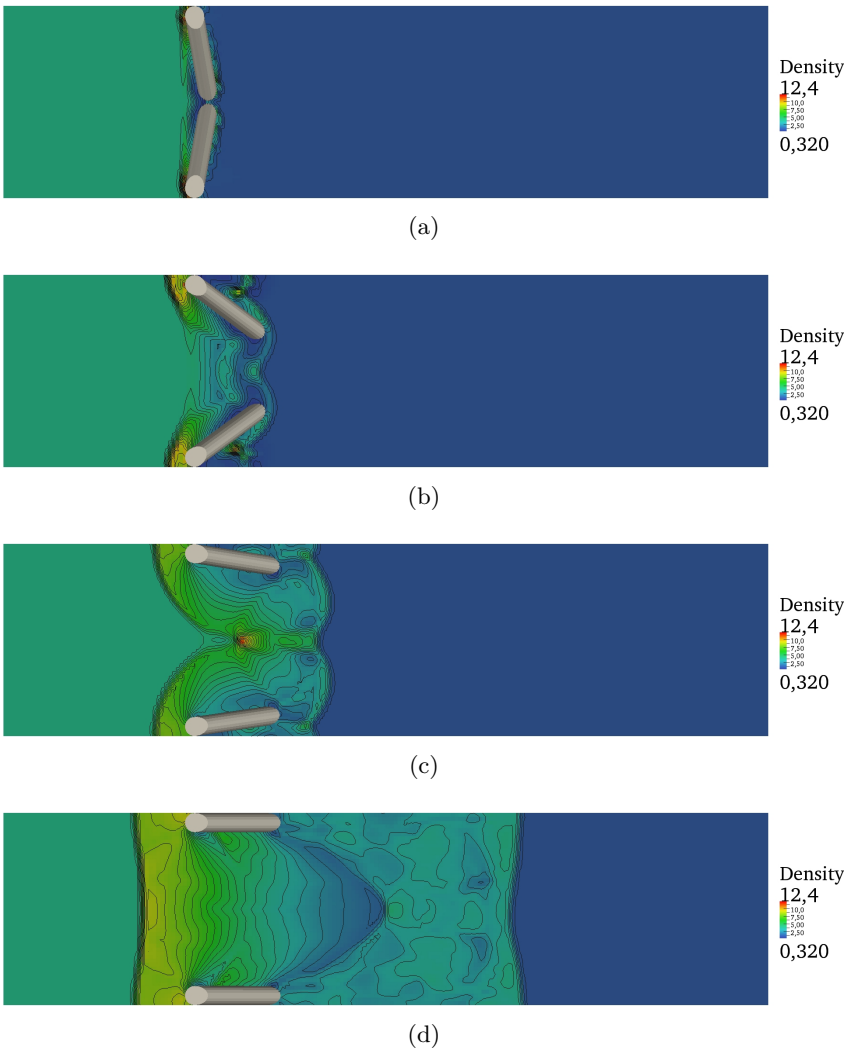

Fig. 2.18: Shock wave/doors interaction: 30 iso-contours of density in the plane $z = 0.25$ m at times $t = 0.02$ s (a), $t = 0.05$ s (b), $t = 0.1$ s (c) and $t = 0.25$ s (d).

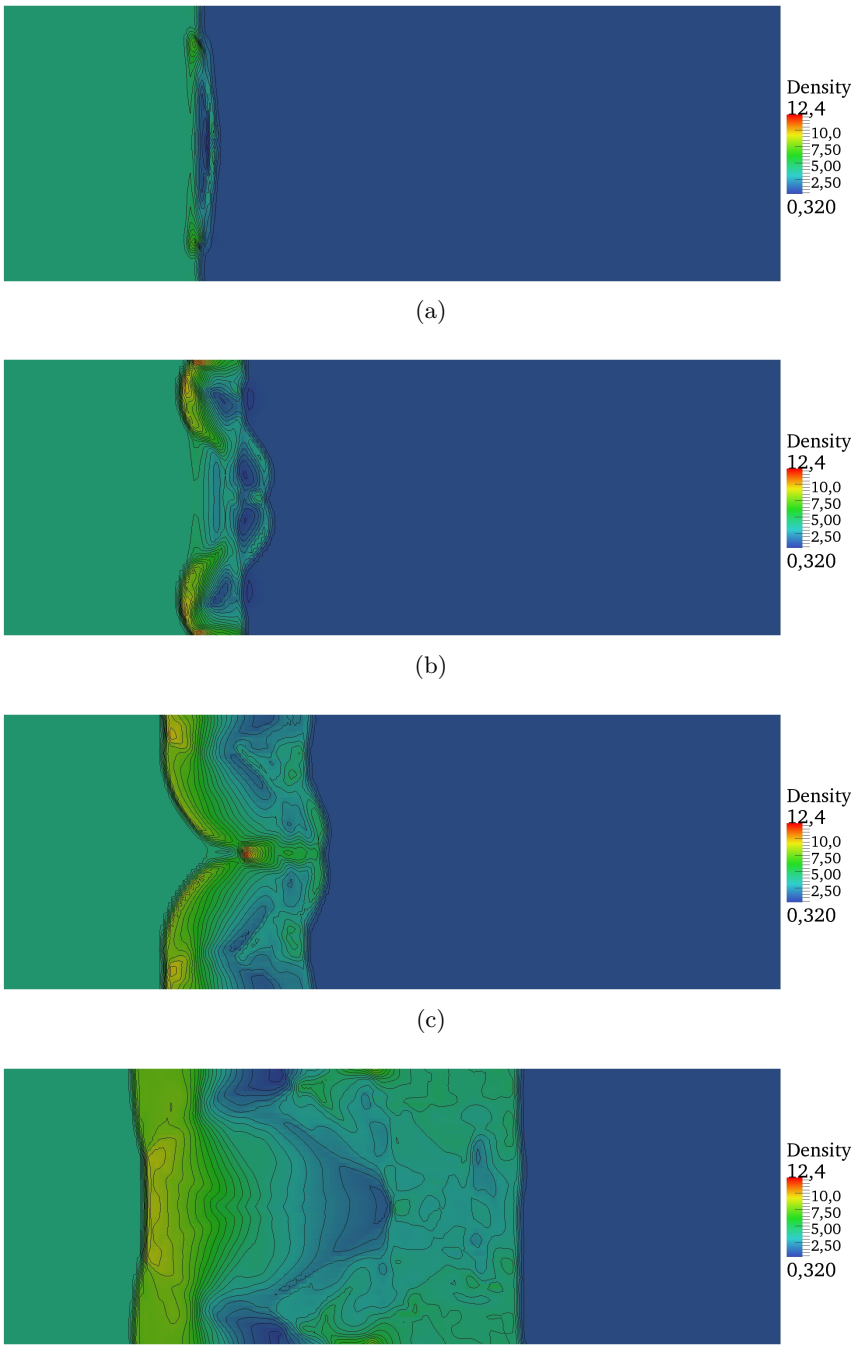

Fig. 2.19: Shock wave/doors interaction: 30 iso-contours of density in the plane $y = z$ at times $t = 0.02$ s (a), $t = 0.05$ s (b), $t = 0.1$ s (c) and $t = 0.25$ s (d).

2.7 Conclusion

We have developed a coupling method between a three-dimensional moving rigid solid and an inviscid compressible fluid, extending the explicit coupling scheme with a two-dimensional rigid solid of [80]. The extension has been achieved through exact geometric intersections of the solid boundary and the fluid grid. The method yields exact conservation of mass, momentum and

energy of the system, and also exhibits important consistency properties, such as conservation of uniform movement of both fluid and solid as well as the absence of numerical roughness on a straight boundary.

The computational cost of the fluid and solid methods essentially results from the evaluation of fluxes on the fluid side and of forces and torques on the solid side. We emphasize that the coupling algorithm evaluates these only once per time step, ensuring computational efficiency. Regarding surface coupling, the algorithm overhead scales as the number of solid faces and as $N^{\frac{2}{3}}$, N being the number of fluid grid cells. In comparison, the fluid flux computation time scales as N.

The presented test-cases allowed us to verify the main properties of the coupling scheme and to illustrate the ability of the method to compute the interaction of strong discontinuities with rigid solids undergoing large displacement. The next step is to move on to more complex test cases and to enrich the algorithm to take into account the deformation and the fracture of the solid. The algorithm has been designed in order to facilitate the extension of these results to solid deformation and fracture. This would require the discretization of the solid body using particles in the context of the Discrete Element method, an adequate reconstruction of the solid boundary resulting from the relative movement between the particles composing the solid, an appropriate procedure to fill the ghost-cells and the definition of a map (not necessarily bijective due to the opening of the fracture in one point) providing the correspondence from the position of the boundary at time t^n to its position at time t^{n+1}.

2.8 Appendix: Flux on mobile boundary

In this section, we present the Finite Volume discretization of a conservative law in the case when the boundaries of the cell are mobile, as considered in [28]. This discretization is used in the Immersed Boundary method in cut-cells, see 2.3.1. For simplicity, we consider the one-dimensional case. The Euler equations (2.1) are given by

$$\frac{\partial U}{\partial t} + \frac{\partial F(U)}{\partial x} = 0, \tag{2.24}$$

where the vector of conservative variables U is given by $U = (\rho, \rho u, \rho E)^t$ and the flux function is given by $F(U) = (\rho u, \rho u^2 + p, (\rho E + p)u)^t$.

We consider a grid in the plane (x, t) defined by the points $x_{i+1/2}$ and the time step Δt which is supposed to be constant for simplicity. The space step is denoted by $\Delta x_i = x_{i+1/2} - x_{i-1/2}$. We denote by U_i^n an approximation of the average value of U in the cell $C_i = \left[x_{i-1/2}, x_{i+1/2}\right]$ at time t^n.

As described in Section 2.3, the solid is superimposed to the fluid grid. Thus, the cell $\left[x_{i-1/2}, x_{i+1/2}\right]$ can be partially covered by the solid. Let us consider the time-space cell $B_i^{n+1/2}$

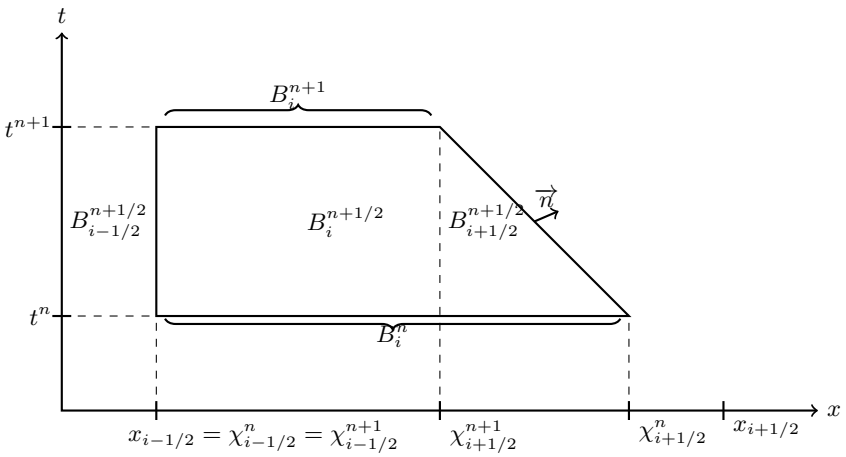

Fig. 2.20: Time-space cell

illustrated in Fig. 2.20, where we consider that the point $\chi_{i-1/2}$ is fixed in time at the point $x_{i-1/2}$ and the point $\chi_{i+1/2}$ varies in time due to the presence of a solid boundary in the cell. We denote by $B_i^n = \left[\chi_{i-1/2}^n, \chi_{i+1/2}^n\right]$ the cell at time t^n, and by $B_i^{n+1} = \left[\chi_{i-1/2}^{n+1}, \chi_{i+1/2}^{n+1}\right]$ the cell at time t^{n+1}. We integrate the conservation law (2.24) in the time-space cell $B_i^{n+1/2}$, and by using the divergence formula, we obtain

$$\int_{\partial B_i^{n+1/2}} (Un_t + F(U(t,x))n_x)\ d\gamma = 0,$$

where the outward normal $\overrightarrow{n}$ on $\partial B_i^{n+1/2}$ has the form $\overrightarrow{n} = (n_t, n_x)$. Taking into account the notation of Fig. 2.20, we infer

$$\begin{aligned}\int_{\partial B_i^{n+1/2}} (Un_t + f(U(t,x))n_x)\ d\gamma = &\int_{B_i^{n+1}} Un_t\, d\gamma + \int_{B_i^n} Un_t\, d\gamma \\ &+ \int_{B_{i-1/2}^{n+1/2}} (Un_t + F(U(t,x))n_x)\ d\gamma \\ &+ \int_{B_{i+1/2}^{n+1/2}} (Un_t + F(U(t,x))n_x)\ d\gamma.\end{aligned}$$

The first two terms are evaluated as

$$\begin{aligned}\int_{B_i^{n+1}} Un_t\, d\gamma &= |B_i^{n+1}|U_i^{n+1} = (\Delta x_i - (x_{i+1/2} - \chi_{i+1/2}^{n+1}))U_i^{n+1}, \\ \int_{B_i^n} Un_t\, d\gamma &= -|B_i^n|U_i^n = -(\Delta x_i - (x_{i+1/2} - \chi_{i+1/2}^n))U_i^n.\end{aligned}$$

We denote by Λ_i^{n+1} and Λ_i^n the volume fractions occupied by the solid in the cell at times t^{n+1} and t^n, respectively given by

$$\Lambda_i^{n+1} = \frac{x_{i+1/2} - \chi_{i+1/2}^{n+1}}{\Delta x_i}, \quad \Lambda_i^n = \frac{x_{i+1/2} - \chi_{i+1/2}^n}{\Delta x_i}.$$

We infer

$$\int_{B_i^{n+1}} Un_t \, d\gamma = \Delta x_i \left(1 - \Lambda_i^{n+1}\right) U_i^{n+1},$$
$$\int_{B_i^n} Un_t \, d\gamma = -\Delta x_i \left(1 - \Lambda_i^n\right) U_i^n,$$

The flux of F on the boundary $B_{i-1/2}^{n+1/2}$ can be approximated by the usual numerical flux $F_{i-1/2}^n$:

$$\int_{B_{i-1/2}^n} F(U(t,x))n_x \, d\gamma \simeq -\Delta t F_{i-1/2}^n.$$

The mean velocity of the point $\chi_{i+1/2}$ between t^n and t^{n+1} is given by

$$w_{i+1/2}^{n+1/2} = \frac{1}{\Delta t}\left(\chi_{i+1/2}^{n+1} - \chi_{i+1/2}^n\right).$$

The mobile boundary segment $B_{i+1/2}^{n+1/2}$ has a normal direction $\overrightarrow{n}$ such that

$$n_x = \frac{1}{\sqrt{1 + (w_{i+1/2}^{n+1/2})^2}}, \quad n_t = -\frac{w_{i+1/2}^{n+1/2}}{\sqrt{1 + (w_{i+1/2}^{n+1/2})^2}}.$$

Thus, we obtain

$$\begin{aligned}\int_{B_{i+1/2}^{n+1/2}} \left(Un_t + f(U(t,x))n_x\right) d\gamma &= \int_{t^n}^{t^{n+1}} \left(-w_{i+1/2}^{n+1/2} U(t, x_{i+1/2}(t)) + F(U(t, x_{i+1/2}(t)))\right) dt \\ &\simeq \Delta t \left(F(U_{i+1/2}^n) - w_{i+1/2}^{n+1/2} U_{i+1/2}^{n+1/2}\right).\end{aligned}$$

Taking into account the particular form of the flux function of F and the fact that the state velocity $U_{i+1/2}^{n+1/2}$ is exactly equal to $w_{i+1/2}^{n+1/2}$, we infer

$$\int_{B_{i+1/2}^{n+1/2}} \left(Un_t + F(U(t,x))n_x\right) d\gamma = \Delta t \left(0, p_{i+1/2}^{n+1/2}, p_{i+1/2}^{n+1/2} w_{i+1/2}^{n+1/2}\right)^t = \Delta t \, \Phi_{i+1/2,\,\text{solid}}^{n+1/2},$$

where $p_{i+1/2}^{n+1/2}$ is the pressure of the state $U_{i+1/2}^{n+1/2}$. Finally, gathering the four terms we obtain

$$(1 - \Lambda_i^{n+1}) U_i^{n+1} = (1 - \Lambda_i^n) U_i^n - \frac{\Delta t}{\Delta x_i}\left(\Phi_{i+1/2,\,\text{solid}}^{n+1/2} - F_{i-1/2}^n\right).$$

3

A time semi-implicit scheme for the conservative coupling of a shocked fluid flow with a deformable structure

This chapter is submitted to Journal of Computational Physics [91].

3.1 Introduction

Fluid-structure interaction phenomena occur in many fields, such as aeronautics, civil engineering, energetics, biology, and in the military and safety domains. In this context for instance, the effects of an explosion on a building involve complex non-linear phenomena (shock waves, cracking, fragmentation, ...) [99, 108], and the characteristic time scales of these phenomena are

extremely short. The driving effect of the fluid-structure interaction is the fluid overpressure, and viscous effects play a lesser role in the dynamics of this type of coupled system. With an eye toward these applications, we consider an inviscid compressible flow with shock waves interacting with a deformable solid object.

Fluid-structure interaction algorithms can be broadly categorized into monolithic and partitioned methods. In the monolithic (Eulerian [34, 74] or Lagrangian [54, 94]) methods, the fluid and the solid equations are solved simultaneously at each time step. However, in most numerical schemes, the fluid is classically described in Eulerian formulation and the solid in Lagrangian formulation. This is possible in partitioned approaches where the fluid and the solid equations are solved separately, and an interface module is used to exchange information between the fluid and the solid solvers to enforce the dynamic boundary conditions at their common interface. Two main types of methods have been developed in this context: Arbitrary Lagrangian-Eulerian (ALE) methods [24, 65] and fictitious domain methods [2, 17, 20, 27, 31, 33, 35, 52, 82, 84, 85]. The ALE method hinges on a mesh fitting the solid boundary, and therefore requires remeshing of the fluid domain when the solid goes through large displacements and topological changes due to fragmentation. Instead, fictitious domain methods, as those considered herein, work on a fixed fluid grid to which the solid is superimposed, and additional terms are introduced in the fluid formulation to impose the boundary conditions at the fluid-solid interface.

Conservative cut-cell Finite Volume methods for compressible fluid-structure interaction have been proposed by Noh [82]. Therein, a Lagrangian method for the solid is coupled with an Eulerian Finite Volume method for the compressible flow satisfying mass, momentum, and energy conservation in the fluid. Such methods have been used in a number of applications [17, 31, 43, 52, 82, 84]. A conservative coupling method between an inviscid compressible fluid and a rigid body undergoing large displacements has been developed in [80, 89] using a cut-cell Finite Volume method. The coupling method is conservative in the sense that (i) mass, momentum, and energy conservation in the fluid is achieved by the cut-cell Finite Volume method as in [82], and (ii) the momentum and energy exchange between the fluid and the solid is balanced. As a result, the system is exactly conservative, up to round-off errors in the geometry of cut-cells. Moreover, the coupling method exhibits interesting consistency properties, such as conservation of uniform movement of both fluid and solid, and absence of numerical roughness on a straight boundary.

The main purpose of this work is to develop a three-dimensional conservative coupling method between a compressible inviscid fluid and a deformable solid undergoing large displacements. By conservative, we mean that properties (i) and (ii) above are satisfied, as in [80, 89], and additionally that a symplectic scheme is used for the Lagrangian solid ensuring the conservation of a discrete energy (which is a close approximation of the physical energy). As a result, the coupled discrete system is not exactly energy-conservative, but we show numerically that our strategy yields long-time energy-preservation for the coupled system. Furthermore, as in [80, 89], the Finite Volume method for the fluid is high-order in smooth flow regions and away from the

solid boundary, while it is first-order near the shocks (due to the flux limiters) and in the vicinity of the solid boundary. Consequently, the coupling method is overall first-order accurate. Still, the use of a high-order method in smooth regions is useful to limit numerical diffusion in the fluid, as discussed in [18]. In any case, the coupling method, which is the focus of this work, is independent of the choice of the fluid fluxes.

While the core of the present method hinges on the techniques of [89] for a rigid solid, many new aspects have to be addressed. A reconstruction of the solid boundary around the solid assembly is needed since the solid deforms through the interaction with the fluid. Furthermore, a time semi-implicit scheme is introduced for the momentum and energy exchange, so as to take into account the deformation of the solid boundary during the time step. The advantage of this scheme with respect to an explicit one is to achieve additional consistency properties, such as the absence of pressure oscillations near a solid wall having only tangential deformation. The time semi-implicit scheme evaluates the fluid fluxes as well as the solid forces and torques only once per time step, which is important for computational efficiency of the scheme. Additionally, we prove that the time semi-implicit scheme converges with geometric rate under a CFL condition, which, under the assumption that the solid density is larger than the fluid density, is less restrictive than the fluid CFL condition.

The paper is organized as follows: Section 2 briefly describes the basic ingredients (which are common with [89]): the fluid and solid discretization methods and the cut-cell Finite Volume method. Section 3 presents the conservative coupling method based on the time semi-implicit procedure. Section 4 discusses several properties of the coupling method. Section 5 presents numerical results on strong fluid discontinuities interacting with two and three-dimensional deformable solids undergoing large displacements. Section 6 contains concluding remarks. Finally, Appendix A provides some background on the Discrete Element method used to discretize the solid, and Appendix B contains some additional ingredients for the convergence proof for the time semi-implicit scheme.

3.2 Basic ingredients

3.2.1 Fluid discretization

For inviscid compressible flow, the fluid state is governed by the Euler equations, which can be written in conservative form as

$$\frac{\partial}{\partial t}U + \frac{\partial}{\partial x}F(U) + \frac{\partial}{\partial y}G(U) + \frac{\partial}{\partial z}H(U) = 0, \tag{3.1}$$

where $U = (\rho, \rho u, \rho v, \rho w, \rho E)^t$ is the conservative variable vector and $F(U)$, $G(U)$, and $H(U)$ indicate the inviscid fluxes

$$F(U) = \begin{pmatrix} \rho u \\ \rho u^2 + p \\ \rho uv \\ \rho uw \\ (\rho E + p)u \end{pmatrix}, G(U) = \begin{pmatrix} \rho v \\ \rho uv \\ \rho v^2 + p \\ \rho vw \\ (\rho E + p)v \end{pmatrix}, H(U) = \begin{pmatrix} \rho w \\ \rho uw \\ \rho vw \\ \rho w^2 + p \\ (\rho E + p)w \end{pmatrix},$$

with ρ the mass density, p the pressure, (u, v, w) the Cartesian components of the velocity vector $\overrightarrow{u}$, and E the total energy. The system is closed by the equation of state for ideal gas: $p = (\gamma - 1)\rho e$, e being the specific internal energy with $E = e + \frac{1}{2}(u^2 + v^2 + w^2)$ and γ the ratio of specific heats ($\gamma = 1.4$ for air).

The discretization of these equations is based on an explicit Finite Volume method on a Cartesian grid. We denote with integer subscripts i, j, k quantities related to the center of cells and with half-integer subscripts quantities related to the center of faces of cells. For instance, the interface between cells $C_{i,j,k}$ and $C_{i+1,j,k}$ is denoted by $\partial C_{i+\frac{1}{2},j,k}$. The time step, which is subjected to a CFL condition, is taken constant for simplicity and is denoted Δt. We introduce the discrete times $t^n = n\Delta t$, for all $n \geq 0$. Let $C_{i,j,k}$ be a fluid cell of size ($\Delta x_{i,j,k}$, $\Delta y_{i,j,k}$, $\Delta z_{i,j,k}$). The Finite Volume scheme for the fluid in the absence of the solid takes the form

$$U_{i,j,k}^{n+1} = U_{i,j,k}^{n} + \Delta t\, \Phi_{i,j,k}^{n+1/2}, \tag{3.2}$$

with the flux $\Phi_{i,j,k}^{n+1/2}$ given by

$$\Phi_{i,j,k}^{n+1/2} = \frac{F_{i-1/2,j,k}^{n+1/2} - F_{i+1/2,j,k}^{n+1/2}}{\Delta x_{i,j,k}} + \frac{G_{i,j-1/2,k}^{n+1/2} - G_{i,j+1/2,k}^{n+1/2}}{\Delta y_{i,j,k}} + \frac{H_{i,j,k-1/2}^{n+1/2} - H_{i,j,k+1/2}^{n+1/2}}{\Delta z_{i,j,k}}, \tag{3.3}$$

where $U_{i,j,k}^{n}$ is a numerical approximation of the exact solution over the cell $C_{i,j,k}$ at time t^n, and $F_{i\pm1/2,j,k}^{n+1/2}, G_{i,j\pm1/2,k}^{n+1/2}, H_{i,j,k\pm1/2}^{n+1/2}$ are numerical fluxes approximating the time-average of the corresponding physical flux over the time interval $[t^n, t^{n+1}]$ and evaluated at $\partial C_{i\pm\frac{1}{2},j,k}$, $\partial C_{i,j\pm\frac{1}{2},k}$, and $\partial C_{i,j,k\pm\frac{1}{2}}$, respectively.

The coupling method presented hereafter is independent from the specific numerical scheme used for the numerical flux calculation in (3.2). In the present work, we use the one-dimensional OSMP scheme [18] of formal order 11 in smooth regions. The three-dimensional extension is achieved through a directional operator splitting which is second-order accurate.

3.2.2 Solid discretization

The deformable moving solid is discretized by the Discrete Element method using a finite number of rigid particles. Each particle is governed by the classical equations of mechanics. The particles interact through forces and torques. The expression of these forces and torques allows one to recover the macroscopic behavior of the solid [69, 81]. We observe that an attractive feature of the Discrete Element method is that it facilitates the handling of rupture by breaking the link between solid particles.

The particles have a polyhedral shape and are assumed to be star-shaped with respect to their center of mass, and their faces are assumed to be star-shaped with respect to their center of mass. We assume that the diameter of the largest inscribed sphere in the solid is larger than two fluid grid cells.

A generic solid particle I is characterised by the following quantities: the mass m_I, the diameter $h_{s,I}$, the position of the center of mass $\overrightarrow{X}_I$, the velocity of the center of mass $\overrightarrow{V}_I$, the rotation matrix $\mathbf{Q}_I$, the angular momentum matrix $\mathbf{P}_I$, and the principal moments of inertia I_I^i, $i \in \{1,2,3\}$. Let $\mathbf{D}_I = \mathrm{diag}(d_I^1, d_I^2, d_I^3)$ with $d_I^i = \frac{1}{2}\left(I_I^1 + I_I^2 + I_I^2\right) - I_I^i$, $i \in \{1,2,3\}$.

The explicit time-integration scheme for the solid in the absence of the fluid consists of the Verlet scheme for translation and the RATTLE scheme for rotation. For particle I, it takes the form

$$\overrightarrow{V}_I^{n+\frac{1}{2}} = \overrightarrow{V}_I^n + \frac{\Delta t}{2m_I}\overrightarrow{F}_{I,\mathrm{int}}^n, \tag{3.4}$$

$$\overrightarrow{X}_I^{n+1} = \overrightarrow{X}_I^n + \Delta t \overrightarrow{V}_I^{n+\frac{1}{2}}, \tag{3.5}$$

$$\mathbf{P}_I^{n+\frac{1}{2}} = \mathbf{P}_I^n + \frac{\Delta t}{4}\mathbf{j}(\overrightarrow{\mathcal{M}}_{I,\mathrm{int}}^n)\mathbf{Q}_I^n + \frac{\Delta t}{2}\boldsymbol{\Upsilon}_I^n\mathbf{Q}_I^n, \tag{3.6}$$

$$\mathbf{Q}_I^{n+1} = \mathbf{Q}_I^n + \Delta t \mathbf{P}_I^{n+\frac{1}{2}}\mathbf{D}_I^{-1}, \tag{3.7}$$

$$\overrightarrow{V}_I^{n+1} = \overrightarrow{V}_I^{n+\frac{1}{2}} + \frac{\Delta t}{2m_I}\overrightarrow{F}_{I,\mathrm{int}}^{n+1}, \tag{3.8}$$

$$\mathbf{P}_I^{n+1} = \mathbf{P}_I^{n+\frac{1}{2}} + \frac{\Delta t}{4}\mathbf{j}(\overrightarrow{\mathcal{M}}_{I,\mathrm{int}}^{n+1})\mathbf{Q}_I^{n+1} + \frac{\Delta t}{2}\tilde{\boldsymbol{\Upsilon}}_I^{n+1}\mathbf{Q}_I^{n+1}, \tag{3.9}$$

where in (3.6), $\boldsymbol{\Upsilon}_I^n$ is a symmetric matrix such that

$$(\mathbf{Q}_I^{n+1})^t\mathbf{Q}_I^{n+1} = \mathbf{I}, \tag{3.10}$$

with $\mathbf{I}$ the identity matrix in $\mathbb{R}^3$, and in (3.9), $\tilde{\boldsymbol{\Upsilon}}_I^{n+1}$ is a symmetric matrix such that

$$(\mathbf{Q}_I^{n+1})^t\mathbf{P}_I^{n+1}\mathbf{D}_I^{-1} + \mathbf{D}_I^{-1}(\mathbf{P}_I^{n+1})^t\mathbf{Q}_I^{n+1} = \mathbf{0}. \tag{3.11}$$

The matrices $\boldsymbol{\Upsilon}_I^n$ and $\tilde{\boldsymbol{\Upsilon}}_I^{n+1}$ are the Lagrange multipliers associated with the constraints (3.10) and (3.11), see [80]. The map $\mathbf{j} : \mathbb{R}^3 \to \mathbb{R}^{3\times 3}$ is such that $\mathbf{j}(\overrightarrow{x})\overrightarrow{y} = \overrightarrow{x} \wedge \overrightarrow{y}$ for all $\overrightarrow{x}$, $\overrightarrow{y} \in \mathbb{R}^3$. The force $\overrightarrow{F}_{I,\mathrm{int}}^n$ and torque $\overrightarrow{\mathcal{M}}_{I,\mathrm{int}}^n$ result from the interaction of particle I with its neighbouring particles, see 3.7 for the expression of these quantities.

The time-integration scheme for the solid being explicit, the time step is restricted by a CFL condition. This condition states that the displacement of each solid particle I during one time-step should be less than the characteristic size of the particle $h_{s,I}$ and the rotation of each particle I during one time-step should be less than $\frac{\pi}{8}$ (see [80]).

In the case of fluid-structure interaction with immersed boundaries, in addition to the fluid and solid CFL condition, the time step is also restricted so that the displacement of the solid is less

than one fluid grid cell size in the course of the time step, so that the solid boundary crosses at most one fluid grid cell per time-step. This condition is less stringent than the fluid CFL condition since the fluid in the vicinity of the solid boundary should have a velocity at least equal to that of the solid.

3.2.3 Cut-cell Finite Volume discretization

The faces of the solid particles in contact with the fluid are collected in the set $\mathfrak{F}$. A generic element of $\mathfrak{F}$ is denoted by $\mathcal{F}$ and is called a wet solid face. The fluid-solid interface consists of all the wet solid faces. Owing to the movement of the solid, the wet solid faces are time-dependent sets in $\mathbb{R}^3$, and we set $\mathcal{F}^n = \mathcal{F}(t^n)$ for all $n \geq 0$. Each wet solid face $\mathcal{F}(t)$ is characterized by its surface $A_{\mathcal{F}}(t)$ and its normal $\overrightarrow{\nu}_{\mathcal{F}}(t)$ (pointing from the solid to the fluid). Finally, we denote by $\Omega_{\text{solid}}(t)$ the solid domain and by $\Omega_{\text{fluid}}(t)$ the fluid domain.

The time-integration scheme is based on a partitioned approach where the coupling is achieved through boundary conditions at the fluid-solid interface. In our case, for an inviscid fluid, we consider perfect slip boundary conditions:

$$\overrightarrow{u}_{\text{fluid}} \cdot \overrightarrow{\nu}_{\text{fluid}} + \overrightarrow{u}_{\text{solid}} \cdot \overrightarrow{\nu}_{\text{solid}} = 0, \quad \boldsymbol{\sigma}_{\text{fluid}} \cdot \overrightarrow{\nu}_{\text{fluid}} + \boldsymbol{\sigma}_{\text{solid}} \cdot \overrightarrow{\nu}_{\text{solid}} = 0,$$

where $\overrightarrow{u}_{\text{fluid}}$ and $\overrightarrow{u}_{\text{solid}}$, $\boldsymbol{\sigma}_{\text{fluid}}$ and $\boldsymbol{\sigma}_{\text{solid}}$, $\overrightarrow{\nu}_{\text{fluid}}$ and $\overrightarrow{\nu}_{\text{solid}}$ are respectively the velocities, stresses, and outward pointing normals for the fluid and the solid.

In the Immersed Boundary method, the solid is superimposed to the fluid grid, leading to fluid-solid mixed cells, thereafter called “cut-cells". Let $C_{i,j,k}$ be a cut-cell. The relevant geometric quantities describing the intersection between the moving solid and the cell $C_{i,j,k}$ are (see Fig. 3.1):

- The **volume fraction** $0 \leqslant \Lambda^n_{i,j,k} \leqslant 1$ occupied by the solid in the cell $C_{i,j,k}$ at time t^n.
- The **side area fraction** $0 \leqslant \lambda^{n+\frac{1}{2}}_{i\pm\frac{1}{2},j,k}, \lambda^{n+\frac{1}{2}}_{i,j\pm\frac{1}{2},k}, \lambda^{n+\frac{1}{2}}_{i,j,k\pm\frac{1}{2}} \leqslant 1$ of each fluid grid cell face averaged over the time interval $\left[t^n, t^{n+1}\right]$.
- The **boundary area** $A^{n+\frac{1}{2}}_{i,j,k,\mathcal{F}}$ defined as the area of the intersection of the wet solid face $\mathcal{F}(t)$ with $C_{i,j,k}$ averaged over the time interval $\left[t^n, t^{n+1}\right]$.

The three-dimensional geometric algorithms used for the detection of the cut-cells and the computation of the intersection between the solid and the fluid grid are described in [89].

On the fluid side, we take into account the presence of the solid by modifying the fluid fluxes in cut-cells. Consider a cut-cell as illustrated in Fig. 3.1. The computation of the time-average of the side area fractions $\lambda^{n+\frac{1}{2}}$ (for simplicity, subscripts related to the fluid grid cells or their faces are omitted when they play no relevant role) and of the boundary area $A^{n+\frac{1}{2}}_{\mathcal{F}}$, as considered in [31], can be very complex in three space dimensions. Instead, as in [80], we evaluate the side area fraction and the boundary area at time t^{n+1} and compute the amount swept by the

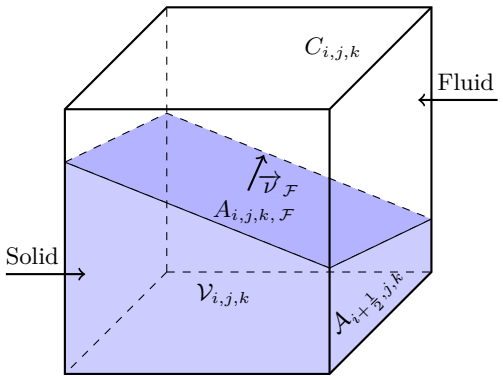

Fig. 3.1: Illustration of a cut-cell $C_{i,j,k}$.

movement of the wet solid face $\mathcal{F}$ during the time step from t^n to t^{n+1} in order to enforce the discrete conservation of the conservative variables. This leads to the following approximation of (3.1):

$$\left(1-\Lambda_{i,j,k}^{n+1}\right)U_{i,j,k}^{n+1}=\left(1-\Lambda_{i,j,k}^{n+1}\right)U_{i,j,k}^{n}+\Delta t\,\Phi_{i,j,k,\,\text{fluid}}^{n+1}+\Delta t\,\Phi_{i,j,k,\,\text{solid}}^{n+1}+\Delta U_{i,j,k}^{n,n+1}. \tag{3.12}$$

The fluid flux $\Phi_{\text{fluid}}^{n+1}$ is now given by (compare with (3.3))

$$\begin{aligned}\Phi_{i,j,k,\,\text{fluid}}^{n+1}=&\frac{\left(1-\lambda_{i-\frac{1}{2},j,k}^{n+1}\right)F_{i-\frac{1}{2},j,k}^{n+\frac{1}{2}}-\left(1-\lambda_{i+\frac{1}{2},j,k}^{n+1}\right)F_{i+\frac{1}{2},j,k}^{n+\frac{1}{2}}}{\Delta x_{i,j,k}}\\&+\frac{\left(1-\lambda_{i,j-\frac{1}{2},k}^{n+1}\right)G_{i,j-\frac{1}{2},k}^{n+\frac{1}{2}}-\left(1-\lambda_{i,j+\frac{1}{2},k}^{n+1}\right)G_{i,j+\frac{1}{2},k}^{n+\frac{1}{2}}}{\Delta y_{i,j,k}}\\&+\frac{\left(1-\lambda_{i,j,k-\frac{1}{2}}^{n+1}\right)H_{i,j,k-\frac{1}{2}}^{n+\frac{1}{2}}-\left(1-\lambda_{i,j,k+\frac{1}{2}}^{n+1}\right)H_{i,j,k+\frac{1}{2}}^{n+\frac{1}{2}}}{\Delta z_{i,j,k}}.\end{aligned} \tag{3.13}$$

The solid flux $\Phi_{\text{solid}}^{n+1}$ resulting from the presence of the solid boundaries in the cell is given by

$$\Phi_{i,j,k,\,\text{solid}}^{n+1}=\frac{1}{V_{i,j,k}}\sum_{\{\mathcal{F}\in\mathfrak{F}\,|\,\mathcal{F}^{n+1}\cap C_{i,j,k}\neq\emptyset\}}\phi_{i,j,k,\,\mathcal{F}}^{n+1},$$

where $V_{i,j,k}$ is the volume of $C_{i,j,k}$ and $\phi_{\mathcal{F}}^{n+1}$ is the solid flux attached to the wet solid face $\mathcal{F}$. Finally the so-called swept amount is given by

$$\Delta U_{i,j,k}^{n,n+1}=\sum_{\{\mathcal{F}\in\mathfrak{F}\,|\,\mathcal{F}^{n+1}\cap C_{i,j,k}\neq\emptyset\}}\Delta U_{i,j,k,\,\mathcal{F}}^{n,n+1},$$

where the term $\Delta U_{\mathcal{F}}^{n,n+1}$ denotes the amount of U swept by the movement of the wet solid face $\mathcal{F}$ during the time step from t^n to t^{n+1}. The detailed procedure to compute these quantities is described in [89], see also [80].

In the cut-cells where the volume fraction Λ is grater than 0.5, we use the conservative mixing described in [52, 80, 89]. In order to compute the fluid fluxes near the fluid-solid interface, we define an artificial state in the cells fully occupied by the solid from the states in the mirror cells relatively to the fluid-solid interface, as described in [89]. The number of mirror cells is typically of the order of the stencil for the fluid fluxes.

3.3 Time semi-implicit coupling with a deformable structure

3.3.1 Solid in presence of fluid

On the solid side, the equations (3.4), (3.6), (3.8), and (3.9), are modified by taking into account the fluid forces and torques applied to the particle I as follows:

$$\overrightarrow{V}_I^{n+\frac{1}{2}} = \overrightarrow{V}_I^{n} + \frac{\Delta t}{2m_I}(\overrightarrow{F}_{I,\text{int}}^{n} + \overrightarrow{F}_{I,\text{fluid}}^{n+1}), \tag{3.14}$$

$$\mathbf{P}_I^{n+\frac{1}{2}} = \mathbf{P}_I^{n} + \frac{\Delta t}{4}\mathbf{j}(\overrightarrow{\mathcal{M}}_{I,\text{int}}^{n} + \overrightarrow{\mathcal{M}}_{I,\text{fluid}}^{n+1})\mathbf{Q}_I^{n} + \frac{\Delta t}{2}\boldsymbol{\Upsilon}_I^{n}\mathbf{Q}_I^{n}, \tag{3.15}$$

$$\overrightarrow{V}_I^{n+1} = \overrightarrow{V}_I^{n+\frac{1}{2}} + \frac{\Delta t}{2m_I}(\overrightarrow{F}_{I,\text{int}}^{n+1} + \overrightarrow{F}_{I,\text{fluid}}^{n+1}), \tag{3.16}$$

$$\mathbf{P}_I^{n+1} = \mathbf{P}_I^{n+\frac{1}{2}} + \frac{\Delta t}{4}\mathbf{j}(\overrightarrow{\mathcal{M}}_{I,\text{int}}^{n+1} + \overrightarrow{\mathcal{M}}_{I,\text{fluid}}^{n+1})\mathbf{Q}_I^{n+1} + \frac{\Delta t}{2}\tilde{\boldsymbol{\Upsilon}}_I^{n+1}\mathbf{Q}_I^{n+1}, \tag{3.17}$$

where $\overrightarrow{F}_{I,\text{fluid}}^{n+1}$ and $\overrightarrow{\mathcal{M}}_{I,\text{fluid}}^{n+1}$ are the fluid forces and torques applied to the particle I. An important point, as reflected by the superscript $(n+1)$ for the fluid forces and torques, is that these quantites are evaluated using the solid position at time t^{n+1} in the context of a time semi-implicit method (in contrast with [89] dealing with a rigid solid). The detailed procedure to compute the fluid forces and torques is described in Section 3.3.3.

3.3.2 Reconstruction of the deformed solid boundary

In the Discrete Element method, the particles can overlap or become separated by small gaps as the solid is compressed or stretched, see Fig. 3.2. However, no fluid should penetrate into the gaps between the particles since the solid is treated here as cohesive. Therefore, we reconstruct a continuous interface around the particle assembly, as close as possible to the actual boundary of the moving particles.

Several choices are possible for the reconstruction. For the sake of simplicity, we focus here on one simple option: the interface is reconstructed as a set of triangles with vertices obtained from a transformation of the vertices of the Discrete Elements lattice at time $t^0 = 0$. Since the faces of the particles are star-shaped with respect to their center of mass, we subdivide all the solid faces into triangles, by connecting the center of mass of the face to all the face vertices. Let us

consider a vertex a_i of the initial Discrete Element lattice: it belongs to one or more polyhedral particles. Let us denote by $\mathcal{P}_{a_i}$ the set of particles which share the vertex a_i and by $\#\mathcal{P}_{a_i}$ the cardinality of the set $\mathcal{P}_{a_i}$. We define the mean vertex $\overline{a}_i^n$ corresponding to a_i at time t^n as the average of the positions of vertex a_i under the rigid body motion of each particle in $\mathcal{P}_{a_i}$:

$$\overline{a}_i^n = \frac{1}{\#\mathcal{P}_{a_i}} \sum_{J \in \mathcal{P}_{a_i}} (\overrightarrow{X}_J^n + \mathbf{Q}_J^n \cdot (a_i^0 - \overrightarrow{X}_J^0)), \tag{3.18}$$

where a_i^0 is the initial position of a_i. The reconstructed fluid-solid interface at time t^n is the set of triangles supported by the center of mass of the polyhedral particle faces and the mean vertices $(\overline{a}_i^n)_i$. This procedure is applied to all the vertices belonging to a polyhedral face of the Discrete Elements in contact with the fluid. A typical boundary reconstruction is shown in Fig. 3.3. Obviously, in the case where the solid amounts to one undeformable particle, the position of the vertex $\overline{a}_i^n$ coincides with that of a_i under the rigid body movement. Note that owing to the above reconstruction, the area of a wet solid face becomes time-dependent.

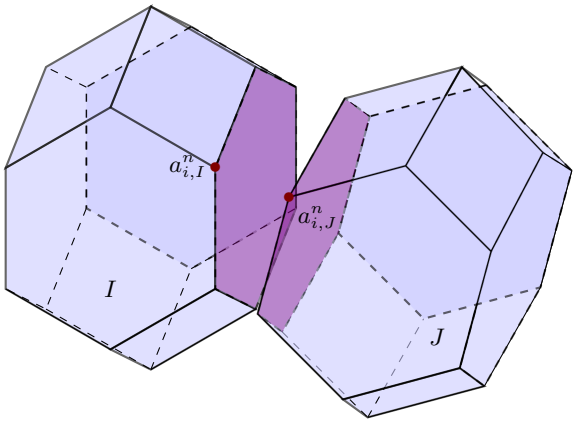

Fig. 3.2: Solid deformation.

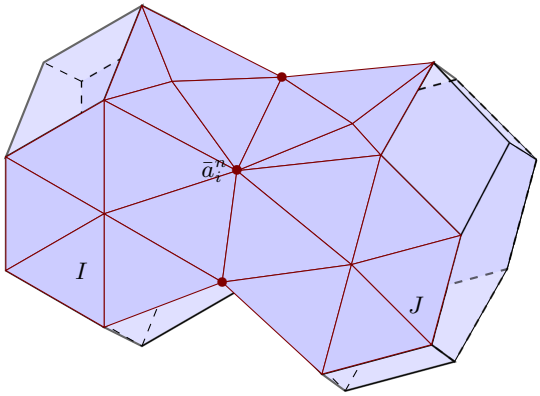

Fig. 3.3: Reconstruction of the deformed solid boundary.

3.3.3 Evaluation of the fluid pressure forces

Owing to the deformation of the solid, the surface of the wet solid face $\mathcal{F}(t)$ evolves during the time-step. The following geometric conservation laws in the cell $C_{i,j,k}$ play an important role in the consistency properties of the coupling method:

$$\lambda_{i+\frac{1}{2},j,k}^{n+1} = \lambda_{i-\frac{1}{2},j,k}^{n+1} - \sum_{\{\mathcal{F} \in \mathfrak{F} \,|\, \mathcal{F}^{n+1} \cap C_{i,j,k} \neq \emptyset\}} \frac{A_{i,j,k,\mathcal{F}}^{n+1}}{\Delta y_{i,j,k}\, \Delta z_{i,j,k}} \nu_{x,\mathcal{F}}^{n+1}, \tag{3.19}$$

$$\lambda_{i,j+\frac{1}{2},k}^{n+1} = \lambda_{i,j-\frac{1}{2},k}^{n+1} - \sum_{\{\mathcal{F} \in \mathfrak{F} \,|\, \mathcal{F}^{n+1} \cap C_{i,j,k} \neq \emptyset\}} \frac{A_{i,j,k,\mathcal{F}}^{n+1}}{\Delta x_{i,j,k}\, \Delta z_{i,j,k}} \nu_{y,\mathcal{F}}^{n+1}, \tag{3.20}$$

$$\lambda_{i,j,k+\frac{1}{2}}^{n+1} = \lambda_{i,j,k-\frac{1}{2}}^{n+1} - \sum_{\{\mathcal{F} \in \mathfrak{F} \,|\, \mathcal{F}^{n+1} \cap C_{i,j,k} \neq \emptyset\}} \frac{A_{i,j,k,\mathcal{F}}^{n+1}}{\Delta x_{i,j,k}\, \Delta y_{i,j,k}} \nu_{z,\mathcal{F}}^{n+1}, \tag{3.21}$$

where $\lambda_{i\pm\frac{1}{2},j,k}$, $\lambda_{i,j\pm\frac{1}{2},k}$, and $\lambda_{i,j,k\pm\frac{1}{2}}$ are the side area fractions of the fluid cell $C_{i,j,k}$ faces. Conditions (3.19), (3.20), and (3.21) can be satisfied exactly by taking the position at time t^{n+1} of the wet solid face $\mathcal{F}(t)$. This is the reason why we consider $A_{\mathcal{F}}^{n+1}$ and $\overrightarrow{\nu}_{\mathcal{F}}^{n+1}$. Such a choice in turn requires to solve the solid with a time-implicit algorithm which could be computationally expensive. We choose a time semi-implicit algorithm which only computes implicitly the position of particles in contact with the fluid by means of an iterative procedure. Moreover, we compute the internal forces between particles only once, since this is the most time-demanding step of the Discrete Element method. This computation is based on the position of particles at time t^n, and the internal forces are then kept fixed in the iterative procedure employed by the time semi-implicit algorithm. In the same way, the fluid pressures $\overline{p}_x^n$, $\overline{p}_y^n$, and $\overline{p}_z^n$ have already been computed and remains fixed during the iterative procedure. For the solid particles in contact with the fluid, we employ an additional index k within the iterative procedure. We compute the forces exerted by the fluid pressure on the surface $A_{\mathcal{F}}^{n,k}$, advance the position of the solid particles having wet faces, while the internal and external pressure forces are kept fixed. We can then update the surface $A_{\mathcal{F}}^{n,k+1}$ and the normal $\overrightarrow{\nu}_{\mathcal{F}}^{n,k+1}$. We iterate the process until convergence. As a result, the fluid force acting on the wet solid face $\mathcal{F}^{n+1}$ is evaluated using the boundary area $A_{\mathcal{F}}^{n+1}$.

We observe that the time-explicit variant (one step in the iterative procedure) in which we take the position at time t^n of the solid wet face $\mathcal{F}(t)$, so that we consider $A_{\mathcal{F}}^n$ and $\overrightarrow{\nu}_{\mathcal{F}}^n$ for the evaluation of the fluid forces, is cheaper but loses some consistency properties because conditions (3.19), (3.20), and (3.21) are no longer satisfied exactly for a deformable solid. We therefore expect pressure fluctuations near a solid boundary deformed tangentially, whereas the slip boundary conditions should not yield such a behavior. A numerical illustration is presented in Section 3.3.5.4.

An important remark is that the above procedure is more efficient than a global time-implicit method. Indeed, the iterative procedure only involves the computation of the positions of the solid particles in contact with the fluid. In addition, the expensive computation of the solid internal forces, fluid fluxes, and swept amount are not carried out during the iterative loop: the only operations involved are the computation of fluid pressure forces, the increment of the particle positions, the computation of the intersection between the solid and the fluid grid cells, and the reconstruction of the solid boundary. Among these operations, the most computationally expensive is the computation of the intersection between the solid and the fluid grid. We assess the efficiency of the time semi-implicit method in Section 4.5. We also prove in Section 3.4 that under a classical CFL condition on the time-step, the above iterative procedure converges at a geometric rate.

3.3.4 Main steps of the time semi-implicit coupling algorithm

At the beginning of the time step from t^n to t^{n+1}, we know the state of the fluid U^n, the position and rotation of the solid particles $(\overrightarrow{X}_I^n, \mathbf{Q}_I^n)$, as well as the velocity of their center of mass and their angular momentum $(\overrightarrow{V}_I^n, \mathbf{P}_I^n)$. For the fluid, we need to compute for all the fluid grid cells the fluxes $F^{n+\frac{1}{2}}, G^{n+\frac{1}{2}}, H^{n+\frac{1}{2}}$, the volume fractions Λ^{n+1} and the side area fractions λ^{n+1}, and the solid fluxes $\phi_{\mathcal{F}}^{n+1}$ and the swept amounts $\Delta U_{\mathcal{F}}^{n,n+1}$ for all the wet solid faces $\mathcal{F}$. For the solid, we need to compute the fluid forces and torques $\overrightarrow{F}_{I,\text{fluid}}^{n+1}$ and $\overrightarrow{\mathcal{M}}_{I,\text{fluid}}^{n+1}$ for all the solid particles I. Recalling the iterative procedure introduced in Section 3.3.3, we use the superscript k for all variables at the k-th step of this procedure. In particular, we denote by $\overrightarrow{F}_{I,\text{fluid}}^{n,k}$ and $\overrightarrow{\mathcal{M}}_{I,\text{fluid}}^{n,k}$ the fluid force and torque at time t^n and at the k-th step of the iterative procedure. The convergence criterion is

$$\max_I \|\overrightarrow{X}_I^{n,k+1} - \overrightarrow{X}_I^{n,k}\| + \max_I h_{s,I} \|\mathbf{Q}_I^{n,k+1} - \mathbf{Q}_I^{n,k}\| \leq \epsilon = 10^{-12}. \tag{3.22}$$

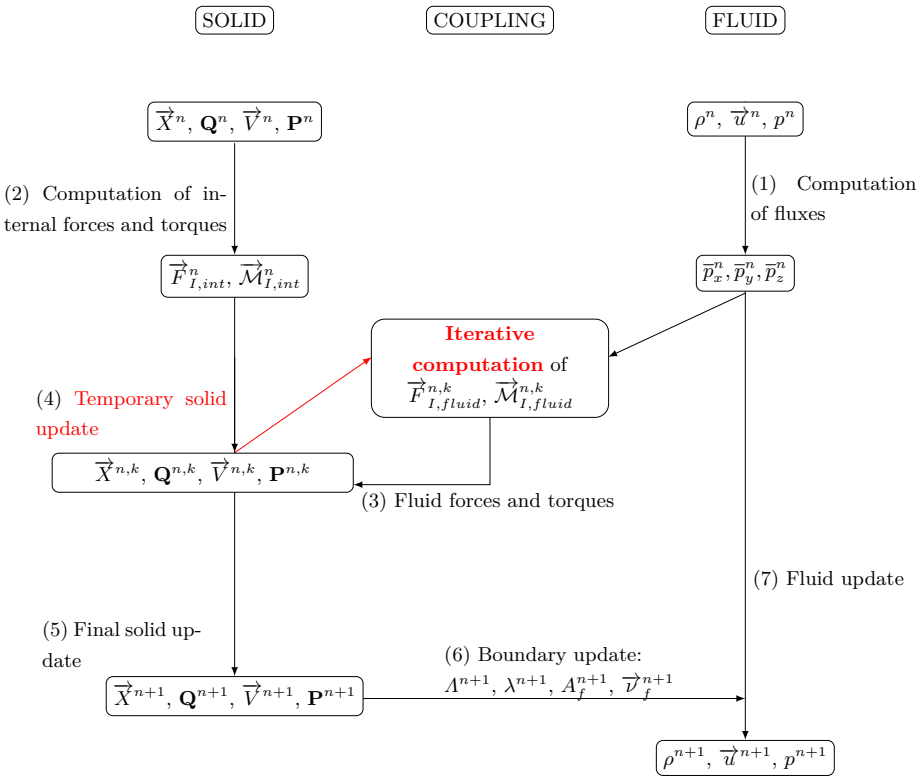

Fig. 3.4: Structure of the semi-implicit scheme

The general structure of the conservative time semi-implicit coupling method is summarized in Fig. 3.4 and can be described by the following seven steps:

1. The fluid fluxes $F^{n+\frac{1}{2}}, G^{n+\frac{1}{2}}, H^{n+\frac{1}{2}}$ used in (3.13) are precomputed at all the cell faces of the fluid grid, without taking into account the presence of the solid. We use the OSMP11 scheme with directional operator splitting. For instance,

$$U_{i,j,k}^{n+1} = L_x(\Delta t)L_y(\Delta t)L_z(\Delta t)\, U_{i,j,k}^{n},$$

where L_x, L_y, L_z are respectively the operators corresponding to the integration of a time step Δt in the x, y and z directions. For instance,

$$L_x(\Delta t)W = W - \Delta t \left(\frac{F_{i+\frac{1}{2},j,k}(W) - F_{i-\frac{1}{2},j,k}(W)}{\Delta x} \right).$$

Thus, formal second-order time accuracy is recovered every six time steps (corresponding to all L_x, L_y, and L_z permutations) if the directional operators do not commute [18]. We denote by $\overline{p}_x^n$, $\overline{p}_y^n$, and $\overline{p}_z^n$ the pressures used in the application of the operators L_x, L_y, and L_z respectively. These pressures are used to determine the forces exerted by the fluid on the solid in step (2).

2. The internal forces and torques are computed based on the position of the solid particles using (3.54) and (3.55).
3. The fluid pressure force acting on a solid particle I used in (3.14)-(3.17) is decomposed as:

$$\overrightarrow{F}_{I,\text{fluid}}^{n,k} = \sum_{\mathcal{F}\in\mathfrak{F}_I} \overrightarrow{F}_{\mathcal{F},\text{fluid}}^{n,k}, \tag{3.23}$$

where $\mathfrak{F}_I$ collects the wet faces of the particle I, and the fluid force $\overrightarrow{F}_{\mathcal{F},\text{fluid}}^{n,k}$ acting on the wet solid face $\mathcal{F}^{n,k}$ is equal to the force exerted by the pressures $\overline{p}_x^n$, $\overline{p}_y^n$, and $\overline{p}_z^n$ on the surface in contact with the fluid:

$$\overrightarrow{F}_{\mathcal{F},\text{fluid}}^{n,k} = \left(-\int_{\mathcal{F}^{n,k}} \bar{p}_x^n\, \nu_{x,\mathcal{F}}^{n,k}, -\int_{\mathcal{F}^{n,k}} \bar{p}_y^n\, \nu_{y,\mathcal{F}}^{n,k}, -\int_{\mathcal{F}^{n,k}} \bar{p}_z^n\, \nu_{z,\mathcal{F}}^{n,k} \right)^t. \tag{3.24}$$

Similarly, the fluid torque $\overrightarrow{\mathcal{M}}_{I,\text{fluid}}^{n,k}$ is decomposed as

$$\overrightarrow{\mathcal{M}}_{I,\text{fluid}}^{n,k} = \sum_{\mathcal{F}\in\mathfrak{F}_I} \overrightarrow{F}_{\mathcal{F},\text{fluid}}^{n,k} \wedge (\overrightarrow{X}_{\mathcal{F}}^{n,k} - \overrightarrow{X}_{I}^{n,k}), \tag{3.25}$$

where $\overrightarrow{X}_{\mathcal{F}}^{n,k}$ is the center of mass of the wet solid face $\mathcal{F}^{n,k}$ and $\overrightarrow{X}_{I}^{n,k}$ the center of mass of the particle I at time $t^{n,k}$.

4. The solid is advanced in time. The position of each particle I is integrated using (3.5), (3.7), and (3.14)–(3.17). We obtain the temporary position of the center of mass $X_I^{n,k+1}$ and its velocity $\overrightarrow{V}_I^{n,k+1}$, the rotation matrix $\mathbf{Q}_I^{n,k+1}$, and the angular momentum matrix $\mathbf{P}_I^{n,k+1}$.
5. Iterate on steps (3) and (4) until convergence using the convergence criterion (3.22) detailed in Section 3.4.
6. The volume fractions Λ^{n+1} and side area fractions λ^{n+1} can then be computed using the final position of the fluid-solid interface. The fluid fluxes in (3.13) are modified using λ^{n+1}. At this stage, we can also calculate the amount swept by the movement of the wet solid face $\Delta U_{\mathcal{F}}^{n,n+1}$.

7. The final value of the state $U_{i,j,k}^{n+1}$ in the fluid grid cell is calculated using (3.12). Owing to the perfect slip conditions at the solid boundary, the solid flux $\phi_{\mathcal{F}}^{n+1}$ is given by

$$\phi_{\mathcal{F}}^{n+1} = \left(0,\, \Pi_{x,\mathcal{F}}^{n+1},\, \Pi_{y,\mathcal{F}}^{n+1},\, \Pi_{z,\mathcal{F}}^{n+1},\, \overrightarrow{V}_{\mathcal{F}}^{n+\frac{1}{2}} \cdot \overrightarrow{\Pi}_{\mathcal{F}}^{n+1}\right)^t, \tag{3.26}$$

where

$$\overrightarrow{\Pi}_{\mathcal{F}}^{n+1} = \left(\int_{\mathcal{F}^{n+1}} \bar{p}_x^n\, \nu_{x,\mathcal{F}}^{n+1},\, \int_{\mathcal{F}^{n+1}} \bar{p}_y^n\, \nu_{y,\mathcal{F}}^{n+1},\, \int_{\mathcal{F}^{n+1}} \bar{p}_z^n\, \nu_{z,\mathcal{F}}^{n+1}\right)^t = -\overrightarrow{F}_{\mathcal{F},\,\text{fluid}}^{n+1},$$

and $\overrightarrow{V}_{\mathcal{F}}^{n+\frac{1}{2}}$ is the velocity of the center of mass of the wet solid face $\mathcal{F}^{n+1}$:

$$\overrightarrow{V}_{\mathcal{F}}^{n+\frac{1}{2}} = V_I^{n+\frac{1}{2}} + \overrightarrow{\Omega}_I^{n+\frac{1}{2}} \wedge (\overrightarrow{X}_{\mathcal{F}}^{n+1} - \overrightarrow{X}_I^{n+1}),$$

where $V_I^{n+\frac{1}{2}}$ results from (3.14) and the angular velocity $\overrightarrow{\Omega}_I^{n+\frac{1}{2}}$ at time $(n+\frac{1}{2})\Delta t$ is defined from the relation

$$\mathbf{j}(\overrightarrow{\Omega}_I^{n+\frac{1}{2}}) = \frac{1}{2}\mathbf{P}_I^{n+\frac{1}{2}}\mathbf{D}_I^{-1}(\mathbf{Q}_I^n + \mathbf{Q}_I^{n+1})^t.$$

We finish the time-step by mixing the small cut-cells and filling the ghost-cells in order to prepare the next time step.

The most computationally expensive steps are steps (1), (2), and (5). The first two steps are independent. The rest of the procedure is localized on the fluid cells and solid particles in contact with the fluid-solid interface. The parallelization of the procedure with domain decomposition (in fluid and solid) has therefore the potential to be scalable. These aspects are not further explored herein.

3.3.5 Properties of the coupling scheme

We briefly review the properties of the coupling scheme. We refer to [80, 89] for the proof in the rigid case; the proof in the case of a deformable solid is similar.

3.3.5.1 Conservation of mass, momentum, and energy

Conservation of mass, momentum, and energy holds for periodic boundary conditions and more generally in all the cases where such properties hold at the continuous level.

Let us note that in the case of a deformable solid without fluid coupling, the time-integration scheme does not ensure the conservation of the exact discrete energy. Like many symplectic schemes, the scheme preserves an approximate discrete energy over long-time simulations. This typically induces fluctuations of the exact discrete energy of the solid around a mean value. Interactions between these fluctuations and the conservative fluid could occur. However, we observed in our numerical results that this was not the case, and that the overall conservation of energy for the system was quite satisfactory. Typically, the variation of energy is 0.01% of the energy exchange in the system in the two-dimensional case and 0.03% in the three-dimensional case.

3.3.5.2 Perfect slipping along a wall

The coupling method preserves exactly a uniform constant flow parallel to a rigid half-space, even in the case where the fluid-solid interface is not aligned with the fluid grid. This result shows that no artificial roughness is produced by the solid walls.

3.3.5.3 Uniform translation

Consider an arbitrarily-shaped rigid body moving at constant velocity and without rotation, immersed in a uniform fluid flowing at the same velocity. Then, the uniform movement of the fluid and the solid is preserved by the coupling method.

3.3.5.4 Tangential deformation velocity

The coupling method preserves a constant fluid state around a wall having only tangential deformation velocity. This case is a prototypical example of the inconsistency of the time-explicit scheme (one step in the iterative procedure). In order to verify this property, we consider the following test case. A rod having a square section is immersed in a gas at constant state $(\rho, \overrightarrow{u}, p) = (1.4 \text{ kg.m}^{-3}, \overrightarrow{0} \text{ m.s}^{-1}, 1 \text{ Pa})$. The Young modulus and Poisson ratio of the rod are, respectively, $E = 7000$ Pa and $\nu = 0$. The rod is discretized with 4 square particles along its length. The two extremal particles are fixed, and the two other particles have an initial velocity $\overrightarrow{V} = 0.25\overrightarrow{e}_x$. The computation is carried out until $t = 0.5$ s. Physically, the rod should exhibit internal deformations, with both ends remaining fixed. As the Poisson ratio is $\nu = 0$ and the force is directed along the axis of the rod, no normal deformation should occur at the surface of the rod. Only tangential deformations of the surface appear on the lateral sides of the rod. As shown in Fig. 3.5, the tangential deformation of the boundary creates pressure oscillations for the time-explicit scheme, whereas the time semi-implicit scheme preserves the constant fluid state. The error for the time-explicit scheme grows when the velocity of the particles is largest. On the contrary, the time semi-implicit scheme is able to eliminate totally the error (up to numerical rounding errors involved in the evaluation of geometric quantities in cut-cells and incomplete convergence of the fixed-point procedure).

3.4 Convergence of the iterative procedure in the time semi-implicit scheme

In this section, we prove the convergence of the iterative procedure in the time semi-implicit scheme under a suitable CFL condition on the time step by interpreting this procedure as a fixed-point iteration on a map that we prove to be contracting.

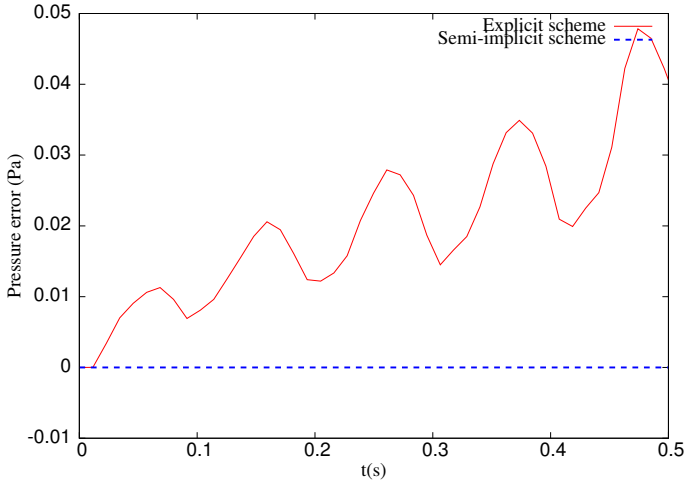

Fig. 3.5: Maximum pressure error as a function of time for the time-explicit and semi-implicit schemes.

3.4.1 Main result

Let $(\overrightarrow{X}^{n,k}, \mathbf{Q}^{n,k}) = \left((\overrightarrow{X}_I^{n,k}, \mathbf{Q}_I^{n,k})\right)_I$ be the geometric state vector collecting the position of the center of mass and the rotation matrix of the solid particles I at the k-th step of the iterative procedure described in Section 3.3.3. We consider the map χ such that $(\overrightarrow{X}^{n,k+1}, \mathbf{Q}^{n,k+1}) = \chi(\overrightarrow{X}^{n,k}, \mathbf{Q}^{n,k})$ denotes the state vector obtained at the $(k+1)$-th step. The map χ is defined more precisely in (3.41)-(3.42) below.

Let $\sigma_{s,I}$ denote the radius of the largest inscribed sphere in particle I, and recall that $h_{s,I}$ denotes the diameter of the particle. We denote by $d_{\min,I}$ and $d_{\max,I}$ respectively the smallest and largest eigenvalues of the matrix $\mathbf{D}_I$. Using the mass and inertia of a sphere of radius $\sigma_{s,I}$ and of the same density $\rho_{s,I}$ as the solid particle I, we obtain

$$m_I \geq \frac{4\pi}{3}\rho_{s,I}\sigma_{s,I}^3, \quad d_{\min,I} \geq \frac{4\pi}{15}\rho_{s,I}\sigma_{s,I}^5, \quad d_{\max,I} \leq \frac{4\pi}{15}\rho_{s,I}h_{s,I}^5. \tag{3.27}$$

We define the real function $x \mapsto K(x)$ as

$$K(x) = \frac{15}{8\pi}x + \frac{165(1+2C(x))}{16\pi}x^3, \quad C = \sqrt{3+\frac{1}{2}x^5}. \tag{3.28}$$

Let I be a solid particle and let $\mathcal{F} \in \mathfrak{F}_I$ be a wet solid face of I. Denote $\overline{p}_{\mathcal{F}}^n = \max\{\overline{p}_x^n, \overline{p}_y^n, \overline{p}_z^n\}$ where the boundary pressures $\overline{p}_x^n$, $\overline{p}_y^n$ and $\overline{p}_x^n$ are defined in Step (1) of Section 3.3.4. Note that these pressures do not change during the fixed-point procedure. Then, the main result proven in Section 3.4.2 below states that, for Δt satisfying the CFL condition

$$\forall I, \quad K\left(\frac{h_{s,I}}{\sigma_{s,I}}\right)\frac{\Delta t^2}{\sigma_{s,I}^2}\sum_{\mathcal{F}\in\mathfrak{F}_I}\frac{\overline{p}_{\mathcal{F}}^n}{\rho_{s,I}} < 1, \tag{3.29}$$

the iterative procedure in the time semi-implicit scheme converges at a geometric rate.

Let us comment on condition (3.29). For a given aspect ratio of the solid particles, the upper bound on the time step Δt resulting from (3.29) is proportional to the maximal diameter of the solid particles $h_{s,I}$. Moreover, the constant involves the ratio $\frac{\overline{p}^n_{\mathcal{F}}}{\rho_s}$: if the solid density is assumed to be larger than the fluid density (which is the case in our intended applications), $\frac{\overline{p}^n_{\mathcal{F}}}{\rho_s}$ is less than the square of the maximal sound celerity of the fluid c^2. Condition (3.29) is compatible with the stability results found in [44]: a very small solid density induces numerical instabilities of the overall explicit coupling strategy. As our bounds are expected to be rather pessimistic, condition (3.29) is in practice less restrictive than the fluid CFL condition. We have verified this assertion on numerous simulations, in which the iterative procedure always converged in less than 7 iterations without explicitly enforcing (3.29). Here and in what follows, unless explicitly mentioned, the vector norm in $\mathbb{R}^3$ is the Euclidean norm, and the matrix norm is the induced spectral norm (i.e., the largest singular value of the matrix).

3.4.2 Proof

This section is devoted to the proof of the above convergence result under the CFL condition (3.29). To this purpose, we show that the map χ involved in the iterative procedure (see (3.41)-(3.42) below) is contracting for the following norm:

$$\|(\overrightarrow{X},\mathbf{Q})\|_\infty = \max_I \|\overrightarrow{X}_I\| + \max_I h_{s,I}\|\mathbf{Q}_I\|. \tag{3.30}$$

3.4.2.1 The map χ

The k-th step of the iterative procedure can be written as follows: For each particle I,

$$\overrightarrow{V}_I^{n,k+1} = \overrightarrow{V}_I^{n} + \frac{\Delta t}{2m_I}\left(\overrightarrow{F}^n_{I,\text{int}} + \overrightarrow{F}^{n,k}_{I,\,\text{fluid}}\right), \tag{3.31}$$

$$\overrightarrow{X}_I^{n,k+1} = \overrightarrow{X}_I^{n} + \Delta t\,\overrightarrow{V}_I^{n,k+1}, \tag{3.32}$$

$$\mathbf{P}_I^{n,k+1} = \mathbf{P}_I^{n} + \frac{\Delta t}{4}\mathbf{j}(\overrightarrow{\mathcal{M}}^n_{I,\text{int}} + \overrightarrow{\mathcal{M}}^{n,k}_{I,\,\text{fluid}})\mathbf{Q}_I^n + \frac{\Delta t}{2}\boldsymbol{\Upsilon}_I^{n,k}\mathbf{Q}_I^n, \tag{3.33}$$

$$\mathbf{Q}_I^{n,k+1} = \mathbf{Q}_I^{n} + \Delta t\,\mathbf{P}_I^{n,k+1}\mathbf{D}_I^{-1}, \tag{3.34}$$

where $\overrightarrow{F}^n_{I,\text{int}}$ and $\overrightarrow{\mathcal{M}}^n_{I,\text{int}}$ denote the internal forces and torques on particle I at time t^n (which are independent of k) and $\overrightarrow{F}^{n,k}_{I,\,\text{fluid}}$ and $\overrightarrow{\mathcal{M}}^{n,k}_{I,\,\text{fluid}}$ denote the pressure forces and torques exerted by the fluid on particle I at time t^n and at the k-th step.

Let $\mathcal{F}$ be a wet solid face and let I be the solid particle to which it belongs. As described in Section 3.3.2, the wet solid face is a triangle. We denote by a_1, a_2, and a_3 its vertices. We orient the triangle $\mathcal{F}$ for a given geometric state $(\overrightarrow{X},\mathbf{Q})$ of the solid by defining the surface and unit normal of $\mathcal{F}$ as

$$A_{\mathcal{F}}(\overrightarrow{X},\mathbf{Q})\overrightarrow{\nu}_{\mathcal{F}}(\overrightarrow{X},\mathbf{Q}) = \frac{1}{2}(\overline{a}_2(\overrightarrow{X},\mathbf{Q}) - \overline{a}_1(\overrightarrow{X},\mathbf{Q})) \wedge (\overline{a}_3(\overrightarrow{X},\mathbf{Q}) - \overline{a}_1(\overrightarrow{X},\mathbf{Q})), \tag{3.35}$$

where we recall from (3.18) that the average position of the vertex $\overline{a}_i(\overrightarrow{X},\mathbf{Q})$ is given by

$$\overline{a}_i(\overrightarrow{X},\mathbf{Q}) = \frac{1}{\#\mathcal{P}_{a_i}} \sum_{J\in\mathcal{P}_{a_i}} (\overrightarrow{X}_J + \mathbf{Q}_J\cdot(a_i^0 - \overrightarrow{X}_J^0)), \tag{3.36}$$

where the superscript 0 refers to values at time $t^0=0$. We define the displacement $\overrightarrow{\xi}_a(\overrightarrow{X},\mathbf{Q})$ of a vertex a with respect to the geometric state at time t^n as follows:

$$\overrightarrow{\xi}_a(\overrightarrow{X},\mathbf{Q}) = \frac{1}{\#\mathcal{P}_a} \sum_{J\in\mathcal{P}_a} \Big(\overrightarrow{X}_J - \overrightarrow{X}_J^n + (\mathbf{Q}_J - \mathbf{Q}_J^n)\cdot(a^0 - \overrightarrow{X}_J^0)\Big), \tag{3.37}$$

so that $\overline{a}(\overrightarrow{X},\mathbf{Q}) = \overline{a}^n + \overrightarrow{\xi}_a(\overrightarrow{X},\mathbf{Q})$. We define the fluid pressure force $\overrightarrow{F}_{I,\,\mathrm{fluid}}(\overrightarrow{X},\mathbf{Q})$ on particle I as

$$\overrightarrow{F}_{I,\,\mathrm{fluid}}(\overrightarrow{X},\mathbf{Q}) = \sum_{\mathcal{F}\in\mathfrak{F}_I} \overrightarrow{F}_{\mathcal{F},\,\mathrm{fluid}}(\overrightarrow{X},\mathbf{Q}), \quad \overrightarrow{F}_{\mathcal{F},\,\mathrm{fluid}}(\overrightarrow{X},\mathbf{Q}) = -\mathbf{P}_{\mathcal{F}}^n A_{\mathcal{F}}(\overrightarrow{X},\mathbf{Q})\overrightarrow{v}_{\mathcal{F}}(\overrightarrow{X},\mathbf{Q}), \tag{3.38}$$

where $\mathbf{P}_{\mathcal{F}}^n = \mathrm{diag}(\overline{p}_x^n,\overline{p}_y^n,\overline{p}_z^n)$. Using (3.35)–(3.38), the fluid pressure force is given by

$$\begin{aligned}\overrightarrow{F}_{\mathcal{F},\,\mathrm{fluid}}(\overrightarrow{X},\mathbf{Q}) = -\frac{1}{2}\mathbf{P}_{\mathcal{F}}^n \Big[&\Big(\overline{a}_2^n - \overline{a}_1^n + \overrightarrow{\xi}_{a_2}(\overrightarrow{X},\mathbf{Q}) - \overrightarrow{\xi}_{a_1}(\overrightarrow{X},\mathbf{Q})\Big)\\ &\wedge\Big(\overline{a}_3^n - \overline{a}_1^n + \overrightarrow{\xi}_{a_3}(\overrightarrow{X},\mathbf{Q}) - \overrightarrow{\xi}_{a_1}(\overrightarrow{X},\mathbf{Q})\Big)\Big].\end{aligned} \tag{3.39}$$

Recall that the mean pressure on each wet solid face is constant during the iterative process. We define the fluid pressure torque $\overrightarrow{\mathcal{M}}_{I,\,\mathrm{fluid}}(\overrightarrow{X},\mathbf{Q})$ on particle I as

$$\overrightarrow{\mathcal{M}}_{I,\,\mathrm{fluid}}(\overrightarrow{X},\mathbf{Q}) = \sum_{\mathcal{F}\in\mathfrak{F}_I} \overrightarrow{F}_{\mathcal{F},\,\mathrm{fluid}}(\overrightarrow{X},\mathbf{Q}) \wedge \Big(\overrightarrow{X}_{\mathcal{F}}(\overrightarrow{X},\mathbf{Q}) - \overrightarrow{X}_I\Big), \tag{3.40}$$

where $\overrightarrow{X}_{\mathcal{F}}(\overrightarrow{X},\mathbf{Q}) = \overrightarrow{X}_{\mathcal{F}}^n + \frac{1}{3}\Big(\overrightarrow{\xi}_{a_1}(\overrightarrow{X},\mathbf{Q}) + \overrightarrow{\xi}_{a_2}(\overrightarrow{X},\mathbf{Q}) + \overrightarrow{\xi}_{a_3}(\overrightarrow{X},\mathbf{Q})\Big)$ is the position of the center of mass of $\mathcal{F}^n$ for the solid geometric state $(\overrightarrow{X},\mathbf{Q})$. We set

$$\overrightarrow{C}_I^n = \overrightarrow{X}_I^n + \Delta t\overrightarrow{V}_I^n + \frac{\Delta t^2}{2m_I}\overrightarrow{F}_{I,\mathrm{int}}^n, \quad \mathbf{\Gamma}_I^n = \mathbf{Q}_I^n + \Delta t\mathbf{P}_I^n\mathbf{D}_I^{-1} + \frac{\Delta t^2}{4}\mathbf{j}(\overrightarrow{\mathcal{M}}_{I,\mathrm{int}}^n)\mathbf{Q}_I^n\mathbf{D}_I^{-1}.$$

Then, owing to (3.31)-(3.34), the map χ for a given geometric state $(\overrightarrow{X},\mathbf{Q})$ for the solid is given by $\chi(\overrightarrow{X},\mathbf{Q}) = ((\chi_{p,I}(\overrightarrow{X},\mathbf{Q}))_I,(\chi_{r,I}(\overrightarrow{X},\mathbf{Q}))_I)$ where

$$\chi_{p,I}(\overrightarrow{X},\mathbf{Q}) = \overrightarrow{C}_I^n + \frac{\Delta t^2}{2m_I}\sum_{\mathcal{F}\in\mathfrak{F}_I}\overrightarrow{F}_{\mathcal{F},\,\mathrm{fluid}}(\overrightarrow{X},\mathbf{Q}), \tag{3.41}$$

$$\chi_{r,I}(\overrightarrow{X},\mathbf{Q}) = \mathbf{\Gamma}_I^n + \frac{\Delta t^2}{4}\Big(\mathbf{j}(\overrightarrow{\mathcal{M}}_{I,\,\mathrm{fluid}}(\overrightarrow{X},\mathbf{Q})) + 2\mathbf{\Upsilon}_I(\overrightarrow{X},\mathbf{Q})\Big)\mathbf{Q}_I^n\mathbf{D}_I^{-1}, \tag{3.42}$$

in such a way that $\overrightarrow{X}_I^{n,k+1} = \chi_{p,I}(\overrightarrow{X}^{n,k},\mathbf{Q}^{n,k})$ and $\mathbf{Q}_I^{n,k+1} = \chi_{r,I}(\overrightarrow{X}^{n,k},\mathbf{Q}^{n,k})$.

3.4.2.2 Estimate on the position of the center of mass

Let $(\overrightarrow{X},\mathbf{Q})$ and $(\overrightarrow{Y},\mathbf{R})$ be two geometric states for the solid particles. Using the expression for $\overrightarrow{\xi}_a$ from (3.37) and the definition (3.30) of the $\|\cdot\|_\infty$-norm leads to

$$\|\overrightarrow{\xi}_a(\overrightarrow{X},\mathbf{Q})-\overrightarrow{\xi}_a(\overrightarrow{Y},\mathbf{R})\|\le\|(\overrightarrow{X}-\overrightarrow{Y},\mathbf{Q}-\mathbf{R})\|_\infty. \tag{3.43}$$

Using the expression of the fluid pressure force from (3.39) together with the triangle inequality, and since $\|\mathbf{P}^n_{\mathcal{F}}\|=\overline{p}^n_{\mathcal{F}}$, we infer that

$$\begin{aligned}\|\overrightarrow{F}_{\mathcal{F},\,\text{fluid}}(\overrightarrow{X},\mathbf{Q})-\overrightarrow{F}_{\mathcal{F},\,\text{fluid}}(\overrightarrow{Y},\mathbf{R})\|\le\frac{\overline{p}^n_{\mathcal{F}}}{2}\Big\{&\Big\|(\overline{a}^n_2-\overline{a}^n_1)\wedge\Big(\overrightarrow{\xi}_{a_3}(\overrightarrow{X},\mathbf{Q})-\overrightarrow{\xi}_{a_3}(\overrightarrow{Y},\mathbf{R})\Big)\Big\|\\
&+\Big\|(\overline{a}^n_2-\overline{a}^n_1)\wedge\Big(\overrightarrow{\xi}_{a_1}(\overrightarrow{X},\mathbf{Q})-\overrightarrow{\xi}_{a_1}(\overrightarrow{Y},\mathbf{R})\Big)\Big\|\\
&+\Big\|(\overline{a}^n_3-\overline{a}^n_1)\wedge\Big(\overrightarrow{\xi}_{a_2}(\overrightarrow{X},\mathbf{Q})-\overrightarrow{\xi}_{a_2}(\overrightarrow{Y},\mathbf{R})\Big)\Big\|\\
&+\Big\|(\overline{a}^n_3-\overline{a}^n_1)\wedge\Big(\overrightarrow{\xi}_{a_1}(\overrightarrow{X},\mathbf{Q})-\overrightarrow{\xi}_{a_1}(\overrightarrow{Y},\mathbf{R})\Big)\Big\|\\
&+\Big\|\Big(\overrightarrow{\xi}_{a_2}(\overrightarrow{X},\mathbf{Q})-\overrightarrow{\xi}_{a_1}(\overrightarrow{X},\mathbf{Q})\Big)\wedge\Big(\overrightarrow{\xi}_{a_3}(\overrightarrow{X},\mathbf{Q})-\overrightarrow{\xi}_{a_1}(\overrightarrow{X},\mathbf{Q})\Big)\\
&\qquad-\Big(\overrightarrow{\xi}_{a_2}(\overrightarrow{Y},\mathbf{R})-\overrightarrow{\xi}_{a_1}(\overrightarrow{Y},\mathbf{R})\Big)\wedge\Big(\overrightarrow{\xi}_{a_3}(\overrightarrow{Y},\mathbf{R})-\overrightarrow{\xi}_{a_1}(\overrightarrow{Y},\mathbf{R})\Big)\Big\|\Big\}.\end{aligned}$$

The first four terms on the right hand side are bounded using (3.43) and the fact that the characteristic size of the solid particles is such that $h_{s,I}\ge\max(\|\overline{a}_2-\overline{a}_1\|,\|\overline{a}_3-\overline{a}_1\|)$. Developing the lest terms, we obtain three contributions which can be estimated separately. For instance, the first contribution is bounded as

$$\begin{aligned}\|\overrightarrow{\xi}_{a_1}(\overrightarrow{X},\mathbf{Q})\wedge\overrightarrow{\xi}_{a_3}(\overrightarrow{X},\mathbf{Q})-\overrightarrow{\xi}_{a_1}(\overrightarrow{Y},\mathbf{R})\wedge\overrightarrow{\xi}_{a_3}(\overrightarrow{Y},\mathbf{R})\|&\\
=\Big\|\overrightarrow{\xi}_{a_1}\wedge(\overrightarrow{X},\mathbf{Q})\Big(\overrightarrow{\xi}_{a_3}(\overrightarrow{X},\mathbf{Q})-\overrightarrow{\xi}_{a_3}(\overrightarrow{Y},\mathbf{R})\Big)&\\
\quad+\overrightarrow{\xi}_{a_3}\wedge(\overrightarrow{Y},\mathbf{R})\Big(\overrightarrow{\xi}_{a_1}(\overrightarrow{X},\mathbf{Q})-\overrightarrow{\xi}_{a_1}(\overrightarrow{Y},\mathbf{R})\Big)\Big\|&\\
\le 2h_{s,I}\|(\overrightarrow{X}-\overrightarrow{Y},\mathbf{Q}-\mathbf{R})\|_\infty,&\end{aligned}$$

where we have used (3.43) and the solid CFL condition on displacement which yields $\|\xi_{a_i}(\overrightarrow{X},\mathbf{Q})\|\le h_{s,I}$, $\|\xi_{a_i}(\overrightarrow{Y},\mathbf{R})\|\le h_{s,I}$ for all $i\in\{1,2,3\}$. Recollecting the above bounds, we infer that

$$\|\overrightarrow{F}_{\mathcal{F},\,\text{fluid}}(\overrightarrow{X},\mathbf{Q})-\overrightarrow{F}_{\mathcal{F},\,\text{fluid}}(\overrightarrow{Y},\mathbf{R})\|\le 5\overline{p}^n_{\mathcal{F}}h_{s,I}\|(\overrightarrow{X}-\overrightarrow{Y},\mathbf{Q}-\mathbf{R})\|_\infty. \tag{3.44}$$

As a result, the positions of the center of mass verify

$$\|\chi_{p,I}(\overrightarrow{X},\mathbf{Q})-\chi_{p,I}(\overrightarrow{Y},\mathbf{R})\|\le\frac{5h_{s,I}\Delta t^2}{2m_I}\sum_{\mathcal{F}\in\mathfrak{F}_I}\overline{p}^n_{\mathcal{F}}\|(\overrightarrow{X}-\overrightarrow{Y},\mathbf{Q}-\mathbf{R})\|_\infty.$$

Using (3.27) to bound m_I, we infer that

$$\|\chi_{p,I}(\overrightarrow{X},\mathbf{Q})-\chi_{p,I}(\overrightarrow{Y},\mathbf{R})\|\le\left\{\frac{15}{8\pi}\frac{h_{s,I}}{\sigma_{s,I}}\frac{\Delta t^2}{\sigma^2_{s,I}}\sum_{\mathcal{F}\in\mathfrak{F}_I}\frac{\overline{p}^n_{\mathcal{F}}}{\rho_{s,I}}\right\}\|(\overrightarrow{X}-\overrightarrow{Y},\mathbf{Q}-\mathbf{R})\|_\infty. \tag{3.45}$$

3.4.2.3 Estimate on the rotation

Using the bound (3.44) on the force, a lengthy but straightforward computation similar to the estimate of the fluid pressure force yields

$$\|\overrightarrow{\mathcal{M}}_{I,\,\mathrm{fluid}}(\overrightarrow{X},\mathbf{Q})-\overrightarrow{\mathcal{M}}_{I,\,\mathrm{fluid}}(\overrightarrow{Y},\mathbf{R})\|\leq\sum_{\mathcal{F}\in\mathfrak{F}_I}11\overline{p}^n_{\mathcal{F}}h^2_{s,I}\|(\overrightarrow{X}-\overrightarrow{Y},\mathbf{Q}-\mathbf{R})\|_\infty.$$

Owing to the construction of the Lagrange multiplier $\boldsymbol{\Upsilon}_I$, recalling the constant C from (3.28), we show in Section 3.4.2.4 that

$$\|\boldsymbol{\Upsilon}_I(\overrightarrow{X},\mathbf{Q})-\boldsymbol{\Upsilon}_I(\overrightarrow{Y},\mathbf{R})\|\leq C\|\overrightarrow{\mathcal{M}}_{I,\,\mathrm{fluid}}(\overrightarrow{X},\mathbf{Q})-\overrightarrow{\mathcal{M}}_{I,\,\mathrm{fluid}}(\overrightarrow{Y},\mathbf{R})\|.$$

Observing that $\mathbf{j}:\mathbb{R}^3\to\mathbb{R}^{3\times3}$ is a linear isometry, the rotation matrices verify

$$\|\chi_{r,I}(\overrightarrow{X},\mathbf{Q})-\chi_{r,I}(\overrightarrow{Y},\mathbf{R})\|\leq\frac{11\,(1+2C)\,h^2_{s,I}\Delta t^2}{4}\|\mathbf{D}_I^{-1}\|\sum_{\mathcal{F}\in\mathfrak{F}_I}\overline{p}^n_{\mathcal{F}}\|(\overrightarrow{X}-\overrightarrow{Y},\mathbf{Q}-\mathbf{R})\|_\infty.$$

Finally, using (3.27) to bound $\mathbf{D}_I$, the rotation matrices verify

$$\|\chi_{r,I}(\overrightarrow{X},\mathbf{Q})-\chi_{r,I}(\overrightarrow{Y},\mathbf{R})\|\leq\left\{\frac{165\,(1+2C)}{16\pi}\frac{h^3_{s,I}}{\rho_{s,I}\sigma^3_{s,I}}\frac{\Delta t^2}{\sigma^2_{s,I}}\sum_{\mathcal{F}\in\mathfrak{F}_I}\overline{p}^n_{\mathcal{F}}\right\}\|(\overrightarrow{X}-\overrightarrow{Y},\mathbf{Q}-\mathbf{R})\|_\infty. \tag{3.46}$$

Collecting (3.45) and (3.46), we obtain

$$\begin{aligned}&\|\chi(\overrightarrow{X},\mathbf{Q})-\chi(\overrightarrow{Y},\mathbf{R})\|_\infty\\&\qquad\leq\max_I\left\{\left(\frac{15}{8\pi}\frac{h_{s,I}}{\sigma_{s,I}}+\frac{165\,(1+2C)}{16\pi}\frac{h^3_{s,I}}{\sigma^3_{s,I}}\right)\frac{\Delta t^2}{\sigma^2_{s,I}}\sum_{\mathcal{F}\in\mathfrak{F}_I}\frac{\overline{p}^n_{\mathcal{F}}}{\rho_{s,I}}\right\}\|(\overrightarrow{X}-\overrightarrow{Y},\mathbf{Q}-\mathbf{R})\|_\infty.\end{aligned}$$

As a result, the map χ is contracting with respect to the norm $\|\,\|_\infty$ under the CFL condition (3.29).

3.4.2.4 Estimate on the Lagrange multiplier in terms of torque

In the estimate on rotation, we have used the control of the Lagrange multiplier $\boldsymbol{\Upsilon}$ by the torque $\overrightarrow{\mathcal{M}}$. We prove this result herein. Owing to (3.42), we can rewrite the difference between two rotation matrices $\chi_{r,I}(\overrightarrow{X},\mathbf{Q})$ and $\chi_{r,I}(\overrightarrow{Y},\mathbf{R})$ as follows:

$$\begin{aligned}(\chi_{r,I}(\overrightarrow{X},\mathbf{Q})-\chi_{r,I}(\overrightarrow{Y},\mathbf{R}))(\mathbf{Q}^n_I)^t\left(\mathbf{Q}^n_I\mathbf{D}_I(\mathbf{Q}^n_I)^t\right)=\frac{\Delta t^2}{4}\Big(&\mathbf{j}(\overrightarrow{\mathcal{M}}_{I,\,\mathrm{fluid}}(\overrightarrow{X},\mathbf{Q}))-\mathbf{j}(\overrightarrow{\mathcal{M}}_{I,\,\mathrm{fluid}}(\overrightarrow{Y},\mathbf{R}))\\&+2\boldsymbol{\Upsilon}_I(\overrightarrow{X},\mathbf{Q})-2\boldsymbol{\Upsilon}_I(\overrightarrow{Y},\mathbf{R})\Big).\end{aligned} \tag{3.47}$$

The left-hand side of (3.47) is composed of the product of differences between one time step incremental rotation matrices by the rotated matrix $\mathbf{D}_I$. Since $\mathbf{D}_I$ is real symmetric, up to changing matrix $\mathbf{Q}^n_I$ (which does not affect the estimate), it is possible to assume that $\mathbf{Q}^n_I\mathbf{D}_I(\mathbf{Q}^n_I)^t=\mathrm{diag}(d_1,d_2,d_3)$ (we omit the index I in d_i for simplicity). We write the incremental rotation matrices using the quaternion notation [49, Sec. VII.5],

$$\chi_{r,I}(\overrightarrow{X},\mathbf{Q})(\mathbf{Q}_I^n)^t = \mathbf{I} + 2e_0\mathbf{j}(\overrightarrow{e}) + 2\mathbf{j}(\overrightarrow{e})^2, \quad e_0 = \sqrt{1-\|\overrightarrow{e}\|_2^2},$$
$$\chi_{r,I}(\overrightarrow{Y},\mathbf{R})(\mathbf{Q}_I^n)^t = \mathbf{I} + 2f_0\mathbf{j}(\overrightarrow{f}) + 2\mathbf{j}(\overrightarrow{f})^2, \quad f_0 = \sqrt{1-\|\overrightarrow{f}\|_2^2},$$

where $\overrightarrow{e}$ and $\overrightarrow{f}$ represent a rotation vector: their direction indicates the axis of rotation and their magnitude is related to the angle of rotation θ by $\|\overrightarrow{e}\|_2 = \sin(\frac{\theta}{2})$.

Since $\mathbf{j}(\overrightarrow{M})$ is skew-symmetric and $\boldsymbol{\Upsilon}$ is symmetric, the right-hand side of (3.47) offers a decomposition of the left-hand side into its skew-symmetric and symmetric parts. Therefore, it can be checked that

$$\frac{\Delta t^2}{4}(\overrightarrow{\mathcal{M}}_{I,\,\mathrm{fluid}}(\overrightarrow{X},\mathbf{Q}) - \overrightarrow{\mathcal{M}}_{I,\,\mathrm{fluid}}(\overrightarrow{Y},\mathbf{R})) = \begin{pmatrix} (d_2+d_3)(e_0e_1 - f_0f_1) + (d_2-d_3)(e_2e_3 - f_2f_3) \\ (d_1+d_3)(e_0e_2 - f_0f_2) + (d_3-d_1)(e_1e_3 - f_1f_3) \\ (d_1+d_2)(e_0e_3 - f_0f_3) + (d_1-d_2)(e_1e_2 - f_1f_2) \end{pmatrix}, \tag{3.48}$$

and that, for all $i,j \in \{1,2,3\}$,

$$\frac{\Delta t^2}{2}(\boldsymbol{\Upsilon}_I(\overrightarrow{X},\mathbf{Q}) - \boldsymbol{\Upsilon}_I(\overrightarrow{Y},\mathbf{R}))_{ij} = \begin{cases} -d_i(\|\overrightarrow{e}\|_2^2 - e_i^2 - \|\overrightarrow{f}\|_2^2 + f_i^2) \text{ if } i = j \\ (d_i - d_j)(e_0e_k - f_0f_k) + (d_i + d_j)(e_ie_j - f_if_j) \\ \text{if } (i,j,k) \text{ is an even permutation of (1,2,3).} \end{cases} \tag{3.49}$$

We introduce the Frobenius norm of a matrix $\|A\|_F^2 = \sum_{i,j=1}^3 A_{ij}^2$ and notice that $\|A\| \le \|A\|_F$. Since the maximal angle of the incremental rotation for one time step is $\frac{\pi}{8}$ owing to the solid CFL condition, we infer that

$$\|\overrightarrow{e}\|_2 = \sin(\frac{\theta}{2}) \le \sqrt{\beta}, \tag{3.50}$$

where we have introduced the parameter $\beta = \frac{1}{4}(2-\sqrt{2+\sqrt{2}})$. The same bound $\|\overrightarrow{f}\|_2 \le \sqrt{\beta}$ also holds. Using Lemma (E.1) of [81], we obtain

$$|e_0 - f_0| \le \sqrt{\frac{\beta}{1-\beta}}\|\overrightarrow{e} - \overrightarrow{f}\|_2. \tag{3.51}$$

Moreover, owing to the definition of e_0 and f_0, we obtain

$$|e_0| \ge \sqrt{1-\beta}, \quad |f_0| \ge \sqrt{1-\beta} \tag{3.52}$$

Since $\frac{2\sqrt{\beta(1-\beta)}}{1-2\beta} = \sqrt{2}-1 < 1$ and $d_i > 0$ for all $i \in \{1,2,3\}$, straightforward inequalities yield (see Section 3.8 for details)

$$\|\boldsymbol{\Upsilon}_I(\overrightarrow{X},\mathbf{Q}) - \boldsymbol{\Upsilon}_I(\overrightarrow{Y},\mathbf{R})\|_F^2 \le \left(3 + \frac{1}{2}\frac{h_{s,I}^5}{\sigma_{s,I}^5}\right)\|\overrightarrow{\mathcal{M}}_{I,\,\mathrm{fluid}}(\overrightarrow{X},\mathbf{Q}) - \overrightarrow{\mathcal{M}}_{I,\,\mathrm{fluid}}(\overrightarrow{Y},\mathbf{R})\|^2. \tag{3.53}$$

3.5 Numerical results

In this section we present numerical results obtained by using the semi-implicit coupling method described and validated earlier. We first consider the interaction of a shock wave with a two- and three-dimensional clamped beam. Then, we simulate the effect of an explosion on an steel cylinder in two space dimensions. Finally, we consider the interaction of a shock wave with a two-dimensional deformable thin shell.

3.5.1 Clamped beam

3.5.1.1 2d clamped beam

Consider a 4m long and 2m large channel with fixed reflecting bottom and top solid boundaries. Periodic boundary conditions are applied to both ends of the channel. Initially, the gas in the channel forms a double shock tube: the states are $(\rho, \overrightarrow{u}, p) = (8\text{kg.m}^{-3}, \overrightarrow{0}\,\text{m.s}^{-1}, 116.5\text{Pa})$ for $0 < x < 1.5\text{m}$, and $(\rho, \overrightarrow{u}, p) = (1.4\text{kg.m}^{-3}, \overrightarrow{0}\,\text{m.s}^{-1}, 1\text{Pa})$ for $1.5\text{m} < x < 4\text{m}$. The fluid domain is discretized with 400×200 elements ($\Delta x = \Delta y = 10^{-2}\text{m}$). A beam is clamped at the bottom of the channel, its center is located at $x = 2\text{m}$. The beam is 0.2857m wide and 1m long. The beam density and Young modulus of the beam are, respectively, $\rho_s = 100\text{kg.m}^{-3}$ and $E = 7000\text{Pa}$, with a Poisson ratio $\nu = 0$. The beam is discretized with 14×50 square particles ($h_s = 2 \times 10^{-2}\text{m}$).

In Fig. 3.6, we show the normal stress in the beam and the pressure profile in the fluid at time $t = 0.08\text{s}$. On the left of the beam, we observe the primary reflected shock followed by successive compression waves induced by the multiple reflections of the shock wave inside the beam.

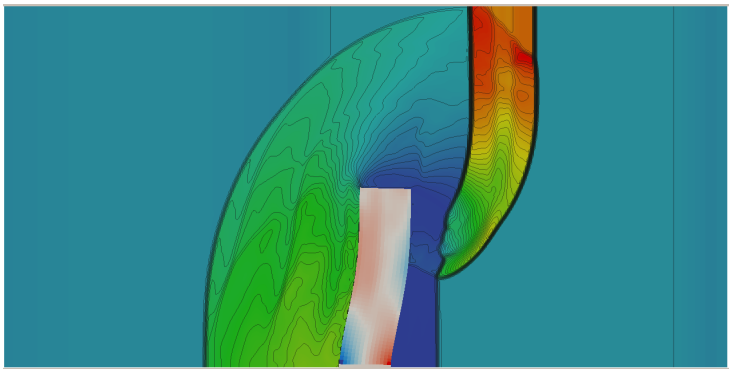

Fig. 3.6: Normal stress in the beam and the pressure profile in the fluid at time $t = 0.08\text{s}$ (50 contours in the fluid from 0 to 160Pa).

In Fig. 3.7, we present the relative energy conservation error, computed as the difference between the initial energy and the discrete energy computed at the different time steps. This energy difference is normalized by the maximum energy exchange between the fluid and the solid,

which is the relevant quantity to evaluate the relative effect of coupling on conservation issues. We observe a small variation of energy, without any clear growth or decrease. The variation of energy is as low as 0.01% of the energy exchange in the system. This fluctuation of energy is not linked to the convergence criterion, but originates from the fluctuation of the discrete energy in the symplectic scheme. However, we observe no energy drift during the simulation. Fig. 3.7 also presents the same result with refined time steps $\Delta t/2$ and $\Delta t/4$. As expected, the energy conservation error decreases to zero with the time step, with second-order accuracy. This shows that the present coupling method ensures a long-term energy conservation of the system in the case of a deformable solid.

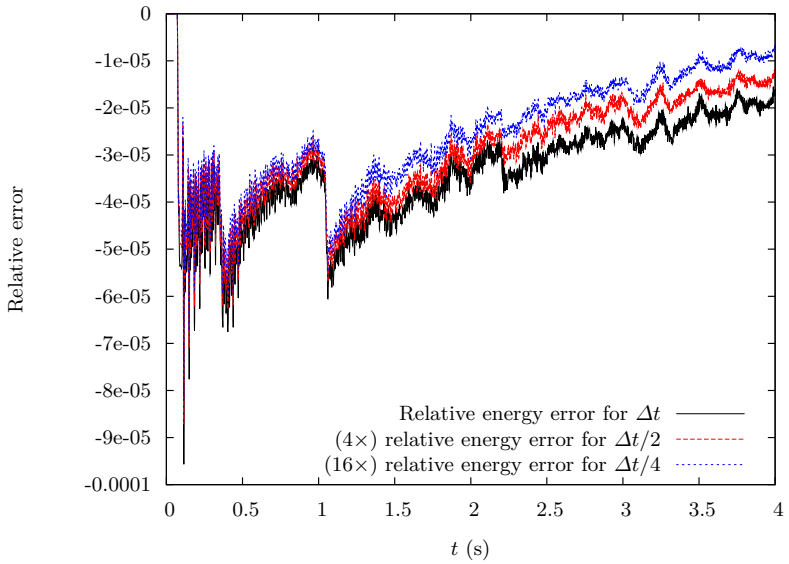

Fig. 3.7: Relative energy conservation error as a function of time for time-steps Δt, $\Delta t/2$ (rescaled by a factor 4) and $\Delta t/4$ (rescaled by a factor 16).

3.5.1.2 3d clamped beam

Consider a 4m long, 2m large, and 2m deep channel. Periodic boundary conditions are applied to both ends of the channel. Initially, the gas in the channel forms a double shock tube: the state is $(\rho, \overrightarrow{u}, p) = (8\text{kg.m}^{-3}, \overrightarrow{0}\,\text{m.s}^{-1}, 116.5\text{Pa})$ for $0 < x < 1.5$m, and $(\rho, \overrightarrow{u}, p) = (1.4\text{kg.m}^{-3}, \overrightarrow{0}\,\text{m.s}^{-1}, 1\text{Pa})$ for $1.5\text{m} < x < 4$m. The fluid domain is discretized with $100 \times 50 \times 50$ elements ($\Delta x = \Delta y = \Delta z = 0.04$m). The beam is 0.2857m wide, 1m long, and 0.2857m high. The beam is clamped at the bottom of the channel, its center is located at ($x = 2$m, $y = 0$m, $z = 1$m). The density, Young modulus, and the Poisson ratio of the beam are identical as in the two-dimensional case. The beam is discretized with 24 tetrahedral particles ($h_x = 0.2857$m, $h_y = 0.1428$m, $h_z = 0.2857$m).

In Fig. 3.8, we show the x-coordinate of the center of mass of the particle situated at the top of the beam during the simulation. In Fig. 3.9, we show the trajectory of the same point in the xy-plane. We observe that the x-coordinate of the center of mass of the particle situated at the top of the beam advances during 0.2s from 2m to 2.0165m and returns quite close to the initial position after the same lapse of time. Indeed, the beam undergoes a quasi-periodic motion composed of various vibration modes (the main one being the first flexure mode), partially damped by the interaction with the fluid and also perturbed by the development of multiple waves within the periodic domain.

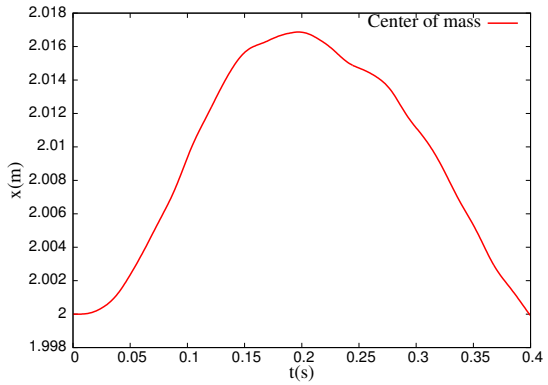

Fig. 3.8: x-coordinate of the center of mass of the particle situated at the top of the beam as a function of time.

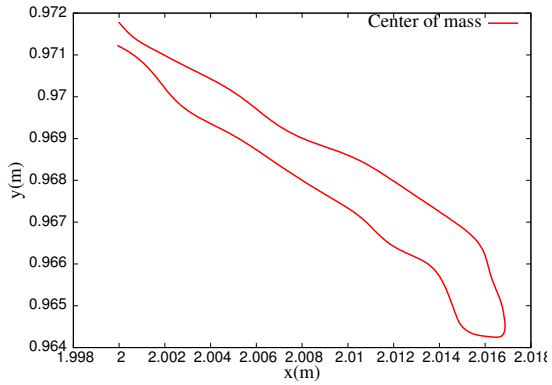

Fig. 3.9: Trajectory of the center of mass of the particle situated at the top of the beam in the xy-plane.

In Fig. 3.10, we present the relative energy conservation error, computed as the difference between the initial energy and the energy computed at the different time steps. This energy difference is normalized by the maximum energy exchange between the fluid and the solid. We observe a small variation of relative energy, without any clear growth or decrease, as low as 0.03%. The same conclusions can be drawn as in the two-dimensional case.

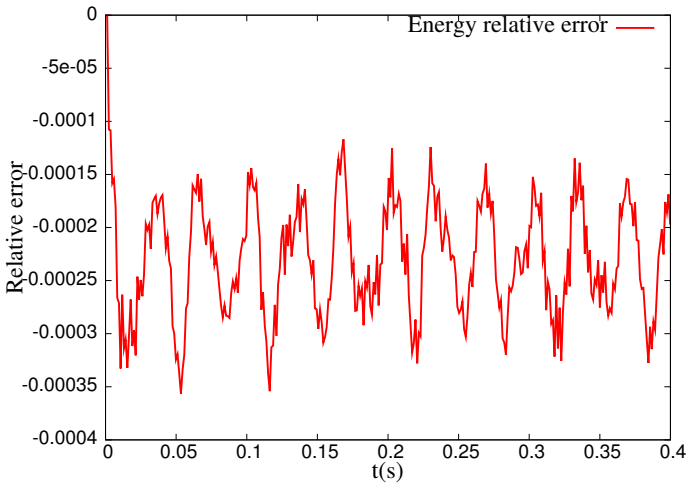

Fig. 3.10: Relative energy conservation error as a function of time.

3.5.2 Deformation of a cylinder filled with gas

In this test case, we simulate the effect of an explosion on a shell formed by a steel cylinder in two space dimensions. The cylinder is initially surrounded by gas at atmospheric pressure and contains gas at 0.1 bar. An overpressure region is initiated in the vicinity of the cylinder resulting in shock waves hitting the solid. This test case is designed to show the ability of the coupling scheme to handle physically relevant parameters and to give insight into the effect of shock waves on tubes filled with gas. This test case is a first step towards rupture test cases in three space dimensions.

The computational domain is the box $[0,\,30] \times [0,\,15]$m. The boundaries of the domain are outflow boundaries with Poinsot–Lele boundary conditions [87]. Initially, the state of the gas is:

$$\begin{cases} \rho = 1.18\text{kg.m}^{-3},\ \overrightarrow{u} = \overrightarrow{0}\,\text{m.s}^{-1},\ p = 101325\text{Pa}, \text{if}\,(x,y) \in D((20,7.5),5.1)\text{m}, \\ \rho = 99.93\text{kg.m}^{-3},\ \overrightarrow{u} = \overrightarrow{0}\,\text{m.s}^{-1},\ p = 50662500\text{Pa}, \text{if}\,(x,y) \in D((13,7.5),1)\text{m} \\ \rho = 0.118\text{kg.m}^{-3},\ \overrightarrow{u} = \overrightarrow{0}\,\text{m.s}^{-1},\ p = 10132.5\text{Pa}, \text{otherwise} \end{cases}$$

where $D((x_0,y_0),R)$ denotes the disk centered at (x_0,y_0) with radius R. The computation is performed on a 800×400 grid. The cylinder is centered at $(20,7.5)$m with a thickness of 0.1m and an interior radius of 5m. The density and the Young modulus are, respectively, $\rho_s = 7860\text{kg.m}^{-3}$ and $E = 210$Pa, with a Poisson ratio $\nu = 0$. The cylinder is discretized with 50 particles along its circumference and 1 particle in thickness. The simulation time is $t = 0.0244$s. In Fig. 3.11, we display the initial density field of the fluid and the initial position of the cylinder.

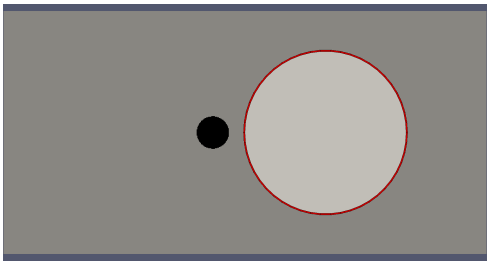

Fig. 3.11: Density profile in the fluid and cylinder position at time $t = 0$s.

After impacting the cylinder, the shock wave partially reflects on the solid and is partially transmitted by the solid to the confined underpressured gas. At the same time, the cylinder is deformed and pressure waves travel along its surface. We observe that the normal stress in the solid travel faster than those in the outer fluid, which in turn travel faster than those in the interior fluid due to the difference in pressures between the inside and the outside of the cylinder. In Fig. 3.12, we show the density field and the deformation of the solid at times 2×10^{-3}s, 4.7×10^{-3}s, 1×10^{-2}s, and 2.44×10^{-2}s. The circular rarefaction wave shed by the solid is caused

by the difference of pressure between the inner and outer field, as the cylinder is not initially at equilibrium. We observe a Richtmyer–Meshkov instability of the contact discontinuity. The cylinder is flattened in the region first impacted by the fluid shock waves. However, the traction inside the solid reaches a maximum at the point opposite to the explosion, due to interactions between the solid normal stress waves. We guess that this point would be at the highest risk of rupture. Indeed, in Fig. 3.13, we display the normal stress in the solid particle closest to the explosion and in the solid particle farthest to the explosion in the course of the simulation. We observe, for both particles, an initial increase of normal stress (compression) due to the impact of the explosion, followed by negative normal stress (traction) due to the relaxation of the solid after impact. Complex interaction between the travelling waves on the surface of the cylinder and the fluid then occur, accounting for successive compression and traction phenomena at both ends of the cylinder. In Fig. 3.14, we display the displacement of the center of mass of the solid particle closest to the explosion and of the solid particle farthest to the explosion in the course of the simulation. We observe that the displacement of the solid particle farthest to the explosion is very small, whereas that of the solid particle closest to the explosion is large. This accounts for the flattening of the cylinder near the explosion impact.

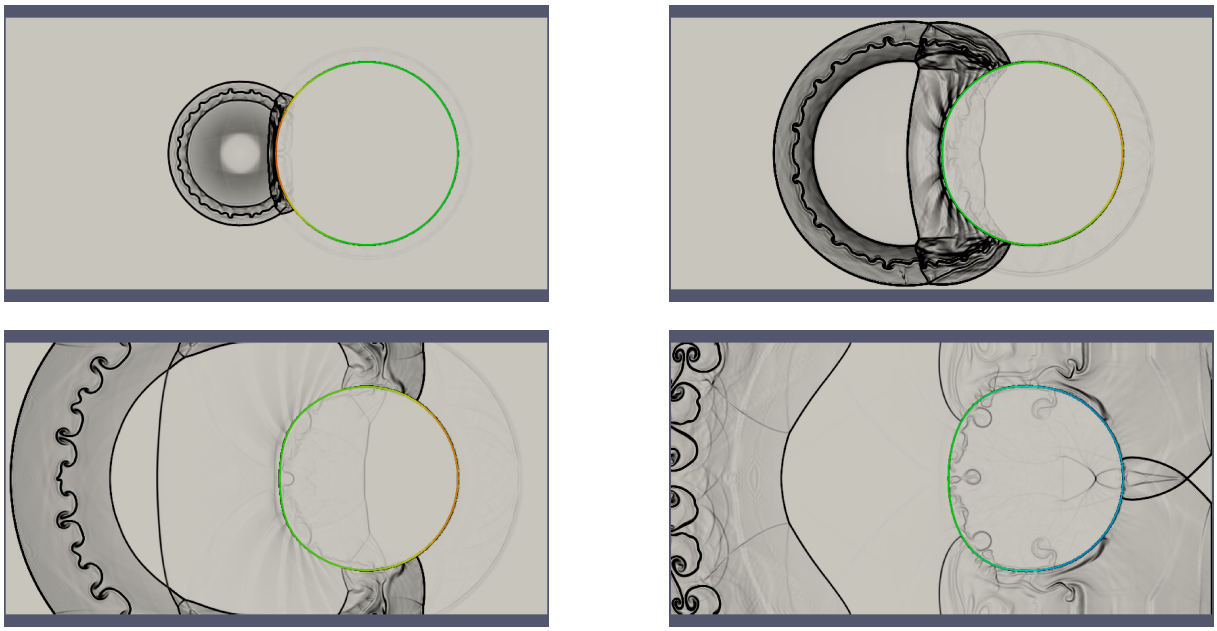

Fig. 3.12: Gradient density field in the fluid and normal stress distribution in the cylinder at four times: 2×10^{-3}s, 4.7×10^{-3}s, 1×10^{-2}s, and 2.44×10^{-2}s from left to right and top to bottom.

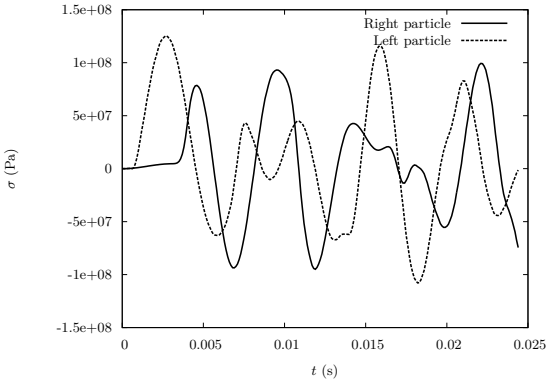

Fig. 3.13: Normal stress profile in the solid particle closest to the explosion (left particle) and in the solid particle farthest to the explosion (right particle) as a function of time.

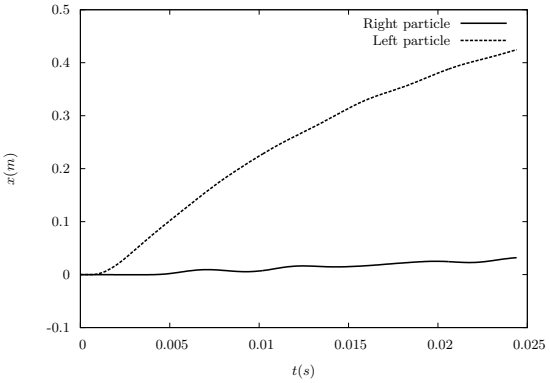

Fig. 3.14: x-coordinate of the center of mass of the solid particle closest to the explosion (left particle) and of the solid particle farthest to the explosion (right particle) as a function of time.

In Fig. 3.15, we present the normal stress in the cylinder at times 2×10^{-3}s, 4.7×10^{-3}s, 1×10^{-2}s, and 2.44×10^{-2}s as a function of the azimuthal angle θ in polar coordinates. At time 2×10^{-3}, we observe the overpressure initiated by the impacting shock wave. At time 4.7×10^{-3}, we observe the interaction at the right tip of the cylinder of the two normal stress waves travelling along the upper and lower parts of the cylinder. The profiles at the two other times result from increasingly complex interactions between pressure waves. We observe that all the solid particles evolve between compression and traction states. The normal stress patterns are symmetric with regards to $\theta = 0$ owing to the symmetry of the problem with respect to $y = 7.5$m. We observe a sequence of rarefaction waves in the vicinity of the cylinder at time 4.7×10^{-3}s in Fig. 3.12. This phenomenon is directly related to the solid discretization: each edge of the polygon approximating the circle generates a rarefaction wave in the fluid flow around the cylinder. Refining the solid discretization to 100 and 200 solid particles along the cylinder perimeter, we observe in Fig. 3.16 that the number of rarefaction waves increases as the discretization is refined. The fluid pressure profile as a function of the azimuthal angle θ displayed in Fig. 3.17 shows that the intensity of each rarefaction wave decreases as the solid discretization is refined. Let us note that the pressure jumps occur exactly at the edge of the solid particles. Apart from these local discrepancies, the pattern of the fluid flow structures does not change significantly as the solid is refined.

3.5.3 Deformable thin shell

In this test case, we consider the interaction of a shock wave with a two-dimensional deformable thin shell. This benchmark was first simulated in [43]. The computational domain is the rectangular box $[0, 1] \times [0, 0.2]$m and is discretized using a 640×128 grid. The shock is initially set

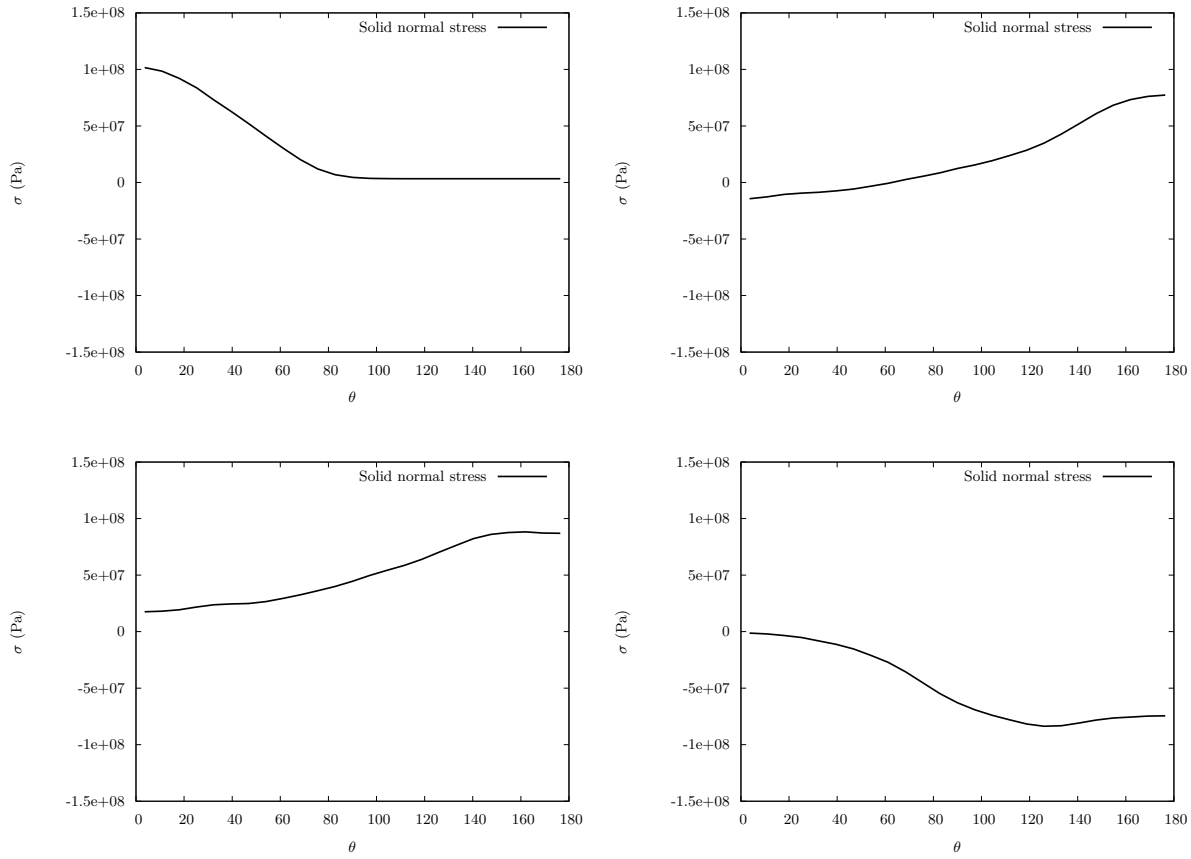

Fig. 3.15: Normal stress profile in the cylinder as a function of azimuthal angle at four times: 2×10^{-3}s, 4.7×10^{-3}s, 1×10^{-2}s, and 2.44×10^{-2}s from left to right and top to bottom.

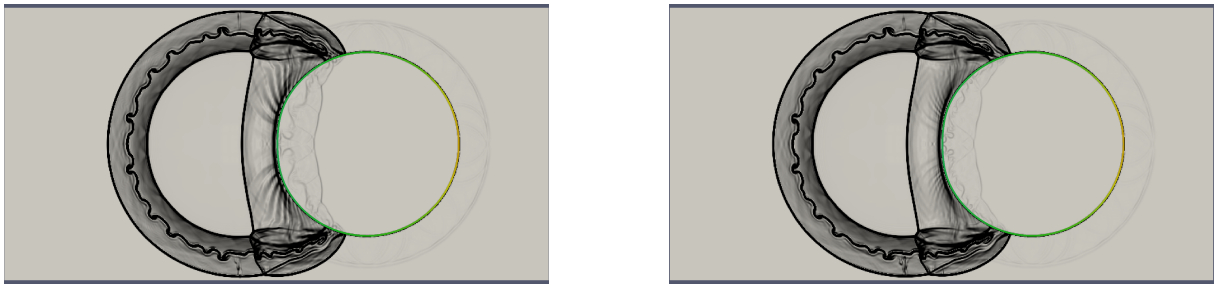

Fig. 3.16: Gradient density field in the fluid and normal stress distribution in the cylinder at time 4.7×10^{-3}s for 100 solid particles (left) and 200 solid particles (right).

up to a Mach number of 3, so that the initial values are

$$\begin{cases} \rho = 3.85 kg.m^{-3},\ p = 10.33 Pa,\ u = 2.69 m.s^{-1},\ v = 0 m.s^{-1}, & x < 0.475 m, \\ \rho = 1 kg.m^{-3},\ p = 1 Pa,\ \overrightarrow{u} = \overrightarrow{0}\, m.s^{-1}, & x \geq 0.475 m. \end{cases}$$

The thin shell is placed at $x = 0.5$m and its length is 0.1m. The thin shell has a density of $\rho_s = 0.0238$kg.m^{-3} and the solid particles links have a stiffness of $k = 2000$N.m^{-1}. The thin

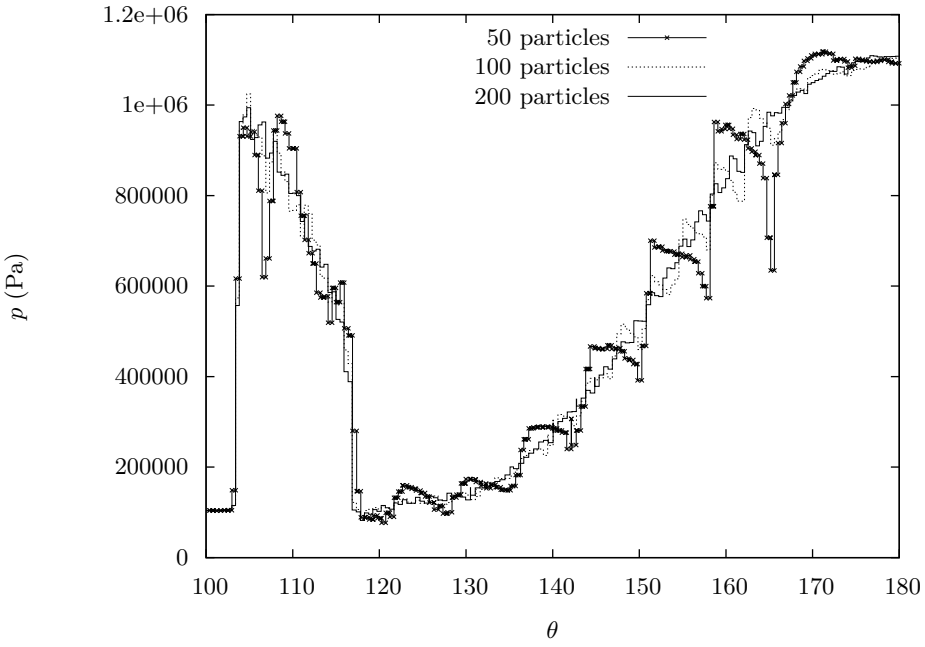

Fig. 3.17: Fluid pressure distribution along the cylinder at time 4.7×10^{-3}s for 50, 100, and 200 solid particles.

shell is discretized with 20 particles. The two extremal particles are fixed. The simulation time is $t = 0.35$s.

The impinging shock wave impacts the thin shell and is partially reflected to the left, while part of the shock wave moves over the thin shell and part of its energy is transferred as kinetic energy. At the same time, the thin shell is deformed due to the increase in pressure resulting in compression waves created by the movement of the thin shell. Complex interactions of waves occur due to solid movements and interaction with walls.

In Fig. 3.18, we show the density field and the deformation of the thin shell at times 0.07s, 0.14s, 0.21s, 0.28s, and 0.35s. Our results are in very good agreement with [43] (Figure 34) on the position of the solid and of the shocks (we use a four times coarser fluid grid, and the thin shell is discretized with the same number of particles).

3.6 Conclusion

We have developed a coupling method for the interaction between a three-dimensional inviscid compressible fluid flow and a deformable structure undergoing large displacements. The method hinges on a cut-cell Finite Volume method for the fluid and a symplectic Discrete Element method for the deformable solid. The coupling method is exactly mass-conservative and exhibits a long-time preservation of the energy for the coupled system. Moreover, the coupling is handled in a time semi-implicit fashion. The computational cost of the fluid and solid methods

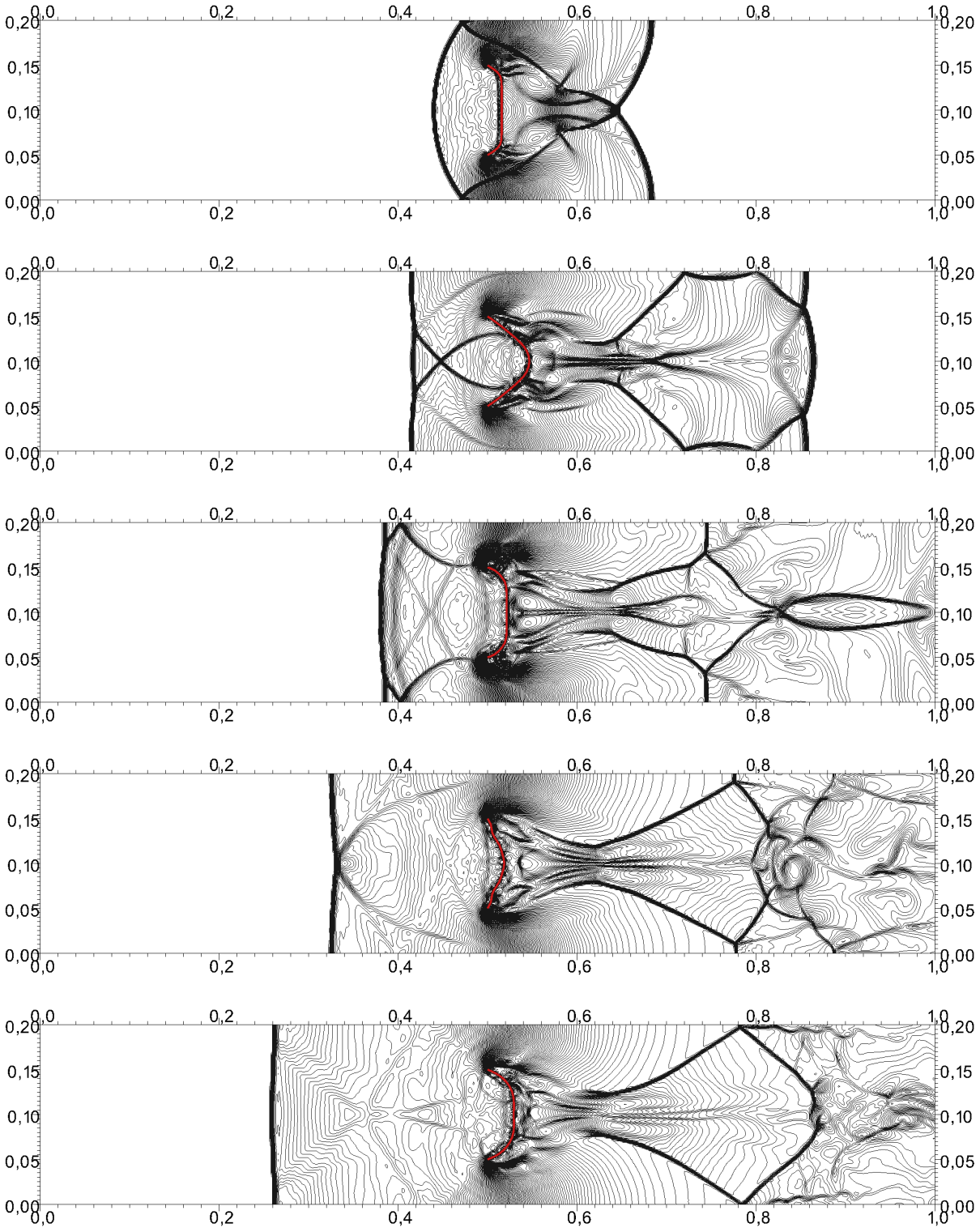

Fig. 3.18: Gradient density field in the fluid and solid deformation at five times: 0.07s, 0.14s, 0.21s, 0.28s, and 0.35s from top to bottom.

essentially results from the evaluation of fluxes on the fluid side and of forces and torques on the solid side. We emphasize that the coupling algorithm evaluates these only once per time step, ensuring computational efficiency. Regarding surface coupling, the algorithm overhead scales as the number of solid faces and as $N^{\frac{2}{3}}$, N being the number of fluid grid cells. In comparison, the fluid flux computation time scales as N.

The presented test cases allowed us to verify the main properties of the coupling scheme and to illustrate the robustness of the method in the case of two- and three-dimensional deformable solids with large displacements coupled to an inviscid compressible flow. The next step is to move on to more complex test cases and to enrich the modelling to take into account the possible fragmentation of the solid. This would require an adequate reconstruction of the solid boundary, an appropriate procedure to fill the ghost-cells, and the definition of a map (not necessarily bijective due to the possible opening of fractures) providing the correspondence from the position of the boundary at time t^n to its position at time t^{n+1}.

3.7 Appendix: The Discrete Element method

This appendix provides some background on the Discrete Element method. The set of neighbouring particles linked to particle I is denoted by τ_I. For each link between the particle I and a neighbouring particle $J \in \tau_I$, we denote by D_{IJ} the distance between these particles and by S_{IJ} the contact surface, see Fig. 3.19. Let $\overrightarrow{G}_{IJ}$, $\overrightarrow{n}_{IJ}$, I^s_{IJ}, and I^t_{IJ} be the center of mass, the exterior normal vector, and the principal moments of the contact surface. Two orthogonal vectors are defined at the contact surface, $\overrightarrow{s}_{IJ}$ and $\overrightarrow{t}_{IJ}$, forming an orthonormal basis with $\overrightarrow{n}_{IJ}$. The initial values of these quantities are denoted with the superscript 0.

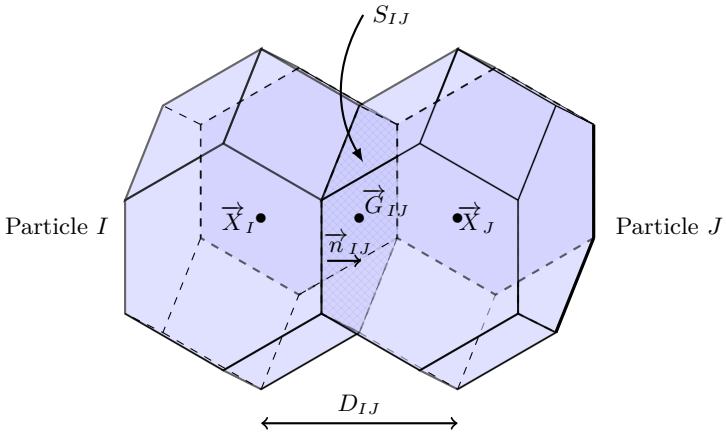

Fig. 3.19: Contact surface between particles

The forces and torques between particles are derived from an Hamiltonian formulation and are designed in order to recover at the macroscopic level a linear elasticity behavior [69, 81]. We

denote by E the Young modulus and by ν the Poisson ratio. The force between particles I and $J \in \tau_I$ is given by

$$\overrightarrow{F}_{IJ} = \overrightarrow{F}^n_{IJ} + \overrightarrow{F}^v_{IJ}, \tag{3.54}$$

where $\overrightarrow{F}^n_{IJ}$ is the shear-compression force and $\overrightarrow{F}^v_{IJ}$ the volumetric deformation force. The shear-compression force is given by

$$\overrightarrow{F}^n_{IJ} = \frac{S_{IJ}}{D^0_{IJ}} \frac{E}{1+\nu} \overrightarrow{\Delta u}_{IJ},$$

where $\overrightarrow{\Delta u}_{IJ} = \overrightarrow{X}_I - \overrightarrow{X}_J + \mathbf{Q}_J \cdot \overrightarrow{X}^0_J \overrightarrow{G}_{IJ} - \mathbf{Q}_I \cdot \overrightarrow{X}^0_I \overrightarrow{G}_{IJ}$ is the displacement vector to the contact surface between I and J. The volumetric deformation force is given by

$$\overrightarrow{F}^t_{IJ} = S_{IJ} \frac{E\nu}{(1+\nu)(1-2\nu)} \varepsilon^v_{IJ} \left(\overrightarrow{n}_{IJ} + \frac{1}{D_{IJ}} \overrightarrow{\Delta u}_{IJ} - \frac{1}{D_{IJ}} (\overrightarrow{\Delta u}_{IJ} \cdot \overrightarrow{n}_{IJ}) \overrightarrow{n}_{IJ} \right),$$

where the volumetric deformation of the link between I and J, $\varepsilon^v_{IJ} = \varepsilon^v_I + \varepsilon^v_J$, is the sum of the volumetric deformation of I and J, where:

$$\varepsilon^v_I = \sum_{J \in \tau_I} \frac{1}{2} \frac{S_{IJ}}{V_I + 3\frac{\nu}{1-2\nu} V^l_I} \overrightarrow{\Delta u}_{IJ} \cdot \overrightarrow{n}_{IJ},$$

where V_I and V^l_I are the volume and the free volume of the particle I respectively. The free volume of the particle I is defined as the sum of the volumes of all pyramidal polyhedra with a free surface as basis and X^0_I as summit. The torque between particles I and J is expressed as

$$\overrightarrow{\mathcal{M}}_{IJ} = \overrightarrow{\mathcal{M}}^t_{IJ} + \overrightarrow{\mathcal{M}}^f_{IJ}, \tag{3.55}$$

where $\overrightarrow{\mathcal{M}}^t_{IJ}$ denotes the torque of force $\overrightarrow{F}_{IJ}$ and $\overrightarrow{\mathcal{M}}^f_{IJ}$ denotes the flexion-torsion torque. The torque of force $\overrightarrow{F}_{IJ}$ is given by

$$\begin{aligned} \overrightarrow{\mathcal{M}}^t_{IJ} = & \frac{S_{IJ}}{D^0_{IJ}} \frac{E}{1+\nu} \left(\mathbf{Q}_I \cdot \overrightarrow{X}^0_I \overrightarrow{G}_{IJ} \right) \wedge \overrightarrow{\Delta u}_{IJ} \\ & + S_{IJ} \frac{E\nu}{(1+\nu)(1-2\nu)} \varepsilon^v_{IJ} \left(\mathbf{Q}_I \cdot \overrightarrow{X}^0_I \overrightarrow{G}_{IJ} \right) \wedge \overrightarrow{n}_{IJ}. \end{aligned}$$

The flexion-torsion torque $\overrightarrow{\mathcal{M}}^f_{IJ}$ is given by

$$\begin{aligned} \overrightarrow{\mathcal{M}}^f_{IJ} = & \frac{S_{IJ}}{D^0_{IJ}} (\alpha_n (\mathbf{Q}_I \cdot \overrightarrow{n}^0_{IJ}) \wedge (\mathbf{Q}_J \cdot \overrightarrow{n}^0_{IJ}) \\ & + \alpha_s (\mathbf{Q}_I \cdot \overrightarrow{s}_{IJ}) \wedge (\mathbf{Q}_J \cdot \overrightarrow{s}_{IJ}) + \alpha_t (\mathbf{Q}_I \cdot \overrightarrow{t}_{IJ}) \wedge (\mathbf{Q}_J \cdot \overrightarrow{t}_{IJ})). \end{aligned}$$

The coefficients α_n, α_s, and α_t are chosen so as to recover the exact flexion and torsion of a beam. For a detailed review on the expression of these forces and torques between particles see [69, 80, 81].

3.8 Appendix: Estimate on the Lagrange multiplier in terms of torque

In Section 3.4.2.4, we have estimated the control of the Lagrange multiplier $\boldsymbol{\Upsilon}$ by the torque $\overrightarrow{\mathcal{M}}$, see (3.53). Herein, we detail the proof of this result.

Using the expression (3.48), we infer that

$$\begin{aligned}\frac{\Delta t^4}{16}\|\overrightarrow{\mathcal{M}}_{I,\,\mathrm{fluid}}(\overrightarrow{X},\mathbf{Q})-\overrightarrow{\mathcal{M}}_{I,\,\mathrm{fluid}}(\overrightarrow{Y},\mathbf{R})\|_2^2 &= (d_2+d_3)^2(e_0e_1-f_0f_1)^2\\ &\quad+2(d_2+d_3)(d_2-d_3)(e_0e_1-f_0f_1)(e_2e_3-f_2f_3)\\ &\quad+(d_2-d_3)^2(e_2e_3-f_2f_3)^2+(d_1+d_3)^2(e_0e_2-f_0f_2)^2\\ &\quad+2(d_1+d_3)(d_3-d_1)(e_0e_2-f_0f_2)(e_1e_3-f_1f_3)\\ &\quad+(d_3-d_1)^2(e_1e_3-f_1f_3)^2+(d_1+d_2)^2(e_0e_3-f_0f_3)^2\\ &\quad+2(d_1+d_2)(d_1-d_2)(e_0e_3-f_0f_3)(e_1e_2-f_1f_2)\\ &\quad+(d_1-d_2)^2(e_1e_2-f_1f_2)^2,\end{aligned}\tag{3.56}$$

and using the expression (3.49), we obtain

$$\begin{aligned}\frac{\Delta t^4}{4}\|\boldsymbol{\Upsilon}_I(\overrightarrow{X},\mathbf{Q})-\boldsymbol{\Upsilon}_I(\overrightarrow{Y},\mathbf{R})\|_F^2 &= d_1^2(e_2^2+e_3^2-f_2^2-f_3^2)^2+2(d_1+d_2)^2(e_1e_2-f_1f_2)^2\\ &\quad+2(d_1-d_2)^2(e_0e_3-f_0f_3)^2\\ &\quad+4(d_1+d_2)(d_1-d_2)(e_1e_2-f_1f_2)(e_0e_3-f_0f_3)\\ &\quad+d_2^2(e_1^2+e_3^2-f_1^2-f_3^2)^2\\ &\quad+2(d_1+d_3)^2(e_1e_3-f_1f_3)^2\\ &\quad+4(d_1+d_3)(d_3-d_1)(e_1e_3-f_1f_3)(e_0e_2-f_0f_2)\\ &\quad+2(d_3-d_1)^2(e_0e_2-f_0f_2)^2+2(d_2+d_3)^2(e_2e_3-f_2f_3)^2\\ &\quad+4(d_2+d_3)(d_2-d_3)(e_2e_3-f_2f_3)(e_0e_1-f_0f_1)\\ &\quad+2(d_2-d_3)^2(e_0e_1-f_0f_1)^2\\ &\quad+d_3^2(e_1^2+e_2^2-f_1^2-f_2^2)^2.\end{aligned}$$

Observing that $(d_1+d_2)^2(e_1e_2-f_1f_2)^2=(d_1-d_2)^2(e_1e_2-f_1f_2)^2+4d_1d_2(e_1e_2-f_1f_2)^2$, yields

$$\begin{aligned}&\frac{\Delta t^4}{4}\|\boldsymbol{\Upsilon}_I(\overrightarrow{X},\mathbf{Q})-\boldsymbol{\Upsilon}_I(\overrightarrow{Y},\mathbf{R})\|_F^2-\frac{\Delta t^4}{8}\|\overrightarrow{\mathcal{M}}_{I,\,\mathrm{fluid}}(\overrightarrow{X},\mathbf{Q})-\overrightarrow{\mathcal{M}}_{I,\,\mathrm{fluid}}(\overrightarrow{Y},\mathbf{R})\|_2^2=\\ &\quad d_1^2(e_2^2+e_3^2-f_2^2-f_3^2)^2+8d_1d_2(e_1e_2-f_1f_2)^2-8d_1d_2(e_0e_3-f_0f_3)^2\\ &\quad+d_2^2(e_1^2+e_3^2-f_1^2-f_3^2)^2+8d_2d_3(e_2e_3-f_2f_3)^2-8d_2d_3(e_0e_1-f_0f_1)^2\\ &\quad+d_3^2(e_1^2+e_2^2-f_1^2-f_2^2)^2+8d_1d_3(e_1e_3-f_1f_3)^2-8d_1d_3(e_0e_2-f_0f_2)^2.\end{aligned}\tag{3.57}$$

Using (3.50) and (3.51), we infer that

$$(e_1e_2 - f_1f_2)^2 = (e_1(e_2 - f_2) + (e_1 - f_1)f_2)^2 \le 2\beta(e_1 - f_1)^2 + 2\beta(e_2 - f_2)^2, \tag{3.58}$$

$$(e_1e_3 - f_1f_3)^2 \le 2\beta(e_1 - f_1)^2 + 2\beta(e_3 - f_3)^2, \tag{3.59}$$

$$(e_2e_3 - f_2f_3)^2 \le 2\beta(e_2 - f_2)^2 + 2\beta(e_3 - f_3)^2. \tag{3.60}$$

Recalling (3.51) and (3.52) yields

$$\begin{aligned}(e_0e_1 - f_0f_1)^2 &= (e_0(e_1 - f_1) + f_1(f_0 - e_0))^2 \ge (e_0|e_1 - f_1| - |f_1| \times |e_0 - f_0|)^2 \\ &\ge \left(\sqrt{1-\beta} - \frac{\beta}{\sqrt{1-\beta}}\right)^2 (e_1 - f_1)^2 \ge \frac{(1-2\beta)^2}{1-\beta}(e_1 - f_1)^2.\end{aligned} \tag{3.61}$$

Using (3.61) and similar expressions leads to

$$(e_1 - f_1)^2 \le \frac{1-\beta}{(1-2\beta)^2}(e_0e_1 - f_0f_1)^2, \tag{3.62}$$

$$(e_2 - f_2)^2 \le \frac{1-\beta}{(1-2\beta)^2}(e_0e_2 - f_0f_2)^2, \tag{3.63}$$

$$(e_3 - f_3)^2 \le \frac{1-\beta}{(1-2\beta)^2}(e_0e_3 - f_0f_3)^2. \tag{3.64}$$

Using (3.58), (3.62), and (3.63), we infer that

$$\begin{aligned}8d_1d_2(e_1e_2 - f_1f_2)^2 &\le 8d_1d_2\left(2\beta(e_1 - f_1)^2 + 2\beta(e_2 - f_2)^2\right) \\ &\le 8d_1d_2\frac{2\beta(1-\beta)}{(1-2\beta)^2}\left((e_0e_1 - f_0f_1)^2 + (e_0e_2 - f_0f_2)^2\right).\end{aligned} \tag{3.65}$$

Using the above bound, we obtain

$$\begin{aligned}8d_1d_2(e_1e_2 - f_1f_2)^2 &+ 8d_2d_3(e_2e_3 - f_2f_3)^2 + 8d_1d_3(e_1e_3 - f_1f_3)^2 \\ &\le 8\frac{2\beta(1-\beta)}{(1-2\beta)^2}d_1(d_2 + d_3)(e_0e_1 - f_0f_1)^2 \\ &\quad + 8\frac{2\beta(1-\beta)}{(1-2\beta)^2}d_2(d_1 + d_3)(e_0e_2 - f_0f_2)^2 \\ &\quad + 8\frac{2\beta(1-\beta)}{(1-2\beta)^2}d_3(d_1 + d_2)(e_0e_3 - f_0f_3)^2.\end{aligned} \tag{3.66}$$

Using the bounds(3.50), (3.63), and (3.64) yields

$$\begin{aligned}d_1^2(e_2^2 + e_3^2 - f_2^2 - f_3^2)^2 &= d_1^2\left((e_2 - f_2)(e_2 + f_2) + (e_3 - f_3)(e_3 + f_3)\right)^2 \\ &\le d_1^2 8\beta\left((e_2 - f_2)^2 + (e_3 - f_3)^2\right) \\ &\le d_1^2 8\frac{\beta(1-\beta)}{(1-2\beta)^2}\left((e_0e_2 - f_0f_2)^2 + (e_0e_3 - f_0f_3)^2\right).\end{aligned}$$

Using the above bound and similar expressions, we obtain

$$\begin{aligned}d_1^2(e_2^2 + e_3^2 - f_2^2 - f_3^2)^2 &+ d_2^2(e_1^2 + e_3^2 - f_1^2 - f_3^2)^2 + d_3^2(e_1^2 + e_2^2 - f_1^2 - f_2^2)^2 \\ &\le 8\frac{\beta(1-\beta)}{(1-2\beta)^2}(d_1^2 + d_2^2)(e_0e_3 - f_0f_3)^2 \\ &\quad + 8\frac{\beta(1-\beta)}{(1-2\beta)^2}(d_1^2 + d_3^2)(e_0e_2 - f_0f_2)^2 \\ &\quad + 8\frac{\beta(1-\beta)}{(1-2\beta)^2}(d_2^2 + d_3^2)(e_0e_1 - f_0f_1)^2.\end{aligned} \tag{3.67}$$

Using the bounds (3.66) and (3.67) in (3.57) and dropping the terms of the form $-8d_1d_2(e_0e_3 - f_0f_3)^2$ yields

$$\begin{aligned}
&\frac{\Delta t^4}{4}\|\boldsymbol{\Upsilon}_I(\overrightarrow{X},\mathbf{Q}) - \boldsymbol{\Upsilon}_I(\overrightarrow{Y},\mathbf{R})\|_F^2 - \frac{\Delta t^4}{8}\|\overrightarrow{\mathcal{M}}_{I,\,\text{fluid}}(\overrightarrow{X},\mathbf{Q}) - \overrightarrow{\mathcal{M}}_{I,\,\text{fluid}}(\overrightarrow{Y},\mathbf{R})\|_2^2 \\
&\quad\le 8\frac{\beta(1-\beta)}{(1-2\beta)^2}(d_1^2+d_2^2)(e_0e_3 - f_0f_3)^2 + 8\frac{2\beta(1-\beta)}{(1-2\beta)^2}d_1(d_2+d_3)(e_0e_1 - f_0f_1)^2 \\
&\qquad + 8\frac{\beta(1-\beta)}{(1-2\beta)^2}(d_1^2+d_3^2)(e_0e_2 - f_0f_2)^2 + 8\frac{2\beta(1-\beta)}{(1-2\beta)^2}d_2(d_1+d_3)(e_0e_2 - f_0f_2)^2 \\
&\qquad + 8\frac{\beta(1-\beta)}{(1-2\beta)^2}(d_2^2+d_3^2)(e_0e_1 - f_0f_1)^2 + 8\frac{2\beta(1-\beta)}{(1-2\beta)^2}d_3(d_1+d_2)(e_0e_3 - f_0f_3)^2.
\end{aligned} \tag{3.68}$$

Without loss of generality, we assume that e_1 is such that $(d_2+d_3) \mid e_0e_1 - f_0f_1 \mid = \max_i\,(d_j + d_k) \mid \ e_0e_i - f_0f_i\ \mid, \{i,j,k\} \in \{1,2,3\}$. Using a reverse triangular inequality, the bound (3.65) and similar expressions, it follows that

$$\begin{aligned}
&\mid (d_2+d_3)(e_0e_1 - f_0f_1) + (d_2-d_3)(e_2e_3 - f_2f_3) \mid \\
&\qquad\qquad \ge (d_2+d_3) \mid e_0e_1 - f_0f_1 \mid - \mid d_2 - d_3 \mid \times \mid e_2e_3 - f_2f_3) \mid \\
&\qquad\qquad \ge (d_2+d_3) \mid e_0e_1 - f_0f_1 \mid \\
&\qquad\qquad\quad - \mid d_2 - d_3 \mid \frac{\sqrt{2\beta}\sqrt{1-\beta}}{1-2\beta}\,(\mid e_0e_2 - f_0f_2 \mid - \mid e_0e_3 - f_0f_3 \mid) \\
&\qquad\qquad \ge \left(1 - \frac{\sqrt{8\beta}\sqrt{1-\beta}}{1-2\beta}\right)(d_2+d_3) \mid e_0e_1 - f_0f_1 \mid,
\end{aligned} \tag{3.69}$$

since $\mid d_2 - d_3 \mid \le d_2 + d_3$ and similar expressions. Squaring (3.69) yields

$$\begin{aligned}
(d_2+d_3)^2(e_0e_1 - f_0f_1)^2 &+ 2(d_2+d_3)(d_2-d_3)(e_0e_1 - f_0f_1)(e_2e_3 - f_2f_3) \\
&+ (d_2-d_3)^2(e_2e_3 - f_2f_3)^2 \\
&\ge (d_2+d_3)^2\left(1 - \frac{\sqrt{8\beta}\sqrt{1-\beta}}{1-2\beta}\right)^2(e_0e_1 - f_0f_1)^2.
\end{aligned}$$

Injecting this bound in (3.56), we deduce that the torque matrices verify

$$\frac{\Delta t^4}{16}\|\overrightarrow{\mathcal{M}}_{I,\,\text{fluid}}(\overrightarrow{X},\mathbf{Q}) - \overrightarrow{\mathcal{M}}_{I,\,\text{fluid}}(\overrightarrow{Y},\mathbf{R})\|_2^2 \ge (d_2+d_3)^2\left(1 - \frac{\sqrt{8\beta}\sqrt{1-\beta}}{1-2\beta}\right)^2(e_0e_1 - f_0f_1)^2. \tag{3.70}$$

Recalling that $\beta = \frac{1}{4}(2 - \sqrt{2+\sqrt{2}})$ we obtain $8\dfrac{\beta(1-\beta)}{(1-2\beta)^2}\dfrac{1}{\left(1 - \frac{\sqrt{8\beta}\sqrt{1-\beta}}{1-2\beta}\right)^2} = 2$. Using the bound (3.70) in (3.68), we infer that

$$
\begin{aligned}
&\frac{\Delta t^4}{4}\|\boldsymbol{\Upsilon}_I(\overrightarrow{X},\mathbf{Q})-\boldsymbol{\Upsilon}_I(\overrightarrow{Y},\mathbf{R})\|_F^2-\frac{\Delta t^4}{8}\|\overrightarrow{\mathcal{M}}_{I,\,\mathrm{fluid}}(\overrightarrow{X},\mathbf{Q})-\overrightarrow{\mathcal{M}}_{I,\,\mathrm{fluid}}(\overrightarrow{Y},\mathbf{R})\|_2^2\\
&\leq 3\times 2\frac{\Delta t^4}{16}\|\overrightarrow{\mathcal{M}}_{I,\,\mathrm{fluid}}(\overrightarrow{X},\mathbf{Q})-\overrightarrow{\mathcal{M}}_{I,\,\mathrm{fluid}}(\overrightarrow{Y},\mathbf{R})\|_2^2\\
&\quad+8\frac{2\beta(1-\beta)}{(1-2\beta)^2}(d_1+d_2+d_3)(d_2+d_3)(e_0e_1-f_0f_1)^2\\
&\leq\left(3+2\frac{d_1+d_2+d_3}{d_2+d_3}\right)\frac{\Delta t^4}{8}\|\overrightarrow{\mathcal{M}}_{I,\,\mathrm{fluid}}(\overrightarrow{X},\mathbf{Q})-\overrightarrow{\mathcal{M}}_{I,\,\mathrm{fluid}}(\overrightarrow{Y},\mathbf{R})\|_2^2\\
&\leq\left(5+\frac{2d_1}{d_2+d_3}\right)\frac{\Delta t^4}{8}\|\overrightarrow{\mathcal{M}}_{I,\,\mathrm{fluid}}(\overrightarrow{X},\mathbf{Q})-\overrightarrow{\mathcal{M}}_{I,\,\mathrm{fluid}}(\overrightarrow{Y},\mathbf{R})\|_2^2.
\end{aligned}
$$

As a result, the Lagrange multipliers are bounded as

$$
\begin{aligned}
\|\boldsymbol{\Upsilon}_I(\overrightarrow{X},\mathbf{Q})-\boldsymbol{\Upsilon}_I(\overrightarrow{Y},\mathbf{R})\|_F^2&\leq\frac{1}{2}\left[\left(5+\frac{2d_1}{d_2+d_3}\right)+1\right]\|\overrightarrow{\mathcal{M}}_{I,\,\mathrm{fluid}}(\overrightarrow{X},\mathbf{Q})-\overrightarrow{\mathcal{M}}_{I,\,\mathrm{fluid}}(\overrightarrow{Y},\mathbf{R})\|_2^2\\
&\leq\frac{1}{2}\left(6+\frac{d_{\max}}{d_{\min}}\right)\|\overrightarrow{\mathcal{M}}_{I,\,\mathrm{fluid}}(\overrightarrow{X},\mathbf{Q})-\overrightarrow{\mathcal{M}}_{I,\,\mathrm{fluid}}(\overrightarrow{Y},\mathbf{R})\|_2^2.
\end{aligned}
$$

Finally, using (3.27) to bound $\mathbf{D}_I$, the Lagrange multipliers verify

$$
\|\boldsymbol{\Upsilon}_I(\overrightarrow{X},\mathbf{Q})-\boldsymbol{\Upsilon}_I(\overrightarrow{Y},\mathbf{R})\|_F^2\leq\left(3+\frac{1}{2}\frac{h_{s,I}^5}{\sigma_{s,I}^5}\right)\|\overrightarrow{\mathcal{M}}_{I,\,\mathrm{fluid}}(\overrightarrow{X},\mathbf{Q})-\overrightarrow{\mathcal{M}}_{I,\,\mathrm{fluid}}(\overrightarrow{Y},\mathbf{R})\|_2^2.
$$

4

A conservative Immersed Boundary method for an inviscid compressible flow coupled with a fragmenting structure

This chapter is submitted to International Journal for Numerical Methods in Engineering [90].

4.1 Introduction

In this chapter, we are interested in the interaction of a shocked fluid with a fragmenting structure. The characteristic time scales of these phenomena are extremely short. The driving effect is the fluid overpressure, and viscous effects play a lesser role in the dynamics of system, so that we consider an inviscid fluid. An important class of methods for fluid-structure interaction hinges on a partitioned approach, where the fluid and the solid equations are solved separately, and an interface module is used to exchange information between the fluid and the solid solvers. Two main types of methods have been developed in this context: Arbitrary Lagrangian-Eulerian (ALE) methods [24, 65] and fictitious domain methods [20, 27, 30, 33, 35, 85, 106]. The ALE

method deforms the fluid domain in order to follow the movement of the structure. This method hinges on a mesh fitting the solid boundaries, and this often involves costly remeshing of the fluid domain when the solid goes through large displacements or fragmentation. Fictitious domain methods work on a fixed fluid grid. The solid is superimposed to the fluid grid, and additional terms are introduced in the fluid solver to impose the fluid boundary conditions at the solid boundary. Such methods can treat large displacements of the solid and changes in the topology of the fluid domain without remeshing. Various types of fictitious domain methods have been proposed. In particular, Conservative Immersed Boundary methods [17, 31, 50, 52, 84, 97] have been developed for elliptic problems and compressible fluids, so that the spatial discretization conserves mass, momentum, and energy.

Coupling fluids with fragmenting structures has already been addressed in the literature. An Immersed Boundary approach for a fluid interacting with a fracturing and fragmenting thin shell was developed in [15, 21]. The method couples a Lagrangian fragmenting thin shell discretized by a Finite Element method and an Eulerian fluid flow discretized by a Finite Volume method on a Cartesian grid. This method uses a Level Set approach to track the immersed solid surface, and a Ghost Fluid method to impose the boundary conditions at the fluid-structure interface. The thin shell fracture criterion is based on a cohesive interface method and uses pre-fractured elements to model the fracture, so that the knowledge of where the fracture will occur is required. An Immersed Particle method [102] was used in [92] for the interaction of a compressible fluid with a fragmenting thin shell, without a priori knowledge of the fracture location. The fracture is modelled by a cracking particle method using a local partition of unity. This method treats both fluid and structure by meshfree particle methods, and the solid is immersed in the fluid. The fluid model is Lagrangian and for very large deformation situations, a reinitialization of the fluid particles is necessary (defaulting energy conservation). Another Immersed Boundary approach for the interaction between a compressible flow and a fragmenting thin shell was developed in [66], also without a priori knowledge of the fracture location. The fluid is discretized using a Finite Volume method. The method for the fragmenting structure combines an Extended Finite Element method (X-FEM) [23, 101] with cohesive law and element deletion.

In this chapter, we develop a conservative method for the three-dimensional interaction between an inviscid fluid and a fragmenting structure. On the fluid side, we consider an inviscid Euler fluid in conservative form discretized using a high-order monotonicity-preserving Finite Volume method with directional operator splitting [18]. On the solid side, we consider a fragmenting solid discretized with the Discrete Element method [81]. This method discretized the solid using particles, and each particle is governed by the classical equations of mechanics. The particles interact through forces and torques. The Discrete Element method treats naturally fragmentation by breaking links between particles and does not need remeshing of the domain. This leads to an effective method for the study of dynamic fragmentation phenomena. A conservative time-explicit coupling algorithm between an inviscid fluid and a three-dimensional rigid or deformable solid without fragmentation was developed in [91, 89], using a conservative Immersed Boundary

technique. Herein, we extend the coupling method of [91, 89] to include the fragmentation of the solid.

In the Discrete Element method, the fracture propagates element by element using a fracture criterion defined at the contact faces between particles. The coupling method is independent of the breaking criterion used in the solid solver in order to break the link between particles. In the present work, we focus on the feasibility study of the coupling method to deal with fragmentation, so that it is sufficient at this stage to employ a simple model for the breaking criterion based on a maximal elongation of particles link.

During the process of fragmentation, vacuum between solid particles can occur due to internal solid fragmentation and to the fact that the velocity of the crack propagation can be larger than the speed of sound in the fluid. This leads to fluid cells where the fluid pressure and the density are zero or very low. We consider the Lax–Friedrichs numerical flux near the vacuum area in order to avoid division by pressure or density. The Lax–Friedrichs flux is able to compute a stable approximation to the Riemann problem in the presence of vacuum [105]. Away from the vacuum, the high-order flux from [18] is used. Furthermore, the coupling algorithm is based on an explicit time-marching procedure. The algorithm does not require remeshing and allows fluid to pass through the opened areas of the structure without any a priori knowledge of where fragmentation occurs. The method deals with three-dimensional solids, and as in the case without fragmentation, the method yields conservation of mass, momentum, and energy of the system. One limitation of the present method is that is does not take into account the possible contact between particles during the ballistic flight after fragmentation.

The paper is organized as follows. In Section 2, we present a brief review in the modelling and simulation of the fragmentation process. In Section 3, we briefly set the notation and recall the conservative coupling method without solid fragmentation. In Section 4, we present the conservative coupling method with fragmentation. In Section 5, we discuss numerical results. Finally, conclusions are drawn in Section 6.

4.2 Solid fragmentation

The solid fracture is the process by which the solid is separated into two or more pieces due to stresses and strains. In the solid fragmentation process, the solid is divided into a large number of small pieces. In the fracture process we can distinguish two steps: initialization and propagation. Irwin [57] proposed a classification of several ways a force may be applied to a solid causing fracture propagation, leading to three modes: the opening mode defined by an elastic stress acting normally to the plane of the crack (mode I), the sliding mode defined by a shear stress acting tangentially to the plane of the crack and perpendicularly to the fracture front (mode II), and the tearing mode defined by a shear stress acting tangentially both to the plane

of the fracture and to the fracture front (mode III). Fracture propagation generally involves a combination of the three modes.

The mechanisms involved in fracturing phenomena depend on the solid material and the type of applied efforts. Depending on the ability of the material to undergo plastic deformation, two fracture processes can be distinguished: brittle and ductile fracture. In brittle materials (ceramics, ice, ...), little plastic deformation occurs, and the fracture propagates rapidly without a significant increase in the applied stress. In ductile materials (most metals), extensive plastic deformation occurs, and further fracture propagation occurs only if the applied stress is increased.

Modelling fracture initialisation and propagation raises the question of how to take into account complex phenomena such as overheating, plasticity, ... In general, the models do not describe at this level of detail the processes that lead to the creation and propagation of the fracture. Generally, the fracturing process is reduced to a law or a criterion, such as the propagation criterion models [13, 64], the cohesive area models [16, 29], the damage volume models [22, 72], the variational models [8], etc. The well-known Griffith fracture model [45] is based on an energy balance which states that there is a balance between the elastic strain energy decrease in the solid and the surface energy increase due to the creation of the fracture.

In the case of Griffith fracture model [45] for a linear elastic material, a theoretical analysis shows that the limiting fracture speed for mode I fracture is the Rayleigh wave speed [9, 26, 39], which can be estimated by the following expression [26, 39]

$$c_R = c_s \frac{0.862 + 1.14\nu}{1+\nu},$$

where ν is the Poisson ratio. The compression wave speed c_p (a wave in which the disturbance is a compression of the medium) and the shear wave speed c_s (a wave in which the disturbance is an elastic deformation perpendicular to the direction of motion of the wave) are given by following formulas:

$$c_p = \sqrt{\frac{E(1-\nu)}{\rho(1+\nu)(1-2\nu)}}, \quad c_s = \sqrt{\frac{E}{2\rho(1+\nu)}},$$

where E is the Young modulus. For mode II and mode III, limiting speeds are the compression and shear wave speed, respectively [9, 26, 39].

Numerical methods used for simulation of solid fragmentation can generally be classified into two categories. The first is given by numerical methods using a mesh of the domain. The most popular example is Finite Element methods. These methods require remeshing of the domain when the fracture propagates. Extended Finite Element methods (X-FEM) [23, 88, 101] and cohesive methods [77] have been developed to avoid the remeshing of the domain. Integral equation methods [59] only need the remeshing of the boundary of the domain. The second category is given by meshfree methods. These methods model the materials using a set of discrete interacting particles. Thus, the solid domain is composed of linked particles. A large number of particles

must be used in order to model the material behaviour accurately. The complexity consists in the expression of these forces and moments. When two particles are in contact, it is necessary to define interaction law between them in terms of forces and moments. Meshfree methods treat naturally fracture, large displacement, dynamic fragmentation, and contact problems. The most popular methods in this category are Smooth Particle Hydrodynamics [70, 78, 93], Discrete Element methods [69, 81], and Lattice models [68, 96].

4.3 Coupling without fragmentation

4.3.1 Fluid discretization

The inviscid compressible flow is modelled by the Euler equations. The equations are written in conservative form expressing conservation of mass, momentum, and energy as follows:

$$\frac{\partial}{\partial t}U + \frac{\partial}{\partial x}F(U) + \frac{\partial}{\partial y}G(U) + \frac{\partial}{\partial z}H(U) = 0, \tag{4.1}$$

where $U = (\rho, \rho u, \rho v, \rho w, \rho E)^t$ with ρ the mass density, p the pressure, (u, v, w) the Cartesian components of the velocity vector $\overrightarrow{u}$, and E the total energy. The pressure is modelled by the state equation of a perfect gas: $p = \rho\,(\gamma - 1)\left(E - \frac{1}{2}(u^2 + v^2 + w^2)\right)$, $\gamma = 1.4$ being the ratio of specific heats, assumed to be constant. The flux functions are given by

$$F(U) = \begin{pmatrix} \rho u \\ \rho u^2 + p \\ \rho uv \\ \rho uw \\ (\rho E + p)u \end{pmatrix}, G(U) = \begin{pmatrix} \rho v \\ \rho uv \\ \rho v^2 + p \\ \rho vw \\ (\rho E + p)v \end{pmatrix}, H(U) = \begin{pmatrix} \rho w \\ \rho uw \\ \rho vw \\ \rho w^2 + p \\ (\rho E + p)w \end{pmatrix},$$

4.3.1.1 Fluid grid

In Immersed Boundary methods, the solid is superimposed to the fluid grid. As a result, some cells of the fluid grid are masked by the solid and are named “solid cells", some others are completely included in the flow domain and are called “fluid cells", and the remaining ones are intersected by the surface of the solid and are referred to as “cut cells" (see Fig. 4.1). We denote by $\Omega_{\text{Solid}}(t)$ the solid domain and by $\Omega_{\text{Fluid}}(t)$ the fluid domain.

We consider a Cartesian fluid grid, and we denote with integer subscripts i, j, k quantities related to the center of cells and with half-integer subscripts quantities related to the center of faces of cells. For instance, the interface between cells $C_{i,j,k}$ and $C_{i+1,j,k}$ is denoted by $\partial C_{i+\frac{1}{2},j,k}$. The relevant geometric quantities describing the intersection between the moving solid and the cut cell $C_{i,j,k}$ are:

– The **volume fraction** $0 \leqslant \Lambda^n_{i,j,k} \leqslant 1$ occupied by the solid in the cell $C_{i,j,k}$ at time t^n.

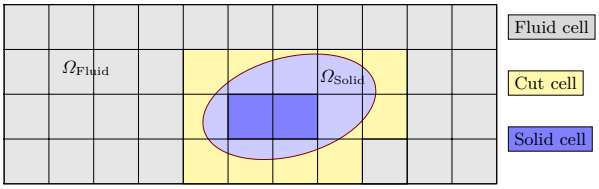

Fig. 4.1: Solid superimposed to the fluid grid

– The **side area fractions** $0 \leqslant \lambda^n_{i\pm\frac{1}{2},j,k}, \lambda^n_{i,j\pm\frac{1}{2},k}, \lambda^n_{i,j,k\pm\frac{1}{2}} \leqslant 1$ of each cell face at time t^n.

The three-dimensional geometric algorithms used for the detection of the cut cells and the computation of the intersection between the solid and the fluid grid are described in [89].

In the explicit Finite Volume scheme, the time-step, denoted by Δt, is subjected to the following CFL stability condition:

$$\Delta t < \min_{i,j,k} \left(\frac{\Delta x_{i,j,k}}{|\overrightarrow{u}_{i,j,k}| + c_{i,j,k}} \right), \tag{4.2}$$

where c is the speed of sound in the fluid, $c^2 = \dfrac{\gamma p}{\rho}$. The time-step is taken constant for simplicity. We introduce the discrete times $t^n = n\Delta t$, for all $n \geq 0$.

4.3.1.2 Fluid cells

Let $C_{i,j,k}$ be a fluid cell ($\Lambda^{n+1}_{i,j,k} = 0$) of size ($\Delta x_{i,j,k}$, $\Delta y_{i,j,k}$, $\Delta z_{i,j,k}$). The Finite Volume formulation takes the form

$$U^{n+1}_{i,j,k} = U^n_{i,j,k} + \Delta t\, \Phi^n_{i,j,k\,\text{fluid}}, \tag{4.3}$$

with the flux $\Phi^n_{i,j,k\,\text{fluid}}$ given by

$$\Phi^n_{i,j,k\,\text{fluid}} = \frac{F^n_{i-1/2,j,k} - F^n_{i+1/2,j,k}}{\Delta x_{i,j,k}} + \frac{G^n_{i,j-1/2,k} - G^n_{i,j+1/2,k}}{\Delta y_{i,j,k}} + \frac{H^n_{i,j,k-1/2} - H^n_{i,j,k+1/2}}{\Delta z_{i,j,k}}, \tag{4.4}$$

where $U^n_{i,j,k}$ is the numerical approximation of the exact solution over the cell $C_{i,j,k}$ at time t^n, and $F^n_{i\pm1/2,j,k}, G^n_{i,j\pm1/2,k}, H^n_{i,j,k\pm1/2}$ are numerical fluxes approximating the time-average of the corresponding physical flux over the time interval $[t^n, t^{n+1}]$ and evaluated at $\partial C_{i\pm\frac{1}{2},j,k}$, $\partial C_{i,j\pm\frac{1}{2},k}$, and $\partial C_{i,j,k\pm\frac{1}{2}}$, respectively. We use the unidimensional One-Step Monotonicity-Preserving (OSMP) high-order scheme [18]. This scheme is derived using a coupled space-time Lax–Wendroff approach, where the formal order of accuracy in the scalar case can be set to an arbitrary order. In the present work, we use order 11. The extension to the multidimensional case is made with a directional operator splitting consisting in solving alternately the one-dimensional problem in each direction [100]. Let L_x, L_y, L_z denote the operators corresponding to the integration over a time-step Δt in the x, y, and z directions, respectively. For instance,

$$L_x(\Delta t)W = W - \Delta t \left(\frac{F_{i+\frac{1}{2},j,k}(W) - F_{i-\frac{1}{2},j,k}(W)}{\Delta x} \right).$$

Then, we define, for example

$$U^{n+1}_{i,j,k} = L_x(\Delta t) L_y(\Delta t) L_z(\Delta t)\, U^n_{i,j,k}.$$

Formal second-order time accuracy is recovered every six time-steps (corresponding to all L_x, L_y, and L_z permutations) if the directional operators do not commute [18]. Finally, we denote by $\overline{p}^n_x$, $\overline{p}^n_y$, and $\overline{p}^n_z$ the pressures used in the application of the operators L_x, L_y, and L_z respectively. These quantities are used in the fluid-structure coupling.

4.3.1.3 Cut cells

We take into account the position of the solid in the fluid domain by modifying (4.3) in the cut cells. In a cut cell $C_{i,j,k}$ ($0 < \Lambda^{n+1}_{i,j,k} < 1$), we consider the following approximation of (4.1):

$$\left(1 - \Lambda^{n+1}_{i,j,k}\right) U^{n+1}_{i,j,k} = \left(1 - \Lambda^{n+1}_{i,j,k}\right) U^n_{i,j,k} + \Delta t\, \Phi^n_{i,j,k,\,\text{fluid}} + \Delta t\, \Phi^n_{i,j,k,\,\text{solid}} + \Delta U^{n,n+1}_{i,j,k}, \tag{4.5}$$

where the fluid flux $\Phi^n_{i,j,k,\,\text{fluid}}$ is now given by (compare with (4.4))

$$\begin{aligned} \Phi^n_{i,j,k,\,\text{fluid}} = & \frac{\left(1 - \lambda^{n+1}_{i-\frac{1}{2},j,k}\right) F^n_{i-\frac{1}{2},j,k} - \left(1 - \lambda^{n+1}_{i+\frac{1}{2},j,k}\right) F^n_{i+\frac{1}{2},j,k}}{\Delta x_{i,j,k}} \\ & + \frac{\left(1 - \lambda^{n+1}_{i,j-\frac{1}{2},k}\right) G^n_{i,j-\frac{1}{2},k} - \left(1 - \lambda^{n+1}_{i,j+\frac{1}{2},k}\right) G^n_{i,j+\frac{1}{2},k}}{\Delta y_{i,j,k}} \\ & + \frac{\left(1 - \lambda^{n+1}_{i,j,k-\frac{1}{2}}\right) H^n_{i,j,k-\frac{1}{2}} - \left(1 - \lambda^{n+1}_{i,j,k+\frac{1}{2}}\right) H^n_{i,j,k+\frac{1}{2}}}{\Delta z_{i,j,k}}. \end{aligned} \tag{4.6}$$

The solid flux $\Phi^n_{i,j,k,\,\text{solid}}$ resulting from the presence of the solid boundaries in the cut cell and the swept amount $\Delta U^{n,n+1}_{i,j,k}$ are detailed in Section 4.3.3.

One possible difficulty with Immersed Boundary methods is that they can involve "small cut-cells" in which the solid volume fraction is greater than, say, 0.5. In order to ensure the CFL stability condition of the fluid scheme on these cells, the time-step should be decreased to an unacceptably small value:

$$\Delta t < \min_{i,j,k} \left(\frac{(1 - \Lambda_{i,j,k})\Delta x_{i,j,k}}{|\overrightarrow{u}_{i,j,k}| + c_{i,j,k}} \right),$$

Several approaches are available to ensure stability without a drastic reduction of the time-step and at the same time preserve the conservation properties of the scheme. For example, [31]

suggests merging small cut-cells with a neighboring fluid cell. Since it is not always possible to find for each small cut-cell a neighboring fluid cell, a conservative mixing of the cut cell with a fluid cell, found in the direction of the outward normal to the solid boundary present in the cut cell is proposed in [52]. Let p be a small cut-cell and let g be the fluid cell in question ($\Lambda_g = 0$). The mixing procedure consists in defining the following exchange terms:

$$E_{pg} = \frac{1}{(2-\Lambda_p)}(U_g - U_p), \quad E_{gp} = \frac{(1-\Lambda_p)}{(2-\Lambda_p)}(U_p - U_g),$$

and setting $U_p \leftarrow U_p + E_{pg}, \quad U_g \leftarrow U_g + E_{gp}$. The mixing procedure is conservative since $(1-\Lambda_p)E_{pg} + E_{gp} = 0$.

4.3.1.4 Solid cells

The stencil used in the OSMP flux function can overlap with the solid. Near the solid, the states needed to calculate the fluid fluxes may be located in cells completely occupied by the solid (solid cells, $\Lambda = 1$). In this situation, we define within these cells an artificial fluid state from the states associated with the mirror cells relatively to the fluid-solid interface.

4.3.2 Solid discretization

The deformable moving solid is discretized by the Discrete Element method using a finite number of rigid particles (Fig. 4.2). Each particle is governed by the classical equations of mechanics. The particles interact through forces and torques. The expression of these forces and torques allows one to recover the macroscopic behavior of the solid [69, 81].

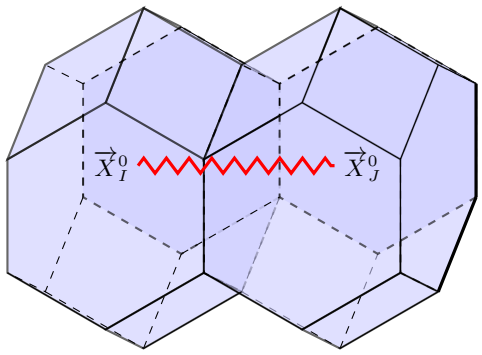

Fig. 4.2: Solid discretization

4.3.2.1 Numerical scheme

Various quantities are attached to a generic solid particle I, namely the mass m_I, the position of the center of mass $\overrightarrow{X}_I$, the velocity of the center of mass $\overrightarrow{V}_I$, the rotation matrix $\mathbf{Q}_I$,

the angular momentum matrix $\mathbf{P}_I$, and the principal moments of inertia I_I^i, $i \in \{1,2,3\}$. Let $\mathbf{D}_I = \mathrm{diag}(d_I^1, d_I^2, d_I^3)$ with $d_I^i = \frac{1}{2}\left(I_I^1 + I_I^2 + I_I^3\right) - I_I^i$, $i \in \{1,2,3\}$. The explicit time-integration scheme for the solid consists of the Verlet scheme for translation and the RATTLE scheme for rotation. For particle I, it takes the following form:

$$\overrightarrow{V}_I^{n+\frac{1}{2}} = \overrightarrow{V}_I^n + \frac{\Delta t}{2m_I}(\overrightarrow{F}_{I,\mathrm{int}}^n + \overrightarrow{F}_{I,\mathrm{fluid}}^n), \tag{4.7}$$

$$\overrightarrow{X}_I^{n+1} = \overrightarrow{X}_I^n + \Delta t \overrightarrow{V}_I^{n+\frac{1}{2}}, \tag{4.8}$$

$$\mathbf{P}_I^{n+\frac{1}{2}} = \mathbf{P}_I^n + \frac{\Delta t}{4}\mathbf{j}(\overrightarrow{\mathcal{M}}_{I,\mathrm{int}}^n + \overrightarrow{\mathcal{M}}_{I,\mathrm{fluid}}^n)\mathbf{Q}_I^n + \frac{\Delta t}{2}\boldsymbol{\Upsilon}_I^n\mathbf{Q}_I^n, \tag{4.9}$$

$$\mathbf{Q}_I^{n+1} = \mathbf{Q}_I^n + \Delta t \mathbf{P}_I^{n+\frac{1}{2}}\mathbf{D}_I^{-1}, \tag{4.10}$$

$$\overrightarrow{V}_I^{n+1} = \overrightarrow{V}_I^{n+\frac{1}{2}} + \frac{\Delta t}{2m_I}(\overrightarrow{F}_{I,\mathrm{int}}^{n+1} + \overrightarrow{F}_{I,\mathrm{fluid}}^n), \tag{4.11}$$

$$\mathbf{P}_I^{n+1} = \mathbf{P}_I^{n+\frac{1}{2}} + \frac{\Delta t}{4}\mathbf{j}(\overrightarrow{\mathcal{M}}_{I,\mathrm{int}}^{n+1} + \overrightarrow{\mathcal{M}}_{I,\mathrm{fluid}}^n)\mathbf{Q}_I^{n+1} + \frac{\Delta t}{2}\tilde{\boldsymbol{\Upsilon}}_I^{n+1}\mathbf{Q}_I^{n+1}, \tag{4.12}$$

where in (4.9), $\boldsymbol{\Upsilon}_I^n$ is a symmetric matrix such that $(\mathbf{Q}_I^{n+1})^t\mathbf{Q}_I^{n+1} = \mathbf{I}$, with $\mathbf{I}$ the identity matrix in $\mathbb{R}^3$, and in (4.12), $\tilde{\boldsymbol{\Upsilon}}_I^{n+1}$ is a symmetric matrix such that $(\mathbf{Q}_I^{n+1})^t\mathbf{P}_I^{n+1}\mathbf{D}_I^{-1} + \mathbf{D}_I^{-1}(\mathbf{P}_I^{n+1})^t\mathbf{Q}_I^{n+1} = \mathbf{0}$. The map $\mathbf{j} : \mathbb{R}^3 \to \mathbb{R}^{3\times 3}$ is such that $\mathbf{j}(\overrightarrow{x})\overrightarrow{y} = \overrightarrow{x} \wedge \overrightarrow{y}$ for all $\overrightarrow{x}$, $\overrightarrow{y} \in \mathbb{R}^3$. The force $\overrightarrow{F}_{I,\mathrm{int}}^n$ and the torque $\overrightarrow{\mathcal{M}}_{I,\mathrm{int}}^n$ result from the interaction of particle I with its neighboring particles, see [69, 81]. The behavior law is here assumed to be linear elasticity, thus the solid is characterised by the Young modulus E and by the Poisson ratio ν. The forces $\overrightarrow{F}_{I,\mathrm{fluid}}^n$ and $\overrightarrow{\mathcal{M}}_{I,\mathrm{fluid}}^n$ are respectively the fluid force and torque applied to the particle I, and are detailed in Section 4.3.3.

4.3.2.2 Definition of fluid-solid interface

The particles have a polyhedral shape and are assumed to be star-shaped with respect to their center of mass, and their faces are assumed to be star-shaped with respect to their center of mass. We define the thickness of the solid particle as the radius of its largest inscribed sphere. We assume that the solid particles have a thickness larger than or equal to two fluid grid cells. The faces of the solid particles in contact with the fluid are collected in the set $\mathfrak{F}$. A generic element of $\mathfrak{F}$ is denoted by $\mathcal{F}$ and is called a wet solid face. The fluid-solid interface consists of all the wet solid faces. Owing to the movement of the solid, the wet solid faces are time-dependent sets in $\mathbb{R}^3$, and we set $\mathcal{F}^n = \mathcal{F}(t^n)$ for all $n \geq 0$. For each wet solid face $\mathcal{F}(t)$, we consider its surface $A_{\mathcal{F}}(t)$ and its normal $\overrightarrow{\nu}_{\mathcal{F}}(t)$ (pointing from the solid to the fluid). As long as the solid deforms without fragmentation a continuous interface around the particle assembly is reconstructed as follows. A vertex a_i of the initial Discrete Element lattice belongs to one or more polyhedral particles. We define the mean vertex $\overline{a}_i$ corresponding to a_i as the average of the positions of vertex a_i under the rigid body motion of each particle which this vertex belongs to. Since the vertices $(\overline{a}_i)_i$ do not remain coplanar in general, the reconstructed fluid-solid interface is the

set of triangles supported by the center of mass of the polyhedral particle face and the mean vertices $(\overline{a}_i)_i$.

4.3.2.3 Time step constraint

The time-integration scheme for the solid being explicit, the time-step is restricted by a CFL stability condition. This condition states that the displacement of each solid particle I during one time-step should be less than the characteristic size of the particles, and the rotation during one time-step should be less than $\frac{\pi}{8}$. In the case of coupling with fluid, an additional condition applies to the displacement of the solid, requiring it to be less than one fluid grid cell size in the course of the time-step, so that the solid boundary crosses at most one fluid grid cell per time-step.

4.3.3 Fluid-solid time integration

The computational cost of the fluid and solid methods lies mainly in the evaluation of fluxes on the fluid side and of forces and torques on the solid side. Both methods being time-explicit, we use a coupling algorithm based on an explicit time-marching procedure. This is reasonable since, in particular, added mass effects are expected to play a minimal role in the present situations. At the beginning of the time-step from t^n to t^{n+1}, we know the state of the fluid U^n, the position and rotation of the solid particles $(\overrightarrow{X}_I^n, \mathbf{Q}_I^n)$, as well as the velocity of their center of mass and their angular momentum $(\overrightarrow{V}_I^n, \mathbf{P}_I^n)$. For the fluid, we need to compute, for each fluid grid cell $C_{i,j,k}$, the fluxes $F_{i\pm1/2,j,k}^{n+\frac{1}{2}}, G_{i,j\pm1/2,k}^{n+\frac{1}{2}}, H_{i,j,k\pm1/2}^{n+\frac{1}{2}}$, the volume fractions $\Lambda_{i,j,k}^{n+1}$, the side area fractions $\lambda_{i\pm1/2,j,k}^{n+1}, \lambda_{i,j\pm1/2,k}^{n+1}, \lambda_{i,j,k\pm1/2}^{n+1}$, the solid fluxes $\Phi_{i,j,k,\text{solid}}^n$, and the swept amount $\Delta U_{i,j,k}^{n,n+1}$. For the solid, we need to compute, for each solid particle I, the fluid forces $\overrightarrow{F}_{I,\text{fluid}}^{n+1}$ and the fluid torques $\overrightarrow{\mathcal{M}}_{I,\text{fluid}}^{n+1}$.

The solid flux for a fluid cut cell $C_{i,j,k}$ is given by

$$\Phi_{i,j,k,\,\text{solid}}^n = \frac{1}{V_{i,j,k}} \sum_{\{\mathcal{F}^n \in \mathfrak{F} \,|\, \mathcal{F}^{n+1} \cap C_{i,j,k} \neq \emptyset\}} \phi_{i,j,k,\mathcal{F}}^n, \tag{4.13}$$

where $V_{i,j,k}$ is the volume of $C_{i,j,k}$, and $\phi_{i,j,k,\mathcal{F}}^n$ is the solid flux attached to the wet solid face $\mathcal{F}^n$ intersecting the cell $C_{i,j,k}$ at time t^{n+1} (as indicated by the notation $\mathcal{F}^{n+1} \cap C_{i,j,k} \neq \emptyset$). To facilitate the computation of the solid flux and of the swept amount, we subdivide each solid face $\mathcal{F}$ into a set of triangles, called sub-faces and generically denoted by f (so that $\mathcal{F} = \cup f$), that are contained in one fluid grid cell (not necessary the same) at times t^n and t^{n+1}. We set $f^n = f(t^n)$ for all $n \geq 0$. The solid flux attached to the face $\mathcal{F}^n$ is then decomposed as

$$\phi_{i,j,k,\mathcal{F}}^n = \sum_{\{f^n \in \mathcal{F}^n \,|\, f^n \subset C_{i,j,k}\}} \left(0,\, \Pi_{x,f}^n,\, \Pi_{y,f}^n,\, \Pi_{z,f}^n,\, \overrightarrow{V}_f^{n+\frac{1}{2}} \cdot \overrightarrow{\Pi}_f^n\right)^t,$$

where

$$\overrightarrow{\Pi}_f^n = \left(\int_{f^n} \bar{p}_x^n \, \nu_{x,f}^n, \int_{f^n} \bar{p}_y^n \, \nu_{y,f}^n, \int_{f^n} \bar{p}_z^n \, \nu_{z,f}^n \right)^t,$$

and $\overrightarrow{V}_f^{n+\frac{1}{2}} = \overrightarrow{V}^{n+\frac{1}{2}} + \overrightarrow{\Omega}^{n+\frac{1}{2}} \wedge (\overrightarrow{X}_f^n - \overrightarrow{X}^n)$ is the velocity of the center of mass of f^n, $\overrightarrow{X}_f^n$ is the center of mass of f^n, while $\overrightarrow{V}^{n+\frac{1}{2}}$ and $\overrightarrow{\Omega}^{n+\frac{1}{2}}$ are, respectively, the average velocity and rotation velocity of the solid particle containing f. Furthermore, the swept amount is given by

$$\Delta U_{i,j,k}^{n,n+1} = \sum_{\{\mathcal{F}^n \in \mathfrak{F} \,|\, \mathcal{F}^{n+1} \cap C_{i,j,k} \neq \emptyset\}} \Delta U_{i,j,k,\mathcal{F}}^{n,n+1},$$

where the term $\Delta U_{i,j,k,\mathcal{F}}^{n,n+1}$ denotes the amount of U swept by the movement of the wet solid face $\mathcal{F}$ during the time-step from t^n to t^{n+1}. We define a piecewise affine map $\Psi_{n,n+1}$ from $\mathcal{F}^n$ to $\mathcal{F}^{n+1}$, so that each sub-face satisfies $f^n = \Psi_{n,n+1}(f^{n+1})$. Then, the swept amount $\Delta U_{i,j,k,\mathcal{F}}^{n,n+1}$ is given by

$$\Delta U_{i,j,k,\mathcal{F}}^{n,n+1} = \frac{1}{V_{i,j,k}} \sum_{\{f^{n+1} \in \mathcal{F}^{n+1} \,|\, f^{n+1} \subset C_{i,j,k}\}} \sum_{\{C_{p,q,r} \,|\, K_f \cap C_{p,q,r} \neq \emptyset\}} \mathcal{V}_{p,q,r} \, U_{p,q,r}^n, \tag{4.14}$$

where $\mathcal{V}_{p,q,r}$ is the signed volume of the intersection between the prism K_f (whose bases are f^n and f^{n+1}) and the fluid grid cell $C_{p,q,r}$. The detailed procedure to compute the above quantities is described in [89], see also [80].

The fluid force acting on the solid particle I is given by

$$\overrightarrow{F}_{I,\text{fluid}}^n = \sum_{\mathcal{F} \in \mathfrak{F}_I} \overrightarrow{F}_{\mathcal{F},\text{fluid}}^n = - \sum_{\mathcal{F} \in \mathfrak{F}_I} \overrightarrow{\Pi}_{\mathcal{F}}^n, \tag{4.15}$$

where $\mathfrak{F}_I$ collects the wet faces of the particle I. Similarly, the fluid torque $\overrightarrow{\mathcal{M}}_{I,\text{fluid}}^n$ is given by

$$\overrightarrow{\mathcal{M}}_{I,\text{fluid}}^n = \sum_{\mathcal{F} \in \mathfrak{F}_I} \overrightarrow{F}_{\mathcal{F},\text{fluid}}^n \wedge (\overrightarrow{X}_{\mathcal{F}}^n - \overrightarrow{X}_I^n). \tag{4.16}$$

The general procedure for the conservative coupling method can be described by the following steps:

- The fluid fluxes used in (4.6) are precomputed at all the cell faces of the fluid grid, without taking into account the presence of the solid.
- The solid internal forces and torques are computed based on the position of the solid particles.
- The fluid pressure forces and torques exerted on the solid are evaluated using (4.15) and (4.16).
- The solid is advanced in time.
- The volume fractions and side area fractions are computed using the new position of the fluid-solid interface. The fluid fluxes in (4.6) are modified using these volume fractions and side area fractions. At this stage, the swept amount is also calculated using (4.14).
- The solid flux is computed using (4.13), and the final value of the fluid state is calculated using (4.5).

– The small cut-cells are mixed and the solid cells are filled in order to prepare for the next time-step.

The fluid and the solid should advance with the same time-step. Thus, we use in the fluid and in the solid solvers the minimum between the fluid and the solid time-steps provided by the respective CFL stability conditions. The general structure of the time-explicit coupling scheme is summarized in Fig. 4.3.

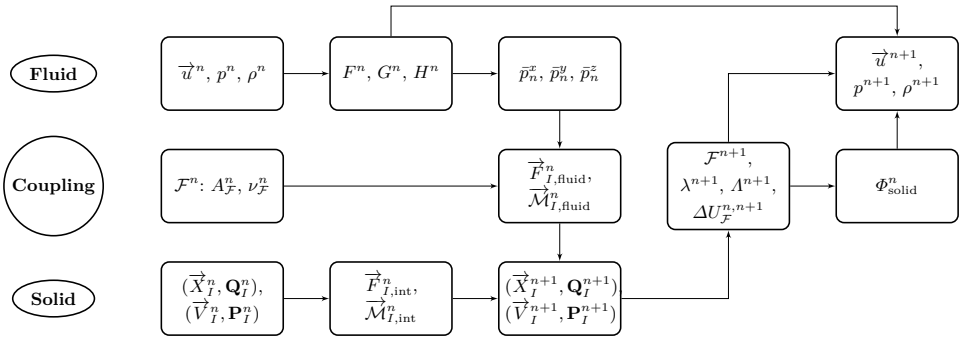

Fig. 4.3: Time-explicit coupling scheme

4.4 Coupling with fragmenting structure

4.4.1 Solid fragmentation in the Discrete Element method

The Discrete Element method deals with solid fragmentation by breaking the link between particles (Fig. 4.4). The fracture propagates element by element using a fracture criterion defined at the contact faces between particles. Dynamic fragmentation using the Discrete Element method has been studied in [73], using both the discrete Camacho–Ortiz criterion [13] and the continuous Denoual et al. criterion [22]. The Camacho–Ortiz criterion expresses damage as a function of crack opening. When the local stress reaches a threshold, it decreases linearly with the crack opening until the fracture is open. The Denoual et al. criterion is a probabilistic criterion where the damage is introduced per unit volume using a Weibull probability distribution.

In the present work, we focus on the feasibility study of the coupling method to deal with fragmentation and we choose a simple breaking criterion, namely the elongation at break of the structure, which measures the ability of the material to elongate before rupture under load. The interaction behaviour law between the particles in term of forces and torques is still taken here linear elastic in order to simplify the presentation and to verify the conservation of energy by the coupling system. More complex laws between particles can be used by integrating them in the expression of internal forces and torques between particles.

The elongation at break $A\%$ is a dimensionless quantity which is a characteristic of the material and which is determined by a tensile test. In the case of a brittle material, the rupture occurs

at the end of the elastic domain. The fracture surface is generally perpendicular to the axis of traction. The elongation at break is very low, for instance, for a cast iron it is in the range $(0.3, 0.8)$, so that a 1m long beam cracks before its elongation reaches 8 mm.

For two neighboring particles I and J, we compute the elongation at break as follows:

$$A\% = 100\,\frac{\|\overrightarrow{X}_I^n - \overrightarrow{X}_J^n\| - \|\overrightarrow{X}_I^0 - \overrightarrow{X}_J^0\|}{\|\overrightarrow{X}_I^0 - \overrightarrow{X}_J^0\|}.$$

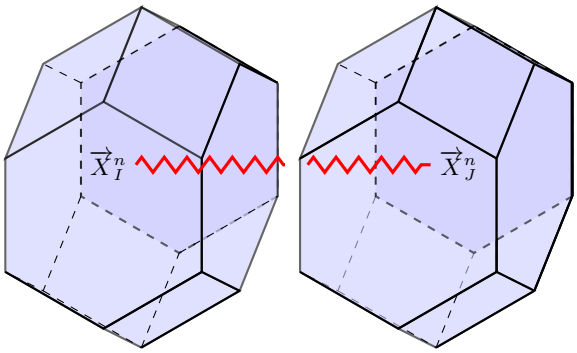

Fig. 4.4: Broken link between particles

The swept amount and the boundary reconstruction are computed for every solid face, including the internal faces for which this treatment is not necessary (since contributions from solid vis-a-vis faces cancel). This allows for an effective management of new wet faces when fracture occurs as all faces follow the same treatment. An alternative approach could be to perform these treatments only for the internal faces for which there is a potential risk of fracture (when the elongation at break is close to a critical level).

4.4.2 Vacuum cells

During the process of fragmentation, vacuum between solid particles can occur due to the fact that the velocity of the crack propagation can be larger than the speed of sound in the fluid. This leads to fluid cells where the fluid pressure and the density are close to zero. Vacuum also occurs in the case of an internal fracture in the solid with no outlet in the fluid domain. In these cases, the solid cells ($\Lambda = 1$) can become cut cells or fluid cells ($0 \leq \Lambda < 1$) because there is a gap between particles, and the fluid occupying this gap has a very low pressure and density. This leads us to consider a new type of cell, the “vacuum cell", which is characterised by $\Lambda \leq 1$ and a fluid state with vanishing density and pressure.

4.4.3 Riemann problem in the presence of vacuum

Once the link between particles is broken, the fluid should penetrate between these particles if there is a path between the fluid and the solid crack. Therefore, we have to compute the

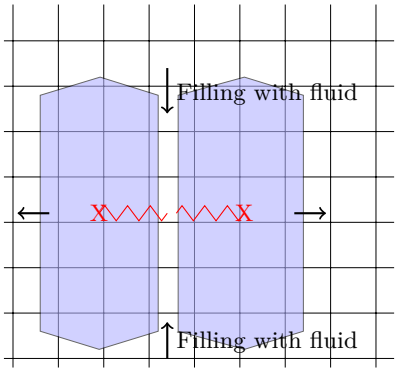

Fig. 4.5: Fluid penetration into the crack due to the broken link between two solid particles

solution of the Euler equations in domains adjacent to regions of vacuum in order to fill the space between particles with fluid.

Let us consider the one-dimensional case of a fluid occupying the region $x < 0$ and a vacuum region in $x > 0$. This leads to the following Riemann problem:

$$U(x,0) = \begin{cases} U_{\text{fluid}}, & \text{if} \quad x < 0, \\ U_{\text{vacuum}}, & \text{if} \quad x > 0, \end{cases}$$

where U_{fluid} and U_{vacuum} are the states in the fluid and vacuum regions, respectively. As in [105], we consider that $U_{\text{vacuum}} = (0, u_0, 0)$, where u_0 is the velocity of the interface between the two regions (due to the gradient of pressure) given by $u_0 = u_{\text{fluid}} + \dfrac{2c_{\text{fluid}}}{\gamma - 1}$, where c_{fluid} is the speed of sound in the fluid such that $c^2_{\text{fluid}} = \dfrac{\gamma p_{\text{fluid}}}{\rho_{\text{fluid}}}$, where u_{fluid}, ρ_{fluid}, and p_{fluid} are the velocity, mass density, and pressure in the fluid region. The analytical solution of this Riemann problem can be found in [105]. Herein, we treat the interface between a vacuum cell and a fluid cell by solving the same Riemann problem, U_{fluid} being the state of the fluid cell in contact with vacuum. This Riemann problem is solved numerically using the Lax–Friedrichs flux, given by

$$F^n_{i+1/2,j,k} = \frac{1}{2}\left(F^n_{i,j,k} + F^n_{i+1,j,k}\right) - \frac{\Delta x_{i,j,k}}{2\Delta t}\left(U^n_{i+1,j,k} - U^n_{i,j,k}\right).$$

We have chosen this flux because it does not involve any division by pressure or density. It is known that this flux is dissipative [67]. The use of the Lax–Friedrichs flux is limited around the crack region. Once a vacuum cell is filled with fluid, it is no longer a vacuum cell, and the usual OSMP flux is used in the subsequent time-steps.

4.4.4 Mixing of small cut-cells

Several solid boundaries may be present in a cut cell after the fragmentation of the solid. Let us consider the situation illustrated in Fig. 4.5. Two vis-à-vis solid particles are present in one

small cut-cell. In the direction of the outward normal to the solid boundary the cells are entirely occupied by the solid, and the neighboring cells are also small cut-cells. Therefore, the usual mixing of small cut-cells cannot be employed. To deal with this situation, we look for a target cell using a recursive algorithm. If the neighboring cells are all either solid cells or small cut-cells, we choose the neighboring cut cell with the largest face aperture as temporary target cell. We iterate until we find a fluid cell or come into a cycle (in this case the target cell is the last cell found before cycling). This ensures that there exists a target cell as well as a fluid path from the original small cut-cell to the target cell.

Let C_{target} be a fluid cell that has been found as a target cell and U_{target} the fluid state in that cell. Let $\mathcal{C}_{i,j,k}$ collect all the small cut-cells having C_{target} as target cell. Defining

$$U_{\text{Mix}} = U_{\text{target}} + \sum_{C_{i,j,k} \in \mathcal{C}_{i,j,k}} (1 - \Lambda_{i,j,k}) U_{i,j,k}, \quad \text{and} \quad V_{\text{Mix}} = 1 + \sum_{C_{i,j,k} \in \mathcal{C}_{i,j,k}} (1 - \Lambda_{i,j,k}),$$

then the new state in C_{target} is $U_{\text{target}} = \dfrac{U_{\text{Mix}}}{V_{\text{Mix}}}$. The new state for all $C_{i,j,k} \in \mathcal{C}_{i,j,k}$ is U_{target}.
The mixing procedure is conservative and ensures that the equivalent volume of a small cut-cell is compatible with the CFL condition (4.2) using the standard-size cells. The mixing procedure is not applied to the vacuum cells. For instance, if we have a vacuum cell due to an internal fracture of the solid, there will be no path between the surrounding fluid and the internal opening. In fact, the vacuum cell is just a fictive part of the fluid domain, and the fluid time-step does not have to take into account this cell.

4.5 Numerical results

In this section, we present numerical results. We first verify the conservation properties of the scheme and the propagation of the fluid in opening fractures in a three-dimensional structure. Then, we simulate the effect of an internal explosion in a steel cylinder in two space dimensions. Finally, we consider an overpressure inside a cube with mobile walls.

4.5.1 Flow through opening fractures in 3d

In this test case, we consider a three-dimensional structure composed of two particles and immersed in a fluid at rest. We assume that one particle is fixed, and that the other is displaced with a prescribed velocity, leading to an opening fracture between the two particles. As the opening velocity is high, a vacuum region is created between the two particles and is progressively filled with fluid. The fluid domain is the box $[0, 2] \times [0, 2] \times [0, 2]$m, and the initial fluid state is given by $(\rho, \overrightarrow{u}, p) = (1.4\text{kg.m}^{-3}, \overrightarrow{0}\,\text{m.s}^{-1}, 1\text{Pa})$. The computation is performed on three uniform grids with reflecting boundary conditions. The first grid contains $(75 \times 75 \times 75)$ cells, the second $(100 \times 100 \times 100)$ cells, and the third grid $(125 \times 125 \times 125)$ cells. The computation

is carried out until $t = 0.25$s. The solid is discretized with two parallelepipedic particles, having the same dimensions (0.4, 0.8, 0.8)m and their centres of mass are located at $(0.8, 1, 1)$m and $(1.2, 1, 1)$m. The first particle, i.e. the left particle, is motionless, and the second particle, i.e. the right particle, has a prescribed velocity $\overrightarrow{V} = 1\overrightarrow{e}_x \text{m.s}^{-1}$.

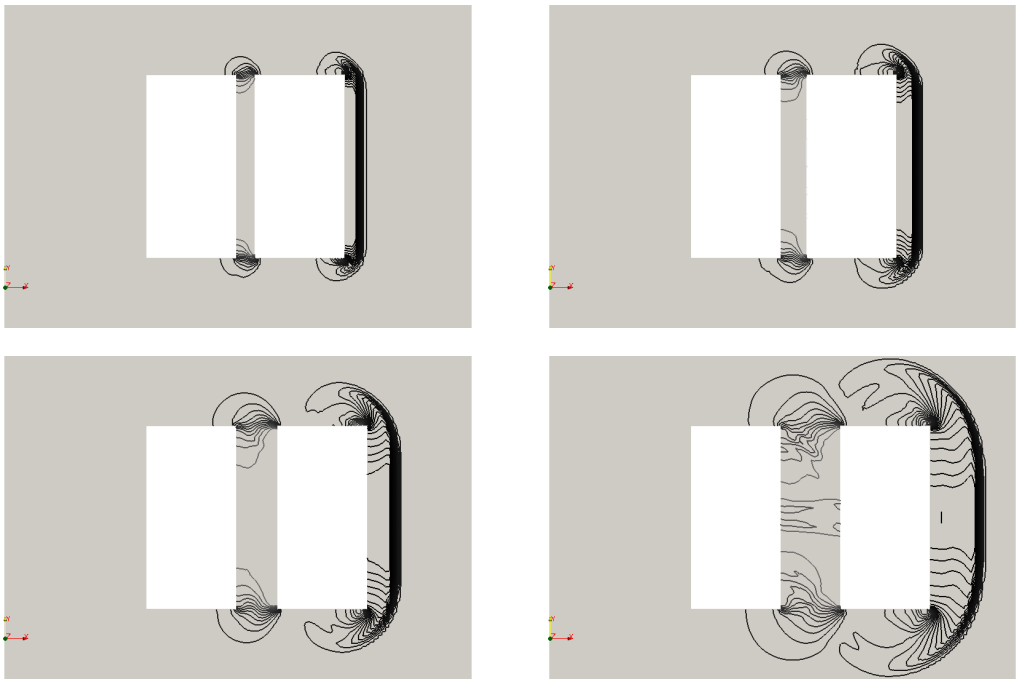

Fig. 4.6: 30 density iso-contours in the plane $\{z = 1\}$m on grid 3 at times 0.07s, 0.1s, 0.15s, and 0.25s from left to right and top to bottom.

Kinetic energy is transferred from the mobile particle to the fluid, and the particle displacement generates a compression wave in the fluid at the right of the moving particle, and a rarefaction wave propagates inside the opening fracture. In Fig. 4.6, we display 30 density iso-contours in the plane $\{z = 1\}$m at times 0.07s, 0.1s, 0.15s, and 0.25s using grid 3. At time $t = 0.07$s, the gap is filled with fluid having low density compared to the density of the external fluid. At later times, the density between the two particles increases, and shock waves propagate over the fluid domain.

The pressure distribution along the line $\{x = 1, z = 1\}$m (this line passes through the middle of the opening fracture) on grids 1, 2, and 3 is shown in Fig. 4.7 at times 0.01s and 0.12s. At time $t = 0.01$s for the three grids the opening fracture is filled with fluid. The opening fracture is very small, and the fluid cells inside the fracture are small cut-cells. The pressure variations are related to the mixing procedure applied to these small cut-cells. At time $t = 0.12$s, as the solid has continued to pull the fluid as a piston, the pressure is very low in the center of the opening fracture. The situation at the edges of the opening fracture resembles that of a shock tube: rarefaction waves are generated in the fluid near the opening edge, while compression waves

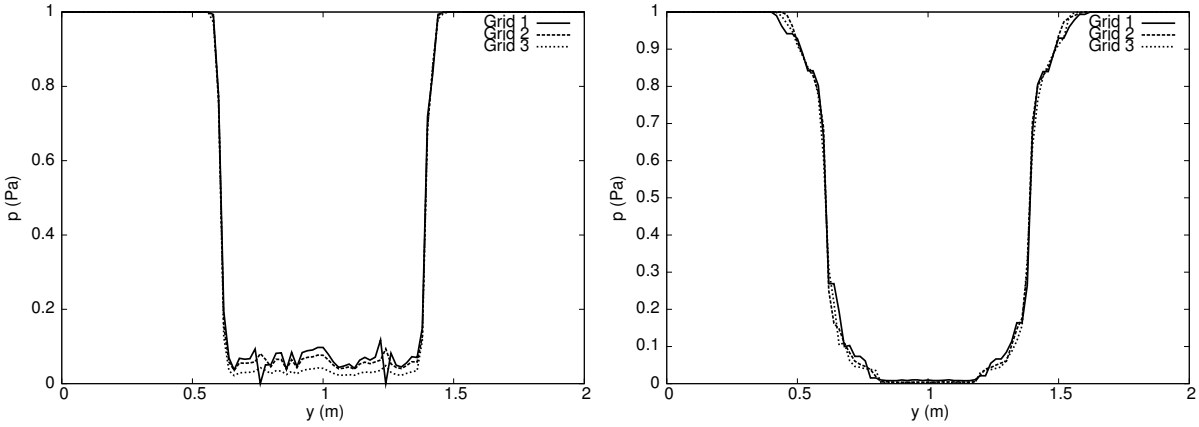

Fig. 4.7: Pressure distribution along the line $\{x = 1, z = 1\}$m on grid 1, grid 2, and grid 3 at times 0.01s (left) and 0.12s (right).

in the fracture tend to increase the pressure inside the fracture. We notice that the pressure inside the opening fracture is fairly well-converged, although the profiles remain slightly grid-dependent. The pressure difference is due to the fact that there is less numerical diffusion when the mesh is refined. The vacuum cells represent 0.2% of the total grid cells for grid 1, 0.15% for grid 2, and 0.12% for grid 3 at the opening time and progressively disappear.

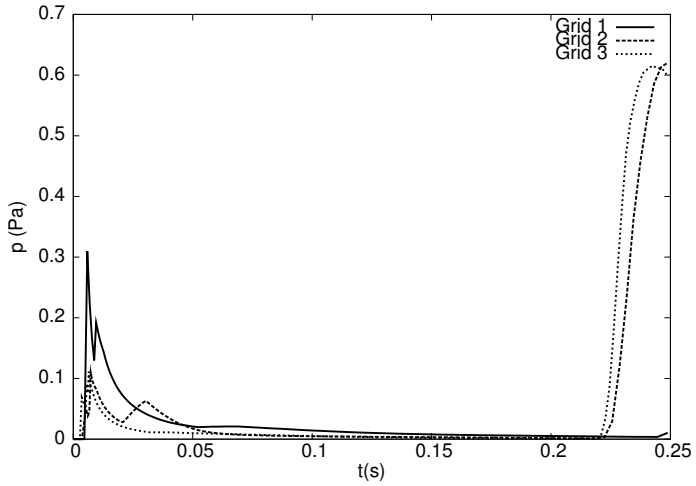

Fig. 4.8: Time evolution of the pressure in the center of the opening fracture for three fluid grids.

Fig. 4.8 illustrates the time evolution of the pressure at the point $(1, 1, 1)$m situated at the center of the opening fracture for the three fluid grids. We observe that the first peak of pressure decreases with mesh refinement. We attribute the existence of these peaks to the mixing procedure, that is grid dependent, once the vacuum cells are filled with fluid. After the time $t = 0.23$s, the pressure increases due to the compression waves that reach the face of the mobile particle (except for grid 1, in which the grid is not fine enough to fully capture these waves).

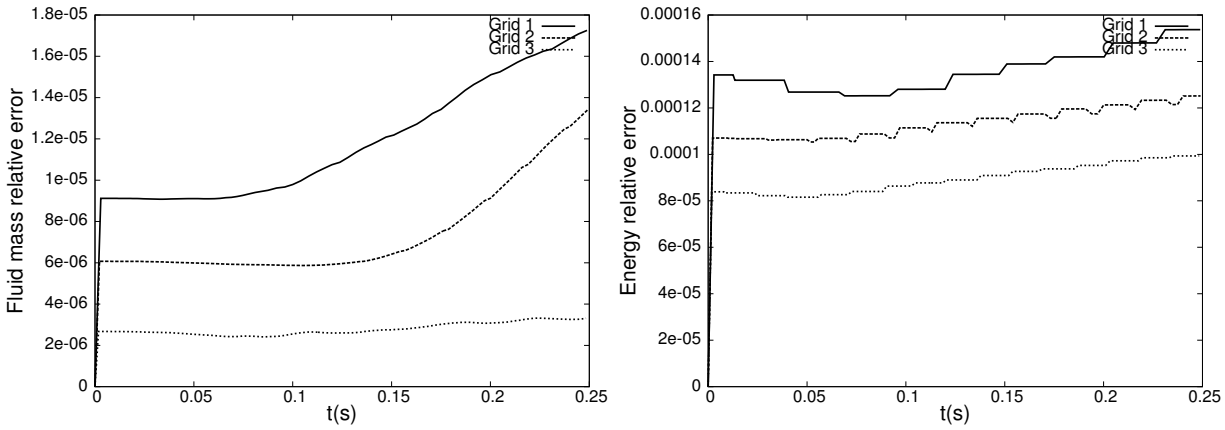

(a) (b)

Fig. 4.9: Relative conservation error on (a) fluid mass and (b) system energy for three fluid grids.

In Fig. 4.9a we present the relative conservation error of fluid mass, computed as the difference between the initial mass and the mass at the different time-steps for the three fluid grids. The mass difference is normalized by the maximum amount of mass swept by the movement of the solid. In Fig. 4.9b we present the relative energy conservation error, computed as the difference between the initial energy and the energy at the different time-steps for the three grids. This energy difference is normalized by the maximum energy exchange between the fluid and the solid. We observe that the relative conservation error on mass and energy is extremely low and decreases with grid refinement. For instance, the relative mass error is as low as 0.003%, and the relative energy error is as low as 0.01% for grid 3. The main effect accounting for mass and energy variations are the round-off errors involved in the evaluation of geometric quantities in cut cells. The variation of the energy is larger than the variation of the mass. This originates from the time-integration scheme for the solid which does not ensure the conservation of the exact discrete energy. Like many symplectic schemes, the scheme preserves an approximate discrete energy over long-time simulations. This typically induces fluctuations of the exact discrete energy of the solid around a mean value [81]. Interactions between these fluctuations and the conservative fluid occur. However, the overall conservation of energy for the system is quite satisfactory.

4.5.2 Internal explosion in a steel cylinder in 2d

In this test case, we simulate an internal explosion in a shell formed by a steel cylinder in two space dimensions. The cylinder is initially surrounded by gas at atmospheric pressure, and contains gas at the same pressure. An overpressure region is initiated inside the cylinder resulting in shock waves impinging the inner cylinder wall. The computational domain is the rectangle $[0, 30] \times [0, 15]$m. The computation is performed on a 600×300 fluid grid. The boundaries of the domain are reflecting boundaries. The cylinder is centered at $(15, 7.5)$m with a thickness of

0.2m and an interior radius of 5m. The cylinder is discretized with 50, 100, and 200 particles along its circumference and 1 particle in thickness. Initially, the state of the gas is

$$\begin{cases} \rho = 99.935\text{kg.m}^{-3},\ \overrightarrow{u} = \overrightarrow{0}\,\text{m.s}^{-1},\ p = 50,662,500\text{Pa} & \text{if } (x,y) \in D((13,7.5)\text{m}, 1\text{m}), \\ \rho = 0.118\text{kg.m}^{-3},\ \overrightarrow{u} = \overrightarrow{0}\,\text{m.s}^{-1},\ p = 10,132.5\text{Pa} & \text{otherwise,} \end{cases}$$

where $D((x_0, y_0), R)$ denotes the disk centred at (x_0, y_0) with radius R. In Fig. 4.10, we display the initial density field of the fluid and the initial position of the cylinder. The density and the Young modulus of the cylinder are, respectively, $\rho_s = 7860\text{kg.m}^{-3}$ and $E = 210\text{GPa}$, with a Poisson ratio $\nu = 0$. In this test case, the elongation at rupture is set at 1%. The simulation time is $t = 0.0244\text{s}$.

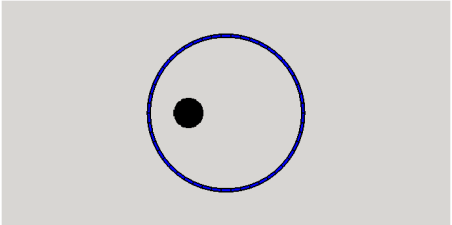

Fig. 4.10: Density profile in the fluid and cylinder position at time $t = 0\text{s}$.

After impacting the inner cylinder wall, the shock wave partially reflects, while part of its energy is transferred as kinetic energy to the cylinder. At the same time, the cylinder is deformed, and pressure waves travel along its surface. In Fig. 4.11, we show the density field in the fluid and the normal stress distribution in the cylinder at times 2.5ms, 5ms, 7ms, 13ms, 20ms, and 24.4ms when the cylinder is discretized with 50 particles. In Fig. 4.12, we show the density field in the fluid and the normal stress distribution in the cylinder at time 24.4ms when the cylinder is discretized with 100 and 200 particles. We notice that, in all three cases the rupture takes place at the left and right side of the cylinder, in approximately the same areas. Convergence of brittle fractures requires a large number of particles [73]. As the solid particles must have a thickness larger than or equal to two fluid grid cells, it would be necessary to use an adaptive meshing refinement in order to study the convergence of brittle fractures. We also notice that the fluid behavior is very similar inside the cylinder independently from the solid discretization. The main difference occurs in the regions where fluid flows through the cracks. The difference in crack patterns mainly changes the contact discontinuity pattern in the fluid outside the cylinder. The shock waves are reflected inside the cylinder and weak compression waves are transmitted by the movement of the solid outside the cylinder near the impacted regions of the cylinder. Several links between particles are broken, and the pressure waves in the solid propagate only in

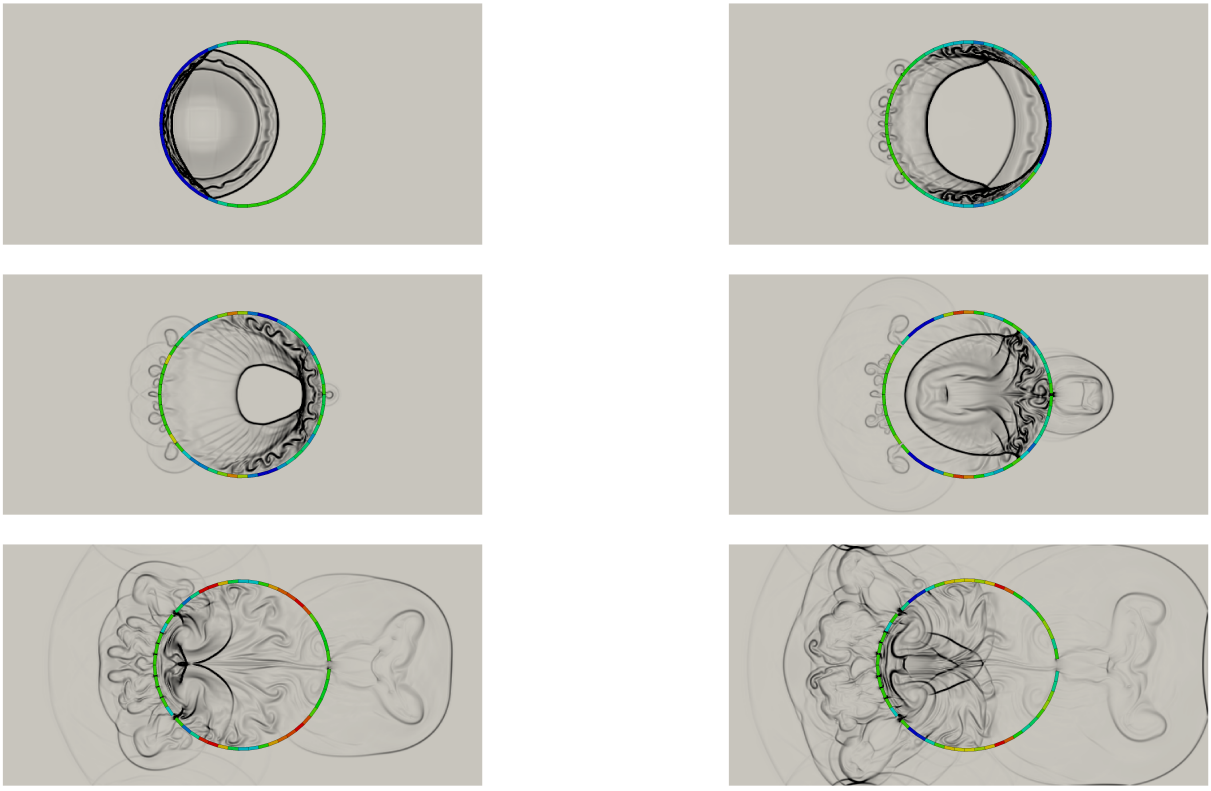

Fig. 4.11: Density field in the fluid and normal stress distribution in the cylinder discretized with 50 particles at times 2.5ms, 5ms, 7ms, 13ms, 20ms, and 24.4ms from left to right and from top to bottom.

(a) (b)

Fig. 4.12: Density field in the fluid and normal stress distribution in the cylinder discretized with (a) 100 particles and (b) 200 particles at time 24.4ms.

a few particles. We remark that the fluid penetrates into the opening gap between the particles and that the shock waves also propagate outside the cylinder. In Fig. 4.13, we illustrate the time evolution of the fluid pressure in the cell containing the point $(10, 7.5)$m situated near the particle closest to the explosion inside the cylinder and in the cell containing the center of the domain $(15, 7.5)$m for the three cylinder discretizations. In Fig. 4.13a, we notice that the pressure increases as the shock wave reaches the point, and then decreases as the shock wave is reflected by the solid boundary near this point. Peaks observed later on are due to reflected

shock waves reaching the point after several other reflections on different points of the inner solid boundary. In Fig. 4.13b, the first peak corresponds to the shock wave passing through the point. The second one corresponds to reflected shock waves that reach the point after several reflections on the inner solid boundary. This second peak is stronger than the first one due to the refocusing of shock waves inside the cylinder. We notice that the pressure patterns are remarkably similar independently from the solid discretization.

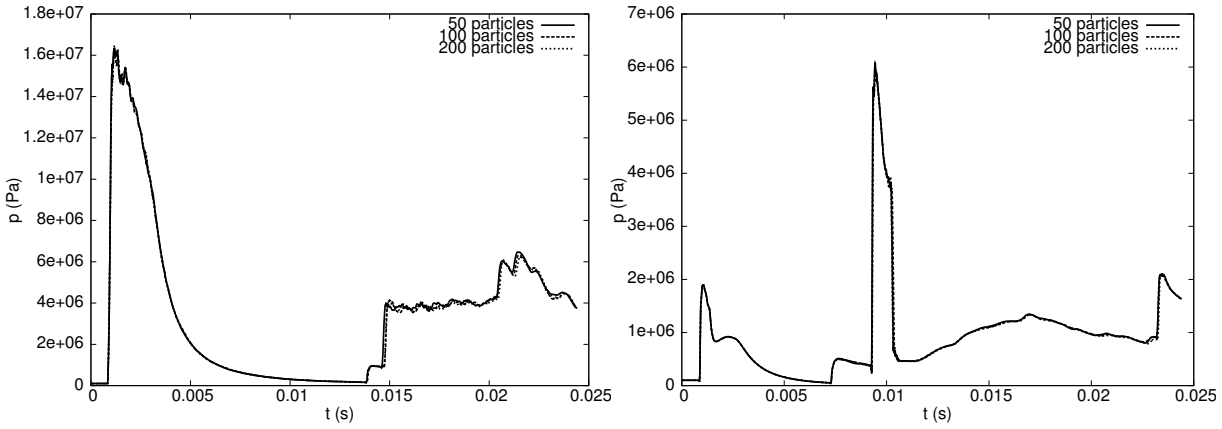

(a) (b)

Fig. 4.13: Time evolution of the fluid pressure in the cell containing (a) the point $(10, 7.5)$m situated near the particle closest to the explosion inside the cylinder and (b) the point $(15, 7.5)$m located at the center of the domain for the three cylinder discretizations.

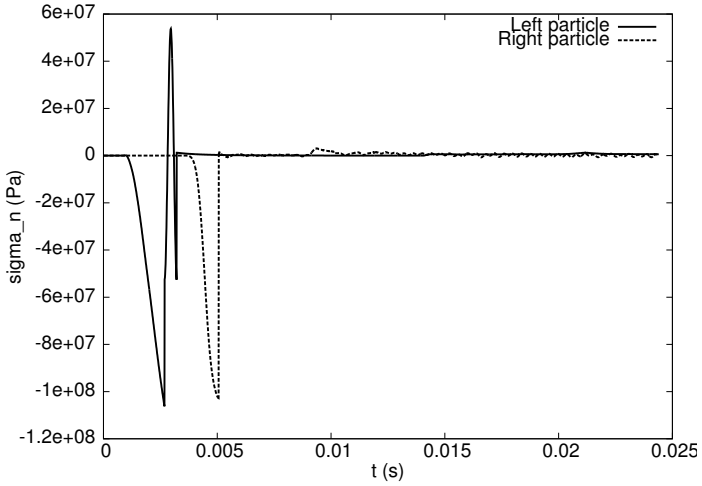

Fig. 4.14: Evolution of the normal stress in the solid particle closest to the explosion (left particle) and in the solid particle farthest to the explosion (right particle) when the cylinder is discretized with 50 particles.

Complex interaction between the waves travelling on the surface of the cylinder and the fluid occur, accounting for successive compression and traction phenomena in the cylinder leading to fractures located in the closest and farthest regions to the explosion. In Fig. 4.14, we display the time evolution of the normal stress in the solid particle closest to the explosion (centred initially at $(9.91006, 7.82023)$m) and in the solid particle farthest to the explosion (centred initially at $(20.0899, 7.82023)$m) when the cylinder is discretized with 50 particles. For the particle closest to the explosion, we notice that the normal stress decreases up to the time $t = 2.6$ms, where the link with one neighbor is broken. Immediately after this moment, the normal stress increases up to the time $t = 3.2$ms when the link with the other neighbor is broken. As the particle has no link with other particles, the normal stress gets back to zero. For the particle farthest to the explosion, the normal stress decreases and reaches its minimum value at time $t = 5$ms, where the link with one neighbor is broken. After that, the normal stress oscillates with a smaller amplitude. The link with the other neighbor is not broken as the normal stress does not reach a high enough value. The particles are enumerated counter-clockwise, the first particle being centred initially at $(20.0899, 7.82023)$m when the cylinder is discretized with 50 particles. In Tab. 4.1, we report for each broken link the number of the two involved particles and the time when the link is broken when the cylinder is discretized with 50 particles. For the particles closer to the explosion, the links are broken when the shock waves impact that region. For the particle farthest to the explosion, the links are broken when the waves travelling on the surface of the cylinder meet. In Fig. 4.15, we show the relative displacement between each particle

Particles	Time (ms)
23 - 24 25 - 26 27 - 28	2.6
20 - 21 30 - 31	2.8
24 - 25 26 - 27	3.2
22 - 23 28 - 29	3.5
1 - 50	5

Table 4.1: Broken links summary.

and its counter-clockwise neighbor at times 7ms, 13ms, 20ms, and 24.4ms when the cylinder is discretized with 50 particles. We observe that the relative displacement between linked particles remains almost zero, whereas it is not the case for the particles with broken links. In Fig. 4.16, we show the relative displacement between each particle and its counter-clockwise neighbor at time 24.4ms when the cylinder is discretized with 100 and 200 particles. Fracture is a threshold phenomenon, thus the symmetry is not exact. The more particles we have, the more breaking

links occur. We notice that fragments are similarly located in all three cases with more fragments on the left side compared to the right side.

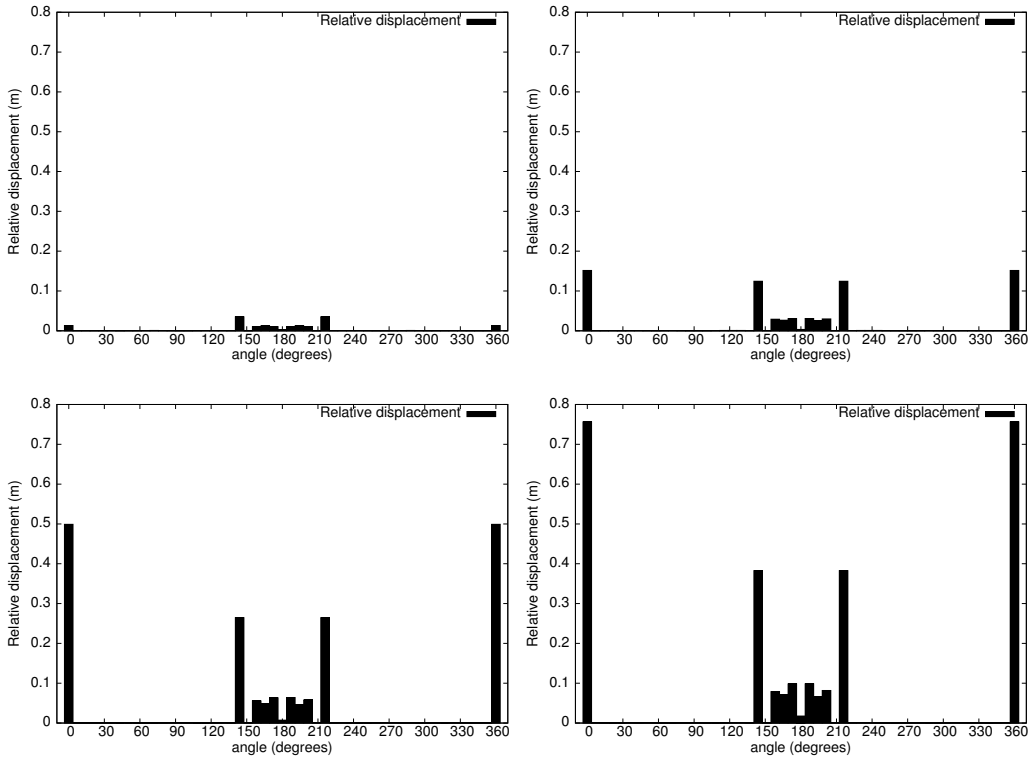

Fig. 4.15: Relative displacement between each particle and its counter-clockwise neighbor at times 7ms, 13ms, 20ms, and 24.4ms from left to right and from top to bottom when the cylinder is discretized with 50 particles.

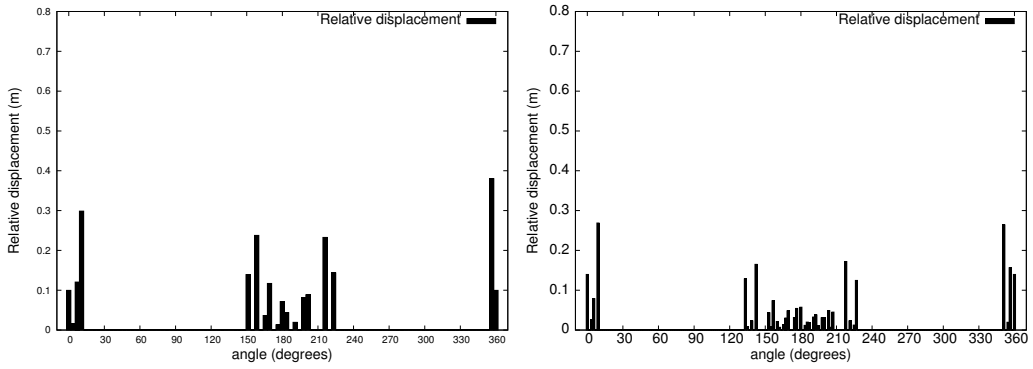

(a) (b)

Fig. 4.16: Relative displacement between each particle and its counter-clockwise neighbor at time 24.4ms when the cylinder is discretized with (a) 100 particles and (b) 200 particles.

In Fig. 4.17, we display the displacement as a function of time of the center of mass of the solid particle closest to the explosion and that of the solid particle farthest to the explosion when the cylinder is discretized with 50 particles. We notice that the closest particle begins its movement along the x-axis around the time $t = 2$ms, while the farthest particle begins its movement along the same axis later on, at time $t = 7$ms. In both cases, the times correspond to a shock wave reaching the particle. The displacement of the closest particle has larger amplitude along the x-axis. The overpressure is higher near this particle, which broke the link with both of its neighbors, followed by a ballistic flight. Concerning the displacement along the y-axis, the closest particle exhibits very little displacement compared to the farthest particle. The farthest particle is still attached to other particles and is subjected to flexion moments from the rest of the solid.

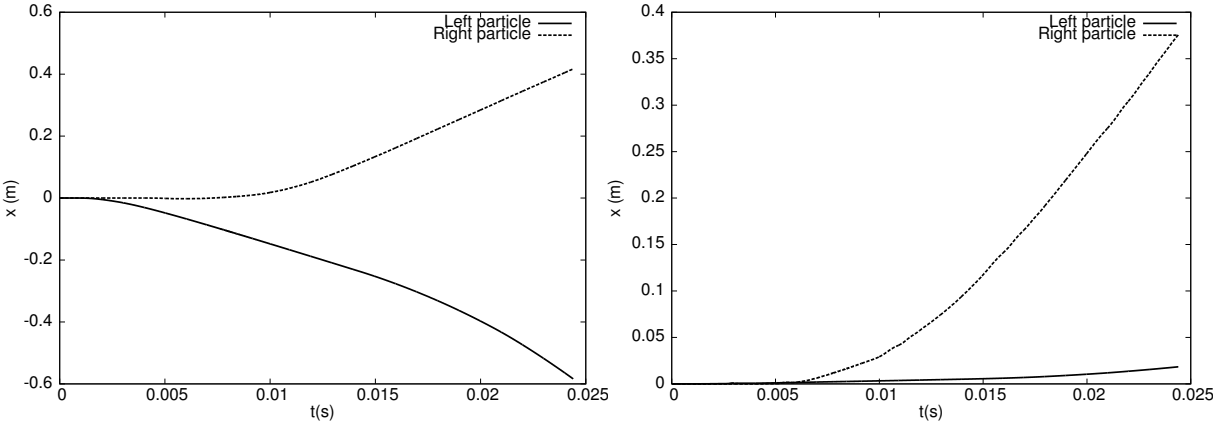

(a) (b)

Fig. 4.17: (a) x-coordinate and (b) y-coordinate of the center of mass of the solid particle closest to the explosion (left particle) and of the solid particle farthest to the explosion (right particle) as a function of time when the cylinder is discretized with 50 particles.

In Fig. 4.18, we show the time evolution of the kinetic solid energy and the dissipated energy when the cylinder is discretized with 50 particles. The dissipated energy exhibits jumps whose amplitudes correspond to energy lost by breaking links between particles. In Fig. 4.19a, we present the relative conservation error of fluid mass (computed as before) for the three cylinder discretizations. As before, the main effect accounting for this variation are the round-off errors involved in the evaluation of geometric quantities in cut cells. The variation of mass is as low as $6 \cdot 10^{-7}\%$ of the mass swept by the solid. In Fig. 4.19b, we present the relative energy conservation error, computed as the difference between the initial energy, the dissipated energy, and the energy at the different time-steps for the three cylinder discretizations. This energy difference is normalized by the maximum energy exchange between the fluid and the solid. We observe a variation of both mass and energy. As before, the main effect accounting for this variation are the round-off errors involved in the evaluation of geometric quantities in cut cells

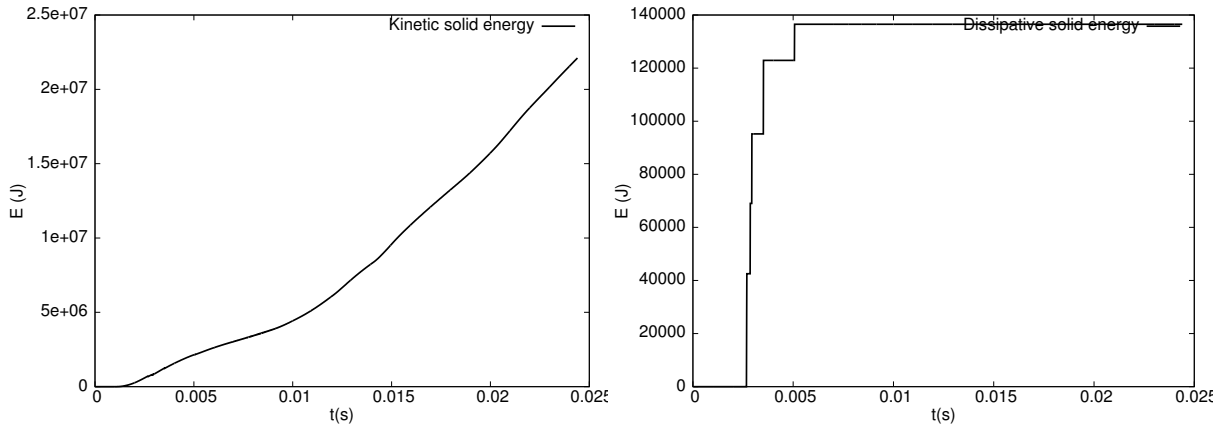

(a) Kinetic solid energy (b) Dissipated energy

Fig. 4.18: Time evolution of the kinetic solid energy and of the dissipated energy when the cylinder is discretized with 50 particles.

and the symplectic time-integration scheme for the solid. When links break, extremely rapid changes in internal forces between particles occur. As the fracture does not occur in exactly the same way for the three discretizations, the energy changes accordingly. The variation of energy is as low as 0.1% of the energy exchange in the system in all three cases, which is a very low level of error.

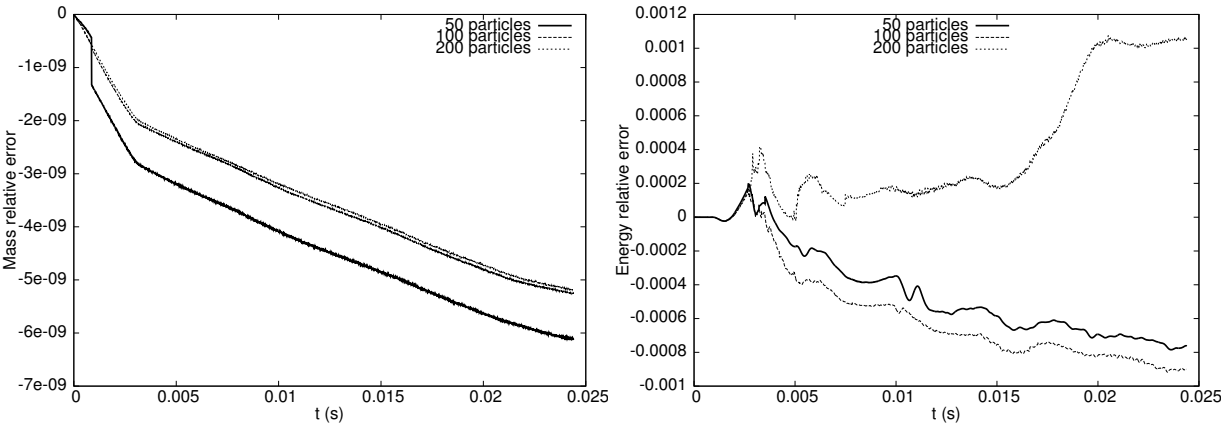

(a) (b)

Fig. 4.19: Relative conservation error on (a) fluid mass and (b) system energy for the three cylinder discretization.

4.5.3 Overpressure inside a cube with mobile walls

In this test case, an overpressure region is initiated inside a rigid cubic structure with mobile walls. In this test case, the rigid walls are not linked, but opening gaps appear between the solid walls as they are pushed away from each other by the shock wave produced by the overpressure. The fluid domain is the box $[0,\,2]\times[0,\,2]\times[0,\,2]$m, and the initial fluid state is given by

$$\begin{cases} \rho = 8.\,\mathrm{kg.m^{-3}},\ \overrightarrow{u} = \overrightarrow{0}\,\mathrm{m.s^{-1}},\ p = 116.5\,\mathrm{Pa} & \text{if } (x,y) \in D((1.1, 1., 1.), 0.1)\,\mathrm{m}, \\ \rho = 1.4\,\mathrm{kg.m^{-3}},\ \overrightarrow{u} = \overrightarrow{0}\,\mathrm{m.s^{-1}},\ p = 1\,\mathrm{Pa} & \text{otherwise}, \end{cases}$$

where $D((x_0, y_0, z_0), R)$ denotes the sphere centred at (x_0, y_0, z_0) with radius R. The computation is performed on a $(100\times100\times100)$ fluid grid with periodic boundary conditions. The simulation time is $t = 1$s. The solid is composed of six particles. Each particle is a parallelepiped representing a mobile wall of the rigid cubic structure. The particles are described in Tab. 4.2. For each particle, we indicate the initial position of its center of mass (Center), and its dimensions (Δx, Δy, and Δz).

Particle	Center (m)	Δx	Δy	Δz
1	(0.65, 1, 1)	0.1	0.8	0.6
2	(1, 0.65, 1)	0.6	0.1	0.6
3	(1, 1, 0.65)	0.8	0.8	0.1
4	(1.35, 1, 1)	0.1	0.8	0.6
5	(1, 1.35, 1)	0.6	0.1	0.6
6	(1, 1, 1.35)	0.8	0.8	0.1

Table 4.2: Characteristics of the six particles forming the cubic structure.

The overpressure generates a shock wave impinging the solid. The shock wave propagates spherically and impacts first particle 4 as it is the closest to the overpressure zone. The shock wave is partially reflected, while part of its energy is transferred as kinetic energy to the particle. In Fig. 4.20, we display density iso-contours at times 0.07s, 0.1s, 0.14s, and 0.3s. The shock waves propagate inside the cubic structure, and reflect on particles leading to their displacements. We notice the displacement of particles due to energy transfer from the fluid. This leads to a gap between particles, so that the fluid can flow outside the cubic structure.

In Fig. 4.21, we display 30 density iso-contours in the plane $(z = 1)$m at times 0.07s, 0.1s, 0.14s, and 0.3s. We notice that as soon as the displacement of the particles leads to gaps, the fluid leaks outside the cubic structure. We also observe a few weak compression waves in the exterior fluid due to the movement of the particles. In Fig. 4.22, we show the displacement as a function of time of the center of mass of each particle. For particles 1 and 4, we display the x-coordinate of their center of mass because the displacements of these particles is along the x-axis due to the symmetry of the problem. Likewise, for particles 2 and 5, we display the y-coordinate of their center of mass, and for particles 3 and 6, we display the z-coordinate of their center of

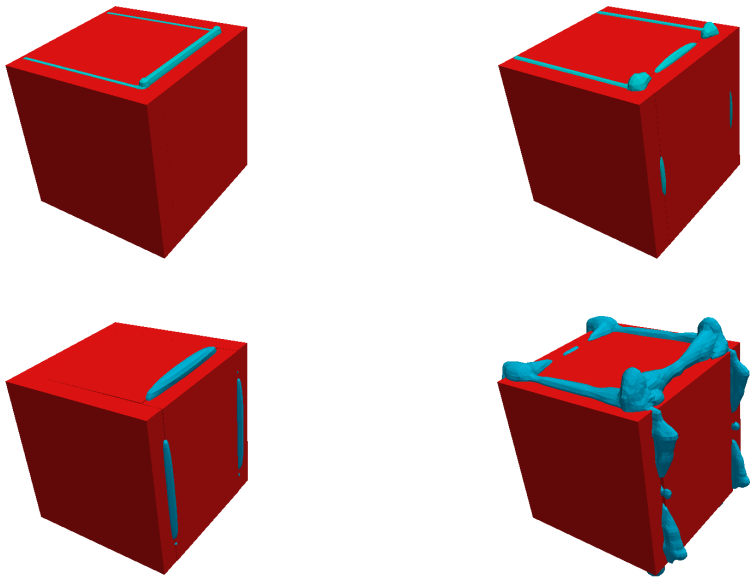

Fig. 4.20: Density iso-contours at times 0.07s, 0.1s, 0.14s, and 0.3s from left to right and from top to bottom.

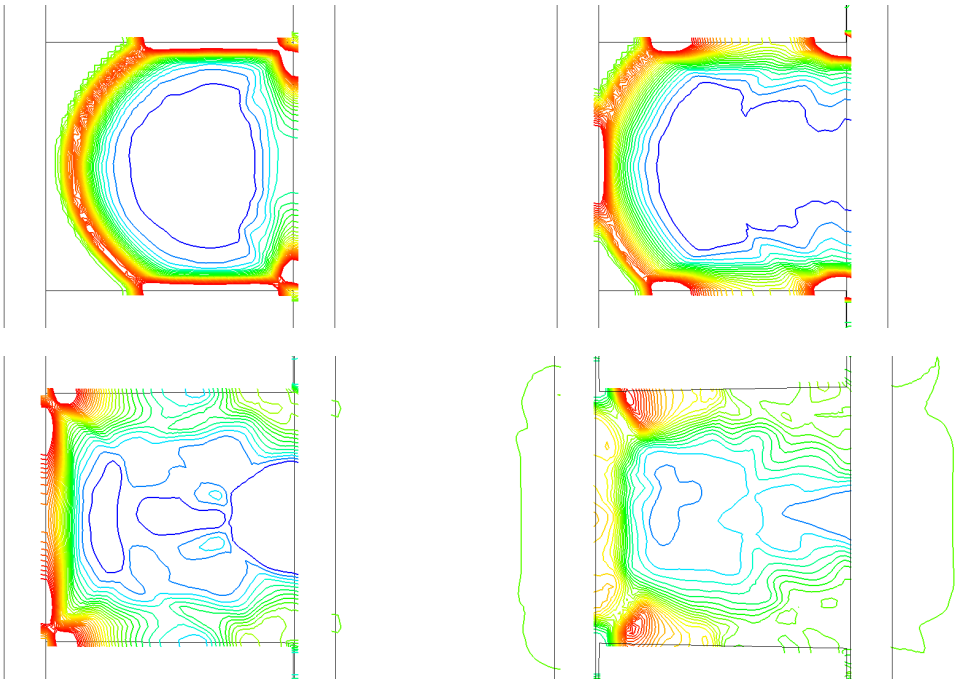

Fig. 4.21: 30 density iso-contours in the plane ($z = 1$)m at times 0.07s, 0.1s, 0.14s, and 0.3s from left to right and from top to bottom.

mass. The overpressure is almost at the center of the solid and the movement in the x, y, and z directions are of same order of magnitude. The movement of the particles is smooth despite successive impinging shock waves. This is due to the effect of particles inertia. At the end of the

simulation, the displacement of the particles is almost equal to half of the particles thickness.

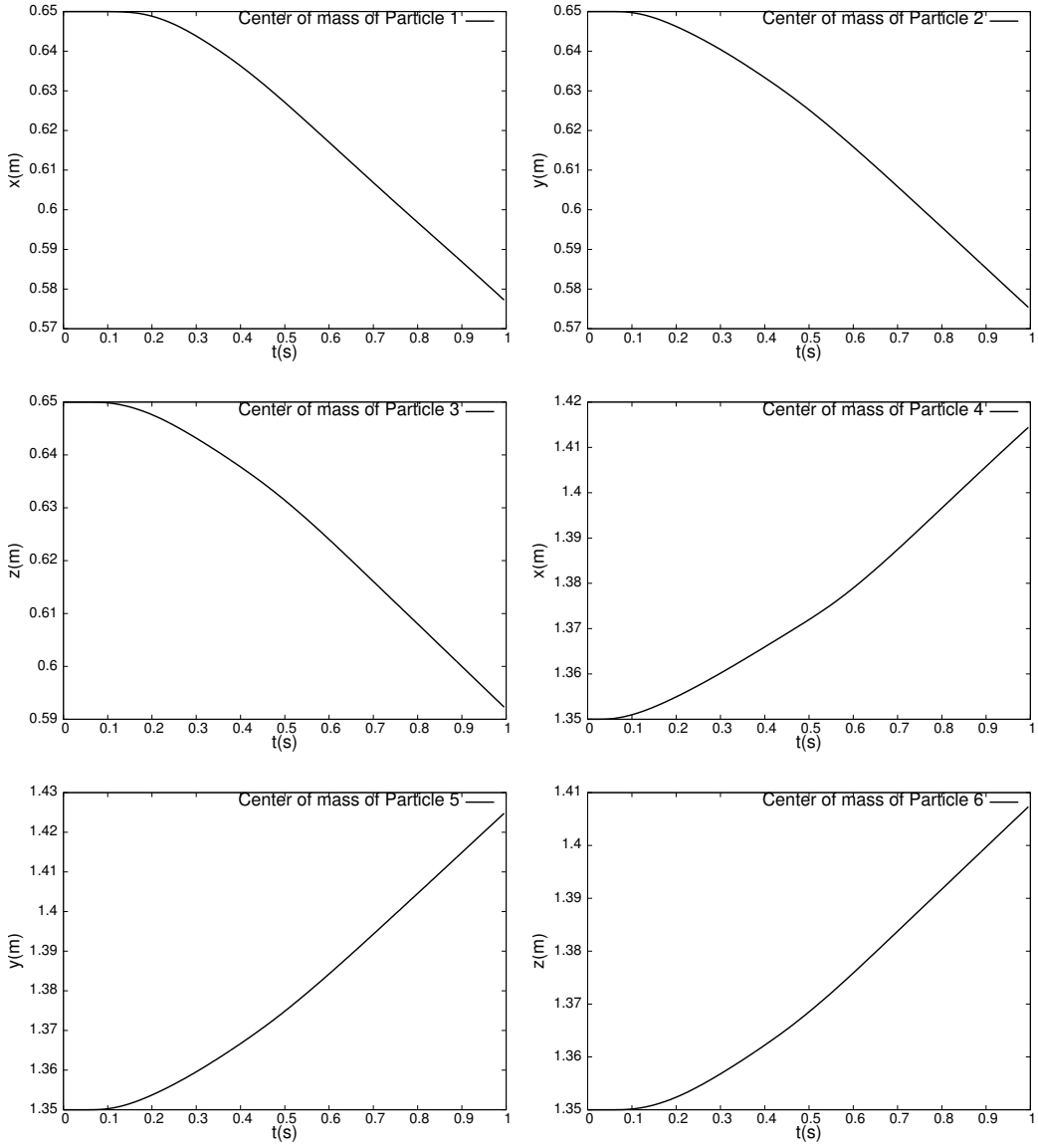

Fig. 4.22: Displacements of the center of mass for the six particles.

The pressure distribution along the line $\{x = 1.3, z = 1\}$m is shown in Fig. 4.23 at times 0.07s, 0.1s, 0.14s, 0.3s, 0.6s, and 0.9s. This line is close to the inner face of particle 4. The pressure varies along the y-axis. At time $t = 0.07$s, the pressure is high at both y-extremities of particle 4. We observe in Fig. 4.22 that the displacement of particle 4 starts around this time. At time $t = 0.1$s which corresponds to the beginning of the displacement of particles 3 and 6, pressure has soared on the extremities while it remains steady in the middle of the face of the particle. At time $t = 0.14$s which corresponds to the beginning of the displacement of particle 1, pressure has decreased even in the middle of the line (underpressure), and we notice a small compression

wave corresponding to the leaking of the fluid through the gap. At time $t = 0.3$s, pressure has slightly increased along the line due to the arrival of the reflected waves on the solid face. The fluid continues to leak between the gaps, and at time $t = 0.6$ we observe that the corresponding compression waves increase since the pressure near particle 4 decreases. At time $t = 0.9$s, the pressure is almost constant along the line.

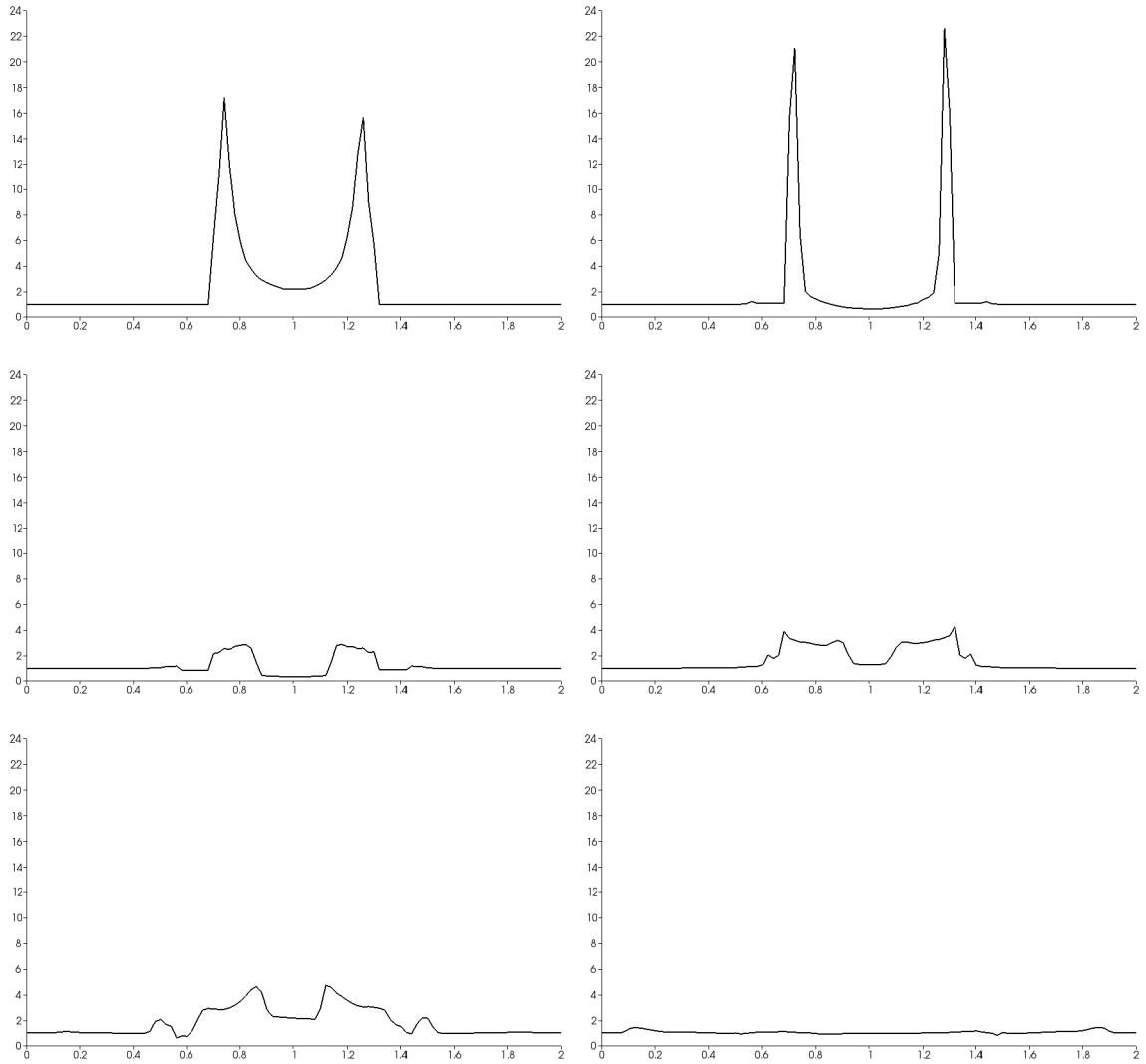

Fig. 4.23: Pressure distribution along the line $\{x = 1.3, z = 1\}$m at times 0.07s, 0.1s, 0.14s, 0.3s, 0.6s, and 0.9s from left to right and from top to bottom.

Fig. 4.24a and Fig. 4.24b illustrate the time evolution of the pressure in the cell containing the points $(1.3, 1.4, 1)$m and $(1.3, 0.6, 1)$m respectively, which are situated at the outside corners of particle 4. We observe initially a small decrease of pressure due to the fact that the fluid is sucked into the gap, then an increase of pressure due to the overpressure leaking from the cube through the opening between particles. The two curves maintain good symmetry despite the coarseness of the mesh. Fig. 4.24c illustrates the time evolution of the pressure in the cell containing the

point $(1.3, 1, 1)$m which is located inside the cubic structure and near particle 4. We observe the initial overpressure, and then the effect of the reflection of the shock waves on particles.

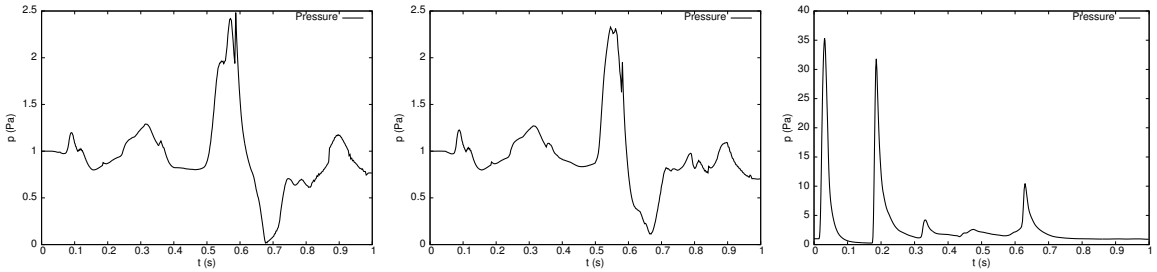

(a) (b) (c)

Fig. 4.24: Evolution of the pressure in the cells containing (a) the point $(1.3, 1.4, 1)$m, (b) the point $(1.3, 0.6, 1)$m, and (c) the point $(1.3, 1, 1)$m.

Fig. 4.25 shows the evolution of the solid energy. Part of the shock waves energy is transferred to the particles as kinetic energy. This energy increases linearly to reach the value of 0.12J at time $t = 0.7$s. In Fig. 4.26a, we present the relative conservation error of fluid mass (computed as

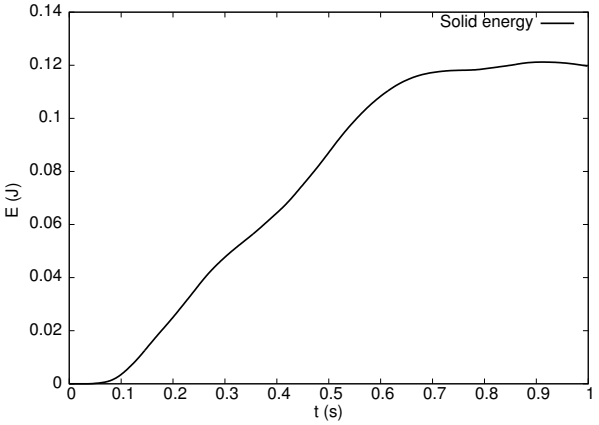

Fig. 4.25: Time evolution of the solid energy.

before), and in Fig. 4.26b, we present the relative energy conservation error (computed as before). We observe a small variation of both mass and energy. As before, the main effect accounting for this variation are the round-off errors involved in the evaluation of geometric quantities in cut cells and the symplectic time-integration scheme for the solid. The variation of mass is as low as 0.003% of the mass swept by the solid. The variation of energy is as low as 0.03% of the energy exchange in the system.

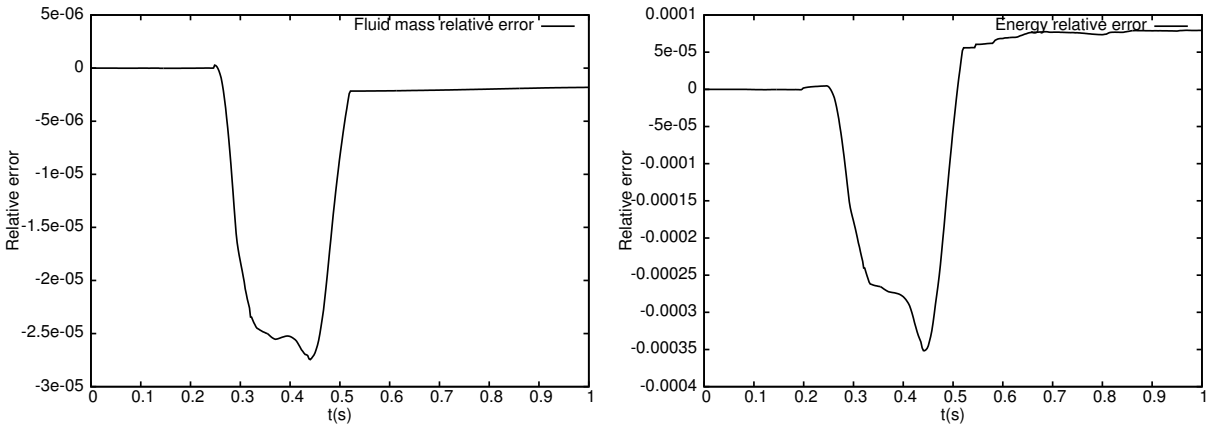

(a) (b)

Fig. 4.26: Relative conservation error on (a) fluid mass and (b) system energy.

4.6 Conclusion

In this chapter, we have developed a conservative method for the three-dimensional interaction between an inviscid compressible flow and a fragmenting structure. On the fluid side, we considered an inviscid Euler fluid in conservative form discretized by a Finite Volume method. On the solid side, we considered a fragmenting solid discretized by a Discrete Element method.

An Immersed Boundary technique was employed through the modification of Finite Volume fluxes in the vicinity of the solid. During the process of fragmentation, vacuum between solid particles can occur, and the Lax–Friedrichs flux was employed to solve the corresponding Riemann problem. The coupling algorithm is based on an explicit time-marching procedure, it does not require remeshing of the fluid or solid domain, and allows fluid to pass through the fractured areas of the structure without any a priori knowledge of where fracture occurs.

The presented numerical simulations allowed us to illustrate the viability of the method in the case of two- and three-dimensional fragmenting solids coupled to an inviscid compressible flow with fluid flows through opening cracks. The prospect for continuing this work is to enrich the algorithm to take into account the possible contact between particles during the ballistic flight after fragmentation and to move on to more complex test cases.

5

Conclusions et perspectives

Dans cette thèse, nous nous sommes intéressés à la simulation numérique de l'effet de l'arrivée d'une onde de choc aérienne sur une structure. Dans ce cadre, le fluide est compressible non-visqueux et le solide subit de grands déplacements et de grandes déformations pouvant aller jusqu'à la fragmentation. Ainsi, les méthodes les plus adaptées sont les méthodes de domaine fictif évitant le remaillage du domaine fluide. Une question importante dans l'interaction fluide compressible-structure est la conservation de la masse, de la quantité de mouvement et de l'énergie. En nous appuyant sur les méthodes de frontières immergées, nous avons développé un algorithme de couplage conservatif entre une structure tridimensionnelle déformable pouvant se fragmenter, discrétisée selon une approche de type Éléments Discrets, et un écoulement compressible non-visqueux discrétisé selon une approche de type Volumes Finis sur une grille cartésienne.

Nous avons développé différentes approches pour l'évaluation des forces et des moments fluides s'exerçant sur la surface du solide en contact avec le fluide, ce qui a conduit à deux algorithmes de couplage en temps : explicite et semi-implicite. Le coût de calcul des méthodes fluide et solide réside principalement dans l'évaluation des flux dans la méthode de Volumes Finis et des forces et moments dans la méthode des Éléments Discrets. Les algorithmes de couplage évaluent ces termes une seule fois par pas de temps, assurant ainsi l'efficacité de la méthode. Le traitement tridimensionnel du couplage pose de nombreuses difficultés géométriques (recherche et calcul des intersections entre des objets tridimensionnels, reconstruction de maillages, etc.). Nous avons présenté les algorithmes géométriques nécessaires à l'implémentation du schéma de couplage. Dans le cas de la fragmentation du solide, nous avons adapté l'algorithme de couplage afin de prendre en compte le changement de topologie, la possible apparition du vide entre les particules et la pénétration du fluide dans la fissure.

La méthode de couplage assure la conservation de la masse, de la quantité de mouvement et de l'énergie totale du système. Elle présente également des propriétés de consistance telles que la conservation du mouvement uniforme d'un solide sans rotation dans un fluide ayant la même vitesse, ainsi que l'absence d'effets de rugosité artificielle sur une paroi rigide. La méthode de couplage semi-implicite en temps a une convergence géométrique sous une condition CFL non

restrictive sur le pas de temps, et elle présente l'avantage de préserver un fluide au repos autour d'une paroi ayant des vitesses tangentielles de déformation.

Nous avons présenté des résultats numériques montrant en particulier la conservation de la masse du fluide et de l'énergie totale du système couplé, et la capacité de la méthode à gérer l'interaction entre un fluide présentant de fortes discontinuités avec d'abord un solide rigide subissant de grands déplacements (une sphère rigide mise en mouvement par une onde de choc), ensuite un solide déformable (une poutre encastrée fléchie par une onde de choc) et enfin un solide qui se fragmente (un cylindre se fragmentant sous l'action d'une explosion interne).

Afin de poursuivre ces travaux, plusieurs voies sont possibles. D'abord, développer un modèle plus riche prenant en compte des phénomènes physiques comme le contact entre particules pendant le vol balistique, les effets visqueux, les effets thermiques... Par exemple, dans le cas de la prise en compte du contact entre deux particules, il pourrait être nécessaire de revoir la reconstruction de l'interface et le calcul de la quantité balayée. Ensuite, améliorer la précision de la méthode au niveau de l'interface, par exemple en optimisant le remplissage des cellules solides et le calcul de la pression à la paroi. Les méthodes de type Ghost fluid développées dans [36], paraissent être une piste intéressante à explorer. Enfin, gagner en temps de calcul en optimisant le code (structure de données, optimisations de boucles, optimisations d'accès mémoire, etc.), en parallélisant les tâches et en utilisant des techniques d'adaptation de maillage. Cela permettrait de se rapprocher de configurations industrielles. Le raffinement de maillage adaptatif concerne principalement le fluide. Nous estimons que ce traitement ne posera pas de difficultés majeures. Enfin, la méthode de couplage étant locale au niveau de l'interface fluide-structure, une parallélisation par une technique de décomposition de domaines peut être envisagée.

Bibliographie

[1] Computational Geometry Algorithms Library. `http://www.cgal.org/`.

[2] R. Abgrall and S. Karni. *Ghost-fluids for the poor : a single fluid algorithm for multifluids*, volume 141 of *Internat. Ser. Numer. Math.*, pages 1–10. Birkhäuser, 2001.

[3] R. Arienti, P. Hung, E. Morano, and J. E. Shepherd. A level set approach to Eulerian-Lagrangian coupling. *J. Comput. Phys.*, 185 :213–251, 2003.

[4] F. P. T. Baaijens. A fictitious domain/mortar element method for fluid-structure interaction. *Int. J. Numer. Methods Fluids*, 35(7) :743–761, 2001.

[5] S. Badia, F. Nobile, and C. Vergara. Fluid–structure partitioned procedures based on Robin transmission conditions. *J. Comput. Phys.*, 227(14) :7027–7051, 2008.

[6] F. Belanger, M. P. Paidoussis, and E. De Langre. Time-marching analysis of fluid-coupled systems with large added mass. *AIAA Journal*, 33(4) :752–757, 1995.

[7] T. Belytschko. Fluid-structure interaction. *Computers & Structures*, 12(4) :459–469, 1980.

[8] B. Bourdin, G. A. Francfort, and J. J. Marigo. The variational approach to fracture. *J. Elasticity*, 91(1-3) :5–148, 2008.

[9] K. B. Broberg. *Cracks and fracture*. Academic Press, 1999.

[10] E. H. Van Brummelen. Added mass effects of compressible and incompressible flows in fluid-structure interaction. *J. Appl. Mech.*, 76(2) :021206, 2009.

[11] E. H. Van Brummelen. Partitioned iterative solution methods for fluid–structure interaction. *Int. J. Numer. Methods Fluids*, 65(1-3) :3–27, 2011.

[12] C. Michler, and S. J. Hulshoff, and E. H. Van Brummelen, and R. De Borst. A monolithic approach to fluid–structure interaction. *Computers & fluids*, 33(5) :839–848, 2004.

[13] G. T. Camacho and M. Ortiz. Computational modelling of impact damage in brittle materials. *Int. J. Solids Structures*, 33(20) :2899–2938, 1996.

[14] P. Causin, J. F. Gerbeau, and F. Nobile. Added-mass effect in the design of partitioned algorithms for fluid-structure problems. *Comput. Methods Appl. Mech. Eng.*, 194(42) :4506–4527, 2005.

[15] F. Cirak, R. Deiterding, and S. P. Mauch. Large-scale fluid–structure interaction simulation of viscoplastic and fracturing thin-shells subjected to shocks and detonations. *Computers & Structures*, 85(11) :1049–1065, 2007.

[16] F. Cirak, M. Ortiz, and A. Pandolfi. A cohesive approach to thin-shell fracture and fragmentation. *Comput. Methods Appl. Mech. Eng.*, 194(21) :2604–2618, 2005.

[17] P. Colella, D. T. Graves, B. J. Keen, and D. Modiano. A Cartesian grid embedded boundary method for hyperbolic conservation laws. *J. Comput. Phys.*, 211(1) :347–366, 2006.

[18] V. Daru and C. Tenaud. High order one-step monotonicity-preserving schemes for unsteady compressible flow calculations. *J. Comput. Phys.*, 193(2) :563–594, 2004.

[19] V. Daru and C. Tenaud. Numerical simulation of the viscous shock tube problem by using a high resolution monotonicity-preserving scheme. *Computers & Fluids*, 38(3) :664–676, 2009.

[20] P. De Palma, M. D. De Tullio, G. Pascazio, and M. Napolitano. An immersed-boundary method for compressible viscous flows. *Computers & fluids*, 35(7) :693–702, 2006.

[21] R. Deiterding, F. Cirak, and S. P. Mauch. Efficient Fluid-Structure Interaction Simulation of Viscoplastic and Fracturing Thin-Shells Subjected to Underwater Shock Loading. *International Workshop on Fluid-Structure Interaction*, page 65, 2009.

[22] C. Denoual, G. Barbier, and F. Hild. A probabilistic approach for fragmentation of brittle materials under dynamic loading. *Comptes Rendus de l'Académie des Sciences-Series IIB-Mechanics-Physics-Chemistry-Astronomy*, 325(12) :685–691, 1997.

[23] J. Dolbow, N. Moës, and T. Belytschko. An extended finite element method for modeling crack growth with frictional contact. *Comput. Methods Appl. Mech. Eng.*, 190(51) :6825–6846, 2001.

[24] J. Donea, S. Giuliani, and J. P. Halleux. An arbitrary Lagrangian-Eulerian finite element method for transient dynamic fluid-structure interactions. *Comput. Methods Appl. Mech. Eng.*, 33(1) :689–723, 1982.

[25] E. H. Dowell and K. C. Hall. Modeling of fluid-structure interaction. *Annu. Rev. Fluid Mech.*, 33(1) :445–490, 2001.

[26] D. Doyen, A. Ern, and S. Piperno. Quasi-explicit time-integration schemes for dynamic fracture with set-valued cohesive zone models. *Comput. Mech.*, 52(2) :401–416, 2013.

[27] Z. Dragojlovic, F. Najmabadi, and M. Day. An embedded boundary method for viscous, conducting compressible flow. *J. Comput. Phys.*, 216(1) :37–51, 2006.

[28] F. Dubois. Lemmes finis pour la dynamique des gaz. *http ://hal.archives-ouvertes.fr/hal-00733937*, 1998.

[29] M. Elices, G. V. Guinea, J. Gomez, and J. Planas. The cohesive zone model : advantages, limitations and challenges. *Eng. Fracture Mech.*, 69(2) :137–163, 2002.

[30] E. A Fadlun, R. Verzicco, P. Orlandi, and J. Mohd-Yusof. Combined immersed-boundary finite-difference methods for three-dimensional complex flow simulations. *J. Comput. Phys.*, 161(1) :35–60, 2000.

[31] J. Falcovitz, G. Alfandary, and G. Hanoch. A two-dimensional conservation laws scheme for compressible flows with moving boundaries. *J. Comput. Phys.*, 138(1) :83–102, 1997.

[32] C. Farhat, K. G. Van der Zee, and P. Geuzaine. Provably second-order time-accurate loosely-coupled solution algorithms for transient nonlinear computational aeroelasticity. *Comput. Methods Appl. Mech. Eng.*, 195(17) :1973–2001, 2006.

[33] C. Farhat, A. Rallu, and S. Shankaran. A higher-order generalized ghost fluid method for the poor for the three-dimensional two-phase flow computation of underwater implosions. *J. Comput. Phys.*, 227(16) :7674–7700, 2008.

[34] N. Favrie, S. L. Gavrilyuk, and R. Saurel. Solid–fluid diffuse interface model in cases of extreme deformations. *J. Comput. Phys.*, 228(16) :6037–6077, 2009.

[35] R. P. Fedkiw. Coupling an Eulerian fluid calculation to a Lagrangian solid calculation with the ghost fluid method. *J. Comput. Phys.*, 175(1) :200–224, 2002.

[36] R. P. Fedkiw, T. Aslam, B. Merriman, and S. Osher. A non-oscillatory Eulerian approach to interfaces in multimaterial flows (the Ghost Fluid method). *J. Comput. Phys.*, 152(2) :457–492, 1999.

[37] H. Forrer and M. Berger. *Flow simulation on Cartesian grids involving complex moving geometries flows*, volume 129 of *Int. Ser. Numer. Math.* Birkhäuser, 1998.

[38] C. Förster, W. A. Wall, and E. Ramm. Artificial added mass instabilities in sequential staggered coupling of nonlinear structures and incompressible viscous flows. *Comput. Methods Appl. Mech. Eng.*, 196(7) :1278–1293, 2007.

[39] L. B. Freund. *Dynamic fracture mechanics*. Cambridge University Press, Cambridge, 1990.

[40] R. Glowinski, T-W. Pan, T. I. Hesla, and D. Joseph. A distributed Lagrange multiplier/fictitious domain method for particulate flows. *Int. J. Multiphase Flow*, 25(5) :755–794, 1999.

[41] R. Glowinski, T-W. Pan, T. I. Hesla, D. Joseph, and J. Periaux. A distributed Lagrange multiplier/fictitious domain method for the simulation of flow around moving rigid bodies : application to particulate flow. *Comput. Methods Appl. Mech. Eng.*, 184(2) :241–267, 2000.

[42] R. Glowinski, T.-W. Pan, and J. Periaux. A Lagrange multiplier/fictitious domain method for the Dirichlet problem. Generalization to some flow problems. *Japan J. Indust. Appl. Math.*, 12(1) :87–108, 1995.

[43] J Grétarsson and R Fedkiw. Fully conservative, robust treatment of thin shell fluid-structure interactions in compressible flows. *J. Comput. Phys.*, 245 :160–204, 2013.

[44] J. T. Grétarsson, N. Kwatra, and R. Fedkiw. Numerically stable fluid–structure interactions between compressible flow and solid structures. *J. Comput. Phys.*, 230(8) :3062–3084, 2011.

[45] A. A. Griffith. VI. The Phenomena of Rupture and Flow in Solids. *Phil. Trans. Roy. Soc.(Lon.) A*, 221 :163–198, 1920.

[46] B. E. Griffith and C. S. Peskin. On the order of accuracy of the immersed boundary method : higher order convergence rates for sufficiently smooth problems. *J. Comput. Phys.*, 208(1) :75–105, 2005.

[47] G. P. Guruswamy and C. Byun. Direct coupling of Euler flow equations with plate finite element structures. *AIAA Journal*, 33(2) :375–377, 1995.

[48] R. D. Guy and D. A. Hartenstine. On the accuracy of direct forcing immersed boundary methods with projection methods. *J. Comput. Phys.*, 229(7) :2479–2496, 2010.

[49] E. Hairer, C. Lubich, and G. Wanner. *Geometric Numerical Integration : Structure-Preserving Algorithms for Ordinary Differential Equations*, volume 31 of *Springer Series Comput. Math.* Springer-Verlag, 2nd edition, 2006.

[50] D. Hartmann, M. Meinke, and W. Schröder. A strictly conservative Cartesian cut-cell method for compressible viscous flows on adaptive grids. *Comput. Methods Appl. Mech. Eng.*, 200(9) :1038–1052, 2011.

[51] G. Hou, J. Wang, and A. Layton. Numerical methods for fluid-structure interaction-a review. *Commun Comput Phys*, 12(2) :337–377, 2012.

[52] X. Y Hu, B. C. Khoo, N. A. Adams, and F. L. Huang. A conservative interface method for compressible flows. *J. Comput. Phys.*, 219(2) :553–578, 2006.

[53] B. Hübner, E. Walhorn, and D. Dinkler. A monolithic approach to fluid–structure interaction using space–time finite elements. *Comput. Methods Appl. Mech. Eng.*, 193(23) :2087–2104, 2004.

[54] S. R. Idelsohn, J. Marti, A. Limache, and E. Oñate. Unified Lagrangian formulation for elastic solids and incompressible fluids : application to fluid–structure interaction problems via the PFEM. *Comput. Methods Appl. Mech. Eng.*, 197(19) :1762–1776, 2008.

[55] S. R. Idelsohn, E. Oñate, F. Del Pin, and N. Calvo. Fluid–structure interaction using the particle finite element method. *Comput. Methods Appl. Mech. Eng.*, 195(17) :2100–2123, 2006.

[56] S. R. Idelsohn, F. Del Pin, R. Rossi, and E. Oñate. Fluid–structure interaction problems with strong added-mass effect. *Comput. Methods Appl. Mech. Eng.*, 80(10) :1261–1294, 2009.

[57] G. R. Irwin. Fracture. *Encyclopedia of Physics, Springer Verlag, Berlin*, 6 :551–590, 1958.

[58] P. R. Beyer Jr. A computational model of the cochlea using the immersed boundary method. *J. Comput. Phys.*, 98(1) :145–162, 1992.

[59] H. Kebir, J. M. Roelandt, and J. Foulquier. A new singular boundary element for crack problems : application to bolted joints. *Eng. Fracture Mech.*, 62(6) :497–510, 1999.

[60] J. Kim, D. Kim, and H. Choi. An immersed-boundary finite-volume method for simulations of flow in complex geometries. *J. Comput. Phys.*, 171(1) :132–150, 2001.

[61] Y. Kim and C. S. Peskin. Penalty immersed boundary method for an elastic boundary with mass. *Phys. of Fluids*, 19(5) :053103, 2007.

[62] E. De Langre. *Fluides et solides.* Editions Ecole Polytechnique, 2002.

[63] E. De Langre. Effects of wind on plants. *Annu. Rev. Fluid Mech.*, 40 :141–168, 2008.

[64] B. Lawn. *Fracture of brittle solids.* Cambridge university press, 1993.

[65] P. Le Tallec and J. Mouro. Fluid structure interaction with large structural displacements. *Comput. Methods Appl. Mech. Eng.*, 190(24) :3039–3067, 2001.

[66] P. D. Lea. *Fluid Structure Interaction with Applications in Structural Failure.* PhD thesis, Northwestern University, 2013.

[67] R. J. LeVeque. *Finite volume methods for hyperbolic problems*, volume 31. Cambridge university press, 2002.

[68] C. Mariotti. Lamb's problem with the lattice model Mka3D. *Geophysical J. Int.*, 171(2) :857–864, 2007.

[69] C. Mariotti and L. Monasse. *From general mechanics to discontinuity, unified approach to elasticity.* Presses des Ponts, 2012.

[70] B. Maurel and A. Combescure. An SPH shell formulation for plasticity and fracture analysis in explicit dynamics. *Int. J. Numer. Methods Eng.*, 76(7) :949–971, 2008.

[71] B. Maury. A fat boundary method for the Poisson problem in a domain with holes. *J. Sci. Computing.*, 16(3) :319–339, 2001.

[72] J. Mazars. *Application de la mécanique de l'endommagement au comportement non linéaire et à la rupture du béton de structure.* PhD thesis, 1984.

[73] V. Michaut. Modeling of the dynamic fragmentation using a discrete element method/ Modélisation de la fragmentation dynamique par la méthode des éléments discrets. *PhD thesis, Ecole Centrale Paris, France*, 2011.

[74] G. H. Miller and P. Colella. A conservative three-dimensional Eulerian method for coupled solid–fluid shock capturing. *J. Comput. Phys.*, 183(1) :26–82, 2002.

[75] R. Mittal and G. Iaccarino. Immersed boundary methods. *Annu. Rev. Fluid Mech.*, 37 :239–261, 2005.

[76] J. Mohd-Yusof. Combined immersed-boundary/b-spline methods for simulations of flow in complex geometries. *Annual Research Briefs. Center of Turbulence Research, NASA Ames/Stanford Univ.*, pages 317–327, 1997.

[77] J. F. Molinari, G. Gazonas, R. Raghupathy, A. Rusinek, and F. Zhou. The cohesive element approach to dynamic fragmentation : the question of energy convergence. *Int. J. Num. Meth. Eng.*, 69(3) :484–503, 2007.

[78] J. J. Monaghan. An introduction to SPH. *Comput. Phys. Communications*, 48(1) :89–96, 1988.

[79] L. Monasse. Analyse d'une méthode de couplage entre un fluide compressible et une structure déformable. *PhD thesis, University Paris-Est, France*, 2011.

[80] L. Monasse, V. Daru, C. Mariotti, S. Piperno, and C. Tenaud. A conservative coupling algorithm between a compressible flow and a rigid body using an Embedded Boundary method. *J. Comput. Phys.*, 231(7) :2977–2994, 2012.

[81] L. Monasse and C. Mariotti. An energy-preserving Discrete Element Method for elastodynamics. *ESAIM, Math. Model. Numer. Anal.*, 46 :1527–1553, 2012.

[82] W. F. Noh. Fundamental Methods of Hydrodynamics. *Methods of Computational Physics*, 3 :117–179, 1964.

[83] H. O. Nordhagen, S. Kragset, T. Berstad, A. Morin, C. Dørum, and S. T. Munkejord. A new coupled fluid–structure modeling methodology for running ductile fracture. *Computers & Structures*, 94 :13–21, 2012.

[84] R. B. Pember, J. B. Bell, P. Colella, W. Y. Crutchfield, and M. L. Welcome. An adaptive Cartesian grid method for unsteady compressible flow in irregular regions. *J. Comput. Phys.*, 120(2) :278–304, 1995.

[85] C. S. Peskin. Numerical analysis of blood flow in the heart. *J. Comput. Phys.*, 25(3) :220–252, 1977.

[86] C. S. Peskin. The immersed boundary method. *Acta numerica*, 11, 2002.

[87] T. J. Poinsot and S. K. Lele. Boundary conditions for direct simulations of compressible viscous flows. *J. Comput. Phys.*, 101 :104–129, 1992.

[88] D. O. Potyondy and P. A. Cundall. A bonded-particle model for rock. *Int. J. Rock Mech. Mining Sciences*, 41(8) :1329–1364, 2004.

[89] M. A. Puscas and L. Monasse. A three-dimensional conservative coupling method between an inviscid compressible flow and a moving rigid solid. *Submitted, http ://hal.archives-ouvertes.fr/hal-00974602*, 2014.

[90] M. A. Puscas, L. Monasse, A. Ern, C. Tenaud, and C. Mariotti. A conservative Immersed Boundary method for an inviscid compressible flow coupled with a fragmenting structure. *Submitted, http ://hal.archives-ouvertes.fr/hal-01071619*, 2014.

[91] M. A. Puscas, L. Monasse, A. Ern, C. Tenaud, C. Mariotti, and V. Daru. Conservative coupling method between an inviscid compressible flow and a deformable structure. *Submitted, http ://hal.archives-ouvertes.fr/hal-00993324*, 2014.

[92] T. Rabczuk, R. Gracie, J.-H. Song, and T. Belytschko. Immersed particle method for fluid–structure interaction. *Int. J. Numer. Methods Engineering*, 81(1) :48–71, 2010.

[93] P. W. Randles and L. D. Libersky. Smoothed particle hydrodynamics : some recent improvements and applications. *Comp. Meth. Appl. Mech. Eng.*, 139(1) :375–408, 1996.

[94] P. B. Ryzhakov, R. Rossi, S. R. Idelsohn, and E. Oñate. A monolithic Lagrangian approach for fluid–structure interaction problems. *Comput. Mech.*, 46(6) :883–899, 2010.

[95] S. K. Sambasivan and H. S. UdayKumar. Ghost Fluid method for strong shock interactions Part 2 : Immersed solid boundaries. *AIAA J.*, 47(12) :2923–2937, 2009.

[96] E. Schlangen and E. J. Garboczi. Fracture simulations of concrete using lattice models : computational aspects. *Eng. Fracture Mech.*, 57(2) :319–332, 1997.

[97] P. Schwartz, M. Barad, P. Colella, and T. Ligocki. A Cartesian grid embedded boundary method for the heat equation and Poisson's equation in three dimensions. *J. Comput. Phys.*, 211(2) :531–550, 2006.

[98] X. Shi and N. Phan-Thien. Distributed Lagrange multiplier/fictitious domain method in the framework of lattice Boltzmann method for fluid–structure interactions. *J. Comput. Phys.*, 206(1) :81–94, 2005.

[99] A. Soria and F. Casadei. Arbitrary Lagrangian–Eulerian multicomponent compressible flow with fluid–structure interaction. *Int. J. Numer. Methods Fluids*, 25(11) :1263–1284, 1997.

[100] G. Strang. On the construction and comparison of difference schemes. *SIAM Journal Numer. Anal.*, 5(3) :506–517, 1968.

[101] N. Sukumar and T. Belytschko. Arbitrary branched and intersecting cracks with the extended finite element method. *Int. J. Numer. Meth. Eng.*, 48 :1741–1760, 2000.

[102] J. W. Swegle and S. W. Attaway. On the feasibility of using smoothed particle hydrodynamics for underwater explosion calculations. *Comput. Mech.*, 17(3) :151–168, 1995.

[103] P. Le Tallec and M. Tidriri. Convergence analysis of domain decomposition algorithms with full overlapping for the advection-diffusion problems. *Math. Comput.*, 68(226) :585–606, 1999.

[104] M. D. Tidriri. Domain decomposition for compressible navier-stokes equations with different discretizations and formulations. *J. Comput. Phys.*, 119(2) :271–282, 1995.

[105] E. F. Toro. *Riemann solvers and numerical methods for fluid dynamics*, volume 16. Springer, 1999.

[106] Y. H. Tseng and J. H. Ferziger. A ghost-cell immersed boundary method for flow in complex geometry. *J. Comput. Phys.*, 192(2) :593–623, 2003.

[107] J. Vierendeels, K. Dumont, and P. R. Verdonck. A partitioned strongly coupled fluid-structure interaction method to model heart valve dynamics. *J. Comput. Appl. Math.*, 215(2) :602–609, 2008.

[108] K. Wang, A. Rallu, J. F. Gerbeau, and C. Farhat. Algorithms for interface treatment and load computation in embedded boundary methods for fluid and fluid–structure interaction problems. *Int. J. Numer. Methods Fluids*, 67(9) :1175–1206, 2011.